Simulating Radiation Effects in Iron with Embedded Oxide Nanoparticles

by

Tomas Lazauskas

A Doctoral Thesis
Submitted in partial fulfilment of the requirements for the award of
Doctor of Philosophy of Loughborough University

July 2014

Abstract

Alloys used in fission and in future fusion reactors are subjected to extreme conditions including high temperatures, corrosive and intense radiation environments. Understanding the processes occurring at the microscopic level during radiation events is essential for the further development of them. As a prospective candidate material for new reactors, oxide dispersion strengthened (ODS) steels have shown good radiation resistance and the ability to trap He into fine scale bubbles, thus preventing swelling and preserving high-temperature strength. This thesis represents the findings obtained by performing computational studies of radiation effects in pure iron, Y-Ti-O systems and a simplified model of ODS using Molecular Dynamics (MD) and on-the-fly Kinetic Monte Carlo (otf-KMC) techniques.

MD studies of radiation damage were carried out in a perfect body-centred cubic (bcc) iron matrix (α-Fe) in which yttria nanoparticles are embedded as a simplified model of an ODS steel. The results have shown how the nanoparticles interact with nearby initiated collision cascades, through cascade blocking and energy absorption. Fe defects accumulate at the interface both directly from the ballistic collisions and also by attraction of defects generated close by. The nanoparticles generally remain intact during a radiation event and release absorbed energy over times longer than the ballistic phase of the collision cascade. Also the nanoparticles have shown ability to attract He atoms as a product of fission and fusion reactions. Moreover, studies showed that He clusters containing up to 4 He atoms are very mobile and clusters containing 5 He or more become stable by pushing an Fe atom out of its lattice position.

The radiation damage study in the Y-Ti-O materials showed two types of residual damage behaviour: when the damage is localized in a region, usually close to the initial primary knock-on atom (PKA) position and when PKA is directed in the channelling direction and creates less defects compared to the localised damage case, but with a wider spread. The Y_2TiO_5 and $Y_2Ti_2O_7$ systems showed increased recombination of defects with increased temperature, suggesting that the Y-Ti-O systems could have a higher radiation resistance at higher temperatures.

The otf-KMC technique was used to estimate the influence of the prefactor in the Arrhenius equation for the long time scale motion of defects in α-Fe. It is shown that calculated prefactors vary widely between different defect types and it is thus important to determine these accurately when implementing KMC simulations. The technique was also used to study the recombination and clustering processes of post-cascade defects that occur on the longer time scales.

Acknowledgements

Firstly I would like to express my gratitude to Gerda Nagrodskytė and my family for their unlimited support during this research and in all my pursuits. I am also very grateful to my supervisors Prof. Roger Smith and Prof. Steven Kenny for giving the opportunity to undertake this PhD and also for providing continued support and guidance. I owe my special thanks to the individuals at Loughborough University, especially in the materials modelling group, who during the course of my studies provided help, encouragement and friendship.

I must also thank Zainab Al Tooq for the help getting started with the project and very productive discussions, Chris Scott for developing the atomic visualisation software and his and Miao Yu's collaboration during the software development, Xiao Gai for the joint work on the He bubbles formation, Marc Robinson for the atomic visualisation and analysis software, Louis Vernon for the initial work on the kinetic Monte Carlo technique and Dr. Carlos F. Sanz-Navarro for the development of the Loughborough Molecular Dynamics package.

Finally, I would like to acknowledge the financial support by EPSRC with Chris Grovenor, Oxford University, the Department of Mathematical Sciences at Loughborough University for providing the necessary facilities for the research and the Loughborough High Performance Computing centre for the computational resources.

Contents

List of Figures

List of Tables

Chapter 1

Introduction and Background

Rapidly growing energy demand and worldwide depletion of fossils fuels force mankind to investigate other energy sources such as nuclear energy. Fission and promising future fusion reactors is one such source, that does not emit greenhouse gasses. Alloys used in these reactors service under extreme conditions like high temperature, chemically reactive and intense radiation environments. This causes severe damage to reactor structures and degrades their physical and mechanical properties. Therefore there is high demand for structural alloys with outstanding properties in order to improve the safety of nuclear reactors and also extend their service time.

Candidate materials for the generation IV reactors include ferritic/martensitic (F/M) steels, austenitic stainless steels, Ni-base alloys and oxide dispersion strengthened (ODS) steels [1]. All these materials have their advantages and disadvantages that must be considered. F/M steels are designed by balancing of ferritic and austenitic stabilizing alloying elements. These steels have good void swelling and creep resistance and also fast radioactive decay, so are friendly to the environment. The biggest concern is their embrittlement at 400 °C and low long-term creep rupture strength at higher temperatures. Austenitic stainless steels show good resistance to creep and corrosion, but suffer from void swelling in a moderate radiation environment. Ni-base alloys are excellent for high temperature applications due

to their high temperature strength and have good creep rupture properties. The drawbacks of these alloys are embrittlement and swelling under neutron radiation environment [2, 3]. ODS alloys have shown good radiation resistance, entrapment of He into fine scale bubbles to avoid swelling and high-temperature strength. They are made through a rather complex mechanical alloying process and their properties are still not fully understood, especially the atomistic processes and mechanisms that are responsible for the better performance by ODS alloys in intense radiation environments. A primary aim of the thesis is to investigate these materials using advanced computational techniques.

1.1 ODS Steels

The development of ODS steels has began in late 1960's and in last decades they became one of the main potential materials for nuclear applications. In order to produce these novel alloys a complicated manufacturing process must be followed, which common steps are given in Figure 1.1 [4, 5].

First, the mixture of different powders is deformed by ball milling, which results in a mechanical alloy with supersaturated precipitates of dissolved Y and O with Ti during hot consolidation. Before the hot consolidation using hot extrusion or hot isostatic pressing (HIPping), the ball milled powder must be canned and degassed. To improve the microstructures of the grains, a sequence of post-extrusion cold and hot workings along with heat treatments are performed on the product.

A usual composition of an ODS alloy is 0.2-0.5 wt% Y_2O_3, 0.2-1.0 wt% Ti, 1-3 wt% W and the rest is Fe. Often addition of 12-14 wt% Cr is used to increase the corrosion-oxidation resistance, where W provides solid solution hardening and Ti is responsible for the formation of fine complex oxides and their homogeneous distribution [7]. The nanoparticles act as a sink for He, by entrapping it into fine scale bubbles, thus providing resistance to embrittlement and void swelling at lower temperatures [5]. Another very important property

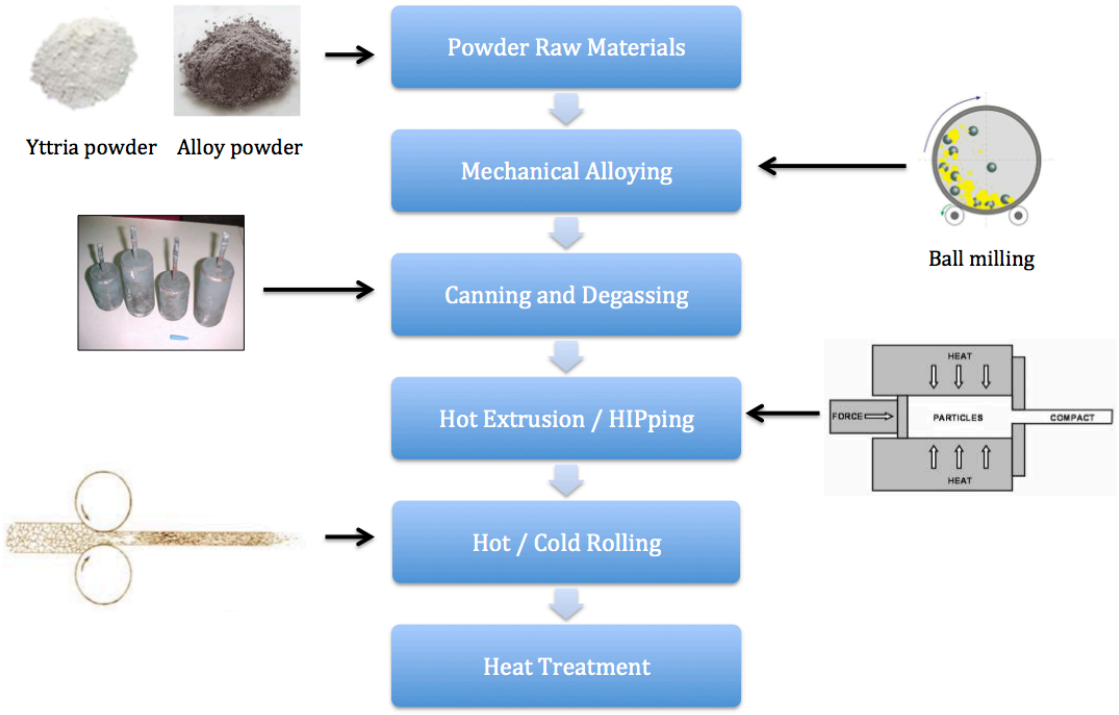

Figure 1.1: The common process of manufacturing ODS alloy. Adopted from [6].

of these nanoparticles is the suppression of the radiation damage to the material.

1.2 Previous Work and Research Aims

Over recent years ODS steels have been studied by scientists around the world as a potential material for the next-generation fusion and future fission reactors. They have shown excellent structural and chemical stability at high temperature and in chemically reactive environments, high creep resistance and are relatively stable under intense neutron radiation. This means that they have potential for an extended service time compared to existing materials in severe radiation conditions [5, 8, 9, 10].

Although there have been a number of experimental studies performed to investigate ODS steel's performance under irradiation [8, 11], the processes that are responsible for the radiation resistant properties and the role of the embedded nanoparticles are still unclear.

The experiments show that compared to base material, ODS steels are more resistant to

radiation damage and that radiation induced defects are similar as reported in ferritic steels. A few suggestions to explain the better ODS performance are summarized by Schäublin *et al.* [11]: oxide particles provide a high number of trapping sites for structural defects; oxide particles bring disorder to the system and systems accumulate less damage in structures when they already contain defects; oxide particles act as sinks for radiation induced defects and provide a catalyst for recombination. Also quite few studies showed that oxide particles are not influenced or influenced insignificantly by irradiation, e.g. by Fe-ion with 0.7 displacements per atom (dpa) [12], by 2.5-15 dpa with neutrons at 670-807K [13], by 5 MeV Ni ions at 500-700°C to doses up to 150 dpa [14]. [14] also reported a reduction in particle size and an increase of their density with increasing irradiation dose.

There are a very limited amount of results from modelling the mechanisms that appear during radiation damage in ODS steels. A recent study by Bodrick *et al.* [15] using Density Functional Theory (DFT) investigated the oxide particle-recombination catalyst behaviour and the results showed the interface between Fe and Y_2O_3 has a long range attraction for structural defects, acting as a strong sink for the defects and allowing recombination.

The other important property of ODS steels, which is also not fully understood, is the ability to entrap He into fine scale bubbles. He atoms are a product of fission and fusion reactions and have a great influence on the bulk microstructures and the alloys used in first wall and blanket structures in fusion and future fission energy systems [16, 17]. Due to the low solubility, helium has a strong tendency to reside in the materials in a form of helium-vacancy clusters or being trapped at the grain boundaries or precipitate interfaces. ODS steels have shown the ability to trap helium into small, high pressure bubbles, thus reducing the amount of He reaching the grain boundaries or sitting in thermally stable helium-vacancy clusters [18].

The behaviour of helium in Fe has been widely investigated by various groups [19, 20, 21], where the studies were carried out to determine such properties as the diffusion behaviour of He interstitials and He clusters, He clustering, the role of helium-to-vacancy ratio in

He clustering etc. Also recent experimental studies have been carried out to study helium bubbles in nanostructured ferritic alloys [22, 23, 24], where the findings show increased helium concentration on nanoparticles, indicating a reduction in He bubble size, thus preventing these alloys from embrittlement.

Even though there are quite extensive experimental studies of helium in ODS materials, this is not the case with the results from modelling. Earlier works studied helium migration in α-Fe, where very low migration energies for He atom were observed, $E_m \approx 0.08eV$ [25]. Only recently improved interatomic potentials to describe He-He and He-Fe interactions were developed [26, 27] and atomistic studies of nucleation of He clusters [21] and He defect binding energies [28] were carried out. The situation with the studies of the effects of helium in ODS by applying atomistic models is even more complicated, since there are no studies published.

In addition, recent work by Barnard *et al.* [29] showed that Y-Ti-O nanoparticles in ODS are more likely to be small oxide phases rather than solute-enriched clusters, thus in this work Y-Ti-O systems are also ivestigated as bulk oxide systems in order to look into the processes occurring during the ballistic phase of radiation damage events. Work by Zhang *et al.* [30] showed that the fluorite Y_2TiO_5 structure is a very radiation-resistant composition with fairly low critical amorphization temperature. Also, it has been suggested that Y_2TiO_5 and $Y_2Ti_2O_7$ may adopt the orthorhombic structure as an additive within ODS steels [31] and their results show that cubic Y_2TiO_5 opposed to fully ordered $Y_2Ti_2O_7$ could greatly enhance the recovery from radiation damage.

It was also observed that defects in the Fe regions of the ODS material behave in the same way as in pure α-Fe systems. Therefore the study of defect evolution in pure α-Fe systems is also very important in order to understand the defect behaviour in ODS systems. There is a large amount of data from experiments and from modelling due to the common use of Fe in nuclear applications. One of the first works was carried out by Johnson [32] in 60's, where the migration energies, atomic configurations and diffusion mechanisms were

studied. The initial work was followed by the study of vacancy-cluster configurations and their binding energies [33], showing the stability of vacancy clusters containing at least 4 vacancies. Recently the potential energy functions describing interactions between iron atoms [34, 35, 36] were developed that can reasonably reproduce such properties of iron systems as lattice parameter, elastic constants, point-defects energies etc. The improvement in the description of the interacting iron atoms allowed scientists to perform studies that can provide understanding in: primary damage formation [37, 38], energy landscapes of small clusters [39] and cascade annealing simulations over long time scales [40, 41, 42, 43, 44]. Most of these studies were focussed to investigate particular aspects of defected α-Fe systems, thus a more complete study is required to provide an insight look of defect evolution, which would help to predict defect evolution in ODS materials.

The increasing computational power of computers and availability of high performance computing clusters also greatly effected the field of material modelling. Previous studies over long time scales were using KMC with pre-calculated tables of possible events, but nowadays more modern techniques allow to calculate such events as He diffusion or defect mobility on the fly.

For the reasons stated above, this thesis is focussed on identifying such processes by modelling radiation damage in simplified models of the ODS systems, α-Fe and bulk Y-Ti-O systems, representing ODS particles.

1.3 The Project

This work is a part of a collaborative research between the United Kingdom and India. Model alloys are produced by Indira Gandhi Centre for Atomic Research (IGCAR), a leading atomic research centre of India. They produce ODS mother tubes and also conduct ion radiation experiments, which are analysed at IGCAR and Oxford University 1.2. High-resolution Transmission Electron Microscopy (HRTEM) studies of produced and irradiated

models were able to identify the crystal structures of the oxide particles and atom probe tomography (APT) analysis allowed to reconstruct the composition of the samples at the atomic level and look into the effects of processing conditions and irradiation on the oxide particles.

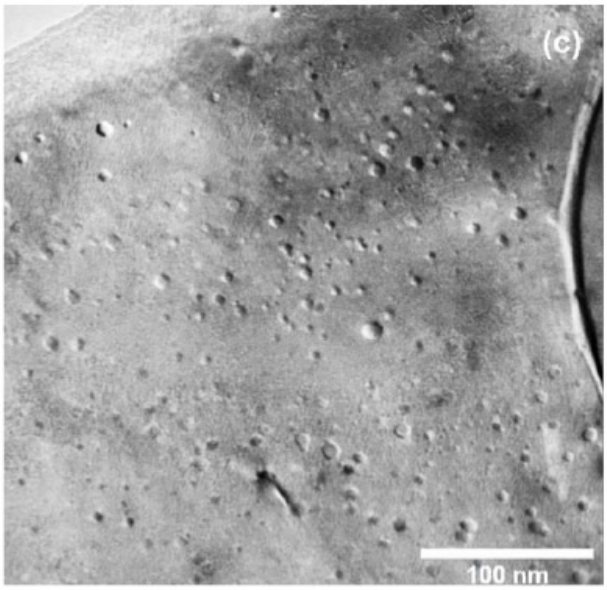

(a)

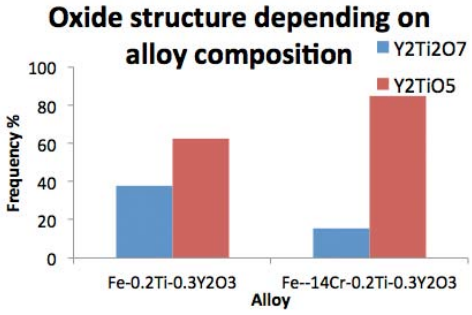

(b)

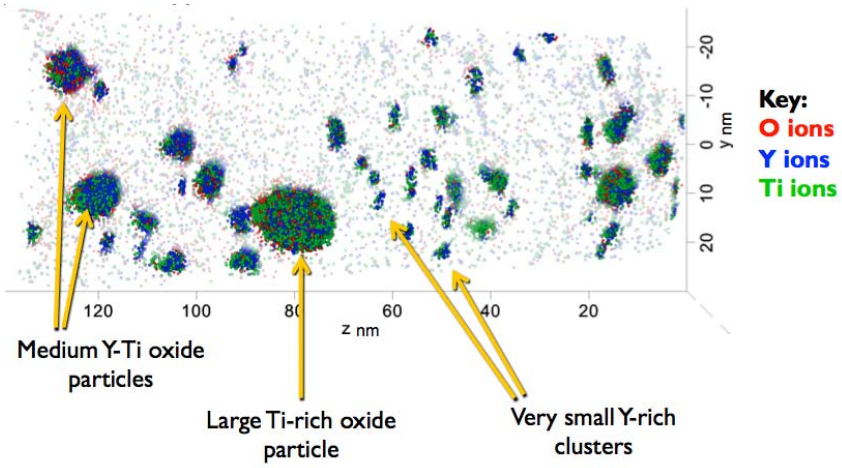

(c)

Figure 1.2: Experimental studies by research partners at IGCAR and Oxford University: (a) - Oxide particles in Fe-14Cr-0.2Ti-0.3Y_2O_3 alloy, (b) - Oxide structure depending on the alloy composition, (c) - A small 3D volume reconstructed using APT. Adopted from [6].

Simulations together with experiments help in providing a wider perspective of the problem and give a deeper look into the processes that happen at the atomistic level. The

simulations can help to link the results obtained before and after irradiation events that cannot be followed on an experimental time scale. Also, computer simulation allows parameters to be changed without performing costly experiments, such as temperature, energy and material composition.

1.4 Modelling of Radiation Damage

This work is based on the study of collision cascades and the processes involved in radiation events in models of ODS. To simulate radiation events the Molecular Dynamics (MD) technique has been used by a number of groups since the first collision cascade simulations done by Gibson in 1960's [45] and it is now one of the standard tools for the investigation.

The collision cascade mechanism happens within the first few ps of the radiation event and is driven by energetic collisions of the nearby atoms effected by the energetic particle (primary knock-on atom) that spreads collision sequences throughout the system. During these few ps, also known as ballistic phase of the radiation event, the initial damage region becomes highly distorted and leads to a "thermal spike", a quick local temperature increase, and thermally driven processes occur. After the ballistic phase, the system is left with metastable defects as it reaches a local minimum and the processes of defect recombination, migration and clustering take place on much longer time scales - the so called "Recovery Phase", which cannot be simulated using MD and other techniques must be employed, such as the Kinetic Monte Carlo (KMC) [46, 40]. The time scale of the radiation event is given in Figure 1.3.

Thus, a hybrid MD - KMC technique is a very powerful tool to model radiation effects as long time evolution of cascades. MD is used to evolve a system during the ballistic phase of a collision cascade and KMC the recovery phase of the same system. In this study the KMC phase is carried out on the fly.

The second half of this work is dedicated to developing this hybrid technique by adding

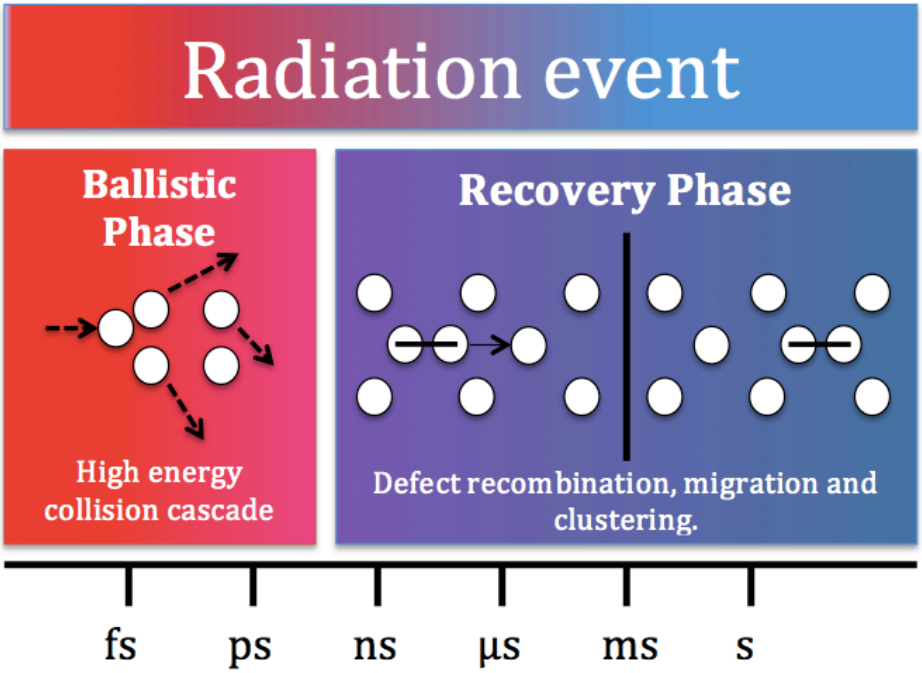

Figure 1.3: Representation of the time scale of radiation events. The ballistic phase occurs during the first few ps when high energy collision cascade takes place, and when system stabilizes to a local minimum. During the recovery phase, that can take ns, ms or even s, defect recombination, migration and clustering happens.

additional functionality to the KMC methodology to ensure accuracy and reliability. Then the developed technique was applied to study the defect motion in radiation damaged α-Fe systems.

1.5 Implemented and Developed Software

The on-the-fly KMC technique (otf-KMC) used in this work was developed in collaboration with colleagues C. Scott and M. Yu from Loughborough University's materials modelling group by adopting the initial work done by L. Vernon [47]. The main contributions to the methods in this work include, but are not limited to: the Dimer + minimum mode following algorithm approach for finding saddle states, ART (activation-relaxation technique), RAT (relaxation and translation), String, NEB (nudged elastic band) and Lanczos methods, Hessian matrix, eigenvalue and prefactor calculations and the reuse of transitions by incorporating 'Nauty'. Contributions were also made to the LboMD (Loughborough Molecular

Dynamics) package. Most of the contributions were associated with interatomic potentials and electrostatic calculations and are described within this thesis. Atomic visualisers developed by M. Robinson and by C. Scott were used for visual data interpretation along side with various scripts that were written for the analysis.

1.6 Thesis Layout

Chapter 1 introduces the research problems and gives reference to some of the previous work on the topic. The thesis contains 6 further chapters where two explain the methodology, followed by three results chapters. The thesis is finalised with the conclusions and future work chapter.

Chapter 2, the first methodology chapter, is dedicated to explain the main concepts of the MD technique and the necessary extensions to it.

Chapter 3, the second methodology chapter, is focussed on the long time scale simulations technique - otf-KMC which was developed during the course of this work with the emphasis on the sections where the technique was improved to gain efficiency and reliability.

Chapter 4 describes the MD simulations that were used to study the radiation effects in ODS and the formation of He bubbles. The results are compared with the similar simulations in pure iron systems.

Chapter 5 is mainly focussed on studying 3 systems representing the structure of the nanoparticles observed in the ODS materials. The preliminary studies are carried out using the MD technique and are focussed on gaining better understanding of the radiation effects in them.

Chapter 6 is dedicated to analyse the influence of the prefactor in the Arrhenius equation and to apply the otf-KMC technique to defect motion in pure iron systems.

Chapter 7, is the final chapter, where all the achieved results are summarised and the potential future studies are highlighted.

Chapter 2

Methodology I: Molecular Dynamics

2.1 Introduction

The Molecular Dynamics (MD) method was introduced in the middle of 20th century by B. J. Alder and T. E. Wainwright and has been used extensively since then [48]. It is designed to describe the behaviour of physical systems at the macroscopic level while simulating the microscopic level by modelling atomic and molecular interactions. The method was firstly used to model hard spheres [49] and with time has been employed for various applications, such as protein-folding problem [50] and radiation simulations [45]. Due to the increasing computational power of computers, the MD method became more and more useful, since systems containing millions of atoms, described by simple pair-wise potentials can be modelled, where more complex potentials limit systems' sizes to thousands of atoms.

MD simulations are based on computing the motion of the N atoms in the system and how the positions and the velocities change with time based on Newton's second law:

$$m_i \frac{d^2 \mathbf{x_i}}{dt^2} = -\nabla V\left(\mathbf{x_1}, ..., \mathbf{x_N}\right), i = 1..N, \tag{2.1}$$

where m_i is the mass of the i-th atom, whose position at time t is $\mathbf{x_i}$. Here the force on each atom is assumed to be derived from a potential function V, which depends only on the

coordinates of the atoms.

2.2 Time Integration

There is no analytical solution for the Newton's equations in MD because of the complicated nature of the potential energy; thus numerical algorithms must be employed. The most widely used algorithm to integrate time in MD simulations is the so called Verlet algorithm, which was promoted in MD simulations by L. Verlet in 1967 [48]. The algorithm is a combination of two Taylor expansions of the position vector $\mathbf{x}$ from time t forward to $t+\Delta t$ and backward to $t-\Delta t$:

$$\mathbf{x}(t+\Delta t) = \mathbf{x}(t) + \frac{d\mathbf{x}(t)}{dt}\Delta t + \frac{1}{2}\frac{d^2\mathbf{x}(t)}{dt^2}\Delta t^2 + \frac{1}{3!}\frac{d^3\mathbf{x}(t)}{dt^3}\Delta t^3 + O(\Delta t^4), \tag{2.2}$$

$$\mathbf{x}(t-\Delta t) = \mathbf{x}(t) - \frac{d\mathbf{x}(t)}{dt}\Delta t + \frac{1}{2}\frac{d^2\mathbf{x}(t)}{dt^2}\Delta t^2 - \frac{1}{3!}\frac{d^3\mathbf{x}(t)}{dt^3}\Delta t^3 + O(\Delta t^4). \tag{2.3}$$

By adding these two expressions we are eliminating odd-order terms:

$$\mathbf{x}(t+\Delta t) = 2\mathbf{x}(t) - \mathbf{x}(t-\Delta t) + \frac{d^2\mathbf{x}(t)}{dt^2}\Delta t^2 + O(\Delta t^4), \tag{2.4}$$

It can be seen the (Equation 2.4) that after the addition, the third-order term is eliminated, thus making this integrator an order more accurate than the Taylor expansion alone. Also the Verlet integrator's steps do not depend on velocities, only on acceleration $\frac{d^2\mathbf{x}(t)}{dt^2}$, which can be derived from intermolecular forces and Newton's second law.

Besides the Verlet algorithm, there are many other numerical algorithms, the like Euler's method, Beeman's, Leap-frog etc. One must carefully choose an algorithm for simulations by keeping in mind that it should conserve energy and momentum and be computationally efficient at the same time. In this work the Velocity Verlet algorithm is used [51], because of its straightforward nature, modest memory usage, computational efficiency and ability to

calculate velocities at each time step. By employing Taylor expansion the Velocity Verlet algorithm can be derived as follows:

$$\mathbf{x}(t+\Delta t) = \mathbf{x}(t) + \frac{d\mathbf{x}(t)}{dt}\Delta t + \frac{1}{2}\frac{d^2\mathbf{x}(t)}{dt^2}\Delta t^2 + O(\Delta t^3), \tag{2.5}$$

$$\mathbf{v}(t+\Delta t) = \mathbf{v}(t) + \frac{d\mathbf{v}(t)}{dt}\Delta t + \frac{1}{2}\frac{d^2\mathbf{v}(t)}{dt^2}\Delta t^2 + O(\Delta t^3), \tag{2.6}$$

$$\mathbf{a}(t+\Delta t) = \mathbf{a}(t) + \frac{d\mathbf{a}(t)}{dt}\Delta t + O(\Delta t^2), \tag{2.7}$$

where $\mathbf{v}(t) = \frac{d\mathbf{x}(t)}{dt}$ and $\mathbf{a}(t) = \frac{d\mathbf{v}(t)}{dt}$. After updating the positions using (2.5) we can derive:

$$\frac{d\mathbf{a}(t)}{dt} = \frac{\mathbf{a}(t+\Delta t) - \mathbf{a}(t)}{\Delta t} + O(\Delta t^2). \tag{2.8}$$

By substituting the last expression into Equation 2.6 we will get an expression in Equation 2.9 to calculate the new velocities, that can be used in Equation 2.5.

$$\boldsymbol{v}(t+\Delta t) = \boldsymbol{v}(t) + \frac{1}{2}\left[\boldsymbol{a}(t+\Delta t) + \boldsymbol{a}(t)\right] + O(\Delta t^2). \tag{2.9}$$

2.3 Boundary Conditions

In MD simulations system sizes usually vary from a few thousand to a few million atoms. This number has increased over the years with evolving computer technology and computational speed, but still it is not even close to modelling a bulk material. For this reason boundary conditions are applied to simulate large systems by modelling only a small part of them, also known as a primary cell.

2.3.1 Periodic Boundary Conditions

When using periodic boundary conditions (PBC) in simulations, we imagine that the primary cell is only a small part of a whole system, which is surrounded by exact replicas, known

as image cells, in all the directions, where periodic boundary conditions are applied. This representation could be understood as a rigid translation of the unit cell containing atoms into all three Cartesian dimensions. Periodic boundary conditions reflect not only the atom positions but also their momenta from primary cell to all image cells. Thus every atom in a unit cell should be thought of not only as interacting with other atoms in the primary cell, but also with nearby image cells atoms. Figure 2.1 represents the main principle of PBC: a particle which goes out of the primary cell through one side, and is brought back into the cell through the opposite site.

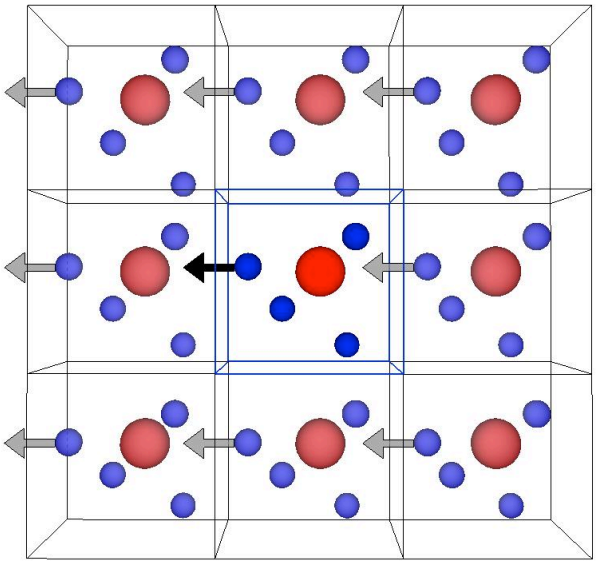

Figure 2.1: Schematic representation of the periodic boundary conditions, where the centre cell (primary cell) is the simulated system and the cells around the primary cell (image cells) responsible for replicating the bulk system effect. The main principle: if a particle leaves the primary cell on one side, it must re-enter the cell on the opposite site.

One must bear in mind that periodic boundary conditions only work well while the simulated event is contained in the simulation box.

2.3.2 Fixed Boundary Conditions

This kind of boundary condition is typically used when an investigated physical process is contained in the interior of a simulation box and causes no or negligible effect on the boundary, thus making the surrounding area of the simulation box stable. Fixing boundaries,

is a common way to ensure process containment. Such as when a large momentum is imparted to a non PBC system and atomic drift is to be avoided. This is depicted schematically in Figure 2.2.

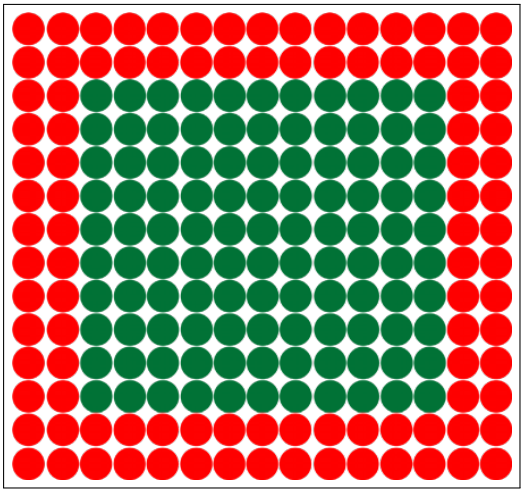

Figure 2.2: Schematic representation of fixed boundary conditions in 2D with two outside atoms layers fixed (shown in red) and the rest atoms allowed to move (shown in green).

2.4 Interatomic Potentials

A good representation of a system's energetics and dynamics depends on the chosen interatomic potentials. When choosing them for a specific system, several things must be considered. Potentials have to reproduce the physical properties of the system under investigation, they also should be computationally effective and preferentially calibrated with experimental results.

Usually one must choose between accuracy and computational speed. High accuracy simulations are usually feasible for small systems where systems consist up to few hundred atoms, e.g. computational chemistry simulations using *ab-initio* methods. The advantage of the more approximate models using potentials, is their ability to study large systems, containing hundreds of thousands or millions atoms.

For the simulations presented here, two types of interatomic potentials were used: pair potentials and Finnis-Sinclair type potentials.

2.4.1 Pair Potentials

Pair potentials have one of the simplest form:

$$E = \frac{1}{2} \sum_{i,j(i \neq j)} V_{ij}\left(r_{ij}\right), \tag{2.10}$$

where E is the total potential energy of the whole system, V_{ij} is the pair potential energy function and r_{ij} is the separation between atoms i and j.

Pair potentials are easy to implement and usually computationally efficient, but they are not always suitable to represent metals due to their inability to reproduce elastic constants accurately [52].

2.4.1.1 ZBL

The well-known screened Coulomb ZBL potential was developed by a group of three authors J. F Ziegler, J. P. Biersack and U. Littmark in 1985 [53]. It is used to describe repulsion of nucleus-nucleus Coulombic interactions at very small distances via screening the electrostatic potential by the outer electrons. The ZBL potential, also known as the universal potential, is widely used in molecular dynamics and other ion implantation simulations because of the accurate repulsive force calculations at close ranges.

As can be seen in Equation 2.11, the ZBL potential depends on three variables - the charges Z_1 and Z_2 on the nuclei, the interatomic separation r and the screening function φ:

$$V_{ZBL}(r) = \frac{1}{4\pi\varepsilon_0} \frac{Z_1 Z_2 e^2}{r} \varphi(\frac{r}{a}), \tag{2.4.11}$$

where e - electronic charge, ε_0 the permittivity of vacuum, a - a screening parameter. At very small distances between interacting atoms the repulsive interaction can be basically represented as Coulombic and when distances increase the electron cloud screening is taken in to account $\varphi(\mathrm{r}) \rightarrow 1$, when $r \rightarrow 0$. The screening parameters and the forms of screening functions are respectively given in Equations 2.4.12 and 2.4.13:

$$a = \frac{0.8854a_0}{Z_1^{0.23} + Z_2^{0.23}}, \tag{2.4.12}$$

$$\varphi(x) = 0.1818e^{-3.2x} + 0.5099e^{-0.9423x} + 0.2802e^{-0.4029x} + 0.02817e^{-0.2016x}, \tag{2.4.13}$$

where a_0 - the Bohr atomic radius = 0.530Å.

Figure 2.3 shows the graphs of the ZBL potential for the atomic pairs used in this thesis against the interatomic separation between the atoms.

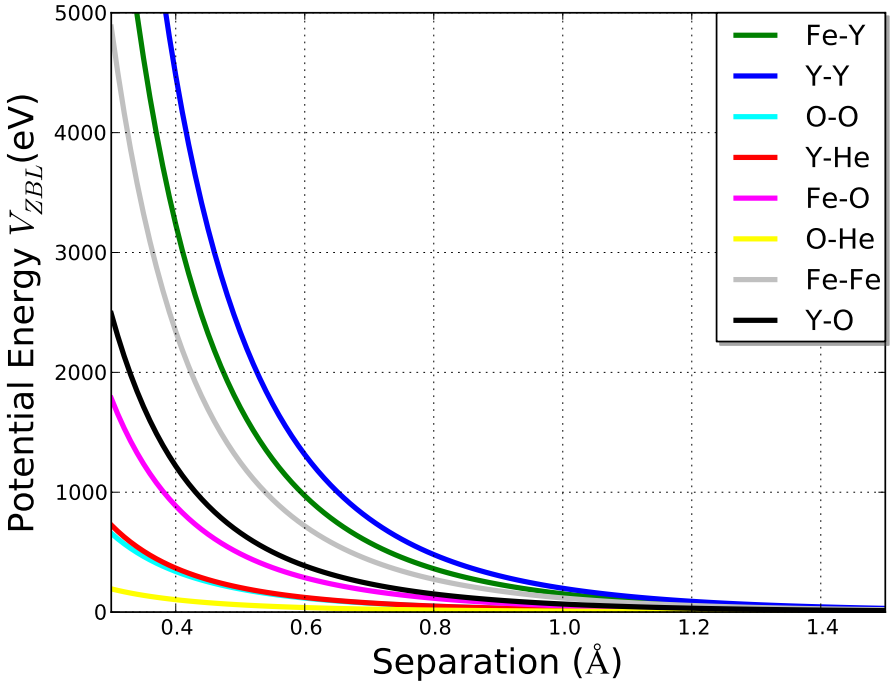

Figure 2.3: The form of the ZBL potential for the pair interactions used in this work.

2.4.1.2 Buckingham

The Buckingham potential is named after its author R. A. Buckingham and extensively used in MD simulations. He suggested it, as an improvement of the Lennard-Jones potential for

the classical equation of state of gaseous helium, neon and argon [54]. This potential also became popular to describe interactions for ionic and semi-ionic solids. The general form is:

$$V(r) = Ae^{-\frac{r}{\rho}} - \frac{C}{r^6}, \tag{2.4.14}$$

here A, ρ and C are constants and r is the interatomic separation.

The right hand term of Equation 2.4.14 represents the van der Waals energy arising from the mutual polarization of interacting atoms and the exponential term describes the potential's repulsiveness.

The Buckingham potential in this work was implemented to estimate interactions between yttria nanoparticle's atoms and also to describe the Y-Ti-O systems.

The constants A, ρ and C describing the yttria nanoparticle's interaction between Y^{+3}-O^{-2} and O^{-2}-O^{-2} are taken from [55] and [56] accordingly. Values for the Y^{+3}-O^{-2} interaction were derived using low-symmetry crystal property information. They are given in Table 2.1 and the potentials' graphs are plotted in Figure 2.4.

Interaction	A(eV)	ρ(Å)	C(Å^6 eV)
Y^{+3}-O^{-2}	1345.1	0.34910	0.0
O^{-2}-O^{-2}	22764.0	0.14900	27.88

Table 2.1: The Buckingham potential constants for describing Y^{+3}-O^{-2} and O^{-2}-O^{-2} interactions within yttria nanoparticle.

To describe the interactions within the Y-Ti-O systems the set of constants were used (see Table 2.2) derived empirically using the relaxed fitting method by fitting to the experimentally measured data [57]. The form of the interactions are plotted in Figure 2.5.

Interaction	A(eV)	ρ(Å)	C(Å^6 eV)
Ti^{+4}-O^{-2}	2088.107	0.2888	0.0
Y^{+3}-O^{-2}	1519.279	0.3291	0.0
O^{-2}-O^{-2}	25.41	0.6937	32.32

Table 2.2: The Buckingham potential constants for describing Ti^{+4}-O^{-2}, Y^{+3}-O^{-2} and O^{-2}-O^{-2} interactions to describe Y-Ti-O systems.

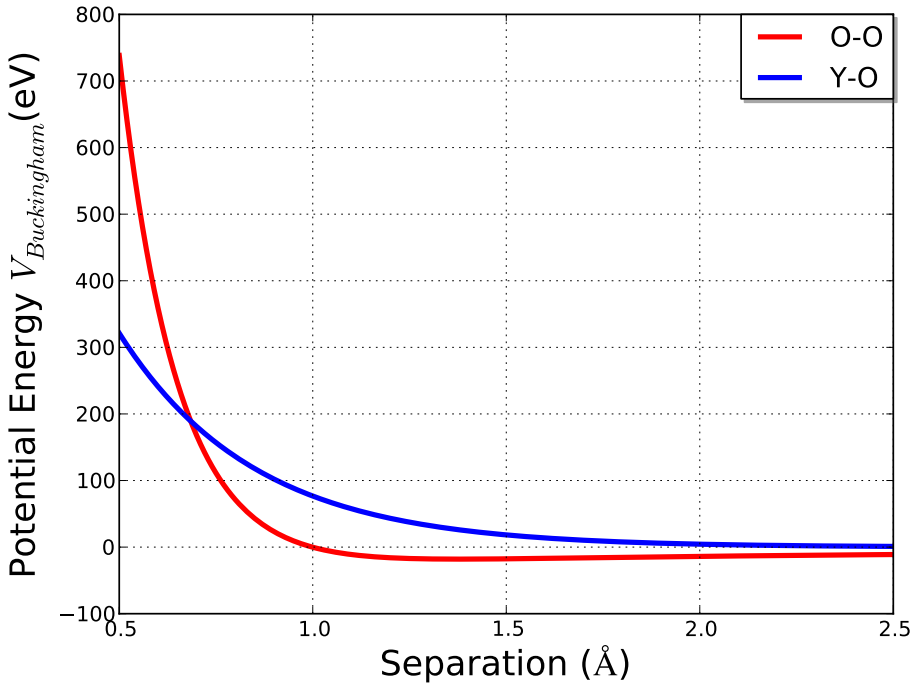

Figure 2.4: The form of the Buckingham potential for the Y^{+3}-O^{-2} and O^{-2}-O^{-2} interactions.

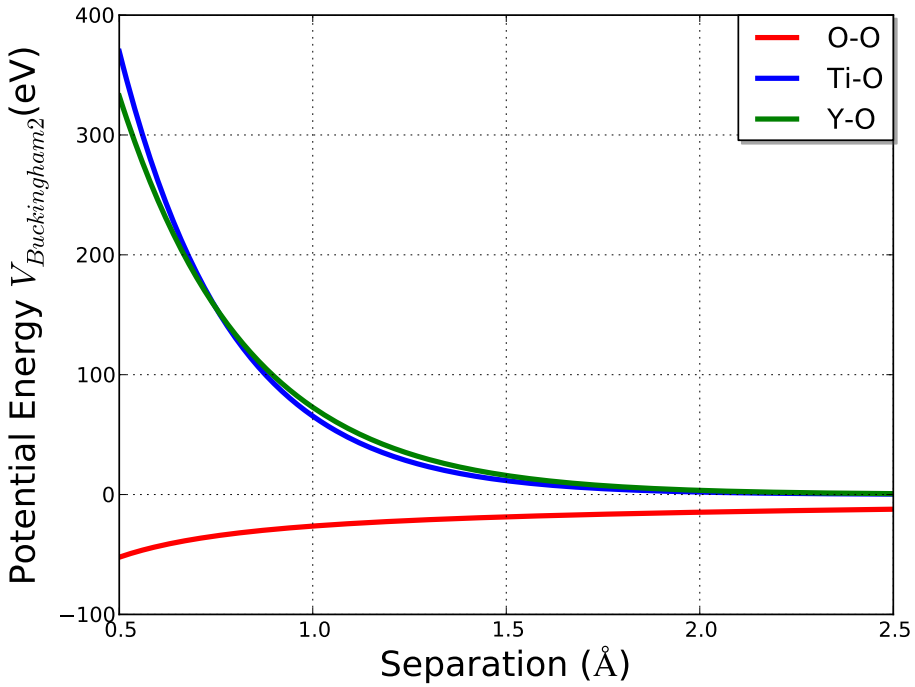

Figure 2.5: The form of the Buckingham potential for the Ti^{+4}-O^{-2}, Y^{+3}-O^{-2} and O^{-2}-O^{-2} interactions to describe Y-Ti-O systems.

2.4.1.3 Morse

Another commonly used pair potential is the Morse potential developed by an American physicist Philip M. Morse [58]. This potential was originally created to represent motions of nuclei in diatomic molecules and later was applied for face-centre and body-centre cubic metals [59]. Due to its simplicity became quite popular for fitting spectroscopic data. The expression of the Morse potential energy is:

$$V(r) = D_e(e^{-2a(r-r_e)} - 2e^{-a(r-r_e)}), \tag{2.4.15}$$

where r_e is the equilibrium bond length, D_e is the potential energy well's depth at the r_e, a is the potential energy well's width and r is the interatomic separation.

In this work we use the Morse potential to describe the attraction between iron and oxygen atoms. Figure 2.6 illustrates the form of Morse potential function used in this work and Table 2.3 gives the values of the parameters. These values were chosen to stabilise the yttria nanoparticle within the iron lattice by providing a weak binding between the O and Fe atoms.

Interaction	$D_e(eV)$	$r_e(\text{Å})$	$a(\text{Å}^{-1})$
Fe-O	0.3	2.5	2.0

Table 2.3: The parameter values for the Morse potential to describe a weak binding between the O and Fe atoms.

2.4.1.4 Aziz

For the He-He interaction the Aziz potential [26] was used, which holds the Hartree-Fock-dispersion form [60] and is reported to have a very good agreement with the *ab-initio* results.

$$V_{Aziz}(x) = \epsilon \left(A \exp\left(-\alpha x + \beta r^2\right) - F(x) \sum_{j=0}^{2} c_{2j+6}/x^{2j+6} \right), \tag{2.4.16}$$

with

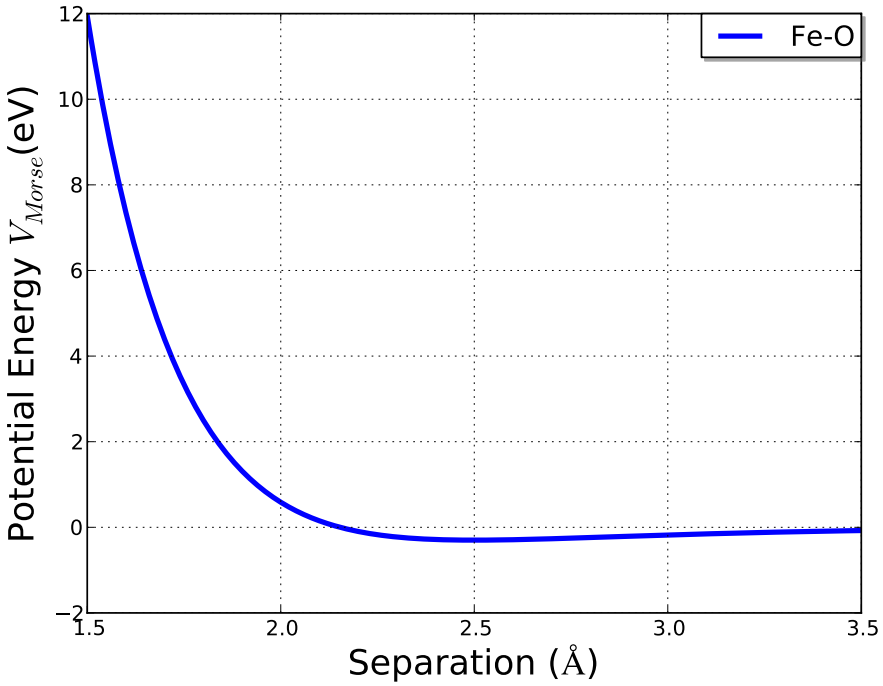

Figure 2.6: The form of the Morse potential for describing a weak binding between the O and Fe atoms.

$$F(x) = \begin{cases} \exp\left[-\left(\frac{D}{x}-1\right)^2\right], & x < D \\ 1, & x \geq D \end{cases}, \tag{2.4.17}$$

where $x = r/r_m$. The values of the constants are given in Table 2.4 and the form of the potential is shown in Figure 2.7.

A	α	c_6	c_8	c_{10}
186924.404	10.5717543	1.35186623	0.41495143	0.17151143
$\beta(\text{Å}^{-1})$	D(Å)	ϵ(K)	r_m(Å)	
−2.07758779	1.438	10.956	0.29683	

Table 2.4: The constant values for the Aziz potential to describe the He-He interaction.

2.4.2 Many-body Potentials

A great improvement in the field of pair potentials was suggested by Finnis & Sinclair (F-S) [52] and Daw & Baskes [61, 62] in 1980s: a many-body potential type 'The Embedded-Atom

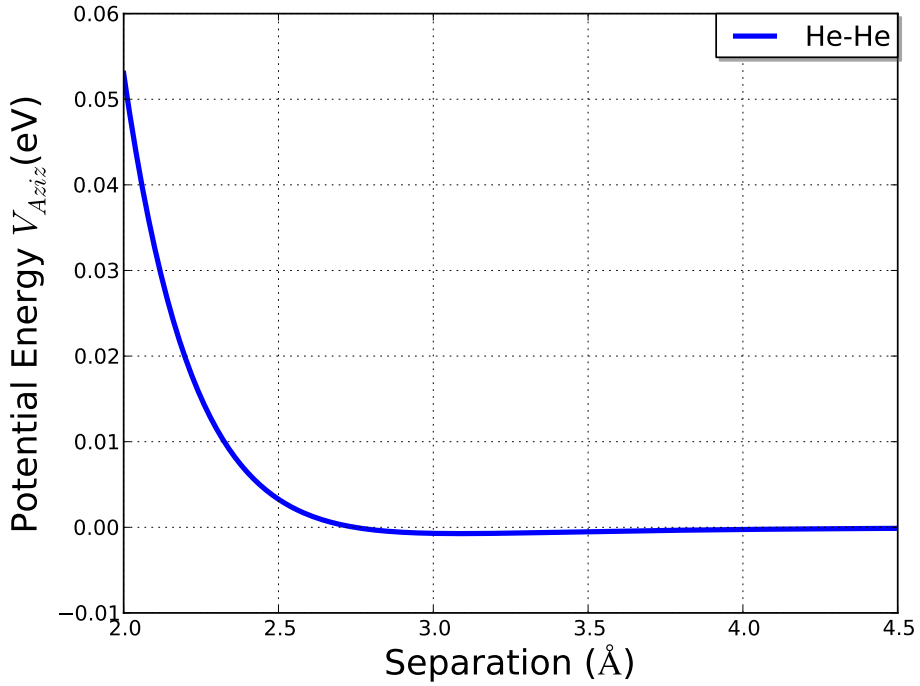

Figure 2.7: The form of the Aziz potential.

Method' (EAM). In this case the energy for an atom is derived from the energy needed to embed an atom in the local electron density by surrounding atoms. The energy calculated by the F-S and EAM methods $V_i^{EAM}(r)$ can expressed as such:

$$V_i^{EAM}(r) = -f(\rho_i(r)) + \frac{1}{2}\sum_j V_{ij}^{pair}(r), \tag{2.4.18}$$

where $V_{ij}^{pair}(r)$ is a central pair potential, $\rho_i(r)$ - electron density and f - an embedding function for the EAM potential specifically.

$$\rho_i(r) = \sum_j \phi_{ij}(r), \quad \phi_{ij}(r) = Z_i(r)Z_j(r)/r, \quad Z(r) = Z_0(s + \beta r^v)e^{-\alpha r}, \tag{2.4.19}$$

here $\phi_{ij}(r)$ is a function between atoms i and j, α, β and v are parameters and Z_0 is the number of valence electrons.

2.4.2.1 Ackland-Mendelev

The Finnis-Sinclair type potential [63] is similar to the generic form, but the form of f in Equation 2.4.18 is $f(\rho) = -A\rho^{\frac{1}{2}}$ and parametrised fits are used as $\phi_{ij}(r)$ to give the potentials a form that is easily implemented. In this work, to describe the Fe-Fe interaction, three different sets of parameters were used [34, 35, 36] where the general form of the potentials to calculate the energy in a N atom system is :

$$E = \frac{1}{2}\sum_{i\neq j=1}^{N} V_{ij}(r_{ij}) - \sum_{i=1}^{N}\left(\sum_{j=1}^{N}\Phi_{ij}(r_{ij})\right)^{1/2}, \tag{2.4.20}$$

where the first part of the expression represents a pair potential and the second the embedded part. Ackland employed cubic splines for the potentials and was able to fit the lattice parameter, elastic constants and cohesive energy of α-Fe. The form is given in Equations 2.4.21 and 2.4.23, with parameters given in Table 2.5.

$$V(r_{ij}) = \sum_{k=1}^{n_a} a_k H\left(r_k - r_{ij}\right)\left(r_k - r_{ij}\right)^3, \tag{2.4.21}$$

a_k, r_k are constants, with the values given in Table 2.5, r_{ij} is the atomic separation between atoms i and j and H is the Heaviside function:

$$H(x) = \begin{cases} 0, & x > 0, \\ 1, & x < 0. \end{cases} \tag{2.4.22}$$

In this work the pair potential (Equation 2.4.21) was splined to the ZBL potential using a sixth order exponential polynomial, with the details given in the later section 2.4.4.

k	1	2	3	4	5	6
a_k(eV/Å^{-3})	−36.559853	62.416005	−13.155649	−2.721376	8.761986	100.000
r_k(Å)	1.180	1.150	1.080	0.990	0.930	0.866025

Table 2.5: Values of the parameters for the pair potential function in the many-body potential for the Fe-Fe interaction described by the Ackland 1997 potential [34].

Similarly cubic splines were used (Equation 2.4.23) for the embedding term in Equation 2.4.20, with the parameters values given in Table 2.6.

$$\Phi(r_{ij}) = \sum_{k=1}^{n_A} A_k H\left(R_k - r_{ij}\right)\left(R_k - r_{ij}\right)^3, \tag{2.4.23}$$

k	1	2
$A_k(\mathrm{eV/\AA}^{-3})$	-36.559853	62.416005
$R_k(\mathrm{\AA})$	1.180	1.150

Table 2.6: Values of the parameters for the embedding term in the many-body potential for the Fe-Fe interaction described by the Ackland 1997 potential [34].

Later this potential was improved [35] by changing the expression of f in Equation 2.4.18 to the one given in Equation 2.4.24. By introducing more cubic splines in the pair term, on average, it gave a better agreement with the lattice parameter, elastic constants, point-defects energies etc, obtained experimentally and by first-principles calculations. Later, it was improved again [36] by recalculation of the parameters and expansion of f as shown in Equations 2.4.24 and 2.4.25.

$$f(\rho) = -\rho^{1/2} + a^f \rho^2. \tag{2.4.24}$$

$$f(\rho) = a_0^f \rho^{1/2} + a_1^f \rho^2 + a_2^f \rho^4. \tag{2.4.25}$$

where a^f, a_0^f, a_1^f and a_2^f are constants.

2.4.2.2 Gao

A new Fe-He potential was recently developed by F. Gao *et al.* [27] in combination with the Ackland 2004 [36] and the Aziz [26] potentials. The potential is based on "s-band model" and has been tested based on *ab-initio* studies by employing a least squares fitting technique. They showed that the calculations achieved with the new potential are in an agreement with

both *ab-initio* and the previous potential calculations and is a good improvement overcoming disadvantages of the previous potentials.

The formalism of the potential is very similar to the one of the Ackland 2004 [36] and has the same form of the pair potential (Equation 2.4.23) and the many-body interaction function (Equation 2.4.25) with the parameter values given in Tables 2.7 and 2.8 accordingly.

k	1	2	3	4	5	6	7
$a_k(\text{eV/Å}^{-3})$	−45.91636	35.55031	164.31987	−1.72746	0.10677	0.07372	0.03824
$r_k(\text{Å})$	1.6155	1.6896	1.8017	2.0482	2.3816	3.5067	3.9028

Table 2.7: Parameters of the pair potential function in the many-body potential for the Fe-He interaction described by the Gao potential [27].

$a_0^f(\text{eV/Å})$	$a_1^f(\text{eV/Å}^{-4})$	$a_2^f(\text{eV/Å}^{-8})$
0.22081	1.36751	3.38226

Table 2.8: Parameters of the many-body interaction function in the many-body potential for the Fe-He interaction described by the Gao potential [27].

The difference comes in how the total electron density is calculated. They derived it from the s-band model and can be written as follows:

$$\rho_i(r) = \sum_j \phi_{ij}(r), \quad \phi_{ij}(r) = N_s r^3 \exp(-2\xi_s r), \tag{2.4.26}$$

where $\xi_s = 12.89363\text{Å}^{-1}$ - an average from the 1s and 4s Hartee-Fock orbitals for He(ξ_{1s}) and Fe(ξ_{4s}) and $N_s = 20.0$Å - represents the s-electron density at the first nearest neighbour distance.

For the close range interaction the repulsive part of the pair potential was connected to the Biersack-Zeigler universal function V_{BZ} [64] and the final form of the interaction is:

$$V_{ij}^{Fe-He}(r_{ij}) = V_{ij}(r_{ij})F(r) + V_{BZ}(r_{ij})\left[1 - F(r_{ij})\right], \tag{2.4.27}$$

where $F(r_{ij}) = 1/\left(1 + \exp\left(-b_f\left(r_{ij} - r_f\right)\right)\right)$ with $b_f = 10.0\text{Å}^{-1}$, $r_f = 0.25$Å.

2.4.3 Electrostatics

Estimation of the electrostatic energy is a big computational challenge in MD simulations. The difficulty arises from the fact that electrostatic energy has a relatively long-ranged r^{-1} decay and large cut-offs must be used, if evaluating a direct sum of such interactions.

In this work three different techniques have been implemented to incorporate electrostatics in to MD and long time scale simulations. First and least efficient is a sum over of all charge interactions expressed by a Coulomb law within the primary cell and with a fixed number of image cells. This technique was used only for comparison and benchmarking with other two, since it is very computationally expensive. The second technique is the Ewald summation, which is usually considered as a standard algorithm to accumulate electrostatic interactions in periodic systems. The third, even more computationally efficient, is the Fennel approximation.

2.4.3.1 Direct summation

This method considers a primary cell containing N electrostatic particles and is surrounded by image cells in directions where periodic boundaries are applied. Then primary cell's electrostatic energy can be expressed by direct summation as follows

$$V_{el.} = \frac{1}{4\pi\varepsilon_0}\frac{1}{2}\sum_{\mathbf{n}}\sum_{i=1}^{N}\sum_{j=1}^{N}{}' \frac{q_i q_j}{|r_{ij}+kL|}, \tag{2.4.28}$$

where image cells are being expressed with integer coordinates $\mathbf{n} = (l, m, n)$, r_{ij} is the distance between electrostatic particles i and j with charges q_i and q_j; L is the primary cell's box length. $\sum'$ indicates that for n = 0, the interaction i = j is omitted.

As can be seen in Equation 2.4.28, this method is very inefficient and computer resources demanding. One of the way of reducing computational costs is by using a cut-off n_{cut} ($n \leq n_{cut}$) as small as possible while maintaining fairly accurate values for E.

2.4.3.2 Ewald Summation

The Ewald summation method was developed in 1921 and named after its author P. P. Ewald [65]. This method has become a standard for estimating electrostatic energy in periodic systems [66]. The idea of this method is to split the conditionally convergent expression (Equation 2.4.28) into two - short and long - absolutely convergent summations which can be computed much faster:

$$
\begin{aligned}
V_{el.} = \quad & \frac{1}{2}\sum_{i=1}^{N}\sum_{j=1}^{N}\left[q_i q_j\left(\sum_{\mathbf{n}}{}' \frac{\operatorname{erfc}\left(\alpha\left|\mathbf{r}_{ij}+\mathbf{n}\right|\right)}{\left|\mathbf{r}_{ij}+\mathbf{n}\right|}\right.\right. \\
& \left.\left. + \frac{1}{\pi L^3}\sum_{\mathbf{k}\neq 0}\frac{4\pi^2}{\left|\mathbf{k}\right|^2}\exp\left(-\frac{\pi^2\left|\mathbf{k}\right|^2}{\alpha^2}\right)\cos\left(\mathbf{k}\cdot\mathbf{r}_{ij}\right)\right)\right] \\
& -\frac{\alpha}{\pi^{\frac{1}{2}}}\sum_{i=1}^{N} q_i^2 + \frac{2\pi}{\left(2\epsilon_S+1\right)L^3}\left|\sum_{i=1}^{N} q_i\mathbf{r}_i\right|^2
\end{aligned}
\tag{2.4.29}
$$

The first term in Equation 2.4.30 represents the short-range part in real space, where α is the damping parameter and is controlled by a real space cut off radius r_c and desired precision ϵ as given in Equation 2.4.30, as $\mathbf{n}$ accounts for the image cells that are being expressed with integer coordinates $\mathbf{n} = (l, m, n)$ to take into account periodic boundary effects within r_c.

$$
\alpha = \sqrt{-\log\left(\epsilon\right)}/r_c. \tag{2.4.30}
$$

The second term in the equation accounts for the long-range interaction in Fourier space, where $\mathbf{k}$ is the reciprocal vector equal to $2\pi\mathbf{n}/L^2$. The last two terms are a particle self-term, where ϵ_S is the dielectric constant of the surrounding medium, and a dipolar term, which is neglected by using $\epsilon_S = \infty$, due to the assumption that conducting boundary conditions are being used and there is no dipole moment.

The original Ewald summation is an O(N^2) algorithm, but with careful choice of param-

eters, thoughtful algorithm development and optimizations, calculation costs can be reduced to $O(N^{\frac{3}{2}})$ or even to $O(N \log N)$.

Even though Ewald summation is a relatively quick and robust method, as with most of the methods, one must choose between accuracy and speed. Therefore, a set of tests were carried out in a pure Y-Ti-O system containing 11,000 atoms to determine the best set of r_c and ϵ parameters.

α	r_c	Δ max diff. (eV/Å^3)	Δ avg. time (s)
0.0001	10.3	–	–
0.0001	8.5	0.24	1.04
0.0001	9.0	0.19	0.70
0.0001	9.5	0.13	0.40
0.0001	10.3	0.0	0.0
0.0002	8.5	0.21	0.51
0.0002	9.0	0.15	0.35
0.0002	9.5	0.07	0.03
0.0002	10.3	−0.09	−0.21
0.0005	8.5	0.15	−0.05
0.0005	9.0	0.07	−0.27
0.0005	9.5	−0.04	−0.41
0.0005	10.3	−0.24	−0.47
0.001	8.5	0.08	−0.51
0.001	9.0	−0.01	−0.63
0.001	9.5	−0.16	−0.68
0.001	10.3	−0.39	−0.63
0.005	8.5	−0.23	−1.09
0.005	9.0	−0.36	−1.11
0.005	9.5	−0.66	−1.14
0.005	10.3	−0.94	−1.07

Table 2.9: Testing parameters of the Ewald summation method to improve the computational time without losing accuracy. Tests were carried out in such a way, that for each pair of parameters, the electrostatic interactions were calculated for two systems: the system which is in a local minimum and the same system with one atom slightly moved (by 0.2Å). Here the Δ max diff. column shows the difference in the infinity norm of the force vectors of the systems and the Δ avg. time - average computational time change with respect to the first line (the reference parameters set).

The data from the tests is given in Table 2.9. The first line shows good accuracy with the direct method, but is rather slow and is used for comparison. To measure the accuracy of the set of parameters, maximum difference in the force component was calculated between two

systems and average evaluation time is measured and then compared to the first line. Three sets of parameters showed good correlation between improved speed and minimum loss in accuracy: $(0.0005, 9.5)$, $(0.001, 9.0)$, $(0.0005, 8.5)$ and were further analysed by checking the scaling with increasing size of a system (Figure 2.8).

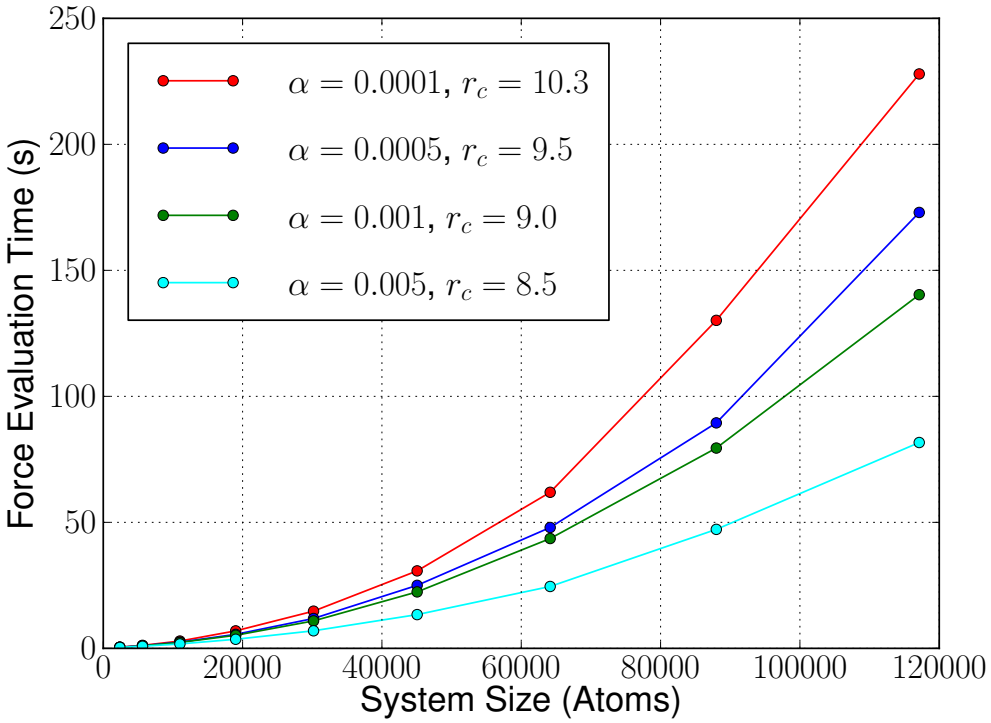

Figure 2.8: The graphs illustrating the scaling of the Ewald summation method, with respect to α and r_c parameters and number of atoms in the systems.

Figure 2.8 shows how computationally expensive the Ewald method is, therefore a good set of parameters is essential. The red graph represents the set of parameters ($\alpha = 0.0001$ and $r_c = 10.3$) obtained by [67] for ionic systems and is used for comparison. Clearly, the other three parameter sets require less computational time, but introduce small changes in the force and energy evaluations. By comparing this scaling data and the changes given in Table 2.9, the ($\alpha = 0.001$ and $r_c = 9$) set has been chosen for this work, as it not only has the smallest change in the maximum force component, but also is faster than the set of parameters obtained by [67].

2.4.3.3 Fennell Approximation

Several studies have been done to investigate alternatives of the Ewald summation in an efficient pairwise fashion. One of the alternatives was suggested by Christoper J. Fennel *et al.* [66]. Their suggestion derived from the Wolf and Zahn methods [68] and shows very similar results to the Smooth Particle Mesh Ewald (SPME) method [69] by comparing the force and torque vectors, computational cost benefits (as pairwise cut-off methods tend to scale almost linearly with respect to the system size) and also, in our case, is easily implemented in the MD package.

$$V_{DSF}(r) = q_i q_j \left[\frac{\mathrm{erfc}(\alpha r)}{r} - \frac{\mathrm{erfc}(\alpha R_c)}{R_c} + \left(\frac{\mathrm{erfc}(\alpha R_c)}{R_c^2} + \frac{2\alpha}{\pi^{1/2}} \frac{\exp(-\alpha^2 R_c^2)}{R_c} \right) \right], \quad (2.4.31)$$

$$F_{DSF}(r) = q_i q_j \left[\left(\frac{\mathrm{erfc}(\alpha r)}{r^2} + \frac{2\alpha}{\pi^{1/2}} \frac{\exp(-\alpha^2 r^2)}{r} \right) - \left(\frac{\mathrm{erfc}(\alpha R_c)}{R_c} + \frac{2\alpha}{\pi^{1/2}} \frac{\exp(-\alpha^2 R_c^2)}{R_c} \right) \right], \quad (2.4.32)$$

where $r \leq R_c$. Equations 2.4.31 and 2.4.33 represent the electrostatic summation method suggested in [66]. This pairwise potential depends on a damping parameter α and the cut-off radius R_c. Authors suggest that one should consider electrostatic damping between $0.2 - 0.25\text{Å}^{-1}$. When α is set equal to 0 we get the undamped case.

By using this potential, functionality and speed can be gained in the MD simulations, but the improvement comes with a loss in agreement with the empirical electrostatic potential as shown in Figure 2.9.

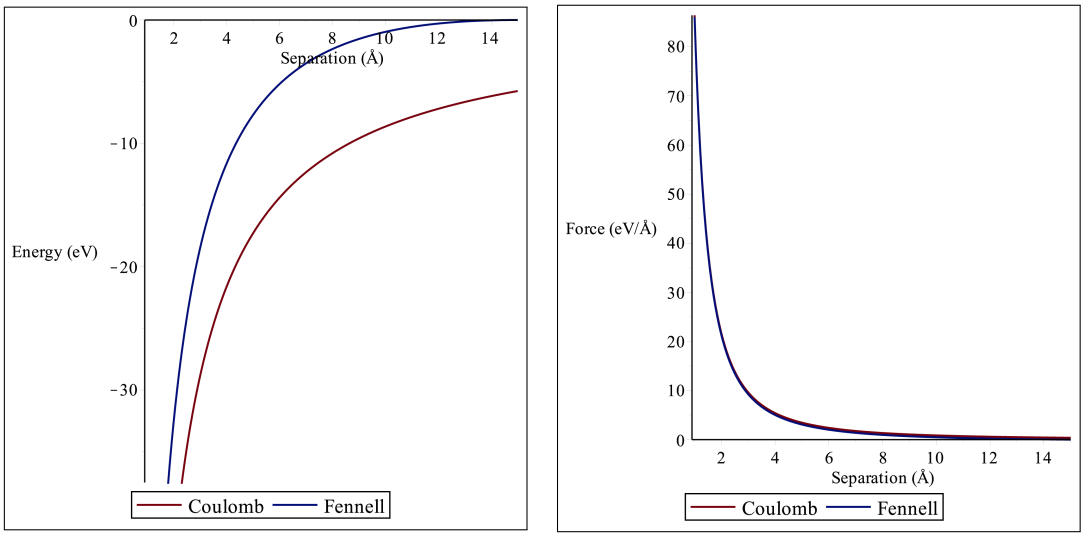

(a) (b)

Figure 2.9: Comparison between the Coulomb electrostatic potential and the Fennel approximation between yttrium (+3) and oxygen (-2) atoms in terms of: (a) - potential energy, (b) - force. Even though the agreement in potential energy is lost, the Fennel approximation gives a very good force evaluation.

2.4.4 Fitting the Potentials

All the potentials in this work are splined to the ZBL [53] screened Coulomb potential, for close particle separation, using a sixth order exponential polynomial. There are numerous methods, such as using sine, cosine based functions, but here a sixth order exponential polynomial (Equation 2.4.33) is used to ensure continuity of V and its first and second derivatives:

$$S(r_{ij}) = e^{C_0+C_1 r_{ij}+C_2 r_{ij}^2+C_3 r_{ij}^3+C_4 r_{ij}^4+C_5 r_{ij}^5}, \tag{2.4.33}$$

where r_{ij} is the atomic separation, $C_0 - C_5$ are the splining constants, obtained for each pair of atoms by solving a system of linear equations:

$$\begin{aligned}
C_0 + C_1 A + C_2 A^2 + C_3 A^3 + C_4 A^4 + C_5 A^5 &= \ln V_1(r_a), \\
C_0 + C_1 B + C_2 B^2 + C_3 B^3 + C_4 B^4 + C_5 B^5 &= \ln V_2(r_b), \\
C_1 + 2C_2 A + 3C_3 A^2 + 4C_4 A^3 + 5C_5 A^4 &= \tfrac{F_1(r_a)}{V_1(r_a)}, \\
C_1 + 2C_2 B + 3C_3 B^2 + 4C_4 B^3 + 5C_5 B^4 &= \tfrac{F_2(r_b)}{V_2(r_b)}, \\
2C_2 A + 6C_3 A + 12C_4 A^2 + 20C_5 A^3 &= \tfrac{G_1(r_a)}{V_1(r_a)} - \left(\tfrac{F_1(r_a)}{V_1(r_a)}\right)^2, \\
2C_2 B + 6C_3 B + 12C_4 B^2 + 20C_5 B^3 &= \tfrac{G_2(r_b)}{V_2(r_b)} - \left(\tfrac{F_2(r_b)}{V_2(r_b)}\right)^2,
\end{aligned} \tag{2.4.34}$$

where V_1 and V_2 are the potential values at r_a and r_b, which are being matched and F_1, F_2 and G_1, G_2, their first and second derivatives, accordingly. There is no concrete method how to calculate r_a and r_b, therefore they were chosen by ensuring the functions are as smooth and continuous as possible.

Then the final form of the pair potentials is:

$$V(r_{ij}) = \begin{cases} V_{ZBL}(r_{ij}), & r_{ij} < r_{\mathrm{a}}, \\ e^{C_0 + C_1 r_{ij} + C_2 r_{ij}^2 + C_3 r_{ij}^3 + C_4 r_{ij}^4 + C_5 r_{ij}^5}, & r_{\mathrm{a}} \le r_{ij} \le r_{\mathrm{b}}, \\ V_{Pot.}(r_{ij}), & r_{\mathrm{b}} < r_{ij} < r_{\mathrm{cut}}, \\ V_{Damp.func.}(r_{ij}), & r_{\mathrm{cut}} \le r_{ij} \le r_{\text{cut-off}}, \\ 0, & r_{ij} \ge r_{\text{cut-off}}, \end{cases} \tag{2.4.35}$$

here $V_{Pot.}$ and $V_{Damp.func.}$ are the interatomic potential and the smooth damping functions respectively. The distances $r_{\mathrm{a}}, r_{\mathrm{b}}, r_{\mathrm{cut}}, r_{\text{cut-off}}$ are the active ranges for the given expressions. All these values depend on the types of the interacting atoms. In the electrostatic case, $V_{Pot.}$ also includes the electrostatic interaction.

As can be seen in Equation 2.4.35 a cut-off range for each pair's potential system is introduced to save computational time. This is done by using a cosine function to smoothly damp the potential energy to 0 between r_{cut} and $r_{\text{cut-off}}$:

$$V_{Damp.func.}(r_{ij}) = \frac{1}{2}(1 + \cos(\pi \cdot x(r_{ij}))) \cdot V_{Pot.}(r_{ij}), \tag{2.4.36}$$

where

$$x(r_{ij}) = \frac{r_{ij} - r_{cut}}{r_{cut-off} - r_{cut}}. \tag{2.4.37}$$

The best constants values found for the Fe-Y-O systems are given in Table 2.10 and for the Y-Ti-O systems in Table 2.11 with the cut-off radii in Tables 2.12, 2.13 accordingly.

Type	C_0	C_1	C_2	C_3	C_4	C_5
$Fe-Fe$	30.24710	−92.53334	142.35034	−110.84666	41.549764	−6.00754
$Fe-O$	4.573143	15.113343	−38.907346	35.795364	−14.835219	2.231974
$Y-Y$	11.83596	−10.44532	4.9658	−0.57136	−0.09153	−0.0014
$Y-O$	16.64432	−51.38949	107.99607	−118.96857	61.95074	−12.15482
$O-O$	−0.91384	64.44073	−209.56762	295.90019	−194.81265	49.00191

Table 2.10: Values of the splining function's constants for the Fe-Y-O systems. The units for C_i are in Å^{-i}.

Type	C_0	C_1	C_2	C_3	C_4	C_5
$O-O$	4.89399	15.23986	−53.56506	67.56640	−37.22622	7.59886
$Ti-O$	26.76794	−125.69354	309.66125	−379.35916	222.76690	−50.09023
$Y-O$	21.76669	−82.15615	180.51136	−202.66134	110.34640	−23.10884
$Ti-Ti$	8.31550	6.12765	−32.51735	32.70442	−4.34158	−4.67541
$Y-Y$	35.51828	−139.65278	283.60803	−296.12652	153.21562	−31.04498
$Y-Ti$	−5.70405	82.83806	−192.38849	201.29568	−99.62413	19.02782

Table 2.11: Values of the splining function's constants for the Y-Ti-O. The units for C_i are in Å^{-i}.

Type	r_a(Å)	r_b(Å)	r_{cut}(Å)	$r_{\text{cut-off}}$(Å)
$Fe-Fe$	0.90	1.90	-	5.2
$Fe-Y$	–	–	3.0	4.0
$Fe-O$	0.80	1.80	4.0	5.0
$Y-Y$	0.50	1.77	7.2	7.4
$Y-O$	0.55	1.40	7.2	7.4
$O-O$	0.50	1.05	7.2	7.4

Table 2.12: Splining intervals and cut-off radii for the Fe-Y-O systems.

Type	r_a(Å)	r_b(Å)	r_{cut}(Å)	$r_{\text{cut-off}}$(Å)
$O-O$	0.60	1.30	9.0	9.2
$Ti-O$	0.55	1.20	9.0	9.2
$Y-O$	0.60	1.30	9.0	9.2
$Ti-Ti$	0.50	0.90	9.0	9.2
$Y-Y$	0.80	1.30	9.0	9.2
$Y-Ti$	0.70	1.00	9.0	9.2

Table 2.13: Splining intervals and cut-off radii for the Y-Ti-O systems.

2.5 Energy minimization

The output of simulations greatly depends on the initial state of the system being simulated. Thus to ensure accurate results, MD simulations must be started from a stable local configuration, a global or at least a local energy minimum. It is done by adjusting the system's structure through the force field generated by the interatomic potentials. Usually energy minimization is the first step during MD simulations after creating a desired system, because it is unlikely that the created system will be in an equilibrium. It may also be the last step in simulations in order to identify stable defects or changes in the system.

In this work mainly three techniques were used for system's energy minimization: the conjugate gradient method, damped MD and L-BFGS-B.

2.5.1 Conjugate Gradient

The original conjugate gradient (CG) method was developed by Fletcher and Reeves in 1964 [70]. The basic idea of this method is: if a function $f(x)$ is quadratic and its gradient vector $g(x)$ can be calculated at any point x, the minimum of any quadratic function $f(x)$ of n arguments will be reached in n CG method iterations, as defined later in the text. In this work all the potential functions are not quadratic, therefore the CG method is a multi-step procedure with a test for convergence.

An iteration of the CG method can be divided into 5 steps:

Step 1. Calculate the gradient function's value:

$$g(\mathbf{x}_n) = -\nabla f(\mathbf{x}_n). \tag{2.5.1}$$

During the first step the search direction is $\mathbf{s}_0 = g(\mathbf{x}_0)$, what is basically a steepest descent method iteration.

Step 2. Compute a new point $\mathbf{x}_{n+1}$:

$$\mathbf{x}_{n+1} = \mathbf{x}_n + \alpha_n \mathbf{s}_n, \tag{2.5.2}$$

where α is the linear search parameter, obtained by minimizing the function $f(x)$ with respect to α in the $\mathbf{s}_n$ direction:

$$\frac{\mathrm{d}f(\mathbf{x}_n + \alpha \mathbf{s}_n)}{\mathrm{d}\alpha} = 0. \tag{2.5.3}$$

The linear search is the most time consuming step of the CG method, thus one must carefully choose a method to adopt. In this work Brent's method [71] is used to estimate α and the Polak-Ribiere [72] method to calculate the γ parameter:

$$\gamma_n = \frac{\|g(\mathbf{x}_{n+1})\|^2 - g(\mathbf{x}_{n+1})^T g(\mathbf{x}_n)}{\|g(\mathbf{x}_n)\|^2}. \tag{2.5.4}$$

Step 3. Calculate $f(\mathbf{x}_{n+1})$, $g(\mathbf{x}_{n+1})$ and find the new direction $\mathbf{s}_{n+1}$:

$$\mathbf{s}_{n+1} = g(\mathbf{x}_{n+1}) + \gamma_n \mathbf{s}_n. \tag{2.5.5}$$

Step 4. Test for convergence. Evaluate the force and see if a minimum has been reached, by checking if the gradient is less than a specified limit ε.

$$g(\mathbf{x}_{n+1}) \leq \varepsilon. \tag{2.5.6}$$

If the minimum is attained, terminate the algorithm, if not - repeat starting with the

step 1.

The main advantage of the CG method is that it requires information only from the previous step and has a very diminutive demand for computer memory and therefore can be applied for large systems. On the other hand, one of the biggest disadvantages of this method is in order to reach the global minimum of a system, the initial guess of $\mathbf{x}_0$ must be close to it, otherwise the method tends to converge to a local minimum.

2.5.2 Damped MD

Another technique used in this work to equilibrate systems is the energy minimization by damping (also known as the damped MD). This technique operates on the idea that a system oscillates in a potential energy well and by the systematic damping of these oscillations the system can be relaxed into a potential energy minimum. The damping is carried out by the Lindhard-Scharff inelastic loss model [73, 74] which scales the atoms' velocities which are further used by the time integrator. The rate at which the excess energy is removed from the system is proportional to the atoms' velocities:

$$\frac{dE}{dt} = -\sum_i \frac{k}{m_i} v_i, \tag{2.5.7}$$

where E is the system's kinetic energy, t is time, m_i and v_i are the i-th atom's mass and velocity magnitude accordingly, and k is the damping coefficient, which controls the energy removal speed from the system (the damping effect).

When using the damped MD technique, the system will reach a minimum potential energy state with rigid atom positions by damped oscillations as shown in the example in Figure 2.10.

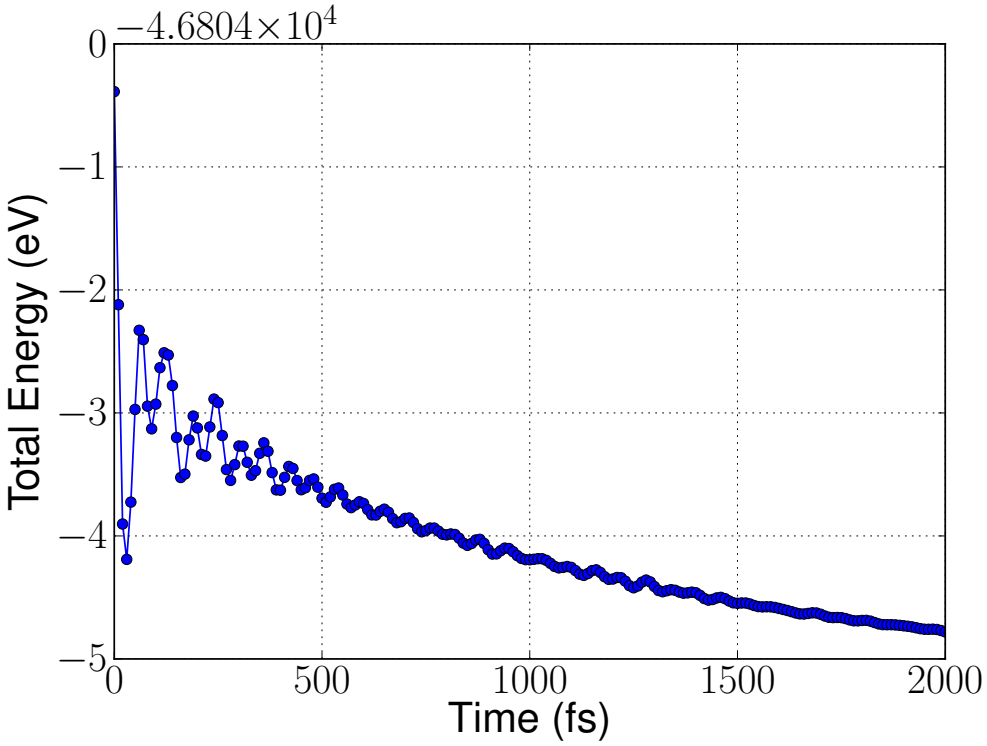

Figure 2.10: Illustration of the energy minimisation using the Damped MD method ($k = 2$) applied on a 2,000 atom bcc Fe system with a single vacancy.

2.5.3 L-BFGS-B

The Broyden-Fletcher-Goldfarb-Shanno (BFGS) optimization algorithm belongs to the quasi-Newton methods family for finding local minima and maxima of functions. The idea behind the method is to approximate the Hessian matrix by an iterative procedure using gradient evaluations and is similar to the CG method.

The method starts with an initial guess $\mathbf{x}_0$ and the initial approximation of the Hessian H_0:

$$H_0\mathbf{p}_0 = -\nabla f(\mathbf{x}_0), \tag{2.5.8}$$

where f is the function being minimized.

Then follows an iterative procedure to update the Hessian approximation H_k:

- **Step 1 - new direction** - finding a new direction $\mathbf{p}_k$ by solving $H_k\mathbf{p}_k = -\nabla f(\mathbf{x}_k)$,

- **Step 2 - line search** - finding a suitable step size α_k and updating $\mathbf{x}_{k+1} = \mathbf{x}_k + \alpha_k \mathbf{p}_k$,
- **Step 3 - new gradient** - calculating new gradient $\nabla f(\mathbf{x}_{k+1})$,
- **Step 4 - Hessian update** - updating the Hessian approximation using:

$$H_{k+1} = H_k + \frac{\left(\nabla f(\mathbf{x}_{k+1}) - \nabla f(\mathbf{x}_k)\right)\left(\nabla f(\mathbf{x}_{k+1}) - \nabla f(\mathbf{x}_k)\right)^T}{\left(\nabla f(\mathbf{x}_{k+1}) - \nabla f(\mathbf{x}_k)\right)^T \alpha_k \mathbf{p}_k} - \frac{H_k \left(\alpha_k \mathbf{p}_k\right)\left(\alpha_k \mathbf{p}_k\right)^T H_k}{\left(\alpha_k \mathbf{p}_k\right)^T H_h \left(\alpha_k \mathbf{p}_k\right)}. \tag{2.5.9}$$

- **Step 5 - repeat** - if the convergence has not been met, go to step 1.

In this work the improved BFGS method (L-BFGS-B) which uses limited amount of memory and allows box constrains for each variable, has been used [75, 76]. L-BFGS-B uses only couple of vectors for the representation of the inverse Hessian matrix, resulting in being a very efficient and well suited for the optimization of functions with a large number of variables. L-BFGS-B method is implemented from the open source library SciPy 0.12.0 for the Python programming language (http://www.scipy.org/).

2.6 Thermalization

In many cases having a system in a local energy minimum is not enough in order to have a good representation of the problem. It is often the case, that a system shows a different behaviour and has a different structure at different temperatures. When studying radiation damage in materials, temperature also plays a big role and has a great influence on the annealing and defect recombination processes.

To control a system's temperature, so called thermostat algorithms are being used. Their whole purpose is to re-scale the velocities of the atoms with a direct link between the kinetic energy and temperature:

$$T = \frac{2}{3}\frac{E_K}{Nk_b}. \tag{2.6.1}$$

There are quite few thermostats and all of them have their advantages and disadvantages. One of the most popular is the Nosé-Hoover thermostat [77]. It governs the atoms' velocities by introducing a friction term coefficient in the equations of motion, which depends on the actual and target kinetic energies. The coefficient is fairly easy to calculate and the method can give a good canonical ensemble of the atoms. One of the its drawbacks - it usually takes longer to reach the required temperature due to big oscillations.

Another popular thermostat follows Langevin dynamics [78]. In this case a small damping constant is used in a modification of the Newton's equations of motion proportional to the velocity, so that the actual temperature matches the target temperature.

In this work, the Berendsen thermostat [79] was most often used to control the temperature of the systems. It works by scaling the atoms' velocities, which are further used within the time integrator. The scaling is carried out according to the change of the temperature with respect to the time which is proportional to the difference between the actual (T) and target (T_0) temperatures:

$$\frac{dT}{dt} = 2\gamma\left(T_0 - T\right), \tag{2.6.2}$$

where γ is a decay constant, which controls the correction of the temperature.

It is proven that the velocity scaling factor per time step Δt can be made exactly equal to $2\gamma\left(T_0 - T\right)$ as follows:

$$\lambda = \sqrt{1 + \frac{\Delta t}{\tau_T}\left(\frac{T_0}{T} - 1\right)}, \tag{2.6.3}$$

where, τ_T is a time constant, which is equal to $(2\gamma)^{-1}$.

Even though a correct canonical ensemble generated by this thermostat cannot be achieved for a small system, the approximation gives roughly correct results for bigger ones, containing

thousands or more atoms.

2.7 Collision Cascades

To simulate collision cascades representing the ballistic phase of radiation events described in section 1.4, an atom, also known as a primary knock-on atom (PKA), is given a certain amount of energy, directed usually in a non-channelling direction and then the system is evolved using the MD equations of motion.

One of the main quantities used to investigate the disorder brought to the system by a collision cascade is the number of residual defects. There are basically two types of defects: an interstitial (an atom positioned away from a lattice site) and a vacancy (an unoccupied lattice site). The third type of defect occurs when a multi-species system is modelled and the atom occupying an atom site which was originally occupied by a different specie atom is called an antisite. In this work, interstitials are visualized as spheres, vacancies as cubes and antisites as wireframe boxes (coloured according to the original atom) with a sphere inside of it representing the current occupying atom (Figure 2.11).

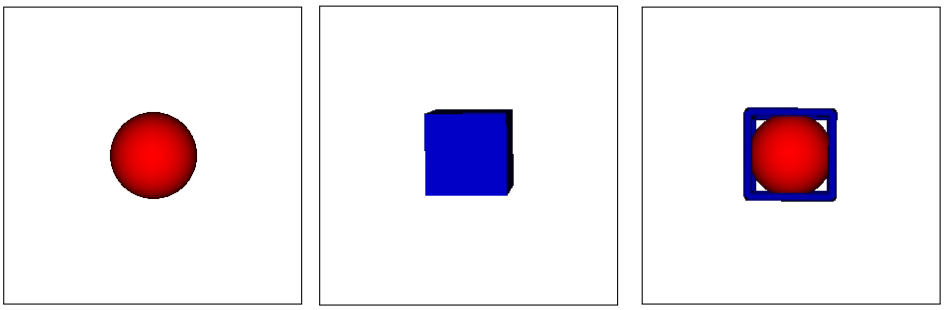

(a) (b) (c)

Figure 2.11: A visual representation of the main types of defects: (a) - O interstitial, (b) - Y vacancy, (c) - Y anti-site occupied by O atom. All defects are coloured and sized by the atom type. The anti-site is represented by an original atom type box contours and by the occupying atom in the middle.

The method to identify defects in the system relies on the vacancy radius R_{vac}. It works by comparing the initial atom positions (reference lattice), with the current atom positions (input lattice). All the atoms that are not within a R_{vac} are identified as defects, e.g. an

interstitial is identified, when an atom's position in the input lattice does not correlate with an unoccupied lattice site in the reference lattice within the vacancy radius. Similarly a vacancy is when a reference lattice site does not correlate with any atom in the input lattice within the R_{vac}.

Every collision cascade simulation can be categorized by the specie and the position of the PKA and also by the PKA's initial kinetic energy. All these factors and the PKA trajectories were chosen for all the systems individually and are described in the result sections of this work.

Chapter 3

Methodology II: Long Time Scale Dynamics

3.1 Introduction

The increasing power and popularity of MD simulations is due to the rapidly increasing computer speeds and the improvement of inter-atomic potentials. Despite that, MD time scale limitations still exist and to reach even one microsecond is still difficult, thus the need of time extending methods is inevitable [80]. Some of the most popular and promising techniques are: parallel replica dynamics, hyper-dynamics, temperature-accelerated dynamics (TAD) and Kinetic Monte Carlo (KMC) methods.

One of the simplest and quite accurate methods is the parallel replica dynamics, which instead of requiring that system should obey transition state theory, requires the system to obey first-order kinetics rules [81]. This method consist of four steps. The first step is the system replication into M copies. During the second step, each of the copies are de-phased by periodically randomizing momenta and eliminating any correlation between the M number of system replicas. The third step, phase exploration, occurs until in one of the replicas a transition is detected. During the fourth step a brief continuation of the transition trajectory

is done. The result from the fourth step then is replicated and the process begins again.

In the hyper-dynamics method, the idea is to transform the system's potential energy surface using a bias potential [82]. This bias must be zero on all the dividing surfaces and shall only increase the system's potential energy around the local minima, thus giving an ability for the system to escape from local minima more rapidly. It is also designed to keep the relative transition rates for different pathways the same.

The main idea for the TAD method, is to increase system's temperature, thus increasing the transition rates. The TAD method relies on the harmonic transition state theory [83]. The idea is to evolve a system at high temperature and when a transition is detected, to use the nudged elastic band method (described later in this chapter), to determine the energy barrier. Transition rates are calculated at a high temperature and can be converted back to low temperature.

For long time scale dynamics simulations in this work, the on-the-fly Kinetic Monte Carlo (otf-KMC) method was applied. This method differs from the traditional Kinetic Monte Carlo simulation in the way that all the transitions that can occur in the system are not known before the simulation starts, but are found during each KMC step using a so-called "on-the-fly" search of transition states. This technique allows one to start simulations from many different random system configurations, but does not guarantee that all possible transitions will be found during each step. When a list of transition events is formed, rates for each transition are computed from transition state theory, making a rate list and then the system is advanced to a new state using the appropriate transition probability.

3.2 Kinetic Monte Carlo

The original KMC algorithm for simulating evolution of a system where the rates of the processes that can occur are known, can be represented as an iterative procedure as follows:

1. Set the initial time (usually t = 0),

2. Make a list of rates in the system r_i regarding the possible events and sum them as $R = \sum_{j=1}^{N} r_j$,

3. Generate a random number P between 0 and R,

4. Cumulatively step through all events until P is exceeded,

5. The transition is selected with respect to the current event and the system is advanced to a new step,

6. The time increment δt during the step is given by $\delta t = -\frac{\log u}{R}$, where u is a random number between 0 and 1,

7. Return to step 2.

This algorithm will be referred as the KMC roulette further on.

The extension to the original KMC method was initially suggested by Henkelman and Jónsson [46], and it was one of the first methods to carry out long time scale dynamics simulations within the harmonic transition state theory (hTST) approximation. They suggested to characterise a system by its local energy minima, do multiple saddle searches on the fly and calculate rates for each individual transition using the hTST. An event is then selected and the simulation clock advanced according to the KMC algorithm. The method was used to study $Al\,(100)$ crystal growth and is known as an otf-KMC method.

Transition state theory operates on the idea of having transition rates between two states calculated only by examining the equilibrium and saddle states of the transition by using the Arrhenius equation:

$$r = \tau \exp\left(-\Delta E / k_B T\right), \tag{3.2.1}$$

where ΔE is the activation energy, k_B - Boltzmann's constant, T - temperature and τ is the pre-exponential coefficient also known as the prefactor.

As can be seen in Equation 3.2.1, transition rates basically depend on two variables, the energy barrier ΔE and the prefactor τ. E is calculated by examining the initial minimum and saddle states of the transition. For this reason it is crucial to determine the saddle states accurately. Various methods, also known as transition search methods, are now described to determine the saddle points.

3.3 Transition Search Methods

Finding transitions during an otf-KMC step is the most vital part of the technique. A "good" set of transitions is necessary in order to capture the processes and also to estimate the simulation time. A "good" set can be thought of as a set that includes most of the possible transitions at the current step, and all those with low barrier heights, since they have the biggest impact on the evolution of a system.

Originally Henkelman and Jónsson [46] proposed to use transition finding algorithms (the Dimer method) in order to make a list of possible events at every step, therefore avoiding manual cataloguing of events and allowing much greater complexity and system's evolution in not pre-determined way by the event catalogue. In this way, transitions can be represented as a set of three states: initial minimum, saddle and final minimum. The saddle state is the most important, since it connects two minima via the minimum energy pathway (MEP) and determines how likely a transition will be picked to advance the system according to its barrier and prefactor. For this reason it is essential to accurately determine saddle states and two groups of methods were investigated: single-ended and double-ended search methods.

3.3.1 Single-ended Search Methods

Single-ended search methods (also known as surface walking methods) share a common idea, that only the initial state of a system is needed to find a saddle state, which separates two system states (local minima). They usually follow the minimum mode of curvature to "climb

up" to the saddle state from the initial minimum. Sometimes a single-ended search method is combined with a double-ended search method, where the single-ended search is used with a low accuracy to find a saddle, then the system is pushed over the saddle and a double-ended method is used to calculate the MEP connecting the two end points and the saddle.

3.3.1.1 Dimer Method

The Dimer method was developed by Henkelman and Jónsson [84] and the idea behind it is to represent a system's state as two images (this pair of images is referred as a "dimer") having almost the same set of coordinates with fixed displacement. The Dimer method can be thought of as a two step algorithm, where the first step is the dimer's movement and the calculation of the acting forces and energies on it (Figure 3.1a). The second step is the rotation of the dimer towards the minimum energy configuration (Figure 3.1b). The Dimer method uses only the first derivative of the potential energy which is advantageous when the second derivative is computationally expensive to estimate or difficult to calculate.

In Figure 3.1a R represents the coordinate of the system's midpoint (state) in 3N dimensional space. Points R_1 and R_2 are the pair images separated from R by ΔR and are orientated in the direction of a unit vector $\hat{\mathbf{N}}$. Initially and every time when the dimer is moved to a new location, the corresponding energies (E_1, E_2) and forces ($\mathbf{F_1}$, $\mathbf{F_2}$) are evaluated. The energy of the dimer is simply a sum of energies of the images $E = E_1 + E_2$, where the force and the energy at the midpoint R, $\mathbf{F}_R$ and E_0, are calculated from the two images (Equation 3.3.1) as follows:

$$\begin{aligned} \mathbf{F}_R &= (\mathbf{F_1} - \mathbf{F_2})/2, \\ E_0 &= \frac{E}{2} + \frac{\Delta R}{4}(\mathbf{F_1} - \mathbf{F_2}) \cdot \hat{\mathbf{N}}. \end{aligned} \tag{3.3.1}$$

The dimer's rotation towards the minimum energy configuration is based on the idea,

that minimizing the dimer's energy E is equal to finding the lowest curvature mode at R, estimated using Equation 3.3.2. This is done by rotating the dimer along the rotational force $\mathbf{F}^{\perp} = \mathbf{F_1^{\perp}} - \mathbf{F_2^{\perp}}$, where $\mathbf{F_i^{\perp}} \equiv \mathbf{F_i} - (\mathbf{F_i} \cdot \hat{\mathbf{N}}) \cdot \hat{\mathbf{N}}, i = 1, 2$.

$$C = \frac{(\mathbf{F_2} - \mathbf{F_1}) \cdot \hat{\mathbf{N}}}{2\Delta R} = \frac{E - 2E_0}{(\Delta R)^2}. \tag{3.3.2}$$

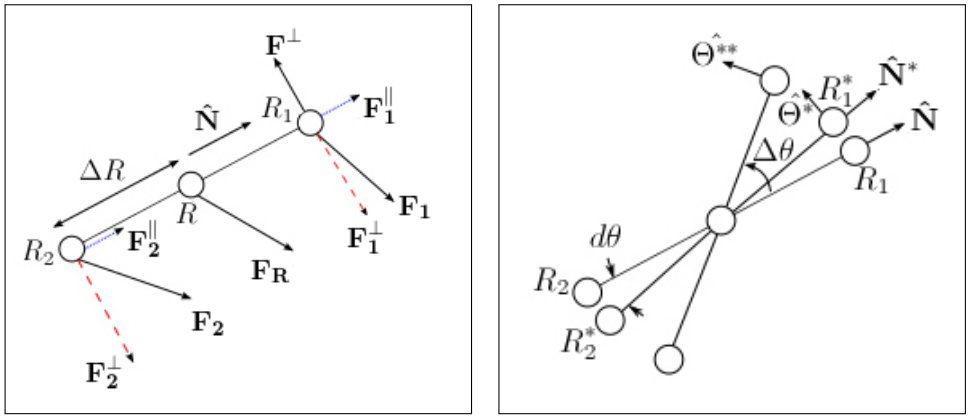

(a) (b)

Figure 3.1: The Dimer method as in [84]. (a) - the definitions of the dimer's midpoint, image points and the acting component and rotational forces on them, (b) - the definitions of the quantities used during the rotation of the dimer.

Figure 3.1b shows the basic steps of the dimer's rotation. A new unit vector $\hat{\mathbf{\Theta}}$, perpendicular to $\hat{\mathbf{N}}$ and parallel to $\mathbf{F}^{\perp}$, is defined to form an orthonormal basis which spans the rotation plane. At first, the dimer is rotated about a small angle $d\theta$, then using the orthonormal basis new image points are calculated (Equation 3.3.3) and the acting forces $\mathbf{F_1^*}$, $\mathbf{F_2^*}$, $\mathbf{F}^* = \mathbf{F_1^*} - \mathbf{F_2^*}$ are estimated.

$$\begin{aligned} R_1^* &= R + \left(\hat{\mathbf{N}} \cos\delta\theta + \hat{\mathbf{\Theta}} \sin\delta\theta\right) \Delta R, \\ R_2^* &= R_1^* - 2\Delta R \hat{\mathbf{N}}. \end{aligned} \tag{3.3.3}$$

The finite difference approximation of the rotational force is given in Equation 3.3.4, which is to be minimised.

$$F' \approx \left| \frac{\mathbf{F}^* \cdot \hat{\mathbf{\Theta}}^* - \mathbf{F} \cdot \hat{\mathbf{\Theta}}}{d\theta} \right|_{\theta = d\theta/2}. \tag{3.3.4}$$

In this work the harmonic approximation of the rotational force $F = A \sin[2(\theta - \theta_0)]$ and its derivative $F' = 2A \cos[2(\theta - \theta_0)]$ are used to approximate the rotation angle $\Delta\theta$ as follows:

$$\Delta\theta = -\frac{1}{2} \arctan \frac{2F_0}{F_0{}'}, \tag{3.3.5}$$

where F_0 and $F_0{}'$ are values of F and F' evaluated at $\theta = 0$.

Then $\Delta\theta$ is used to minimise the dimer's energy with the CG method using the modified Newton method [84] as the line search.

After the minimization by rotation, the dimer will be oriented along the local lowest curvature mode and it is followed by the dimer's translation. Depending on the curvature value C, calculated using Equation 3.3.2, two schemes are used. First, when the curvature value is positive, the dimer is allowed to move out of that region by big steps. Second, when the curvature has a negative value, it means the dimer is getting closer to the saddle point and the saddle point is approached by smaller steps. The two cases can be expressed as follows:

$$\mathbf{F}_{trans} = \begin{cases} -\mathbf{F}^{\parallel}, & C > 0, \\ \mathbf{F} - 2\mathbf{F}^{\parallel}, & C < 0, \end{cases} \tag{3.3.6}$$

where $\mathbf{F}$ is the real force acting on the dimer, $\mathbf{F}^{\parallel}$ - the component of the force parallel to the $\hat{\mathbf{N}}$ and given by: $\mathbf{F}^{\parallel} = \mathbf{F}_{\mathbf{1}}^{\parallel} + \mathbf{F}_{\mathbf{2}}^{\parallel}$.

3.3.1.2 Activation-Relaxation Technique (ART)

The Activation-Relaxation Technique (ART) was introduced by Barkema and Mousseau [85, 86]. As can be inferred from the name of the technique: it consists of two steps: 1)

Activation: starting from a local minimum, the system is advanced to a local saddle point; 2) Relaxation: the system is pushed over the saddle point and relaxed to a new minimum. In this work only the activation step of the technique to approach the saddle is considered, since the relaxation for all the single-ended search methods is basically the same.

The main concept of the ART method is to initiate a random movement of an atom, by randomly displacing it from its original position in the local minimum configuration. This action causes a change in the force, which will be used for an iterative procedure to move the system to a saddle point by following the redefined force $\boldsymbol{G}$, expressed as follows:

$$\boldsymbol{G} = \boldsymbol{F} - (1+\alpha)\,(\boldsymbol{F}\cdot\Delta\boldsymbol{X})\,\Delta\boldsymbol{X}, \tag{3.3.7}$$

where $\boldsymbol{F}$ is the $3N$-dimensional force vector acting on the atoms in the system, $\Delta\boldsymbol{X}$ is a $3N$-dimensional unit vector pointing from the initial system configuration to the current position and α is a positive number.

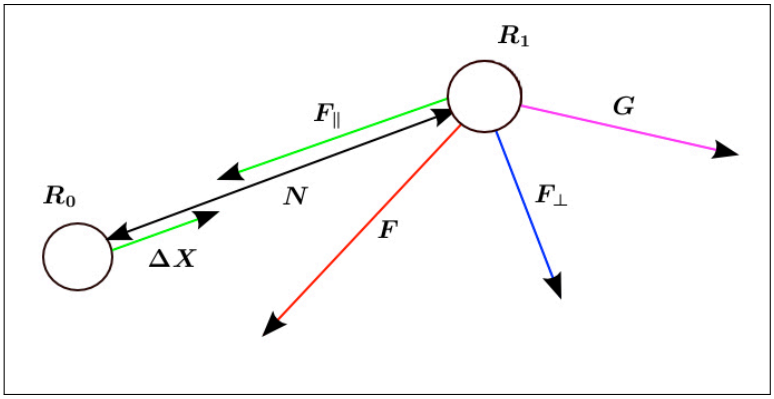

Figure 3.2: Schematic illustration of an iteration of the ART method's activation step: $\boldsymbol{R_0}$ and $\boldsymbol{R_1}$ represent the initial and current system states; $\boldsymbol{N}$ is the displacement vector between them; $\boldsymbol{F}$ is the acting force on the system at $\boldsymbol{R}_1$, with the parallel $\boldsymbol{F}_\parallel$ and perpendicular $\boldsymbol{F}_\perp$ components; $\Delta\boldsymbol{X}$ is a unit vector pointing from $\boldsymbol{R_0}$ to $\boldsymbol{R_1}$ and $\boldsymbol{G}$ is the new constructed force.

As can be seen in Figure 3.2, the new force $\boldsymbol{G}$ has the same sign as $\boldsymbol{F}$ in the direction perpendicular to $\Delta\boldsymbol{X}$ and an opposite sign of $\boldsymbol{F}$ in the direction parallel $\Delta\boldsymbol{X}$. The scalar variable α controls the "magnitude" of the new force $\boldsymbol{G}$ in the direction parallel to $\Delta\boldsymbol{X}$, i.e. the bigger the value of α, the more the force $\boldsymbol{G}$ is directed in the opposite direction of

$\Delta \boldsymbol{X}$. In other words, the scalar variable α, controls the climb away from the initial local minimum.

The iterative process of calculating $\boldsymbol{G}$ and moving atoms in the direction of it, results in the system climbing up the energy landscape hill, where the top of the hill represents a saddle point. The iterative process's stop criterion was slightly changed compared to the original one proposed by Barkema and Mousseau. The idea was to stop the activation step when both $\boldsymbol{F}$ and $\boldsymbol{G}$ are zero. In the implementation used in this work, such stopping criterion was not always effective and a stopping criterion used by Vernon [47] was employed, where the direction of $\boldsymbol{F}$ is monitored, waiting for the part of $\boldsymbol{F}$ which is parallel to $\Delta \boldsymbol{X}$ to have a positive sign, meaning that the iterative procedure has crossed a saddle point.

The values for scalar variable α and the step size by which atoms' positions are moved along the direction of $\boldsymbol{G}$ were obtained by Vernon [47] and accordingly are 0.625 and 0.00467.

3.3.1.3 ART *Nouveau*

The ART *Nouveau* (ARTn) method [39] is an improvement of the original ART method, described previously in the section 3.3.1.2. The main difference is that instead of following the direction of a newly created force vector to find a saddle point, the direction of the eigenvector, corresponding to the lowest eigenvalue of the Hessian matrix of the potential energy function, is followed.

The technique starts at the system's local minimum and a random displacement $\delta \boldsymbol{q}^i$ is initiated at it. Then all the subsequent images are generated, according to Equation 3.3.8:

$$\boldsymbol{q}_k^i = \boldsymbol{q}_{k-1}^i + \frac{\delta x_A}{\|\delta \boldsymbol{q}^i\|} \delta \boldsymbol{q}^i, \tag{3.3.8}$$

where δx_A is a step size of the atoms' displacement and $\boldsymbol{q}_k^i$ represents the system at the k-th iterative step of the i-th saddle point search attempt. At each step, before the calculation of a new system state, the current system state is relaxed in the hyperplane orthogonal to $\delta \boldsymbol{q}^i$ and the lowest eigenvalue λ_1 of the Hessian is obtained. If the lowest eigenvalue is positive

the iterative process is continued. If the value of λ_1 is negative, it is assumed that the system is in a region close to a saddle point. Then the convergence to a saddle point is achieved by the iterative procedure (Equation 3.3.9) which follows the eigenvector $\boldsymbol{v}_1$ corresponding to the λ_1:

$$\boldsymbol{q}_n^i = \boldsymbol{q}_{n-1}^i + \frac{\delta x_A}{\|\boldsymbol{v}_1\|}\boldsymbol{v}_1. \tag{3.3.9}$$

As in the previous step, each system state is relaxed in the hyperplane orthogonal to $\boldsymbol{v}_1$ and the lowest eigenvalue λ_1 of the Hessian is obtained. The stopping criterion of the step is the same as is used in the original ART method. If the lowest eigenvalue λ_1 becomes positive the entire activation step is restarted. To estimate the lowest eigenvalue, the well known Lanczos algorithm combined with the Q-R method can be used as is explained in the following sections 3.3.1.6 and 3.3.1.7.

3.3.1.4 Relaxation and Translation Method

The relaxation and translation (RAT) method, developed by Vernon [47] (see Figure 3.3), shares some similarities with the dimer method: both of them uses force decomposition into parallel and perpendicular components. But unlike the Dimer method, it operates only with one point in the 3N dimensional potential energy landscape and as can be inferred from its name consists of two steps: relaxation and translation.

During the translation step, the search point is moved along the vector $\mathbf{N}$ by certain step size S_{trans}. Initially, the vector $\mathbf{N}_0$ is a random unit vector, which for all the other steps $\mathbf{N}_i, i \geq 1$ is constructed by combining the previous vector $\mathbf{N}_{i-1}$ and $\widetilde{\mathbf{R}}_i$, that joins the original step search point $\mathbf{R}_{i-1}$ with the relaxed point $\mathbf{R}_i$ according to Equation 3.3.10. The initial scalar translation step size S_{trans_0} is 0.0075Å and during all the other steps re-evaluated according to the number of iterations during the relaxation step: if the number is less than 3, the step size is multiplied by 1.2, otherwise it is divided by 2, as it was found by Vernon

[47] to give good accuracy and speed.

$$\widetilde{\mathbf{R}}_i = (\mathbf{R}_i - \mathbf{R}_{i-1}),$$
$$\mathbf{N}_i = 0.5 \cdot \mathbf{N}_{i-1} + \widetilde{\mathbf{R}}_i. \tag{3.3.10}$$

The relaxation step is used to relax the component of the force acting on the point $\mathbf{R}'$ and perpendicular to the vector $\mathbf{N}$. This step may require large movements within the plane. The idea of this step is simple: to ensure a reasonable efficiency, the relaxation step must be adjusted according to the change of the system's energy. If the change $\left(F_{T_j} - F_{T_{j-1}}\right)/F_{T_j}$ is less than 20%, the relaxation step needs to be more aggressive and is increased by 20%. If the change is greater than 20%, it means that the method approaches a saddle state and the step size must be smaller in order to accurately determine the saddle, thus it is lowered by a factor of two.

Figure 3.3 represents a schematic illustration of the RAT method which is terminated (assuming that a saddle point was found), if one of the atoms moves more than 0.3 Å from its initial position and the dot product between the force vector and the vector $\widetilde{\mathbf{R}}_i$ is greater than 0.5 eV. The last statement implies, that a point $\mathbf{R}$ has crossed the saddle point and is going down the "hill" (on the other side).

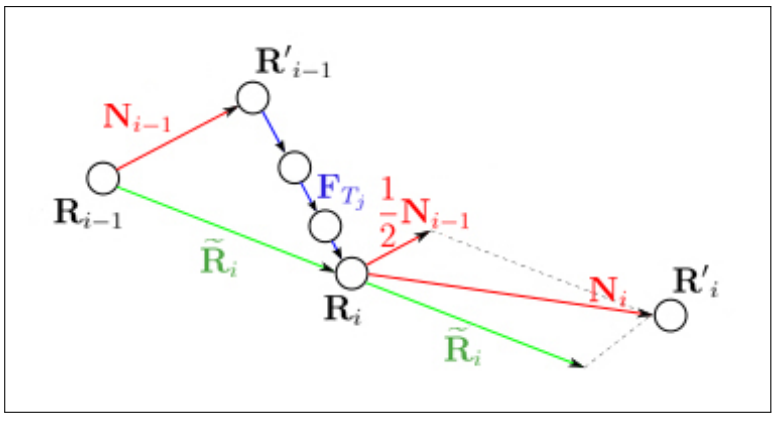

Figure 3.3: Schematic representation of the RAT method, where $\mathbf{R}_i$ are points representing system states, $\mathbf{R}'_i$ - translated points, $\mathbf{N}_i$ - translation unit vectors, $\mathbf{F}_{T_i}$ - vectors, perpendicular to $\mathbf{N}_i$.

3.3.1.5 Minimum Mode Following Algorithm

One of the first suggestions to use eigenvectors of the Hessian for approaching saddle points were made by Cerjan and Miller [87] in the early 90's. The biggest drawback is the computationally expensive construction of the full Hessian matrix in order to solve the eigenvalue problem. There are several different ways to approach this problem by approximating the lowest eigenvalue without diagonalising the Hessian.

The basic idea behind all the minimum mode following methods is to invert the force along the eigenvector corresponding to the lowest eigenvalue of the Hessian using the following formula:

$$\mathbf{F}^{eff} = \mathbf{F} - 2\left(\mathbf{F} \cdot \mathbf{v}_{min}\right)\mathbf{v}_{min}, \tag{3.3.11}$$

where $\mathbf{F}^{eff}$ is the effective force driving the system to a saddle point, $\mathbf{F}$ is the actual force and $\mathbf{v}_{min}$ is the eigenvector corresponding to the lowest eigenvalue. With the $\mathbf{F}^{eff}$ so defined, the rank 1 saddles become local minima and local optimisation algorithms can be used to found them.

Different authors suggest different ways to effectively approximate or estimate $\mathbf{v}_{min}$. The Dimer method [84] (see section 3.3.1.1) is one of the most popular methods to approximate $\mathbf{v}_{min}$ by the orientation of two replicas of the system.

A combination of the Dimer method and the Conjugate Gradient method by A. Pederson [88] is shown to be an effective way to locate first order saddle points. The suggested procedure, at iteration n, uses one displacement along the search direction, determined by a linear combination of the previous direction $\mathbf{d}_{n-1}$ and the current gradient $\mathbf{F}$, instead of linear search:

$$\mathbf{d}_n = \mathbf{F} + \beta_n \mathbf{d}_{n-1}, \tag{3.3.12}$$

here n is the iteration number and β_n is estimated by the Polak-Ribiére formula:

$$\beta_n = \frac{\mathbf{F}(\mathbf{x}_n) \cdot \mathbf{F}(\mathbf{x}_n) - \mathbf{F}(\mathbf{x}_{n-1})}{\mathbf{F}(\mathbf{x}_{n-1}) \cdot \mathbf{F}(\mathbf{x}_{n-1})}, \tag{3.3.13}$$

where $\mathbf{x}_n$ is the phase space point of the system.

Both methods were implemented, but it was found that, that in terms of unique successful searches, a combination of the BFGS minimisation algorithm [75, 76] and the Hessian matrix diagonalisation using the Lanczos method [89] followed by the QR method was found to be the most appropriate. In this work, this combination of methods will be addressed as the Minimum Mode Following Algorithm (MMFA).

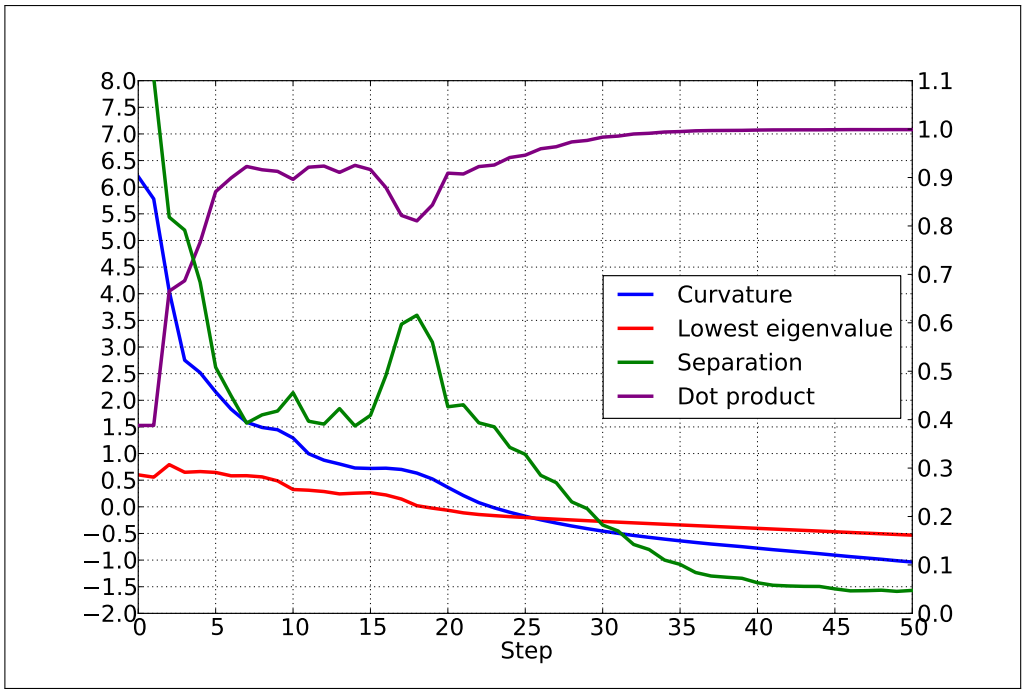

Figure 3.4: A graph showing the correlation (left y axis) between the curvature calculated using the Dimer method and the lowest eigenvalue, calculated with the Lanczos algorithm (described in the following section). The difference between vectors associated with them in terms of separation (as Euclidean norm between two vectors) and a dot product (right y axis).

It was also found that a combination of the Dimer method with the MMFA has a good mixture of accuracy and speed when looking for saddle points. At first the Dimer method is used to arrive in the vicinity of a saddle state and then when the lowest eigenvalue becomes negative a switch to MMFA takes place. In order to check the relation between the Dimer's curvature and the lowest eigenvalue tests were carried out in the α-Fe system with a single

⟨110⟩ dumbbell defect which can be summarized in Figure 3.4.

The tests checked the correlation between the Dimer's curvature and the lowest eigenvalue every dimer step. As can be seen (Figure 3.4), at the beginning of the Dimer method, the Dimer's curvature overestimates the value of the lowest eigenvalue, but when the curvature approaches zero (around step 25-30), the separation (Euclidean norm) between the Dimer vector (the vector between two images) and the eigenvector, corresponding to the lowest eigenvalue, becomes very small and the dot product of those vectors is almost equal to 1. This indicates that both vectors are similar and point in almost the same direction. Thus, when a combination of the Dimer method and MMFA is used, the switch between these two methods is carried out when the dimer's curvature becomes negative.

3.3.1.6 Lanczos Algorithm

The well known Lanczos algorithm is a very powerful technique to save computational time while calculating eigenvalues and eigenvectors of a symmetric matrix. The algorithm is an iterative procedure [89] and operates on the idea of converting a symmetric matrix to a tridiagonal symmetric matrix as follows:

Listing 3.1: Lanczos algorithm

```
1 β_1 = 0; v_0 = 0; v_1 = normalised random vector.
2 for i in range(1, m)
3             w_i = A v_i
4             α_i = w_i · v_i
5             w_i = w_i − α_i v_i − β_i v_{i−1}
6             β_{i+1} = ||w_i||
7             v_{i+1} = w_i / β_{i+1}
8 end;
```

where A is a symmetric matrix (in our case it is the Hessian at a certain phase space point of the system), α_i and β_i are the elements of the tridiagonal result matrix (Equation 3.3.14), m - the size of the symmetric matrix and $\mathbf{v}_i$ are the orthonormal Lanczos basis vectors.

$$T = \begin{bmatrix} \alpha_0 & \beta_1 & 0 & \cdots & 0 \\ \beta_1 & \alpha_1 & \beta_2 & \cdots & 0 \\ 0 & \beta_2 & \alpha_2 & \cdots & 0 \\ 0 & \ddots & \ddots & \vdots & 0 \\ 0 & 0 & \beta_{n-2} & \alpha_{n-2} & \beta_{n-1} \\ 0 & 0 & 0 & \beta_{n-1} & \alpha_{n-1} \end{bmatrix} \tag{3.3.14}$$

The effectiveness of the Lanczos method also comes from the approximation of $\mathbf{A}\mathbf{v}_i$ by the difference in the Taylor expansion forces around the phase space point $\mathbf{x}+\delta\mathbf{v}_i$ with error either $O(\delta^2)$ (Equation 3.3.15) or $O(\delta^3)$ (Equation 3.3.16) as follows:

$$\mathbf{A}\mathbf{v}_i = -\frac{\mathbf{f}\left(\mathbf{x}+\delta\mathbf{v}_i\right) - \mathbf{f}\left(\mathbf{x}\right)}{\delta} + O\left(\delta^2\right) \tag{3.3.15}$$

$$\mathbf{A}\mathbf{v}_i = -\frac{\mathbf{f}\left(\mathbf{x}+\delta\mathbf{v}_i\right) - \mathbf{f}\left(\mathbf{x}-\delta\mathbf{v}_i\right)}{2\delta} + O\left(\delta^3\right) \tag{3.3.16}$$

where $\delta \ll 1$.

It is known, that due to the computational errors, the exact orthogonality of the Lanczos basis is not being preserved [90]. To deal with this problem, the least squares method (LSM) is used as follows:

$$\mathbf{v}_i = \mathbf{v}_i - \mathbf{L}_i\mathbf{s}_i, \tag{3.3.17}$$

where $\mathbf{L}_i$ is an orthonormal Lanczos basis consisting of $i-1$ Lanczos vectors $\mathbf{v}_j$ ($\mathrm{j} = \overline{1, i-1}$) and $\mathbf{s}_i$ is the least squares method's (LSM) solution of the problem: $\mathbf{L}_i\mathbf{s}_i = \mathbf{v}_i$. As can be

seen, Equation 3.3.17 removes the non-orthogonal error from the Lanczos vector.

Empirical tests showed that the orthogonal correction by the LSM is sufficient while the number of the Lanczos basis vectors is lower than 50. Otherwise, the LSM method contribution to the overall computational costs per Lanczos iteration increases significantly and the difference between time taken by the Lanczos method compared to explicit calculations of the eigenvalues and eigenvectors of the Hessian matrix is small.

The iterative Lanzcos procedure is stopped when the desired convergence of the lowest or other (specified by the user) eigenvalue (calculated using the QR method (see subsection 3.3.1.7) on the tridiagonal matrix) is reached by checking if the relative change of the eigenvalue is less than the specified value. The default tolerance used in the simulations is 0.01, since the tighter tolerance did not have a significant impact on the results.

3.3.1.7 QR Method

The well known QR algorithm is one of the best procedures to estimate eigenvalues and eigenvectors of a symmetric matrix. In the developed software the QR method specially developed to work with tridiagonal symmetric matrices [91] was implemented from the well known Linear Algebra PACKage (LAPACK) library. The implemented routines dstev and dystevx are specially designed for calculating full and selective set of eigenvalues and eigenvectors of the symmetric tridiagonal matrix accordingly.

The idea behind the iterative QR method is to decompose a given matrix A into orthogonal matrix Q and upper triangular matrix R (Equation 3.3.18) and use these matrices to produce a sequence of matrices (Equation 3.3.19), which tend to a diagonal matrix, where diagonal values r_0, ..., r_{n-1} from the matrix $\mathbf{R}_l$ converge to the eigenvalues of the matrix $\mathbf{T}$ when l$\rightarrow \infty$.

$$\mathbf{A}_i = \mathbf{Q}_i\mathbf{R}_i. \qquad (3.3.18) \qquad \mathbf{A}_{i+1} = \mathbf{R}_i\mathbf{Q}_i. \qquad (3.3.19)$$

3.3.2 Double-ended Search Methods

The double-ended search methods (also known as the interpolation methods) use both the initial and final system configurations (local minima on the potential energy surface) to find the MEP and the maximum energy point on it, which determines the activation energy barrier. Usually double-ended search methods are more accurate than single-ended methods, but also require more computational resources and if there are several migration pathways between two minima, double-ended search methods tend to find only the MEP.

3.3.2.1 Nudged Elastic Band Method

The Nudged Elastic Band Method (NEB) was developed by H. Jónsson *et al.* in 1998. Where given the initial and final system configurations (images), the method starts by creating a chain of evenly separated intermediate images and calculates acting forces on them as shown in Figure 3.5. Spring interactions are added between neighbouring images, thus imitating an elastic band and ensuring the continuity of the path. In order to have a good path convergence to the MEP, the spring force must not interfere with the true force. This is done by calculating the tangent to the path at each image, at every iteration and decomposing the true and spring forces into parallel and perpendicular forces to the path. Only the parallel component of the spring force and perpendicular of the true force are included in the calculations and this force projection is referred as "nudging".

In this work an improved tangent estimation is used, which was suggested by G. Henkelman and H. Jónsson [92]. They changed the original estimation by using different tangent definitions according to the energies of the nearby images, thus eliminating the cases, when the method did not converge to the MEP:

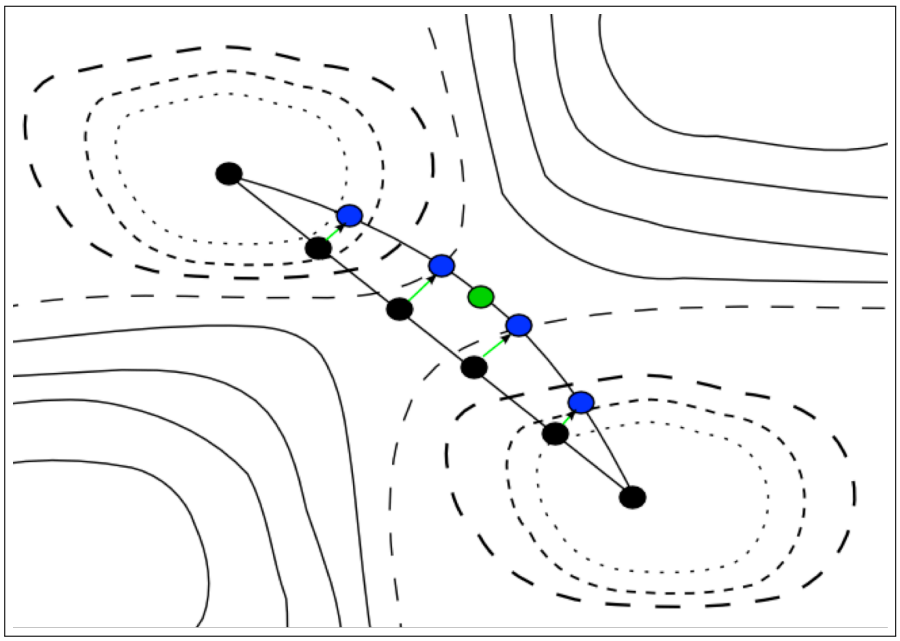

Figure 3.5: Schematic representation of the NEB method; where the black points represent the initial NEB images and the blue points are for the final NEB images joined by the MEP. Acting forces on images are shown as green arrows. The green point depicts the saddle point.

$$\tau_i = \begin{cases} \tau_i^+ & \text{if} \quad E_{i+1} > E_i > E_{i-1}, \\ \tau_i^- & \text{if} \quad E_{i+1} < E_i < E_{i-1}, \\ \tau_i^+ \Delta E_i^{max} + \tau_i^- \Delta E_i^{min} & \text{if} \quad E_i < E_{i-1} < E_{i+1}, \\ \tau_i^+ \Delta E_i^{min} + \tau_i^- \Delta E_i^{max} & \text{if} \quad E_i > E_{i-1} > E_{i+1}, \end{cases} \tag{3.3.20}$$

where $\mathbf{R}_i$ is atoms' positions of an image i, $\tau_i^+ = \mathbf{R}_{i+1} - \mathbf{R}_i$, $\tau_i^- = \mathbf{R}_i - \mathbf{R}_{i-1}$, E_i is the energy of image i ($E_i = E(\mathbf{R}_i)$) and $\Delta E_i^{max} = \max\left(|E_{i+1} - E_i|, |E_{i-1} - E_i|\right)$, $\Delta E_i^{min} = \min\left(|E_{i+1} - E_i|, |E_{i-1} - E_i|\right)$.

The magnitude of the spring force, which is parallel to the tangent vector, is evaluated by Equation 3.3.21 and depends not only on the normalized tangent vector $\hat{\tau}_i$, but also on the spring constant k and the spacing between adjacent images.

$$\mathbf{F}_i^S = k\left(|\mathbf{R}_{i+1} - \mathbf{R}_i| - |\mathbf{R}_i - \mathbf{R}_{i-1}|\right)\hat{\tau}_i. \tag{3.3.21}$$

Finally, the total force acting on an image $\mathbf{F}_i$ is considered to be the sum of the spring

force $\mathbf{F}_i^S$ and the perpendicular component of the true force ($\mathbf{F}_i^{true}$) $\mathbf{F}_i^P$:

$$\mathbf{F}_i^P = \mathbf{F}_i^{true} + \mathbf{F}_i^{true} \cdot \hat{\tau}_i, \tag{3.3.22}$$

and

$$\mathbf{F}_i = \mathbf{F}_i^S + \mathbf{F}_i^P. \tag{3.3.23}$$

After the tangent vector and acting force evaluation for each image, minimization is carried out through simultaneous relaxation of each image by translating all n image points $\mathbf{R}_i$ into a higher $3Nn$ dimensional space and then this final point is relaxed to a minimum which represents the MEP.

Another important improvement to the NEB method by G. Henkelman and H. Jónsson [93] was done in order to improve accuracy of barrier height estimation and was also implemented in the code. They suggested to add additional steps to the NEB method to increase the accuracy. Usually a saddle point lies between two NEB images and the barrier will not be estimated accurately. The solution is very simple: every few relaxation steps, the force of the highest energy image is modified according to Equation 3.3.24, thus removing the spring force and only the real force is reflected parallel to the tangent vector. This improvement not only relaxes images on the MEP, but also converges the highest energy image to the saddle point.

$$\mathbf{F}_{i_{max}} = \mathbf{F}_{i_{max}}^{real} - 2\,\mathbf{F}_{i_{max}}\big|_{\parallel \tau_{i_{max}}}. \tag{3.3.24}$$

3.3.2.2 String Method

Even though the NEB method is a very robust method, it has a disadvantage of having a user defined spring constant k. If k is chosen too small, the elastic band may be a poor description of the MEP, and if it is chosen too big, the method will converge only slowly

and will require a lot of force calculations. The String method [94, 95] avoids this issue by constraining the distance between images, by allowing them to move along interpolated path.

The String method, similarly to the NEB, starts by linearly interpolating images between two system's states on either side of the dividing surface and placing them equally spaced. Then follows a two step iteration procedure until the convergence criterion is met. The first step, guides the pathway towards the MEP, by calculating string tangent vectors on each image and the second one performs relaxation, which is similar to the role of the springs in NEB, to redistribute images along the string.

The other advantage of the String method is that it does not require fixed end images of the pathway. The only requirement is to have them splitting the potential energy surface by having one end in one local minimum region and the other in another.

In the developed otf-KMC code, the simplified version of the String method is implemented [96]. This version kept the reinterpolation of the images along the string, but removed all other complex calculations. At each iteration images are allowed to relax by a short distance along the direction of the real force. In this way, the biggest part of the displacement is due to the images relaxing towards the minima, but there is also a small force component that brings them towards the MEP.

3.4 Atom Lists and Volumes

In order to save computational time during the force evaluation procedure, different radii were used to create atom lists on which forces must be evaluated without losing accuracy. It is possible to use such lists when interatomic potentials, describing the system of interest, have a rather small cut-off. In this work, atom lists were used when the α-Fe system was evolved using the KMC technique.

It was calculated, that in order to have accurate evaluations of the energy and forces

acting on an atom, atoms within 8.5Å must be included, as it shown in Figure 3.6. This radius is called the "inclusion radius" throughout this work.

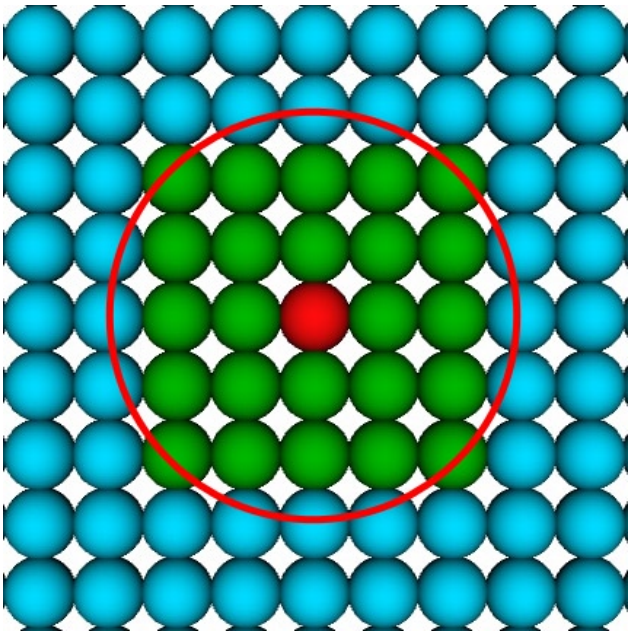

Figure 3.6: 2D representation of the inclusion radius in α-Fe system: to have a good estimate of the energy and force acting on the Fe atom (red), atoms within a 8.5Å radius must be included (green). Even though the energetics of the red atom will be evaluated accurately, is not necessarily the case for the green atoms, and if needed, atoms within the same radius must be included around them.

Also in order to speed up simulations, different types of atom lists (volumes) are created to ensure minimum usage of computational power. The sizes of the volumes are controlled by the user of the KMC code and are created around residual defects in the system. The volumes are in ascending order of size as graphically presented in Figure 3.7.

- **Initial search radius** - this radius serves two purposes. The first one is to group residual defects into one cluster if defects are not separated by more than this value (typically the distance would be to the second nearest neighbour, 2.9Å). This region is termed as a "**defect volume**" (DV) through this work and is one of the main characteristics in this otf-KMC technique.

  The second purpose is to create an initial list of atoms to be randomly displaced and used by one of the single-ended saddle search methods.

- **Graph radius** - is used to classify defect volumes according to their topology. A list of atoms surrounding a particular defect (or defect cluster) is created according the graph radius. Then by using "Nauty" (see section 3.7.1), connectivity graphs are generated and unique hash keys are assigned to them. The best value found for this radius is 4.1Å (to the third nearest neighbour).

  Also the graph radius is used to search for so called "combined volumes". If two defects volumes are separated by a graph radius or less, a combined volume will be constructed, by joining them together. The main purpose for creating combined volumes is to find transitions that include atom movements in both volumes, where they could be missed while running searches on the volumes individually. Transitions found within combined volumes are not saved for further reuse.

- **Search move radius** - controls how many atoms will be included while searching for saddle points using one of the the single-ended methods. The atoms around initial defects within this radius are included, by forming a search move volume. A typical value is 5.0Å.

- **Saddle converge radius** - sets an additional radius around search move volume, to include even more atoms for a better convergence to a saddle point with the minimum mode following algorithm.

- **Inclusion radius** - this radius defines an additional layer of atoms, required to estimate correct energetics on the atoms.

3.5 Prefactor

When a saddle state is determined by one of the transition search methods, the next issue is to determine the prefactor for this particular transition, which describes the jump frequency between local minima through the saddle. In this work two options were considered - the

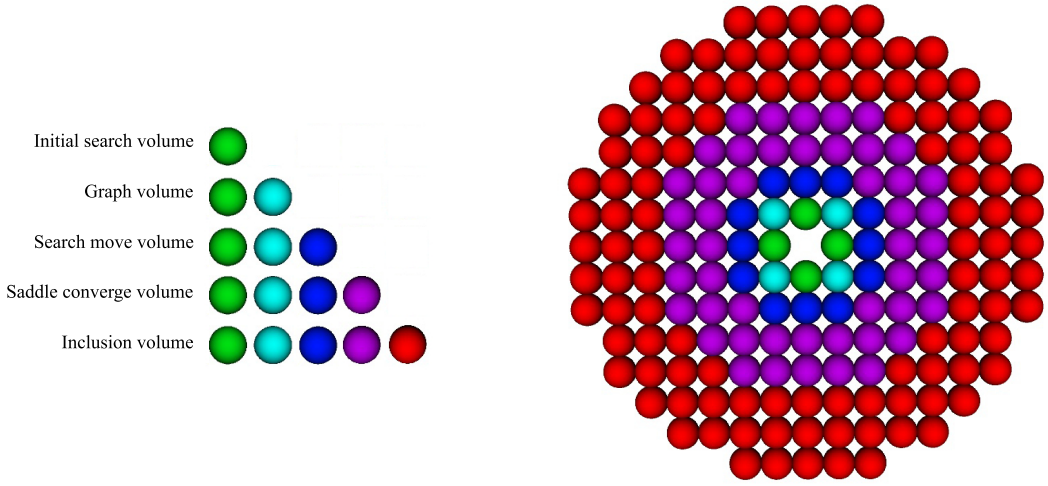

Figure 3.7: Representation of different atomic volumes used throughout the KMC algorithm around a vacancy defect: to create a defect volume (initial search volume), to classify a defect volume (graph volume), to look for saddles (search move volume), to converge to a saddle (saddle converge volume) and to estimate energetics of the saddle converge volume (inclusion volume).

fixed prefactor with a value of $10^{13}s^{-1}$ and the calculated one, using the Vineyard equation [97]:

$$\tau = \frac{\prod_{j=1}^{N} \upsilon_j}{\prod_{j=1}^{N-1} \upsilon_j^*}, \tag{3.5.1}$$

where υ and υ^* are the normal frequencies for vibrations at the initial (local minimum) and saddle states respectively.

The normal frequencies used in Equation 3.5.1, at the initial and saddle states, are derived from the eigenvalues using Equation 3.5.2. Eigenvalues are calculated by numerically constructing the Hessian H (Equation 3.5.3) and then applying the DSYEV routine from the Linear Algebra Package (LAPACK).

$$\upsilon = \frac{\sqrt{\lambda}}{2\pi}, \tag{3.5.2}$$

here, λ is the eigenvalue of the Hessian matrix from which the normal frequency υ is derived. This Hessian is determined numerically whose i-j th element is given by:

$$H_{i,j} = \frac{1}{2\sqrt{m_i m_j}} \left(\frac{F_i^{j+} - F_i^{j-}}{2\delta} + \frac{F_j^{i+} - F_j^{i-}}{2\delta} \right), \tag{3.5.3}$$

where F_i^{j+} is the force acting on i-th component due to the positive ('-' - negative) displacement in the j-th components position, δ is the displacement (0.001Å) and m_i is atomic mass of the i-th atom. To gain accuracy, the element $H_{i,j}$ is calculated as an average of the symmetric elements.

The study of the influence of the calculated prefactor in long time scale simulations of defect motion in α-Fe has been carried out and is given in section 6.1.

3.6 Transition Search Algorithm

Through careful testing and consideration of the previously described methods (see section 3.3), in this work an eight step procedure was implemented to find transitions on a defect volume, that showed both, good accuracy and speed.

- **Step 1: Initial displacement** - the procedure starts by displacing atoms, that are within the initial search radius in the initial search volume, from a randomly picked atom in the volume.

- **Step 2: Saddle search** - after the initial displacement, the Dimer method (see section 3.3.1) is being used to approach a saddle state, which is connected with the initial minimum state via the minimum energy path. The Dimer method was chosen because it is not only one of the most robust methods, but also it estimates the curvature, which is directly linked with the lowest mode, without additional force evaluations.

- **Step 3: Convergence to a saddle** - when the Dimer gets in the vicinity of a saddle, the procedure switches to use the minimum mode following algorithm. The switch is carried out when the Dimer's curvature becomes negative.

- **Step 4: Estimate eigenvalues** - if prefactors are calculated on the fly, the eigenvalues at the saddle state are calculated, as is mentioned in section 3.5 and together with the initial eigenvalues are used to calculate the prefactor for this transition later on.

- **Step 5: Check of the saddle's rank** - if prefactors are calculated on the fly, it is important to ensure that the rank of the saddle point is equal to 1, that means it has only one negative eigenvalue. If the saddle has rank 2 (there are two negative eigenvalues), the Vineyard's equation is invalid and the prefactor cannot be calculated. To ensure, that the saddle has rank of 1, the original minimum mode following algorithm suggested by Pedersen [88] is used to climb down from a rank 2 saddle state, to a rank 1.

- **Step 6: Uniqueness check of the saddle** - once the saddle state is approximated, the procedure must determine if it is a valid result by comparing the separation between previously found saddle states for the same defect volume. If the separation is small, less then (0.5Å), the result is discarded as a duplicate and the procedure is stopped.

- **Step 7: Find the final minimum** - to find the final minimum joined by the MEP through the saddle state, the system at the saddle state is given a little push in the direction of the vector from the initial minimum state to the saddle state. Then this minor displacement is followed by a minimization procedure that uses two methods: the first one is the classical steepest descent method with lose tolerance of 10^{-1}eV/Å and the second one is the L-BFGS-B method with a tight tolerance of (10^{-3}eV/Å). The first method is used to approach the final minimum quickly with as little computational costs as possible and then the minimisation is finished with the L-BFGS-B method, which works best when the initial system state is in the vicinity of a minimum.

- **Step 8: Calculate the rate value** - if the previous steps were successful, the transition search algorithm finishes by calculating the rate value for the found transition using the Arrhenius equation (Equation 3.2.1). The prefactor is either calculated on

the fly or using the default value of $10^{13}s^{-1}$. $10^{13}s^{-1}$ was found to be a typical value for many transitions.

If in any of the steps the algorithms fail to complete their tasks, the transition search is dismissed as unsuccessful. A detailed activity diagram representing the transition search algorithm is given in Figure 3.8 and a schematic illustration on a potential energy surface in Figure 3.9.

3.7 Reuse of Transitions

The otf-KMC technique is based on the idea of searching for possible transitions every step (iteration) on the fly and then randomly picking one transition from the list and advancing the system to a new state, according to their rates.

Usually movements of the atoms that represent the system's transition from one state to another are contained in a local area, surrounding a certain defect or a combination of defects, and do not have or have a negligible effect on the atom positions outside that local area.

The idea of the reuse of transitions is to "recycle" previously found transitions within those areas that were not effected by the chosen transition. This idea was suggested by El-Mellouhi *et al.* in [98] and an interpretation of it was developed during the course of this work to improve the efficiency of the KMC software which has been developed in a way described in the following subsections.

3.7.1 Nauty

"Nauty" (No AUTomorphisms, Yes?) was written by Brendan D. McKay [99, 100] in the early 90's and has been developed constantly since then. It can be thought as a set of very fast procedures (written in C programming language) for computing automorphism groups of graphs and digraphs with possibility to produce canonical labelling.

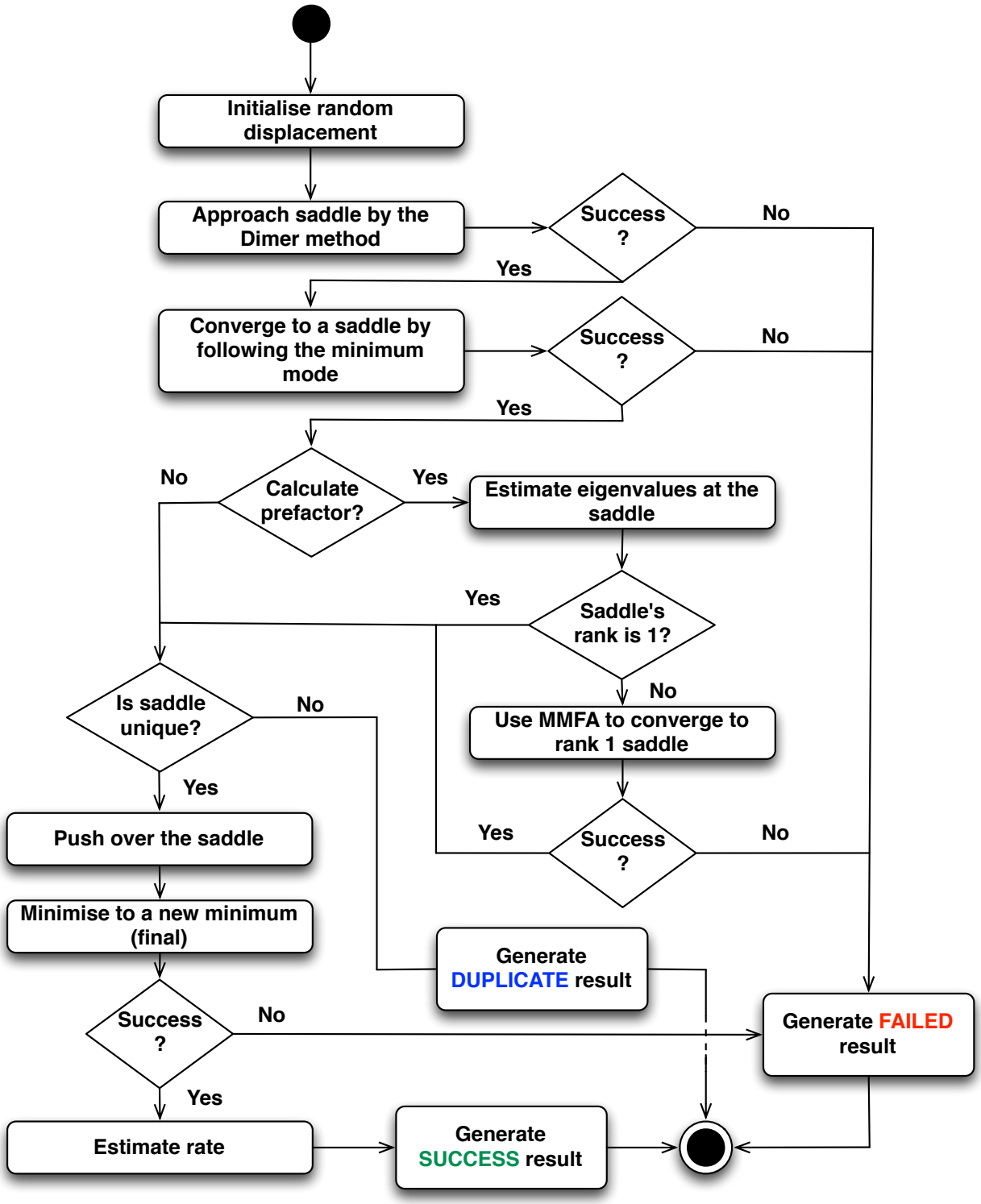

Figure 3.8: Activity diagram representing the transition search algorithm to find transitions on a defect volume.

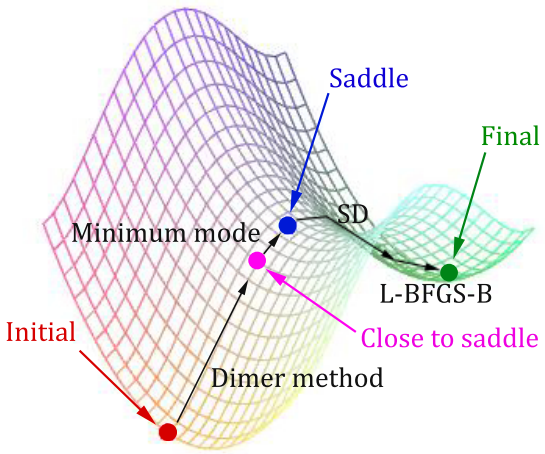

Figure 3.9: Schematic illustration of the transition search algorithm working on a potential energy surface.

"Nauty", in this work, is mainly used for two purposes: to check if two graphs (two defect volumes) are identical and if so, to describe the isomorphism between them.

Dealing with the first task is quite easy, since "Nauty" can generate a hex number (a hash key) depending on the graph's isomorphism group. It is assumed that two graphs can share the same hash key only if they share the same isomorphic group. So basically the comparison of two DVs is done by comparing their hash keys, if they are the same, DVs are regarded as isomorphic.

When two graphs are identified as isomorphic, the isomorphism from one graph to another can be obtained from "Nauty" expressed in the form of a sequence of pairs $v_i - w_i$, where v_i is a vertex of the first graph and w_i is a vertex of the second graph.

In other words, with the help of "Nauty" a check if two DVs are similar can be performed and if so, the corresponding atoms between two DVs can be determined and the transformation matrix which transforms one defect volume's atom positions to another's can be estimated.

To illustrate how "Nauty" assigns hash keys to defect volumes a simple example is given with one vacancy defect (Figure 3.10a). First of all only atoms within the graph radius are

selected for the further analysis (Figure 3.10b) and the connectivity graph is created (Figure 3.10c) with respect to all the atoms in the system. Atoms are assumed to be connected if the separation between them is less than the graph radius. Then, "Nauty" produces a hash key (Figure 3.10d) that is unique for all the configurations which share the same connectivity graph.

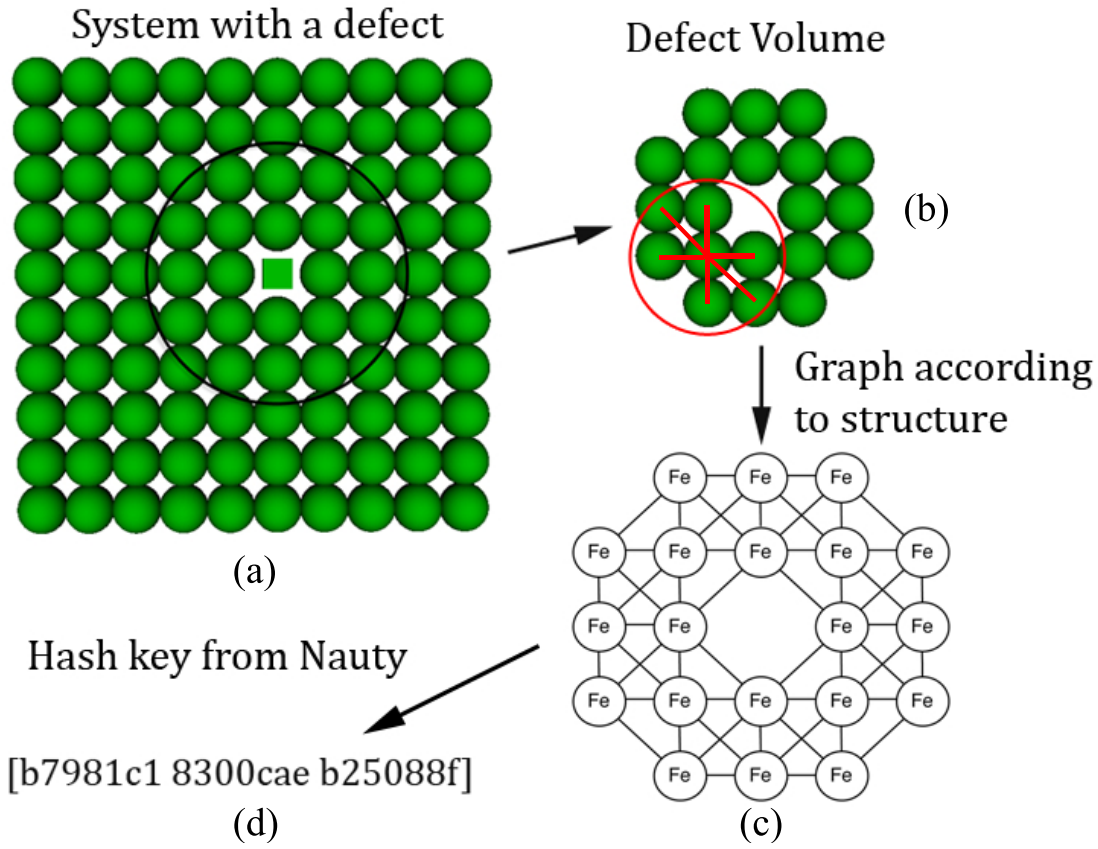

Figure 3.10: Schematic representation of how "Nauty" assigns a hash key to a defect volume, given through a 2D vacancy example: (a) - finding atoms in the graph volume, (b) - finding the connectivity between the atoms, (c) - creating a graph according to the connectivity and (d) - generating a hash key depending on the graph with "Nauty".

3.7.2 Transformation Matrix

When two DVs are identified as isomorphic and the corresponding atoms between two atoms sets are identified, a transformation matrix **A** (Equation 3.7.1) can be estimated.

$$\mathbf{AX} = \mathbf{X}', \tag{3.7.1}$$

where $\mathbf{A}$ is the transformation matrix, $\mathbf{X}$ - a vector representing a point (an atom) in the first defect volume and $\mathbf{X}'$ is its representation found by "Nauty" in the second one. Equation 3.7.1 can be expressed as follows:

$$\begin{pmatrix} a_{11} & a_{12} & a_{13} \\ a_{21} & a_{22} & a_{23} \\ a_{31} & a_{32} & a_{33} \end{pmatrix} \begin{pmatrix} x \\ y \\ z \end{pmatrix} = \begin{pmatrix} x' \\ y' \\ z' \end{pmatrix}. \tag{3.7.2}$$

The transformation matrix holds the information how one defect volume's atoms should be rotated/scaled/reflected in order to get the second volume's atoms positions. In other words, the transformation matrix transforms one defect volume's atoms positions into another's.

In order to find the transformation matrix $\mathbf{A}$, an overdetermined linear equation system (OLES) is formed by using all the atoms from both of volumes and their relations. A completely determined linear equation system is not suitable for this kind of problem, since it is very unlikely, that the solution found, by using only a set of volume atoms, will be fit to represent the transformation for the rest of the atoms in the defect volumes. For this particular reason, the OLES is followed by the method of least squares to approximate a "best solution".

Three OLES (Equation 3.7.3) derived from Equation 3.7.2 are solved and the result (the coordinates a_{ij} of the transformation matrix $\mathbf{A}$) is obtained.

$$\begin{pmatrix} x_{11} & x_{12} & x_{13} \\ x_{21} & x_{22} & x_{23} \\ \dots & \dots & \dots \\ x_{n1} & x_{n2} & x_{n3} \end{pmatrix} \begin{pmatrix} a_{i1} \\ a_{i2} \\ a_{i3} \end{pmatrix} = \begin{pmatrix} x'_{1i} \\ x'_{2i} \\ \dots \\ x'_{ni} \end{pmatrix}, i = \overline{1,3} \tag{3.7.3}$$

where n is the number of atoms in the volumes; i - the coordinate number by which OLES is created; (x_{j1}, x_{j2}, x_{j3}) represents j-th atom in the first volume; x'_{jk} is the j-th atom's k-th coordinate from in the second volume; a_{il} $(l = \overline{1,3})$ is the transformation matrix's coordinates that are being estimated.

It is important to note, that the OLES are created so the atom x_j from the first volume corresponds to the atom x'_j from the second volume. During the calculation atoms' positions (x_{j1}, x_{j2}, x_{j3}) and $\left(x'_{j1}, x'_{j2}, x'_{j3}\right)$ are centred to the origin according to the mass centres of each DV.

Also before an atom transformation from one DV to another, both defect volumes have to be centred at the Euclidean origin and returned at the defect volume's original centre of mass after the transformation is applied. This is done, because the 3x3 transformation matrix does not hold the translation information.

3.7.3 Reuse Algorithm

As it was stated before in this work, transitions are described by three sets of atoms - initial, saddle and final states of a transition. When an initial state of a DV shares an isomorphic group with one of the previously investigated DV's initial state, transitions from the previous investigation can be reutilised instead of completing a new set of transition searches.

It is done by following an algorithm that was developed during the course of this work:

- **Step 1: Find the transformation matrix** - transforming previously found saddle and final states is done by using the transformation matrix (Equation 3.7.1), where $\mathbf{X}$ is an atom from the previously investigated DV and $\mathbf{X}'$ is an atom in the current DV. When the transformation matrix is found, it can be applied on final and saddle states to transform them from one volume to another.

- **Step 2: Reuse of the final state** (optional) - it is optional for the user of the software to choose whether the final states should be reused. Choosing not to reuse them, saves

computational time, but then some information about the reused transitions is not calculated. If the final states are being reused using Equation 3.7.1, atom positions after the procedure must be adjusted according to the current surrounding atoms, since it is very likely that the original DV, from which the transition was reused, had a slightly different configuration compared with the DV for which the reuse was done. The adjustment is carried out by applying the L-BFGS-B equilibration method.

- **Step 3: Reuse of the saddle state** - the reuse of a saddle state is done by applying Equation 3.7.1. For the same reasons stated in Step 2, adjustments to the atoms according to the surrounding atoms must be done after the transformation of the their positions. In this case is done by converging to the saddle point with the MMFA (see sec. 3.3.1.5) to climb up the saddle point.

- **Step 5: Estimate eigenvalues** - as in the transition search algorithm (see section 3.6), when prefactors are calculated on the fly, the eigenvalues at the saddle state are estimated and together with the initial eigenvalues are used to calculate the prefactor for the reused transition later on.

- **Step 6: Check the saddle's rank** - again, when prefactors are calculated on the fly, the rank of the saddle state must be equal to 1. If the rank is equal to 2, the MMFA suggested by Pedersen [88] is employed to climb down from a rank 2 saddle state, to a rank 1 saddle state.

- **Step 7: Uniqueness check of the saddle** - the same procedure, as in the transition search algorithm, is used to check whether the reused saddle is unique, if not, the result is discarded as a duplicate.

- **Step 8: Calculate the rate value** - if the previous steps were successful, the reuse algorithm finishes by calculating the rate value for the reused transition using the Arrhenius equation (Equation 3.2.1) with the default or the calculated prefactor value.

A failure at any of the steps forces the transition to be discarded as a failure. A detailed activity diagram explaining the developed transition reuse algorithm is given in Figure 3.11 and a schematic illustration on a potential energy surface in Figure 3.12.

3.7.4 Example

To illustrate this technique in action, a simple example is given below, where a system with two vacancies is considered (Figure 3.13). Since these two defects are well separated, the defect volumes around them have almost the same symmetry and therefore they share the same hash key ($b7981c1_8300cae_b25088f$). The isomorphism can be defined between them by solving the over-determined linear equation system and it was found that the transformation matrix is approximately equal to the identity matrix, due to the high symmetry of the defects.

in this example a transition has been found for the vacancy in the lower left corner, where it jumps to its first nearest neighbour position. The transition is defined by the initial (Figure 3.13a), saddle (Figure 3.13b) and final (Figure 3.13c) states. Instead of running computationally expensive saddle point searches for the vacancy in the top right corner, the transition reuse procedure can be applied. After applying the procedure, a new transition for the latter vacancy can be found as shown in Figures 3.13e and 3.13f.

It is very clear that two single vacancies in the relaxed bcc structure will have isomorphism between the defect volumes which are almost identical.

3.8 on-the-fly Kinetic Monte Carlo Algorithm

The fundamental steps of the otf-KMC method, suggested by Henkelman and Jónsson [46], can be summarised into an acitivity diagram as follows (Figure 3.14):

The first step is the identification of defects present in the system. It is crucial to locate defects in order to minimise the search space by limiting the volume where the searches are initiated, thus making transition search algorithms and the KMC technique more efficient.

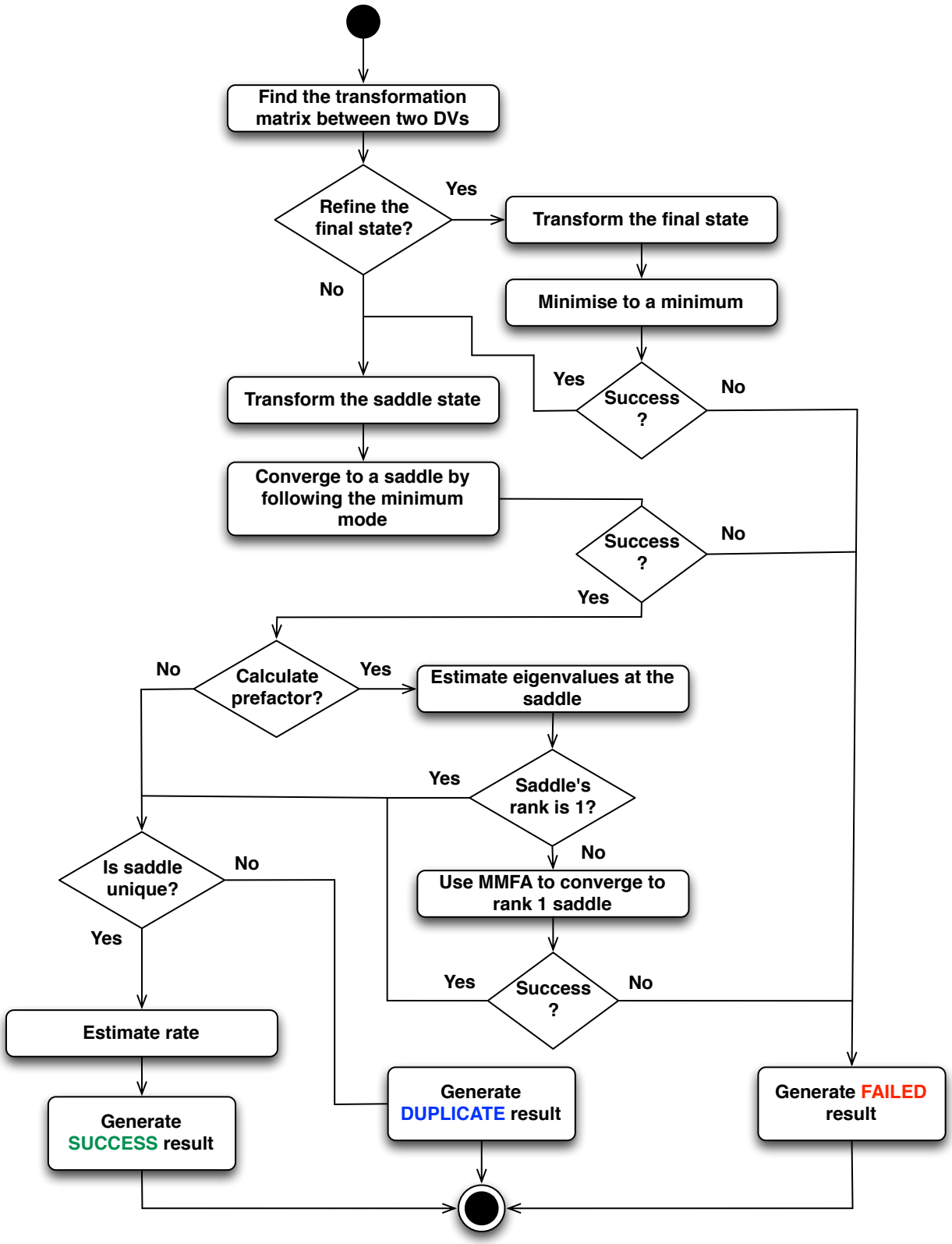

Figure 3.11: Activity diagram representing the reuse algorithm to reuse saddle and optionally final states.

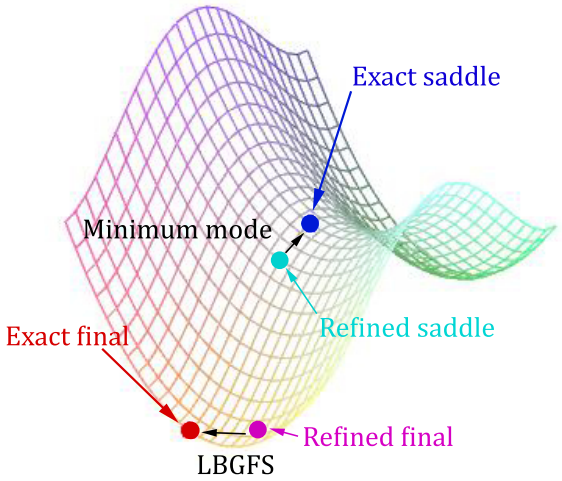

Figure 3.12: Schematic illustration of the reuse algorithm working on a potential energy surface.

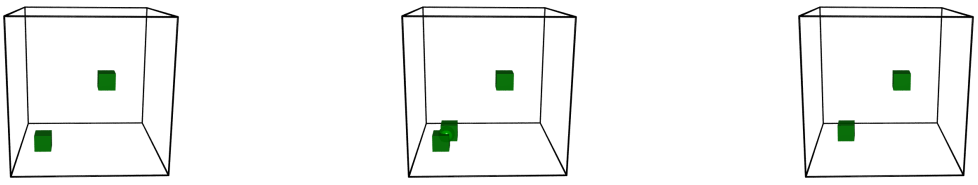

(a) search: initial state (b) search: saddle state (c) search: final state

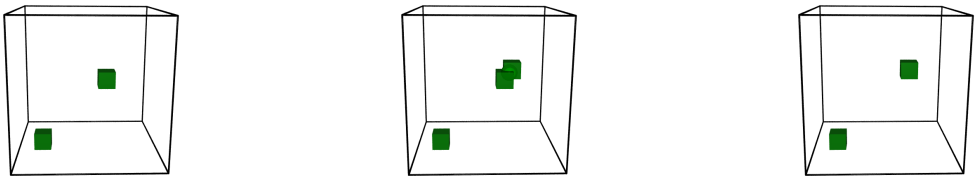

(d) reuse: initial state (e) reuse: saddle state (f) reuse: final state

Figure 3.13: An example of the reuse algorithm on two defects volumes containing a vacancy.

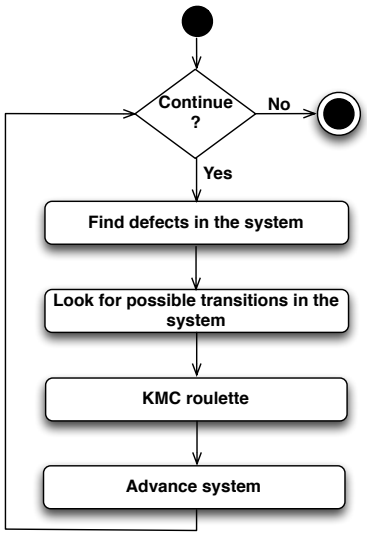

Figure 3.14: Activity diagram of the fundamental otf-KMC steps.

The next step is where a saddle search method is employed to find possible transitions from the current state and estimate rate values for each of them. Then, the next step is the KMC roulette technique, which picks a random transition as a new state and calculates the elapsed simulation time between current state and the new one. And lastly, the system is advanced to a new state.

The otf-KMC software used in this research is a further improvement to the original suggestion by Henkelman and Jónsson [46]. The software was written from scratch by adopting the initial work done L. Vernon [47]. The activity diagram for the developed software is given in Figure 3.15.

The otf-KMC is usually continued for a specific number of steps or until the simulation time is achieved. During each step the technique starts by identifying defects (see sec. 2.7) by comparing the current system with a reference lattice and checking their atom positions. Then each defect is localised and characterised by a defect volume and a graph key associated with it is produced.

If a defect volume has been explored previously, by running saddle searches and the outcome was saved, instead of rerunning the searches again, the successful migrations are reused (see sec. 3.7) in order to save computational time.

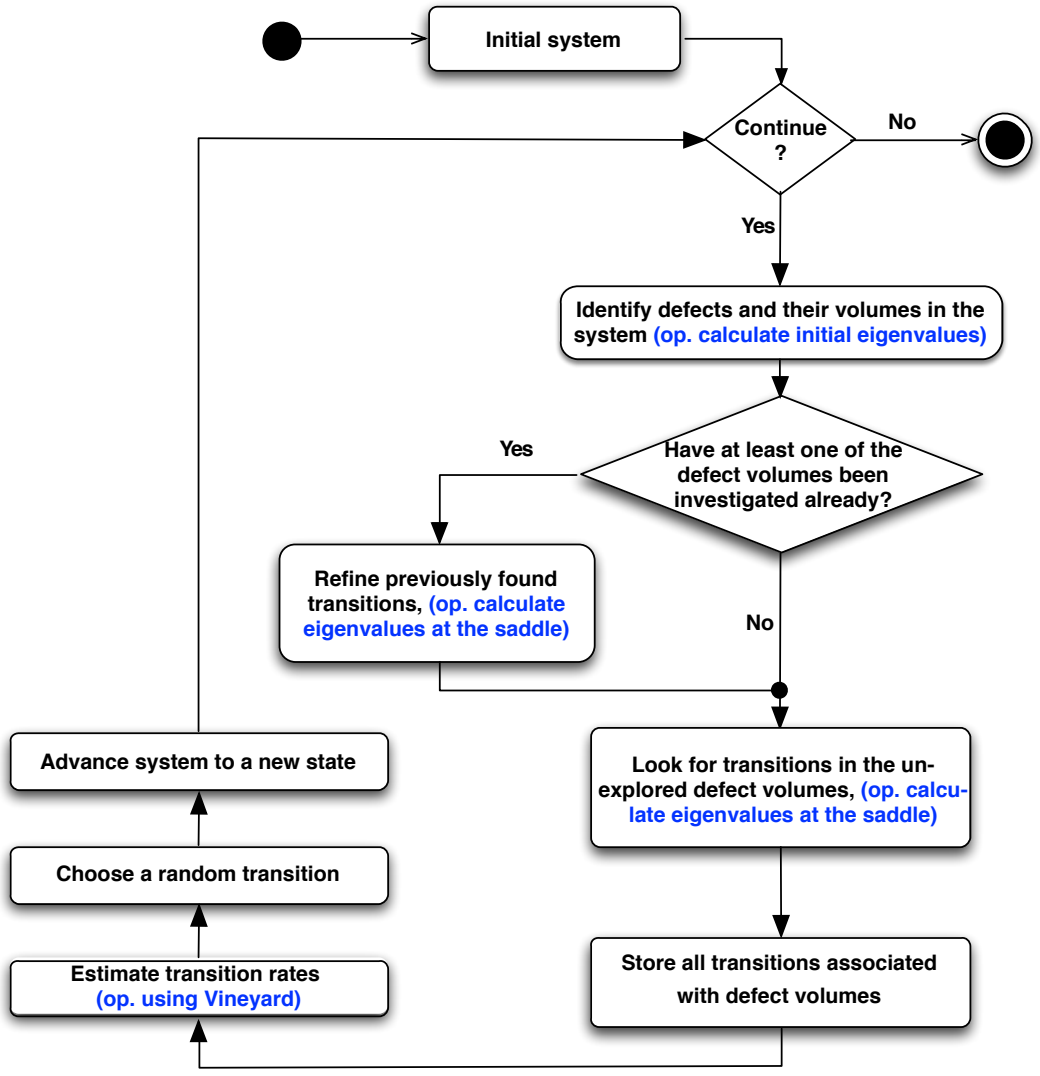

Figure 3.15: Activity diagram of the developed otf-KMC technique. The functionality written in blue is optional.

If the defect volume has not been previously explored, a set of searches (see sec. 3.6) of migration mechanisms is launched in order to find the saddle and final states describing them. The successful searches are then saved for further possible reuse and the transition rates for the reused and/or found transitions are estimated. If a user chose to calculate prefactors on the fly, eigenvalues at the saddle are estimated and used for the calculations of the rate values.

After that the KMC roulette technique is used to pick a migration transition to a new final state to which the system is evolved and the simulation clock advanced accordingly. Then the routine is repeated for the new system state during the next otf-KMC step.

Figure 3.16 shows the the client-server model in order to perform the otf-KMC tasks, such as transition searches and reuse, in parallel. The main idea behind the parallelisation is to split the KMC algorithm into small tasks that can be done concurrently on clients thus ensuring minimum work done on the server. The work is split in this way: the server is in charge of all the procedures that are done in series and cannot be split, such as identifying defects, calculating rate values and choosing transitions. It also allocates jobs on clients to do the initial eigenvalue calculations if prefactors are calculated on the fly, to refine previously found transitions and to run transition searches. It establishes communication with clients to send the data needed to perform their tasks and to gather results for further actions. The average number of cores used to run otf-KMC simulations was 60.

3.9 Summary

The otf-KMC technique detailed in this chapter was developed during the course of this work in collaboration with C. Scott and M. Yu. The performance of the technique and the individual methods was measured at various stages of the development to ensure robustness, reliability and applicability of the software. The key features of the technique are:

- easy adaptation of new methods, as the Dimer, RAT, NEB etc,

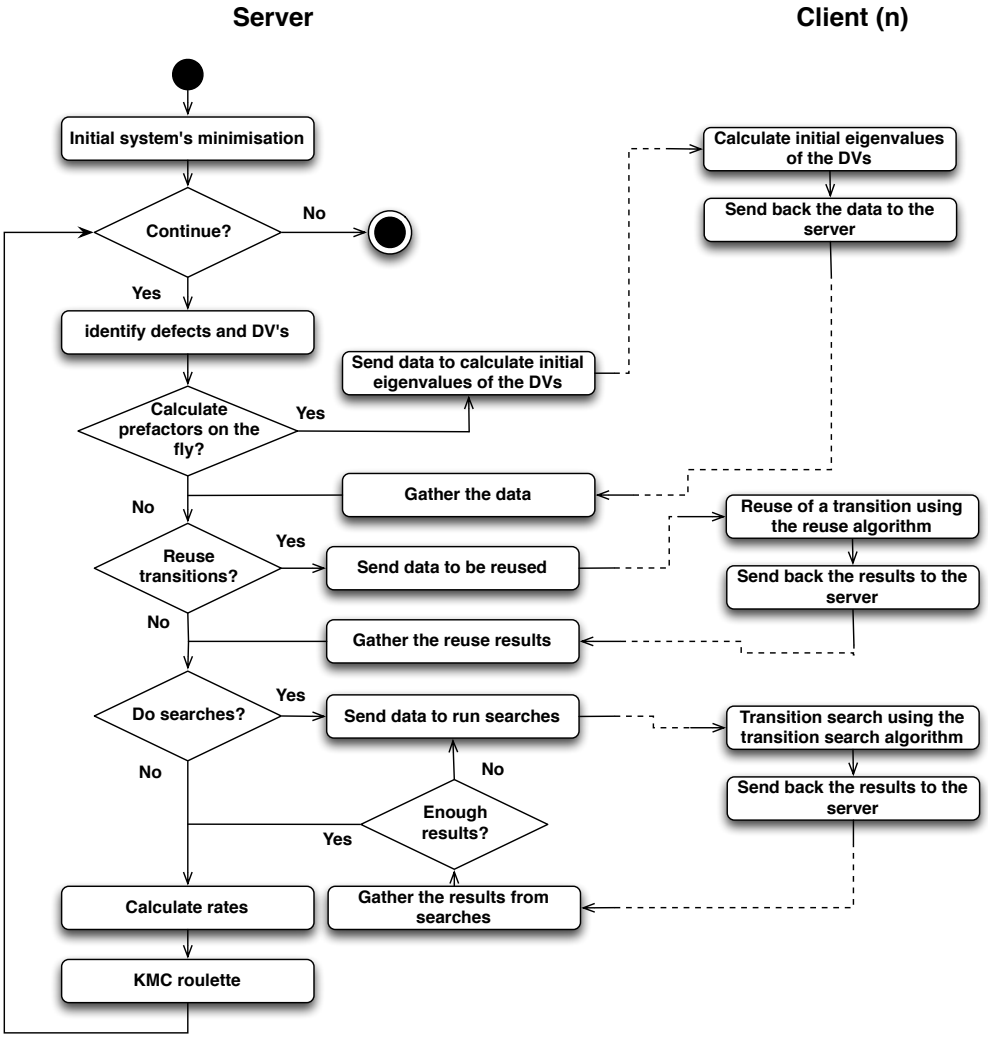

Figure 3.16: The client-server model for the parallelisation of the otf-KMC technique.

- ability to group several methods, e.g. to maximise performance during the minimisation of a final state, the SD and L-BFGS-B methods are combined,
- performance can be increased by using the inclusion radius,
- option to reuse previously found transitions, thus saving computational time,
- good performance and scalability on high performance computing clusters.

The technique was applied to study the influence of the prefactor in the Arrhenius equation (Equation 3.2.1), to simulate long time scale evolution of defects in α-Fe and compared with other techniques by evolving α-Fe containing 50 vacancies (see chapter 6). It was also

used to study Ni-Cr systems by Zainab Al Tooq [101] and helium bubble formations by Xiao Gai [102].

Chapter 4

Simulating Radiation Effects in ODS Steel

This chapter presents results regarding the modelling of radiation effects in α-Fe and α-Fe with embedded nanoparticles. In the first section, an algorithm, to create a simplified model of an ODS alloy, is described. This is followed by radiation damage and He bubble formation studies. The findings provide an insight into the atomistic processes and mechanisms that help to provide a better understanding of the improved performance of ODS alloys in intense radiation environments.

The radiation damage results were published in [103] and the findings on He bubble formation are to be published in collaboration with Xiao Gai [102].

4.1 Modelling the Structure of the ODS System

The systems used in the simulations (see Table 4.1) consist of a body-centred cubic structured iron lattice with a stoichiometric yttria nanoparticle placed at the approximate centre of the system. An approximate yttria concentration of 0.3 at% was used in accordance with some of the experimental data from IGCAR [104]. To described the model, interatomic potentials were used with the details given in section 2.4: the Fe-Fe interactions are described by the

Ackland 1997 potential, Fe-O interactions - by the Morse potential, Fe-Y - the ZBL and for the Y-O the Buckingham type potential combined with a fixed charge Coulomb interaction estimated using the Fennel approximation.

The Y_2O_3 nanoparticle is initially created outside the bcc iron simulation box as a sphere of a certain radius in the bixbyite crystal structure and then placed within the iron matrix by removing corresponding iron atoms. It was found that the best way to embed a nanoparticle was to use Delaunay's triangulation [105] method, implemented from the Python Visualisation ToolKit (VTK) library. This was used to remove all the iron atoms, whose position are overlapped by the triangulated surface within a specified radius around each yttria atom. A schematic illustration of the procedure is given in Figure 4.1, with the steps described in detail. Then the lattice is relaxed to ensure a stable local configuration using the damped MD technique.

In order to estimate the gap size that should be left between the yttria particle and the iron atoms, a study of the Y_2O_3 cluster formation energy E_f (calculated using Equation 4.1.1) and its dependency on the void size was undertaken.

$$E_f = E_c + (m - s)E_{vac} - N_{Fe}E_{Fe}^{bulk} - N_Y E_Y^{bulk} - N_O E_O^{bulk}, \tag{4.1.1}$$

where E_c represents the lattice energy with the yttria nanoparticle, E_{vac} is the vacancy formation energy in a pure bcc iron lattice, $N_X E_X^{bulk}$ (where X = Fe, Y or O) is the number of atoms multiplied by the atom's bulk energy, s is the number of atoms in a cluster and m is the number of iron vacancies. It should be noted that with this methodology, the embedded nanoparticles are non-commensurate with the bcc Fe lattice but maintain their basic bixbyite cubic structure albeit with some distortion at the Fe interface. The structures were relaxed and the gaps with the minimum formation energy were chosen.

The void size is determined from the radius by which iron atoms are removed around each atom from the nanoparticle as shown in Figure 4.1. The study was carried out using 11 different sized yttria nanoparticles with the gap size (distance between the nearest particles

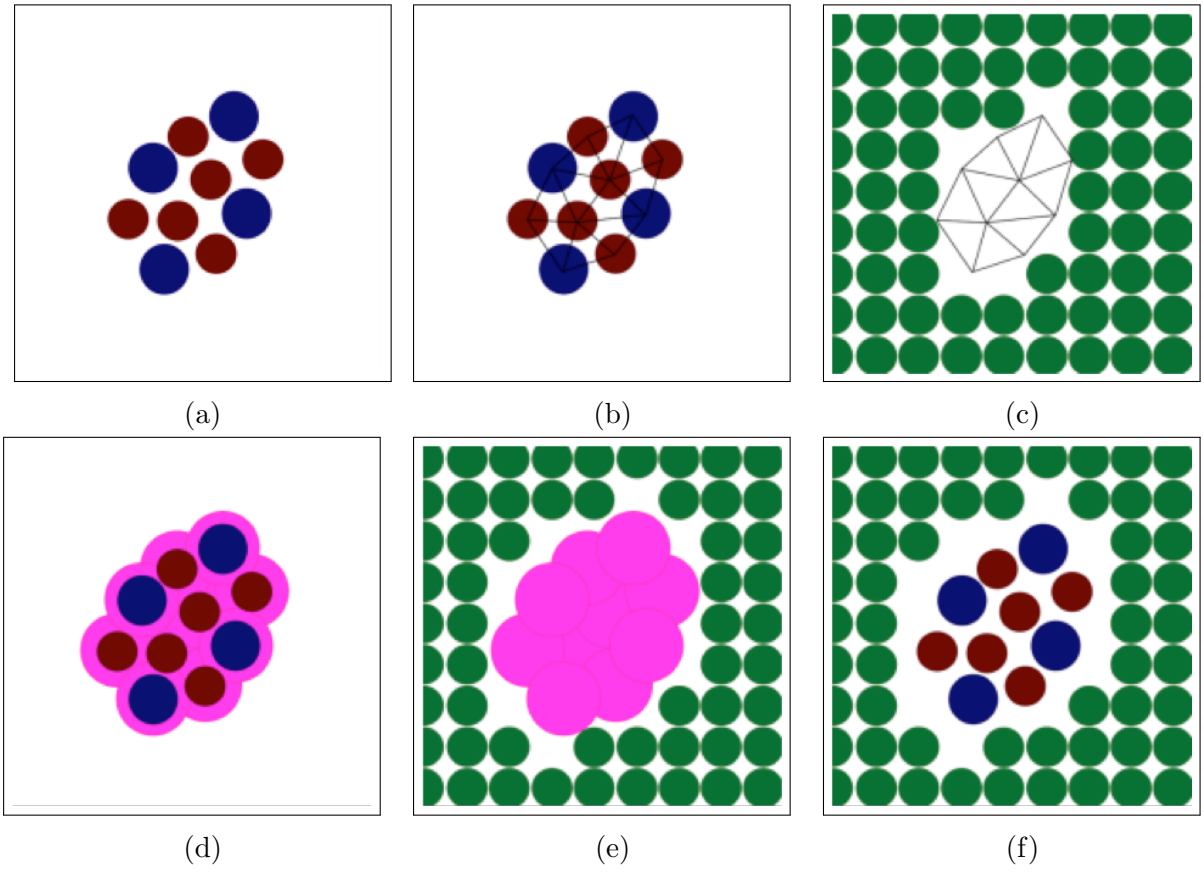

Figure 4.1: A schematic illustration of the yttria positioning procedure in the bcc Fe lattice. The steps are: (a) generate the yttria particle, (b) triangulate the yttria particle's surface using the Delaunay's triangulation, (c) overlap the triangulated surface in the Fe system and remove the internal Fe atoms, (d) create surrounding surfaces around each yttria particle, (e) identify the overlapping Fe atoms, (f) remove the overlapping Fe atoms.

in the cluster and the matrix before relaxation) varied from 0.6 Å to 2.4 Å. The value of 1.6 Å for the gap size was found to be optimal (see Figure 4.2) for all the studied yttria nanoparticles.

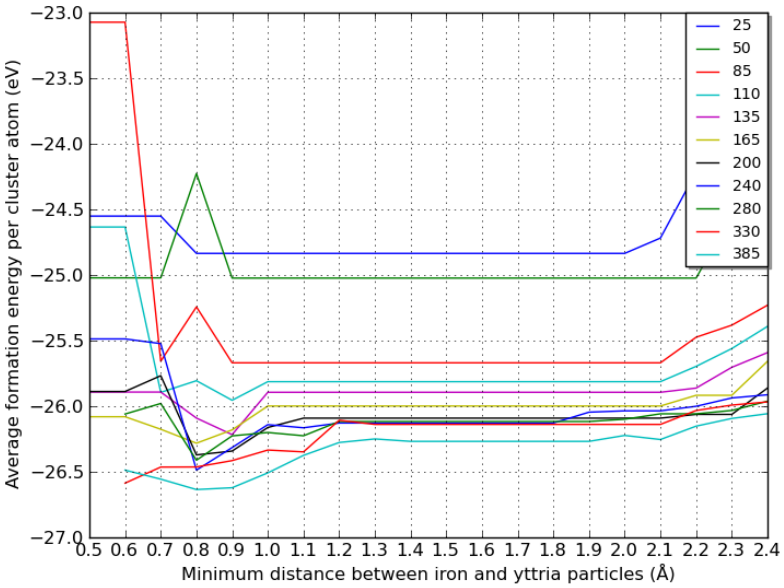

Figure 4.2: Study of yttria nanoparticle's average formation energy per atom dependency on the yttria nanoparticle's size and the minimum distance between yttria and Fe atoms.

The size of the systems A and B in Table 4.1 were chosen to keep the agreement with the observed concentration of yttria and to have nanoparticles that are most likely to be formed according to the same experimental data. System C was chosen to have a greater concentration of yttria in order to save computational time by using a smaller system.

	Number of atoms	Yttria concentration	Atoms in the nanoparticle	System size Å × Å × Å
A	127,867	0.3 at%	385	114.3 × 114.3 × 114.3
B	53945	0.3 at%	165	85.7 × 85.7 × 85.7
C	53867	0.71 at%	385	85.7 × 85.7 × 85.7

Table 4.1: System sizes for the different models used in the simulations. All systems have a Y_2O_3 nanoparticle placed near the centre of the lattice.

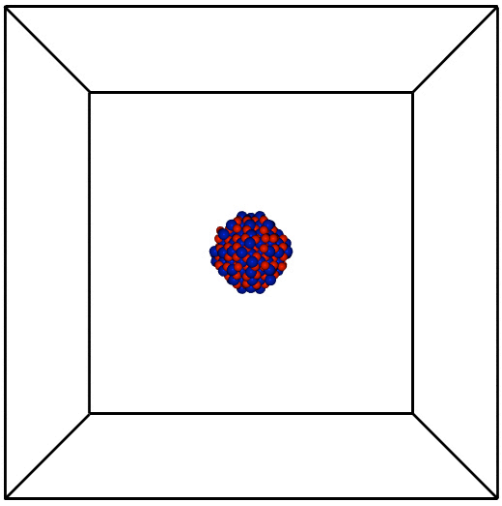

Figure 4.3: ODS system's example with the nanoparticle embedded in the Fe matrix where only the atoms corresponding to the yttria nanoparticle are shown. Blue and red spheres represent yttrium and oxygen accordingly. The size of the simulation box is that given by system A in Table 4.1 so the box sides are 114 Å in length.

4.2 Simulating Radiation Damage

4.2.1 Simulating Radiation Damage with MD

To simulate the radiation damage cascade using MD, a certain amount of energy was imparted to an Fe atom in the system, the primary knock-on atom (PKA). Energies between 0.5 and 5 keV were chosen, but with most statistics obtained for 1 keV cascades. The results strongly depend on the initial direction of the PKA and sufficient sampling must be done to obtain good statistics. For a perfect bcc structured lattice the sampled region is constructed by picking a centering atom in a unit cell and dividing the cell with the symmetry planes. The region is then sampled over 66 different directions within the lattice from [1 0 0] to [1 1 0] and [1 1 1] with a step size of 0.1 in y and z coordinates as it is shown in Figure 4.4.

In the embedded nanoparticle case, the situation is even more complicated since the crystal symmetry is broken. Despite the break in symmetry, the same sampling process was used with the directions chosen as shown in Figure 4.4. Eight sets of simulations were performed for System A from Table 4.1, in which the distance of the PKA from the nanoparticle's centre was varied between 16 Å and 57 Å in order to simulate various PKA distances and

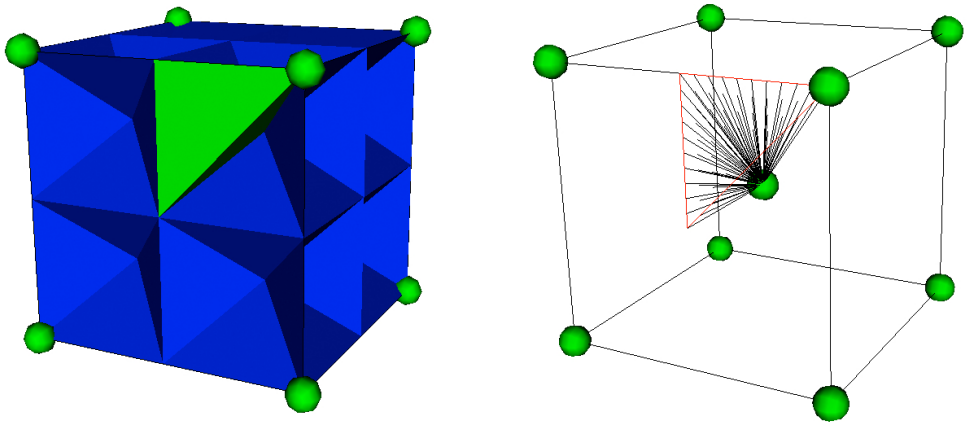

(a) (b)

Figure 4.4: (a) - the bcc structure's irreducible region, (b) - the irreducible region sampled by 66 directions starting from from [1 0 0] to [1 1 0] and [1 1 1], with a step size of 0.1 for y, z components.

positions around the yttria nanoparticle (Figure 4.5). These PKA atoms were chosen to give a representative sample of different cases. For larger distances at 1 keV, the PKA's energy is dispersed away from the embedded particle. Most of the simulations were carried out with a 1 keV PKA energy and directed towards the nanoparticle.

All simulations have periodic boundary conditions applied. These results only weakly depend on whether the temperature of the system is initially 0 K or room temperature. Thus for the purposes of a direct comparison between trajectories in the pure Fe and the embedded nanoparticle case, all the simulations here were carried out on systems originally at 0 K. To describe the residual damage after a collision cascade, the systems were investigated by comparing their initial and final states and looking for residual defects and other effects of radiation damage. In total more than 600 simulations were carried out to provide statistics.

4.2.2 Simulating Radiation Damage in Pure bcc Fe

As mentioned before, results were conducted by running collision cascade simulations with PKA energies from 0.5 to 5 keV by sampling the bcc structure's symmetry zone. It is well known that irrespective of the PKA energy, the radiation damage, after the collisional phase of the cascade, consists of a vacancy rich region close to the initial PKA site surrounded by

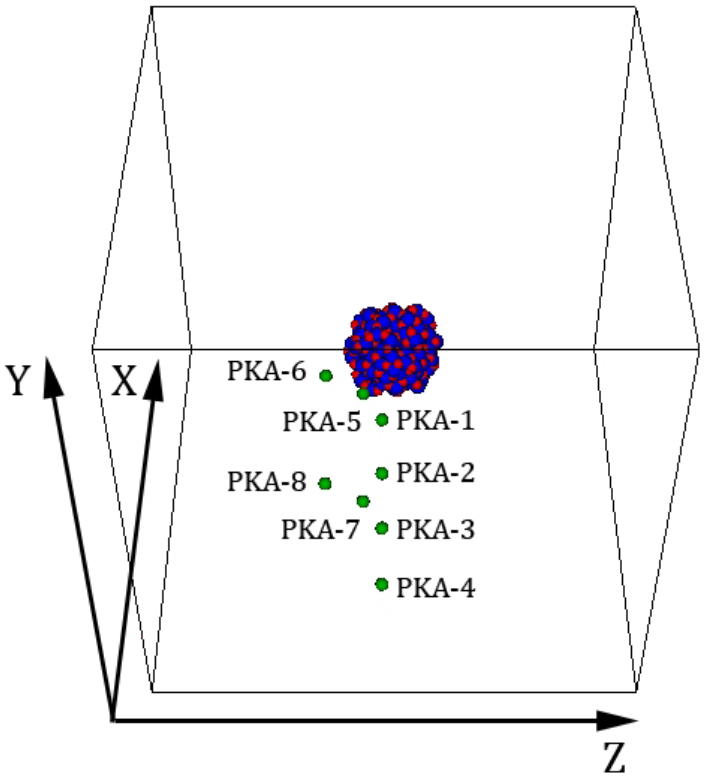

Figure 4.5: The chosen PKA atoms for the 1 keV simulations in the system with the embedded nanoparticle. Simulations were started by directing the PKA atoms in 66 directions towards the nanoparticle.

outlying interstitials, see e.g. [106, 107, 108]. The PKA energy determines the number of vacancies formed and the extent and size of the interstitial loops, as is shown in Figure 4.6.

Radiation damage in bcc iron has been extensively studied by many groups around the world [32, 106, 37, 109, 110, 111, 112] where the studies were conducted to understand the role of the cascade energy and temperature, the influence of the interatomic potentials, stability of the defects and other properties. Therefore the data from the radiation damage simulations in pure Fe is used only for the comparison reasons with the systems containing an yttria nanoparticle.

4.2.3 Simulating Radiation Damage in a Simplified ODS Model

Defect analysis of 1 keV collision cascades done in pure Fe and an ODS model (system A) shows an interesting evolution of the number of iron interstitials. As a first example a study

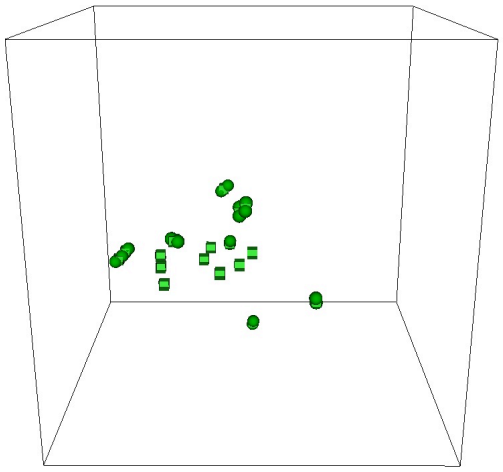

Figure 4.6: Typical residual defects spread after a radiation damage event in pure Fe contains a vacancy rich region close to the initial PKA site surrounded by outlying interstitials.

between these two systems is given in Figure 4.7, where the PKA position is 1, as it is shown in Figure 4.5.

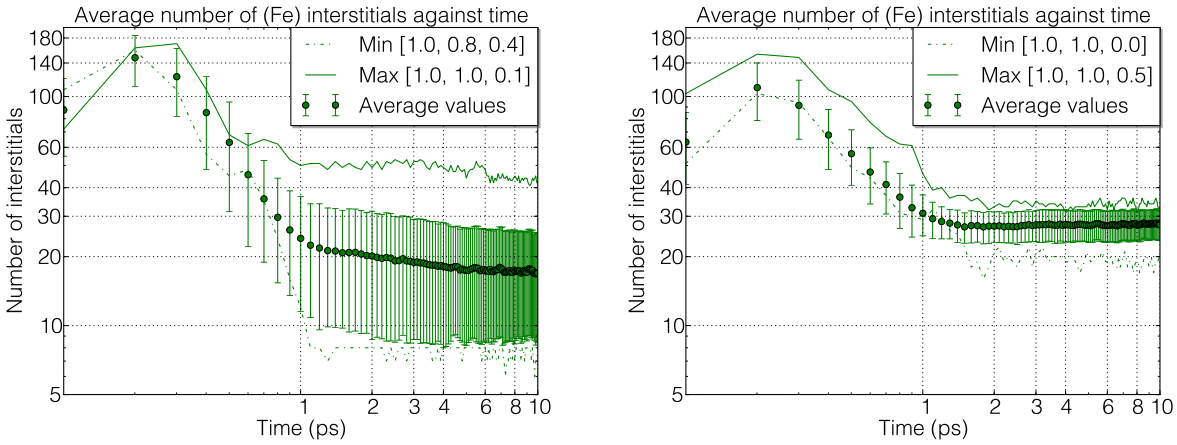

(a) Iron system (b) Model of ODS system

Figure 4.7: Comparison of defect (iron interstitial) numbers sampled over 66 directions for 10 ps. Circles indicate average defect number in the system every 100 fs with 1 σ error bars.

Clear differences can be observed between these two cases. In both systems the peak defect numbers occur during the first two hundred femto-seconds (the ballistic phase), after which recombination processes take place. The average peak number of interstitials in the iron system is ≈ 148 with standard deviation ≈ 33 at 200 fs compared to ≈ 110 and ≈ 30 accordingly in the embedded nanoparticle system at the same time. Significant differences

between the systems remain even after the recombination process. At the end of the simulation the average number of interstitials in the iron system is ≈ 18 with standard deviation ≈ 8, compared to 28 and 3 in the ODS system. This would appear at first sight to be contrary to the expectation that the nanoparticles would increase radiation tolerance and result in fewer defects. If, however, the interstitial defects located at the interface between the nanoparticle and the matrix are not counted as true defects but as reconfiguration of Fe atoms around the nanoparticle, then the situation changes significantly.

If the defects, that are located on the surface of the nanoparticle, are excluded, then the closer the PKA is initiated to the yttria nanoparticle the lower the defect count is (Figure 4.8) compared to defect numbers in the pure iron system (Figure 4.7a); especially the cases in Figures 4.8a, 4.8b and 4.8c, 4.8d. But as the PKA distance from the nanoparticle increases, as expected, the defect count approaches that for pure Fe and there are not many defects on the surface.

The defect number comparison tells only a part of the story and a deeper examination of the mechanisms by which the interstitials are formed at this interface and how the nanoparticle itself behaves when subjected to impact by the energetic Fe particles is carried out.

4.2.3.1 Effect of the Nanoparticle on the Cascades

A common feature of the collision cascades is the ability of the yttria nanoparticle to prevent damage spread as illustrated in Figure 4.9. In this example two collision cascades are compared by choosing the PKA at the same position in both, the pure Fe system and one containing a nanoparticle, and directing it in the [1 0.6 0.5] direction with 1 keV kinetic energy. Numbers in square brackets refer to the relative velocity components parallel to the coordinate axes, with the x-component normalised to 1. (Figure 4.9 (a,b,c)) and (Figures 4.9 (d,e,f)) represent systems of pure iron and ODS model accordingly.

In Figure 4.9 only the Fe defects in the system and the atoms from the yttria particle are

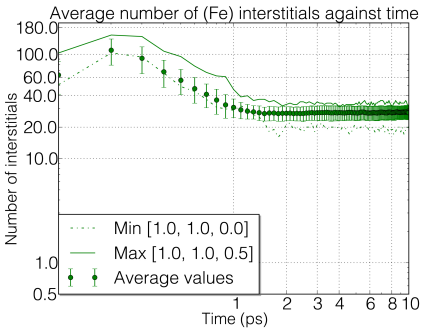

(a) PKA 1 - 19 Å

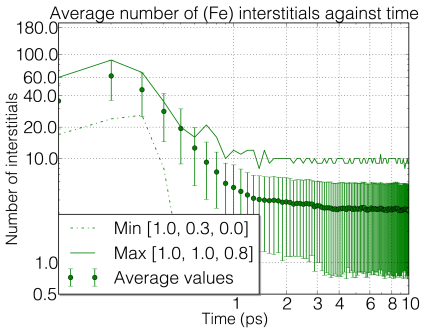

(b) PKA 1 (without interface defects)

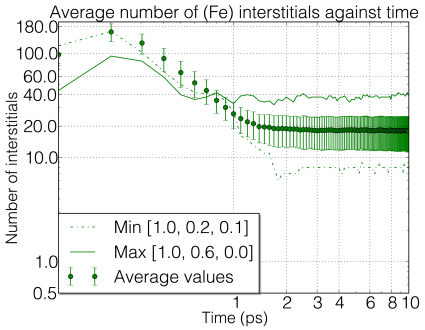

(c) PKA 2 - 31 Å

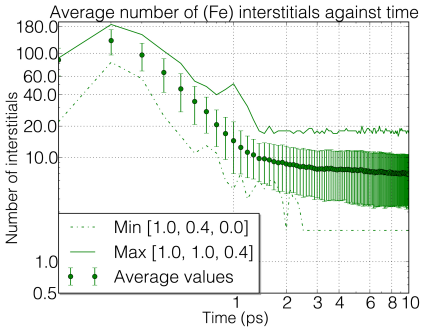

(d) PKA 2 (without interface defects)

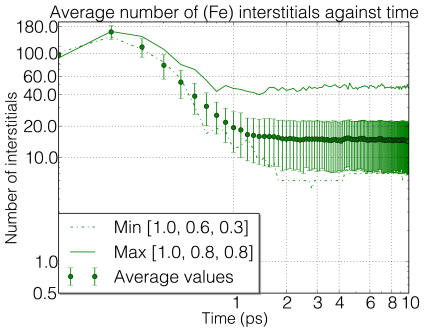

(e) PKA 3 - 44 Å

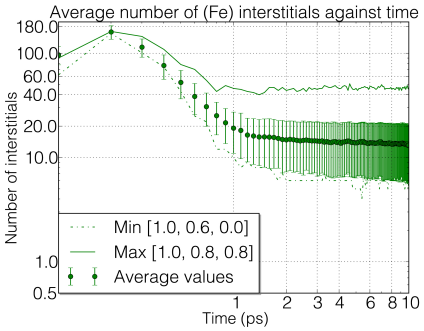

(f) PKA 3 (without interface defects)

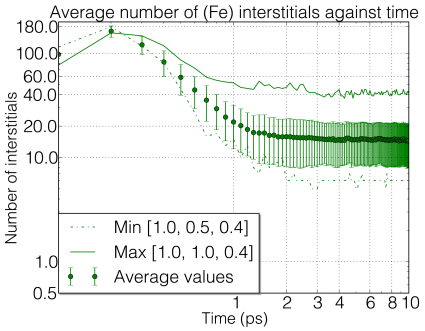

(g) PKA 4 - 56 Å

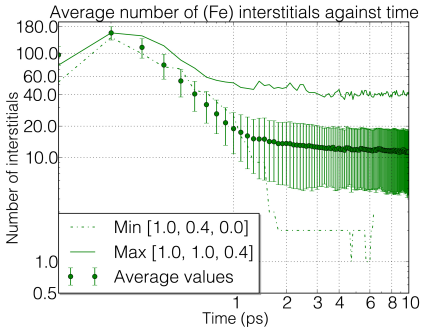

(h) PKA 4 (without interface defects)

Figure 4.8: The number of interstitial defects in the model of ODS system after 1 keV collision cascades in 66 directions. The chosen PKA atoms are located at different distances from the centre of yttria nanoparticle, varying from 16 Å to 57 Å.

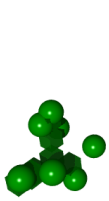

(a) 25 fs - iron system

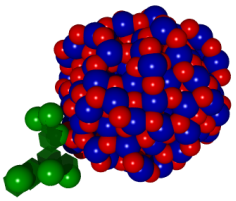

(b) 25 fs - ODS system

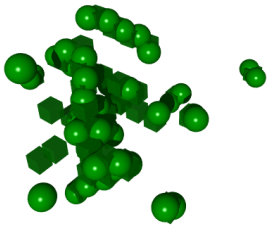

(c) 500 fs - iron system

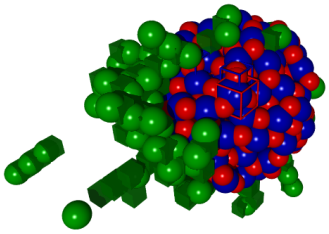

(d) 500 fs - ODS system

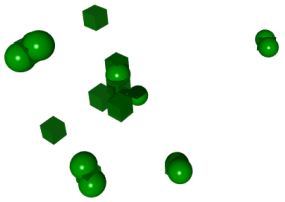

(e) 1250 fs - iron system

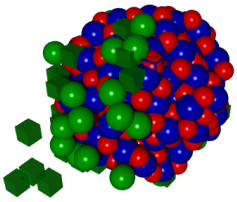

(f) 1250 fs - ODS system

Figure 4.9: Snapshots of collision cascade evolution in the pure iron and the embedded nanoparticle systems for the initial same PKA direction at 1 keV. Yttrium is represented by blue spheres and oxygen by red spheres. Green spheres are Fe interstitials and green cubes are Fe vacancies. Fe atoms that remain on lattice sites are not shown.

shown. At the very beginning of the cascade, both cases have a similar defect configuration (Figures 4.9a and 4.9b), but there are differences after 500 fs and 1250 fs. In the ODS system the cascade is effectively blocked by the nanoparticle and almost every interstitial is located on the nanoparticle's surface with a vacancy cluster at the origin of collision cascade. In the pure Fe case the cascade is more spread out. Although only one cascade is shown here, the result is typical of many of the different collision cascades that were analysed.

A key feature of the process is that Fe atoms can relocate to positions within the nanoparticle during the ballistic phase of the cascade if they have enough energy to penetrate the nanoparticle. However in all cases considered the Fe atoms were ultimately ejected from within the nanoparticle to reside at the interface.

These are not the only mechanisms by which defects form at the interface. Interstitial defects that form close to the particle can migrate there as it shown in Figure 4.10. Here a dumbbell interstitial (DB) is initially formed less than 10 Å from the particle but is attracted there in the later stages of the cascade.

In this example the PKA atom was directed in the [1 0.2 0.0] direction with 1 keV kinetic energy. At the very beginning of the simulation, the collision cascade spreads out next to the yttria nanoparticle, as is shown in the snapshot at 500 fs in Figure 4.10a. After the ballistic phase of the cascade, defect combinations can be identified (Figure 4.10b). By following the evolution of two defects (numbered 1 - interstitial and 2 - DB), it can be clearly seen in Figure 4.10c that both defects move towards to the yttria nanoparticle in the direction [1 1 0] where after 4600 fs (Figure 4.10d) both reside at the nanoparticle's surface. Similar mechanisms were noticed in most of the simulations when interstitials occur in a region close to the yttria nanoparticle.

By plotting histograms of defects numbers against the distance from the yttria nanoparticle over the collision cascade simulation time, an approximate range within which interstitial type defects are attracted towards a nanoparticle can be estimated. As an example, the data from one of the collisions cascade simulations is presented in Figure 4.11, which shows the

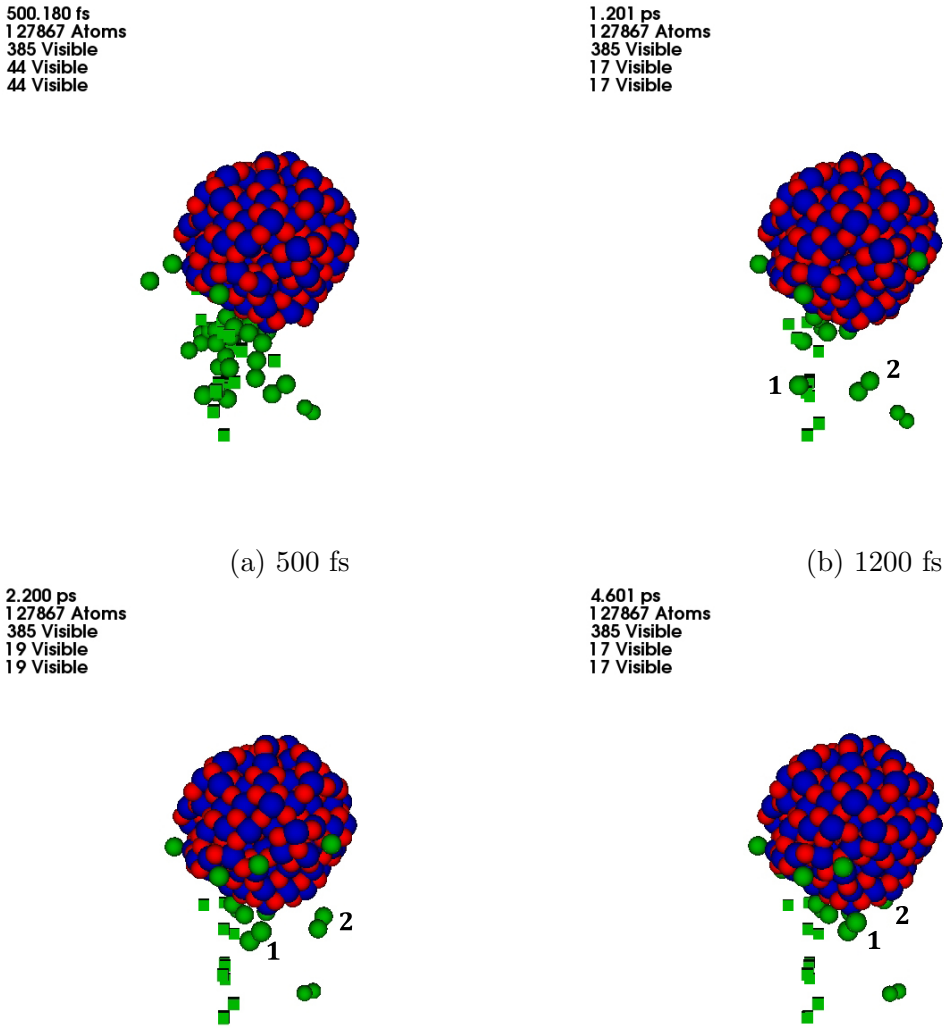

(a) 500 fs

(b) 1200 fs

(c) 2200 fs

(d) 4600 fs

Figure 4.10: Snapshots of a 1 keV collision cascade showing defect attraction to the nanoparticle during the cascade relaxation process.

tendency that can be seen in all other investigated cases.

By analysing the data given in the form of distribution of the interstitial type defects with respect to the distance from the yttria nanoparticle, it can be seen that initially more than half of the accounted defects are situated on the surface of the nanoparticle (Figure 4.11a). This is due the PKA, which is pointed towards the nanoparticle and transfers most of its energy to it. Also, as can be seen in the same figure, there are defects situated along the pathway between initial PKA region and the nanoparticle. At the later stages, 400-500 fs, clearly recombination occurs and the defect numbers decrease, but also the numbers of defects around the nanoparticle's surface starts to increase indicating that defects tend to be situated on it (Figures 4.11b and 4.11c). Further evolution of the system (1-2 ps., Figures 4.11d and 4.11e) shows that region within $3.5 - 10.0$ Å from the nanoparticle becomes free of interstitial type defects and the further increase of defects around the surface is observed. Around 5 ps (Figure 4.11f) the system stabilizes and the only events left are rare ones, that can happen on longer time scales then MD can model. Small changes in defect numbers can be seen around the surface due to the release of the energy by the nanoparticle and Fe atoms rearranging accordingly. The same mechanism does not apply for the Fe vacancies due to their higher migration energy barriers.

When a collision cascade is initiated next to the yttria nanoparticle, not all the Fe atoms get trapped inside and ejected. Moving Fe atoms can arrive with enough kinetic energy to pass through the nanoparticle and cause structural damage to the material on the other side as shown in Figure 4.12.

In this example a semi-channelling [1 0.3 0.0] direction was chosen from the same PKA position and the same initial kinetic energy as in the previous example. After 25 fs (Figure 4.12a), the iron atom still has approximately 700 eV of kinetic energy when entering the nanoparticle. It then passes through the yttria atoms and after 100 fs (Figure 4.12b) leaves, retaining less than 100 eV of its kinetic energy. It then causes damage on the other side of the nanoparticle (Figure 4.12c) and after recombination processes only defects accumulated

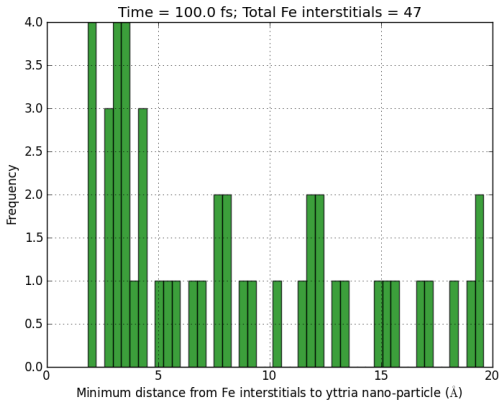

(a) 100 fs

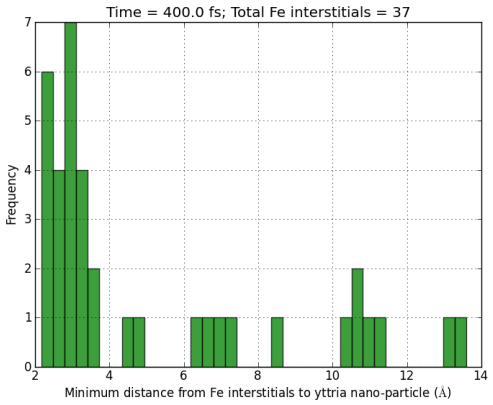

(b) 400 fs

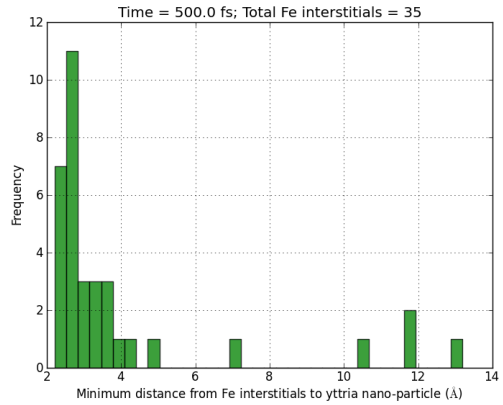

(c) 500 fs

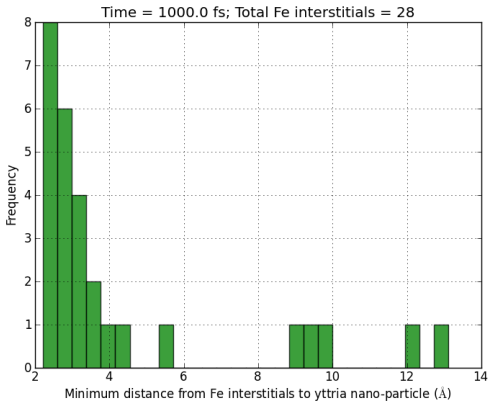

(d) 1 ps

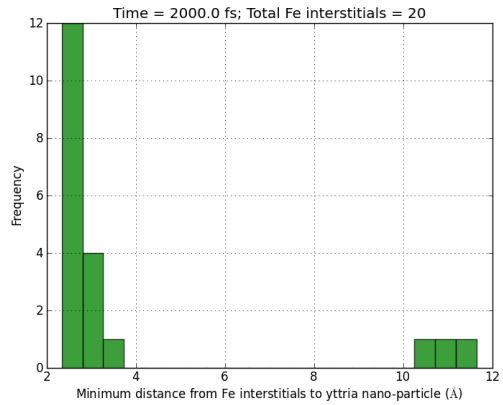

(e) 2 ps

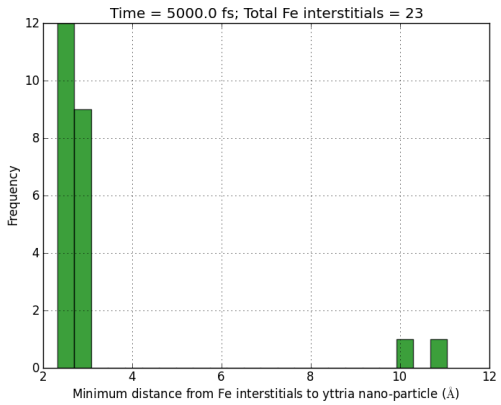

(f) 5 ps

Figure 4.11: Histograms of the distance between the interstitial type defects and the yttria nanoparticle during 1keV collision cascade simulation. Each histogram represents the system at a certain simulation time. This shows that there is an interstitial free region surrounding the nanoparticle.

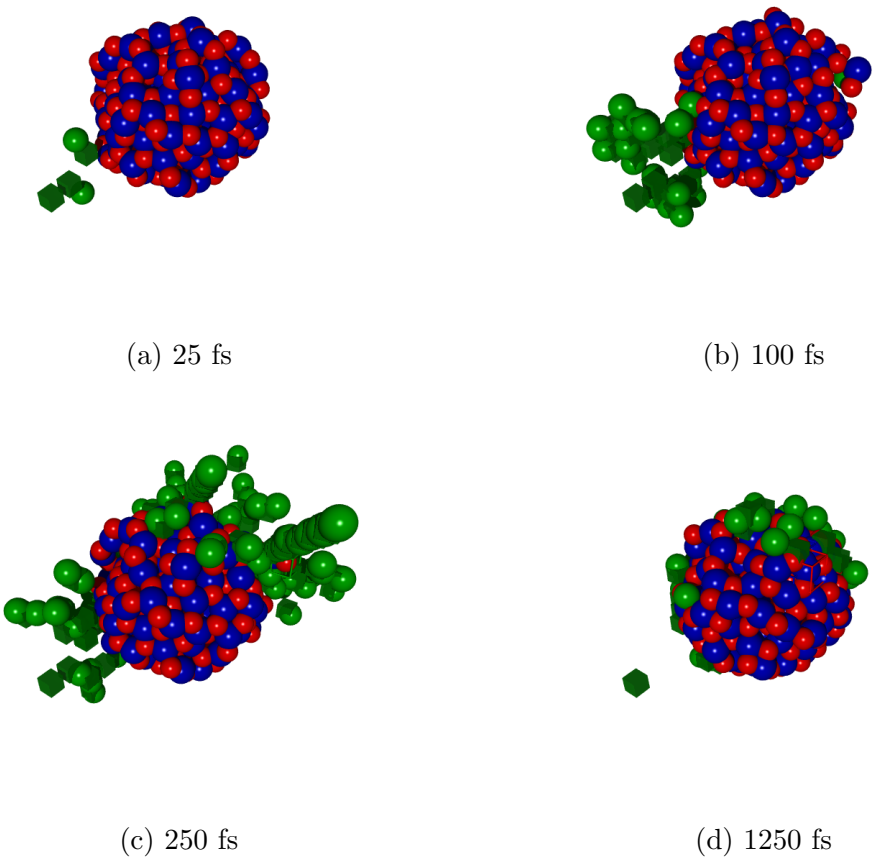

(a) 25 fs

(b) 100 fs

(c) 250 fs

(d) 1250 fs

Figure 4.12: Snapshots of a collision cascade evolution near the nanoparticle when the Fe recoil passes through it.

around the surface of the nanoparticle remain.

In Figure 4.13 statistics are presented from the 66 target directions from the PKA situated 19 Å from the nanoparticle, by presenting the number of iron atoms passing through the nanoparticle (Figure 4.13a), and the atom energies on entering and leaving (Figure 4.13b). Black circles in Figure 4.13a indicate the direction when the nanoparticle acted as 'a wall' and none of the iron atoms passed through; red circles indicate the direction with one iron atom passing through and yellow - two iron atoms. The black bars in Figure 4.13b represent the iron atom's energy when it leaves the nanoparticle and the red bar is the energy absorbed by the nanoparticle. It can be seen that the nanoparticle can absorb up to 850 eV of energy without permanent displacement of atoms.

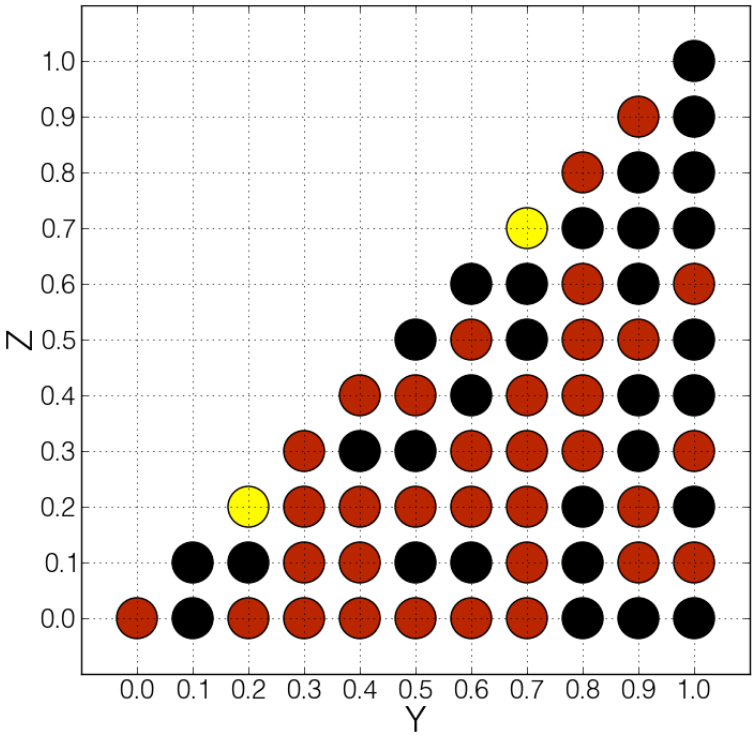

(a) The number of iron atoms passing through the nanoparticle according to initial PKA direction: black - 0, red - 1, yellow - 2.

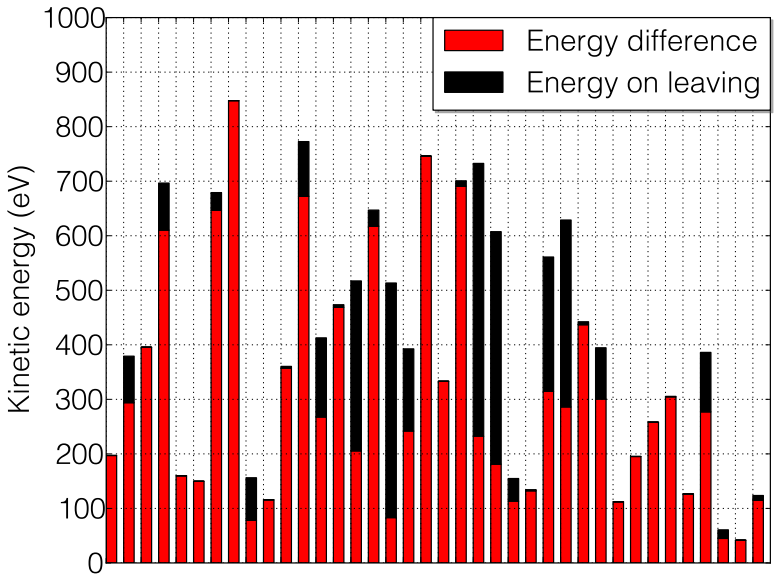

(b) Kinetic energies of iron atoms passing through the yttria nanoparticle: red - absorbed energy, black - remaing energy.

Figure 4.13: Analysis of number iron atoms passing through the yttria nanoparticle and their energies.

4.2.3.2 Effect of the Cascade on the Nanoparticle

The effect of the cascade on the nanoparticle can be examined by plotting the kinetic energy of its constituent atoms as a function of time. For this purpose it is useful to convert their kinetic energy into an effective temperature T and plot T against time as shown in Figure 4.14. It is clearly seen that much of the kinetic energy from the collision cascade is absorbed by the atoms in the nanoparticle. However Figure 4.9 shows that none of the atoms in the nanoparticle were displaced into the Fe matrix. This was a feature of all the 1 keV cascades and is consistent with calculations of collision cascades in ceramic materials which have a much higher displacement threshold energy than in metals [67].

Figure 4.14a illustrates an important feature of the collisional process. After the initial temperature peak, energy is more gradually released into the system and the nanoparticle temperature equilibrates with its surroundings over a longer time scale than that for which the collision cascade is modelled, which is terminated when the defect numbers become stabilised. By calculating the temperature of atoms within a certain radius of the nanoparticle its evolution can be followed. Figure 4.14b shows the gradual diffusion of the nanoparticle's absorbed energy as a function of time. This suggests a mechanism by which the radiation damage can be reduced. The nanoparticle absorbs kinetic energy which would otherwise be used in the production of Fe defects and by releasing the energy more slowly over a longer time scale it is then converted into atomic vibrations rather than permanent displacements. Thus the region close to the nanoparticle remains 'hot' after the cascade has begun to subside which allows for higher mobility of the defects in this region. Figures 4.14c-d show how the radial distribution function for the atoms within the nanoparticle [113] typically changes after irradiation. Initially (at 0.0 ps) the atoms in the nanoparticle have a mainly cubic form. After irradiation (at 10.0 ps) the features in the radial distribution function does not change significantly according to the oxygen plot, but a shift to the left can be seen in the yttrium case. Some of the simulations were continued to 100.0 ps as can be seen in Figures 4.14c-d. Whereas the O distribution does not change in time, but there is a shift in the

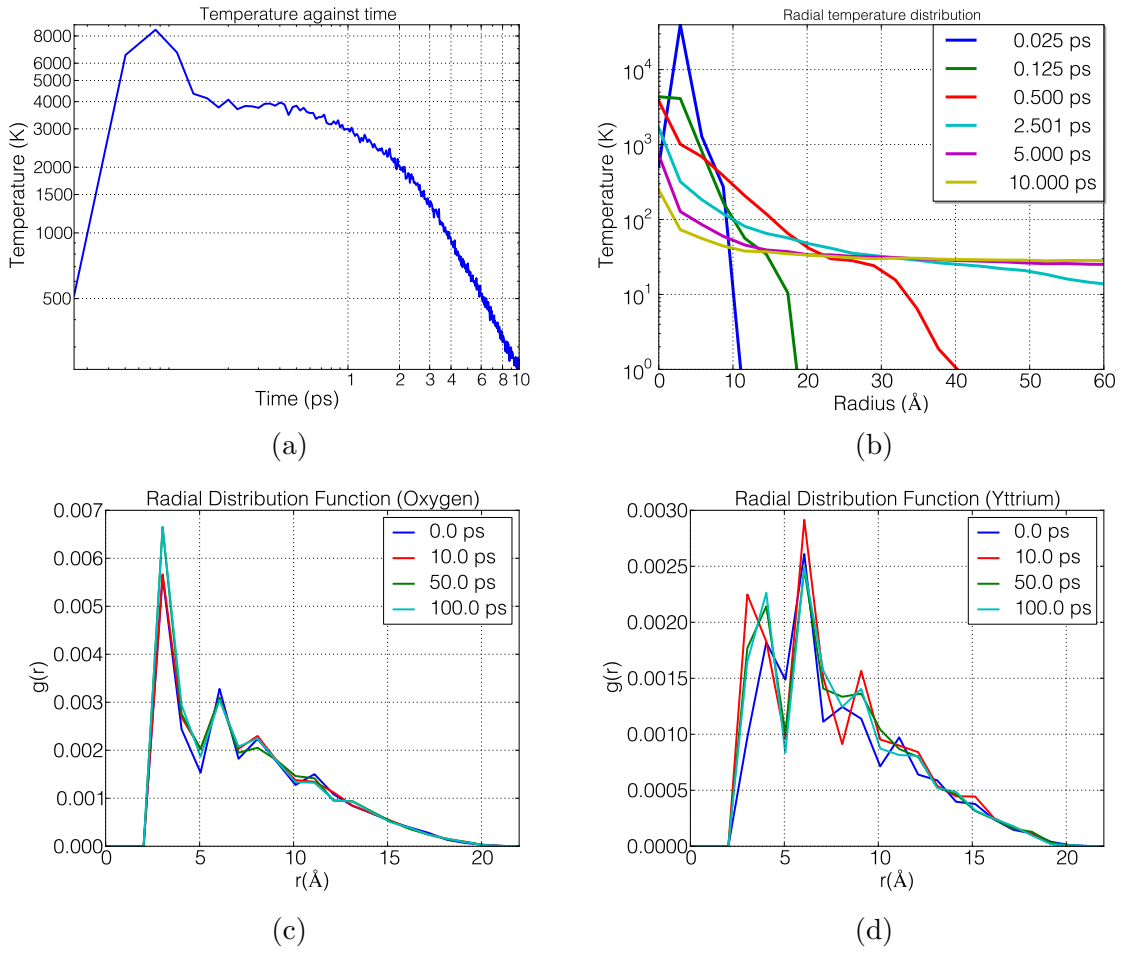

Figure 4.14: (a) - The effective temperature evolution of the atoms comprising the yttria nanoparticle calculated from their kinetic energy, (b) - the temperature evolution of the Fe matrix atoms measured from the nanoparticle's surface, (c-d) - the radial distribution function of the oxygen and yttrium atoms as a function of time.

yttrium graph at 10 and 50 ps but after 100 ps, the distribution is very similar to the initial distribution. Experimentally a shift of yttrium atoms from their exact projected positions has also been observed [114].

4.2.3.3 Higher PKA Energies and Different Nanoparticle Sizes

Some simulations were also carried out for different PKA energies and different nanoparticle sizes for qualitative comparison with fewer trajectories and therefore poorer statistics. Similar processes to those found for 1 keV were observed. By simulating collision cascades in systems B and C (Table 4.1) and comparing the results, where the PKA energy was varied

from 0.5 keV up to 5 keV, an increase of defect numbers in the system with larger nanoparticles was observed with defects again accumulating on the larger nanoparticle's surface.

In the 1 keV simulations yttria nanoparticles have shown good resistance to the radiation damage, remaining mainly intact and such tendency remains during the higher energy collision cascades also. Only few atoms are ejected from the nanoparticle following head on collisions at high energy. An example is shown in Figure 4.15 for a 5 keV PKA that was initiated close to the yttria nanoparticle's surface. In this case a single O atom was ejected from the nanoparticle which also creates residual damage along it's trajectory in the Fe lattice. This is consistent with the preliminary MD results from the group at IGCAR in pure Y_2O_3 showing that it is much easier to displace atoms from the oxygen sub-lattice. However, in most 5 keV cases the trajectories initiated in the Fe region failed to dislodge atoms from the embedded yttria particle into the Fe matrix with the nanoparticle absorbing most of the collisional energy.

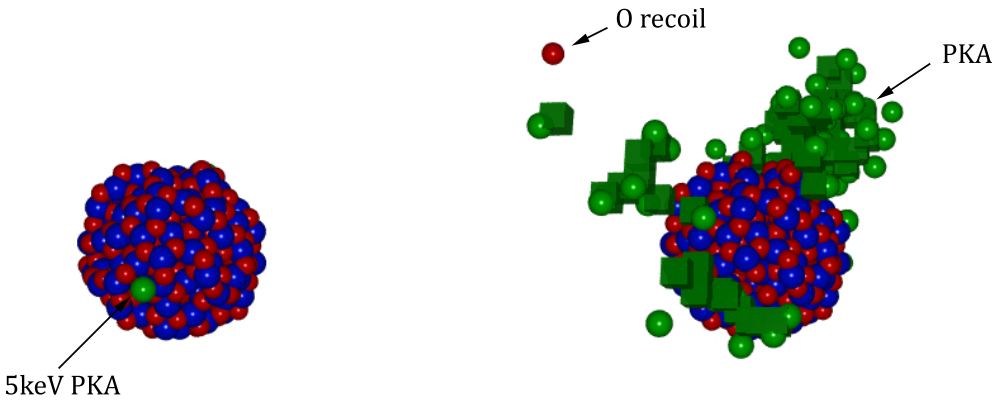

(a) Before a collision with the nanoparticle (b) After a collision with the nanoparticle

Figure 4.15: A 5 keV collision cascade simulation with the PKA initiated close to the nanoparticle.

4.3 Simulating He Bubble Formation

4.3.1 Systems and Modelling Technique

The methodology, similar to the one used by Yang *et al.* [21], using MD was implemented to study the formation and the diffusion of He bubbles within two systems: α-Fe and the simplified ODS system (previously described in section 4.1). To describe interactions between atoms, interatomic potentials, given in Table 4.2, were used with the details given in section 2.4.

Interaction	Potential	Interaction	Potential
$Fe-Fe$	Ackland 2004 [36]	$O-He$	ZBL [53]
$He-He$	Aziz[26]	$Y-He$	ZBL [53]
$Fe-He$	Gao [27]	$Y^{+3}-Y^{+3}$	ZBL [53] + Fennell approx. [66]
$Fe-Y$	ZBL [53]	$Y^{+3}-O^{-2}$	Lewis [55] + Fennell approx. [66]
$Fe-O$	Morse [58]	$O^{-2}-O^{-2}$	Catlow [56] + Fennell approx. [66]

Table 4.2: Interatomic potentials used for simulating He bubble formation in Fe and ODS systems.

Systems for the simulations in α-Fe were created by simply generating a system size of $30a_0 \times 30a_0 \times 30a_0$, where a_0 is the lattice parameter, containing 54,000 atoms. As for the ODS systems, the same mechanism, described in section 4.1, was used.

The initially created system then is minimized to its equilibrium by using the L-BFGS-B method and He atoms are randomly distributed in the system, by keeping the concentration of them equal to 1,000 appm (atomic parts per million). Once again, the system is minimized and, finally, thermalized with the Berendsen thermostat up to 500 K for 20 ps. The concentration and the temperature were chosen to meet the average conditions in the nuclear applications [17]. Examples of both types of systems are given in Figure 4.16.

To generate statistics 10 Fe-He systems were created and evolved with MD for 1 ns. Then 4 of them were picked, with respect to different type of clusters observed and evolved up to 5 ns. As for the ODS systems, two different systems were created in 54,000 bcc structured Fe lattice containing 0.3 at% and 0.71 at% of yttria. The first one is to represent an ODS system in accordance with the experimental data from IGCAR [104] and the second - to

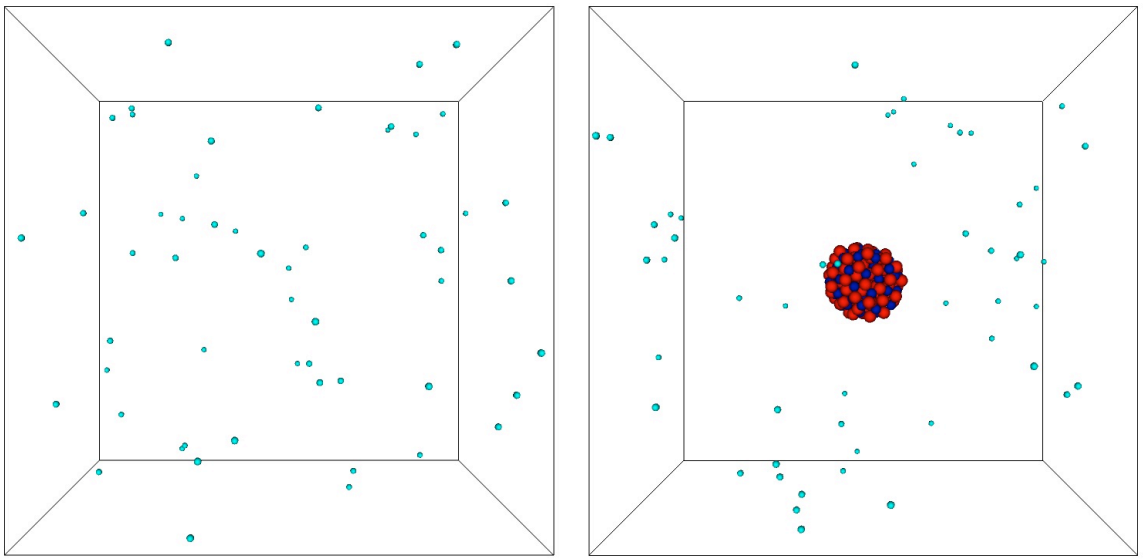

(a) (b)

Figure 4.16: Examples of the systems with random He distribution to simulate He bubble formation mechanisms. Only helium (light blue spheres) atoms and atoms corresponding to the yttria nanoparticle (red - oxygen, dark blue - yttrium) are shown. (a) - pure bcc Fe system, (b) - ODS system.

represent an average size nanoparticle with a higher at% of yttria

4.3.2 Results

By investigating simulations in bcc Fe systems, it was seen that He tends to accumulate into clusters over rather short time scales (ns). This is due to the very high mobility of the interstitial He atoms and their clusters. The bigger they become, the less mobile they are, due to the higher migration energies. It was observed, that when a He cluster reaches a critical size of 4 atoms, it can force an iron atom out of its position and become trapped (a bubble) in the vacancy defect. The same findings were reported by Yang *et al.* in [21]. Clusters containing 5 He atoms in all the simulations shown an immediate ejection of an iron atom, which becomes a split interstitial which may diffuse away form the bubble (Figure 4.17).

Also bubbles varying in sizes from 5 atoms up to 12 were observed. When a bubble size reaches 10 He atoms, another Fe atom is pushed out making a $He_{10}V_2$ bubble. Formation energies of He bubbles were studied by Gai [102], and the calculations agree with the results

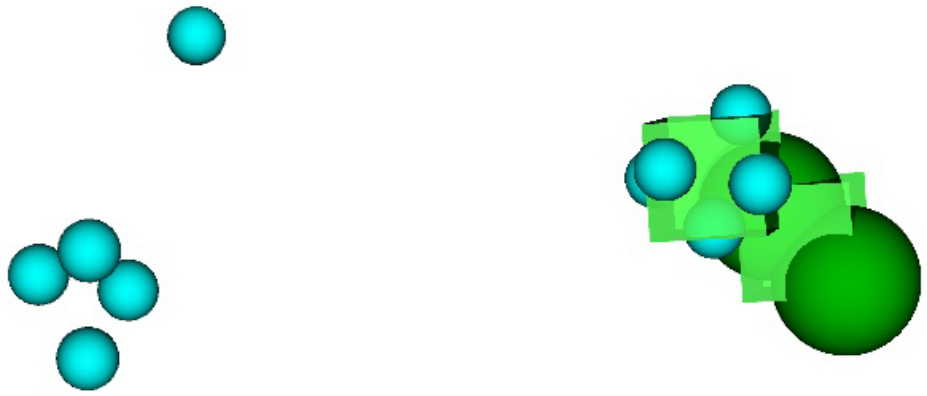

(a) (b)

Figure 4.17: Clustering of He: (a) - slightly mobile 4 He cluster with a highly mobile He interstitial in the vicinity, (b) - the He interstitial joins the 4 He cluster, which pushes out a Fe atom which forms a split interstitial defect. The 5 He cluster stabilizes in the vacancy.

found in this work, done by applying the visual and defect analysis.

The average number of He interstitials in the 10 Fe-He systems, which were evolved for 1 ns, is 6 (out of 54 initially generated) and indicates high tendency of clustering. The average numbers of He bubbles containing 5, 6, 7 and 8 He atoms are 1.9, 0.9, 0.8, 0.8 accordingly, thus showing that even bigger He clusters are likely to form on such short time scales. In two of the ten simulations, helium bubbles containing 12 atoms have also been seen. An example of a system, containing various size bubbles after 1 ns of simulation time in a pure Fe system, is given in Figure 4.18.

As was previously mentioned, 4 systems, out of 10, were continued to be evolved up to 5 ns. In all the cases the outcome was very similar: the highly mobile He interstitials and He clusters, containing up to 3 He atoms, clustered into He bubbles and at the end of the simulation only stable bubbles and defects, formed during the bubble formation, are left in the system, as showed in Figure 4.19 with a frequency diagram with respect to the cluster sizes. He evolution into bigger bubbles can be seen through the comparison of Figures 4.18 and 4.19, that represents the same system after 1 ns and 5 ns simulation time accordingly.

Similar studies were carried out in the ODS model system. The behaviour of He atoms

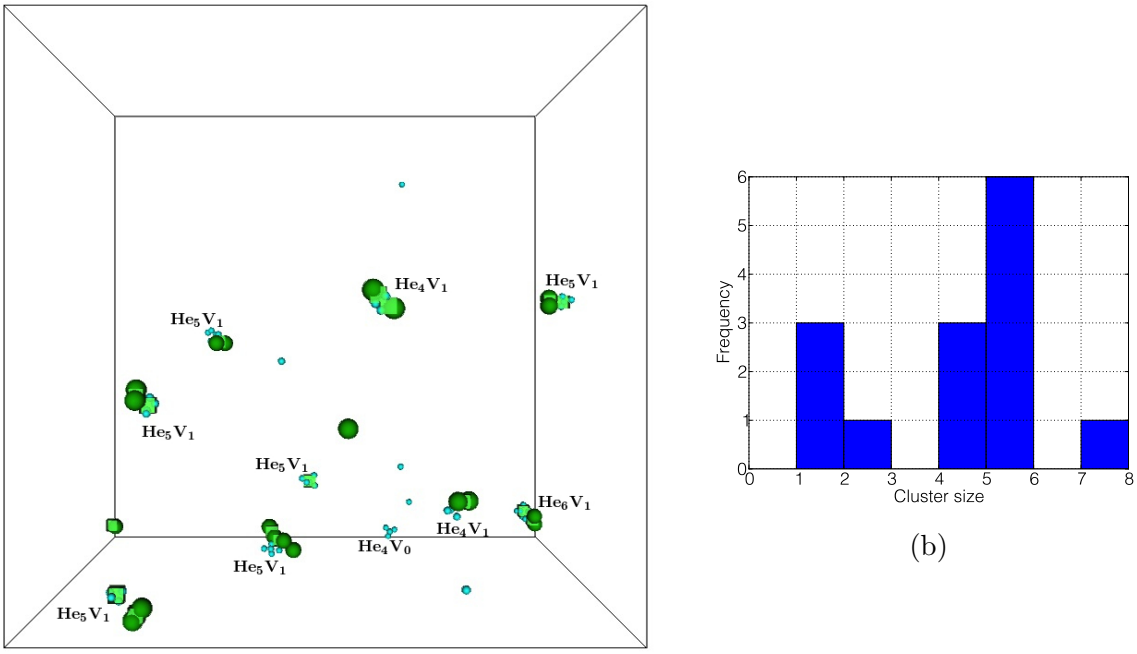

(a) (b)

Figure 4.18: (a) - Fe system containing 1000 appm of He, after being evolved for 1 ns, (b) - a histogram of the He cluster sizes in the system.

were very similar to the one that was seen in Fe systems, when He atoms were not in the vicinity of the nanoparticle. However, an important feature of the ODS material was also captured: He tends to accumulate on the surface of the nanoparticle (see Figure 4.20).

The yttria concentration in the system plays a non-negligible role in these simulations. After calculating statistics of two systems with 0.3 and 0.71 at% of yttria, it was seen, that the system with the bigger nanoparticle traps more He atoms on its surface (Figure 4.21). The volume of the nanoparticle and its surface is roughly 0.3 % and 1.5 % of the total volume of the system, however the average percentage of He sitting on the surface is $\approx$ 13% and 20% accordingly. This means that even a small nanoparticle can have a quite big portion of the He from the system trapped on its surface and protecting the system from the formation of He bubbles. The trapped He decorates the surface of the nanoparticle and does not cluster into a bubble.

Analysis of the He cluster sizes between these three types of systems did not indicate any significant change, when the nanoparticle is present in the system (see Figure 4.22).

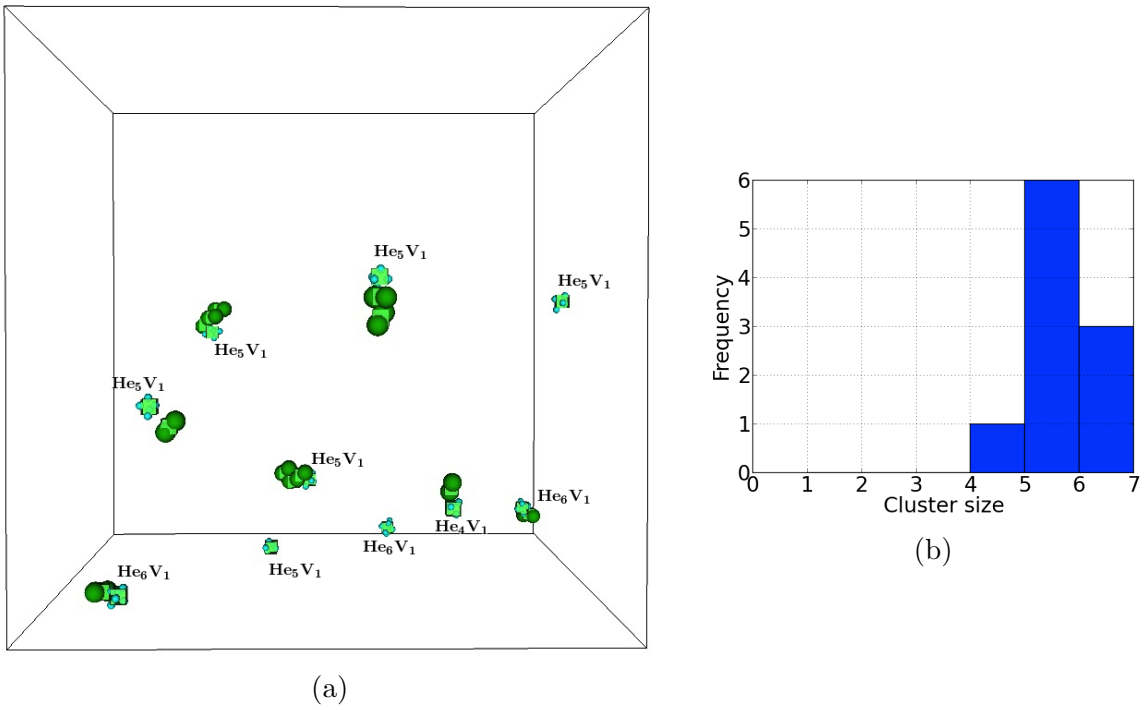

(a) (b)

Figure 4.19: (a) - Fe system containing 1000 appm He, after being evolved for 5 ns. (b) - Histogram of He cluster frequency in the system.

4.4 Discussion and Conclusions

The aim of this chapter was to apply MD simulations to determine the influence of the yttria nanoparticles embedded in bcc Fe on irradiation effects. The chosen potentials were tested separately in a bulk yttria system to confirm that the bixbyite crystal structure was stable at high temperatures. For the small nanoparticles considered here, the structure embedded in the Fe lattice is not commensurate with the bcc lattice and there is relaxation away from the perfect bixbyite structure at the interface. There is some experimental evidence that larger nanoparticles do form a commensurate structure with the Fe lattice so an improvement to the interaction potentials used here, for example, using a variable charge methodology should be a future priority. However to develop a variable charge model for the Fe-Y-O interactions that would capture this feature is beyond the scope of this thesis. The interface therefore acts as a trap for defects and Fe interstitials occur by a direct blocking mechanism, by ejection of Fe interstitials from the nanoparticle or by attraction.

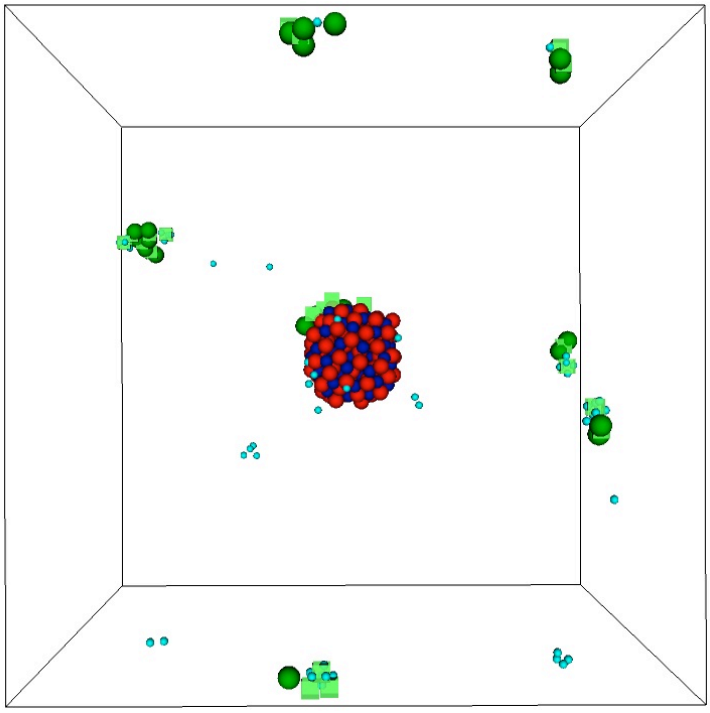

Figure 4.20: An ODS system with 0.3 at% of yttria and randomly distributed He with 1000 appm concentration after being evolved for 1 ns. A part of helium atoms instead of clustering into bubbles, accumulates on the surface of the nanoparticle.

Results from the collision cascade simulations have shown how the cascades interact with the yttria nanoparticles. Different behaviours and processes can be seen: when a collision occurs in an yttria-free region, the irradiation, as expected, is similar to the one observed in the pure bcc iron system. However, when it is initiated close to a nanoparticle, the nanoparticle can act as a block to the propagation of a collision cascade. In this case the energy can be "transferred" to the yttria nanoparticle, so instead of creating residual defects in the Fe lattice structure, the energy is absorbed by the yttria nanoparticle and gradually released through atomic vibrations over longer time scales then the MD simulation. There is a partial disordering of the nanoparticle structure during this process but after large times the nanoparticle structure is similar to that before irradiation.

Fe defect attraction to the nanoparticle interface can also occur, thus lowering the number of residual defects in the bulk crystal structure. This effect was noticed by coupling visual analysis of the defects and studying the distribution of interstitial type defects with

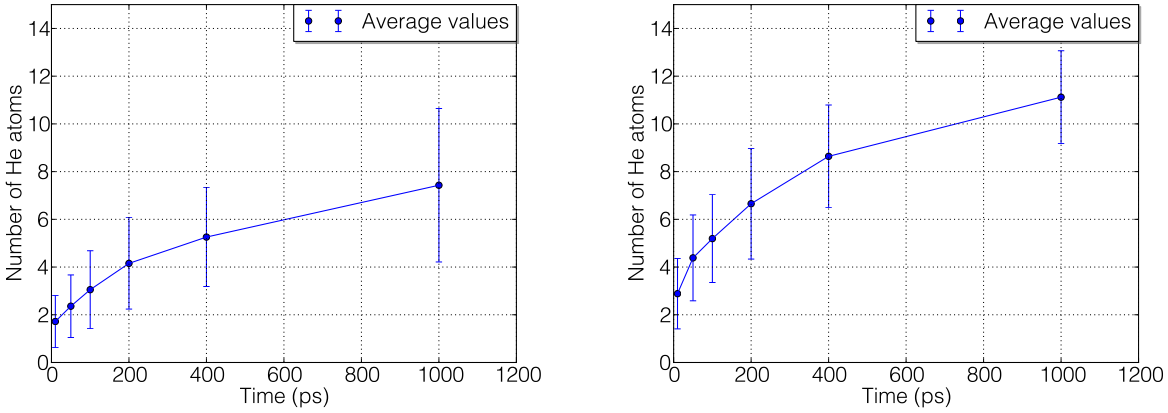

(a) (b)

Figure 4.21: Average number He atoms situated on the surface of the nanoparticle after 1 ns simulation: (a) system containing 0.3 at% yttria as a nanoparticle, (b) system containing 0.71 at% of yttria. Circles indicate average values with 1 σ error bars.

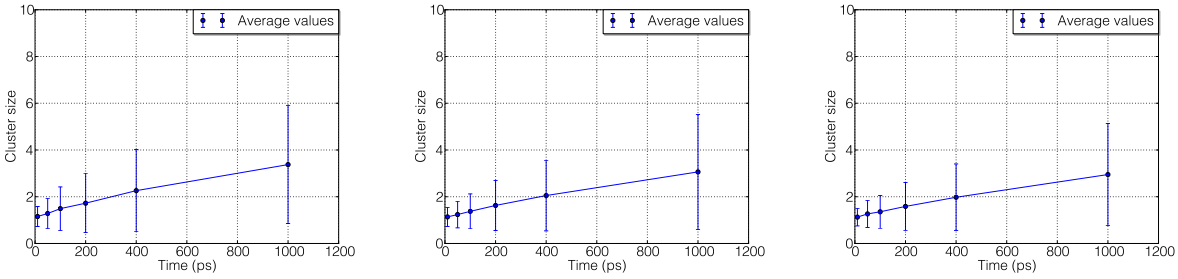

(a) (b) (c)

Figure 4.22: Average He cluster sizes after 1 ns simulation in three types of systems: (a) - Pure Fe, (b) - ODS containing 0.3 at% yttria, (c) - ODS containing 0.71 at% yttria.

respect to the distance from the yttria nanoparticle. An active region of $3.5 - 10.0$ Å from the nanoparticle has been determined to be free of interstitial type defects in most of the simulations, thus suggesting defect attraction within it towards the nanoparticle, which was also confirmed by tracking individual defects in the same region.

The results for higher energy PKAs (5 keV) show that only in the event of a near head-on collision with an incoming energetic Fe atom, does the ejection of an O atom from the cluster occur. The results give therefore some hint that the ODS materials might be more radiation resistant than the pure metal.

Results from the He clustering simulations have shown how yttria nanoparticles interact

with helium atoms. Also, interesting behaviours of He clusters were observed in pure Fe systems, where clusters containing up to 4 He atoms are mobile and clusters containing 5 or more become stable by pushing a Fe atom out of its position. Simulations up 5 ns showed that He tends to cluster rapidly and the end of simulations, systems contained only stable He bubbles.

Systems with yttria nanoparticle showed the ability to trap He on their surface and the amount of He concentrated on the surface greatly depends on the size of the nanoparticle. One of the nanoparticle's properties, to reduce the size of He clusters, has not been seen since large bubbles have not been modelled. It also might be due to the method chosen to simulate He accumulation in the systems. Normally He atoms are produced by transmutation reactions and gradually introduced into the matrix. Therefore, before another introduction of He into the system, He atoms that are present can diffuse and find a trapping site to precipitate. When the whole amount of He is introduced at once, He atoms do not need to diffuse as much to find a precipitation site. Nonetheless, the results from the simulations show significant evidence of the nanoparticle's ability to trap helium.

These results depend on the interatomic potentials and cannot be considered as quantitative, but the tendencies seen in the simulations provide a substantial insight of the processes.

Chapter 5

Simulating Radiation Damage in Y-Ti-O systems

This chapter presents preliminary results from the collision cascade investigations in three systems: Y_2O_3, Y_2TiO_5 and $Y_2Ti_2O_7$ which represent nanoparticles found in the ODS steels. Before the radiation damage simulations are undertaken, the study was focused on constructing minimum energy crystal structures from the potential description by varying structural parameters: a_0, b_0 and c_0 lattice constants and oxygen displacement δ, as these will not be exactly the same as the experimental values. This is followed by radiation damage studies which give an insight look in to the atomistic processes that undergo in the systems during low energy collision cascade events.

5.1 Determination of the Minimum Energy Structures of the Y-Ti-O Systems

The chosen potentials for Y_2O_3, Y_2TiO_5 and $Y_2Ti_2O_7$ model systems, used in the radiation damage simulations, were tested by minimising the energies of the perfect crystals and fitting their structures through the adjustments of lattice constants and oxygen displacement. The

implemented Buckingham type potential (see section 2.4.1.2) has the parameter values (see Table 2.2) derived empirically using the relaxed fitting method, by fitting to the experimentally measured data [57]. Another available potential for these systems is also a Buckingham type potential [115], but it was designed for a charge-neutral model and it was unable to recreate the structures of the systems as they were determined experimentally.

Originally the Nelder-Mead Simplex Method [116] was implemented from the Python SciPy 0.12.0 scientific library. During each iteration of the Simplex Method, a new system is created using the optimized structure parameters. Y_2O_3 and $Y_2Ti_2O_7$ are cubic systems with two structural variables: a_0 (lattice constant), which describes the size of the cube and oxygen displacement δ, which describes the relaxation of the oxygen atoms from the perfect lattice sites, where Y_2TiO_5 is a rectangular system described by three structural variables: a_0, b_0 and c_0 lattice constants.

Then the systems are relaxed to their local minimum energy configurations by the BFGS method [75] and thermalised up to 500K with the Berendsen thermostat [79] for 10 ps. It was observed, that systems tend to get trapped into local minimum configurations and the method did not converge to a global energy minimum. Therefore a more straightforward method was used instead: by varying the ranges of the lattice constants and oxygen displacement, a structure with the lowest energy and the best agreement between potential energies of the system after initial creation, after minimisation and after thermalisation steps is chosen to represent the bulk material in the radiation damage simulations. At first a large interval with a big step size is used for all the structural variables in the structure. Then the intervals are narrowed and smaller step sizes are used until the desired accuracy of the variables is reached.

Other properties, such as bulk modulus and elastic constants, were not tested since the potential by Bush *et al.* [57] was not designed to reproduce them and cannot be compared with the experimental data.

5.1.1 Y_2O_3

Y_2O_3, also known as *Yttria*, has a bixbyite structure (space group Ia-3, T_h^7) with atoms in the following Wyckoff positions [117]:

Y at 8*e*: $\left[\left(\frac{1}{4},\frac{1}{4},\frac{1}{4}\right),\ \left(\frac{1}{4},\frac{3}{4},\frac{3}{4}\right),\ \left(\frac{3}{4},\frac{1}{4},\frac{3}{4}\right),\ \left(\frac{3}{4},\frac{3}{4},\frac{1}{4}\right)\right]$;

O at 24*e*: $\pm\left[\left(u,0,\frac{1}{4}\right),\ \left(\frac{1}{4},u,0\right),\ \left(0,\frac{1}{4},u\right),\ \left(\bar{u},\frac{1}{2},\frac{1}{4}\right),\ \left(\frac{1}{4},\bar{u},\frac{1}{2}\right),\ \left(\frac{1}{2},\frac{1}{4},\bar{u}\right)\right]$;

O′ at 48*e*: $\pm[(x,y,z),\ \left(x,\bar{y},\frac{1}{2}-z\right),\ \left(\frac{1}{2}-x,y,\bar{z}\right),\ \left(\bar{x},\frac{1}{2}-y,z\right),\ (z,x,y),\ \left(\frac{1}{2}-z,x,\bar{y}\right),$ $\left(\bar{z},\frac{1}{2}-x,y\right),\ \left(z,\bar{x},\frac{1}{2}-y\right),\ (y,z,x),\ \left(\bar{y},\frac{1}{2}-z,x\right),\ \left(y,\bar{z},\frac{1}{2}-x\right),\ \left(\frac{1}{2}-y,z,\bar{x}\right)]$,

where $\delta = -0.0327, x = 0.3907, y = 0.1520, z = 0.3804$ and lattice constant a_0=10.604 Å (27^o C).

Bixbyite structure can be thought as a fluorite structure with oxygen occupying three fourths of the positions and vacancies situated on the opposite corners of the cube as shown in Figure 5.1.

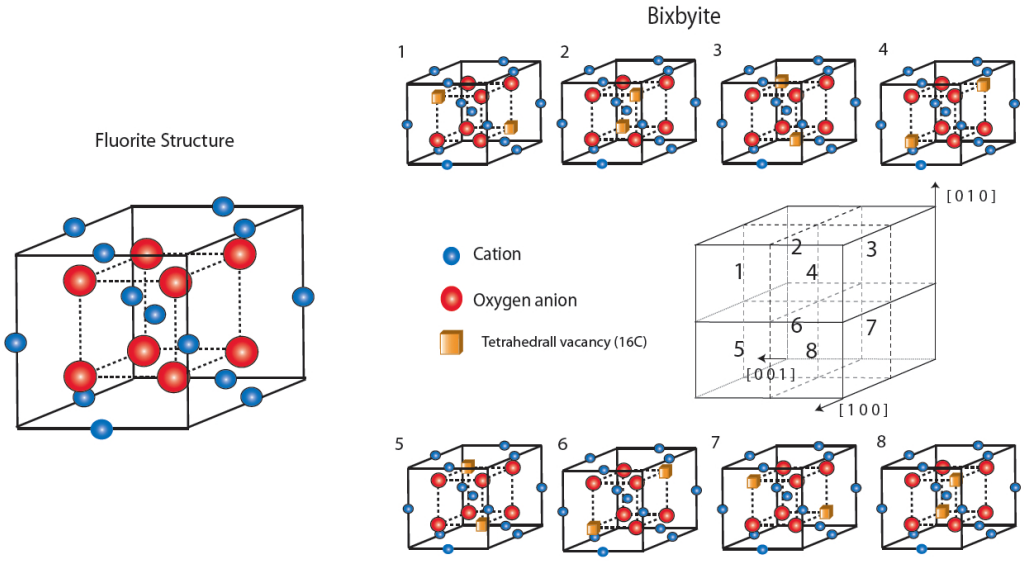

Figure 5.1: Schematic representation of the fluorite and the bixbyite structures. This image is taken from [118].

For Y_2O_3, a $3a_0 \times 3a_0 \times 3a_0$ supercell, where a_0 is the lattice constant, was set up to determine the best values of a_0 and the oxygen displacement δ. It was found that $\delta = -0.03$Å irrespective of the value of a_0 gave the lowest system energy and this value was then used to determine the lattice constant a_0. Figure 5.2a shows the change of the supercell's energy in

a narrow interval of a_0. The found minimum value 10.41Å is in a reasonable agreement with the experimental results from [117], therefore the set of parameters where $a_0 = 10.41$Å and $\delta = -0.03$Å was used to create bigger systems ($8a_0 \times 8a_0 \times 8a_0$, 40,960 atoms) to simulate radiation damage.

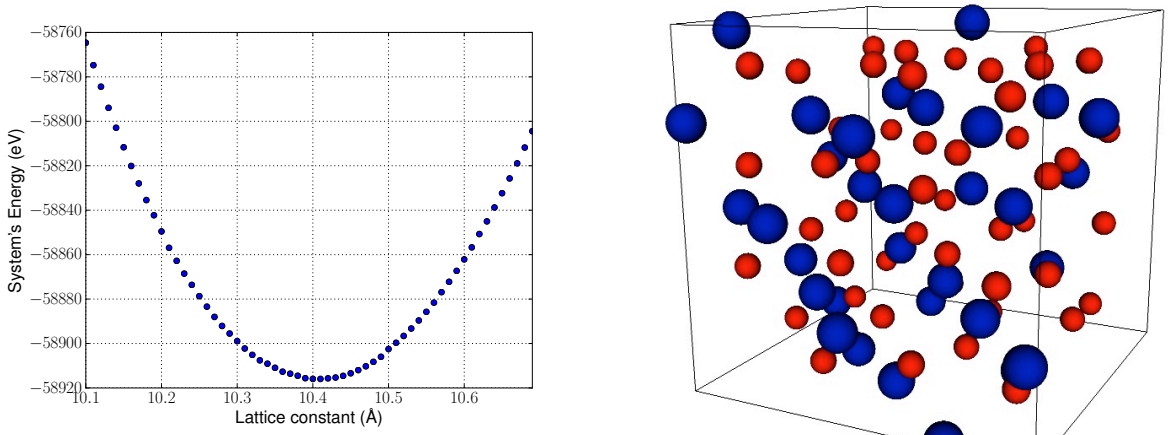

(a)

(b)

Figure 5.2: (a) - Estimation of the lattice constant for Y_2O_3, with $\delta = -0.03$Å. (b) - Y_2O_3 unit cell's structure when $a_0 = 10.41$Å and $\delta = -0.03$Å, blue spheres represent yttria, red - oxygen atoms.

5.1.2 Y_2TiO_5

Y_2TiO_5 has a stable orthorhombic crystal structure under 1330°C, which is quite complicated (space group $Pnma$, D_{2h}^{16}) and has atoms in Wyckoff positions of: $4c$: $[(x, 1/4, z)$; $(-x + 1/2, 3/4, z + 1/2)$; $(-x, 3/4, -z)$; $(x + 1/2, 1/4, -z + 1/2)]$ positioned in the mirror planes $y = 1/4$ and $y = 3/4$ [119].

To determine lattice constants for Y_2TiO_5, a $3a_0 \times 9b_0 \times 3c_0$ supercell was used, where a_0, b_0 and c_0 are the lattice constants. The tests were carried out by adjusting all of them. The optimum values were found to be equal to $a_0 = 10.33$Å, $b_0 = 3.49$Å, $c_0 = 11.15$Å and are in a good agreement with the experimentally determined values: $a_0 = 10.35$Å, $b_0 = 3.7$Å and $c_0 = 11.25$Å [120]. The comparison between calculated and experimental internal free

parameters x, z are specified for each atom and the values are given in Table 5.1.

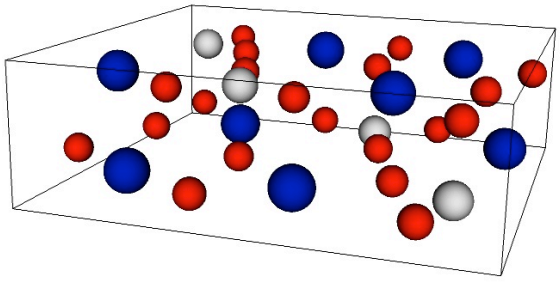

Figure 5.3: Y_2TiO_5 unit cell's structure when $a_0 = 10.33$Å, $b_0 = 3.7$Å and $c_0 = 11.15$Å; blue spheres represent yttria, red - oxygen and silver - titanium atoms.

Atom	Experimental		Calculated	
	x	y	x	y
Y(1)	0.1156	0.2231	0.1073	0.2060
Y(2)	0.1366	0.5578	0.1273	0.5498
Ti	0.1745	0.8806	0.1704	0.8551
O(1)	0.4947	0.1024	0.5049	0.1013
O(2)	0.2229	0.0449	0.2426	0.0255
O(3)	0.2594	0.7340	0.2582	0.7224
O(4)	0.5085	0.6601	0.5105	0.6401
O(5)	0.2690	0.3833	0.3127	0.3740

Table 5.1: Comparison of the experimental [119] and the calculated relative atoms' positions. Units are in fractions of a_0.

The newly calculated atom positions and the lattice constants were used to create $8a_0 \times 23b_0 \times 7c_0$ size systems containing 41,216 atoms for the radiation damage simulations.

5.1.3 $Y_2Ti_2O_7$

$Y_2Ti_2O_7$ has a pyrochlore structure (space group $Fd\bar{3}m$, O_h^7) and has atoms in Wyckoff positions of: Y at 16d: $(1/2, 1/2, 1/2)$, Ti at 16c: $(0, 0, 0)$, O at 48f: $(\delta, 1/8, 1/8)$, O' at 8b: $(3/8, 3/8, 3/8)$. In order to better understand the pyrochlore structure, it can be thought as

a defective fluorite, with structural vacancies in every 1/8 unit cell [121] as shown in Figure 5.4.

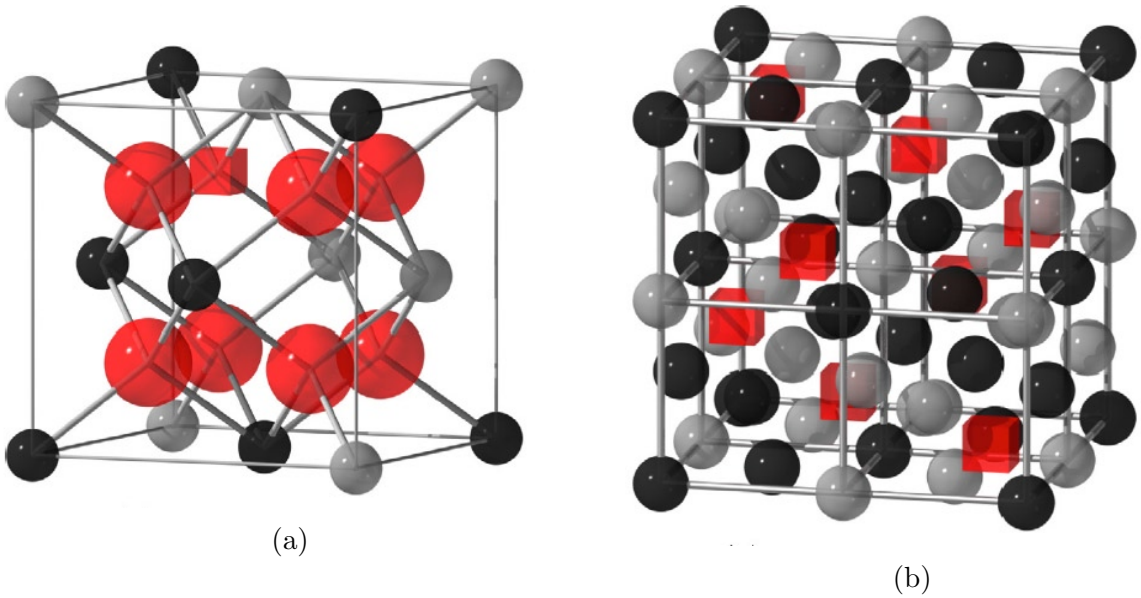

(a) (b)

Figure 5.4: Schematic representations of: (a) - defective fluorite unit cell as a 1/8 of the full unit cell of pyrochlore, with oxygen atoms represented as the red spheres, (b) - unit cell of pyrochlore without oxygen atoms for clarity. The red cubes represent the structural oxygen vacancies. These images are taken from [121].

Similarly to the Y_2O_3 case, a $3a_0 \times 3a_0 \times 3a_0$ supercell was used to determine the lattice constant a_0 and the oxygen displacement δ. Results showed structural stability with $\delta = 0.32$Å and the system with minimum energy difference, when $a_0 = 10.01$Å, was chosen (Figure 5.5). These parameters agree with the experimental values [119]: $a_0 = 10.09$Å and $\delta = 0.328$Å and were used to create $8a_0 \times 8a_0 \times 8a_0$ size systems, containing 45,056 atoms, for collision cascade simulations.

5.2 Simulating Radiation Damage

As was explained in the previous chapter (see sec. 4.2.1), to simulate a radiation damage cascade, a certain amount of energy is imparted to a PKA in the system. During radiation damage simulations, results depend crucially on the initial direction of the PKA. When a system has a rather simple structure (e.g. bcc), PKA directions can be chosen by sampling

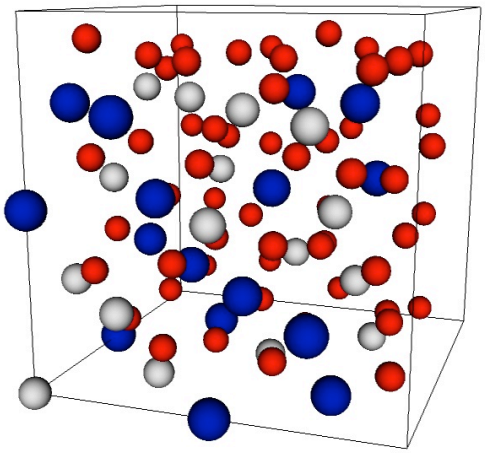

Figure 5.5: $Y_2Ti_2O_7$ unit cell's structure when $a_0 = 10.01$Å and $\delta = 0.32$Å; blue spheres represent yttria, red - oxygen and silver - titanium atoms.

an irreducible region. In the cases of Y_2O_3, Y_2TiO_5 and $Y_2Ti_2O_7$ systems, due to the complexity of their crystal structures, random directions in 3 dimensions were chosen. The PKA directions were sampled by solving the Thompson problem - finding the minimum energy configuration of N point charges on a sphere [122, 123] and directing the trajectories in the directions of the point charges from a PKA located at the centre of the sphere.

This was done by randomly distributing N points on a sphere followed by a minimisation of the effective force using the CG method:

$$\mathbf{F}_i^{eff} = \mathbf{F}_i^{true} - \left(\mathbf{F}_i^{true} \cdot \mathbf{r_i}\right) \mathbf{r_i}, \tag{5.2.1}$$

where

$$\mathbf{F}_i^{true} = -\nabla \phi_i \left(\mathbf{r_1}, \mathbf{r_2}, ..., \mathbf{r_n}\right), \tag{5.2.2}$$

$$\phi_i \left(\mathbf{r_1}, \mathbf{r_2}, ..., \mathbf{r_n}\right) = \sum_{i \neq j} \frac{1}{r_{ij}}, \tag{5.2.3}$$

$$r_{ij} = \left|\mathbf{r}_i - \mathbf{r}_j\right|. \tag{5.2.4}$$

As in [123], to ensure an on sphere point location, the positions are renormalized during each minimisation step:

$$\mathbf{r}_i = \frac{\mathbf{r}_i}{|\mathbf{r}_i|}. \tag{5.2.5}$$

Typical values of N used in this work were: 50, 60 and 100, where the minimisation of the latter is illustrated in Figure 5.6.

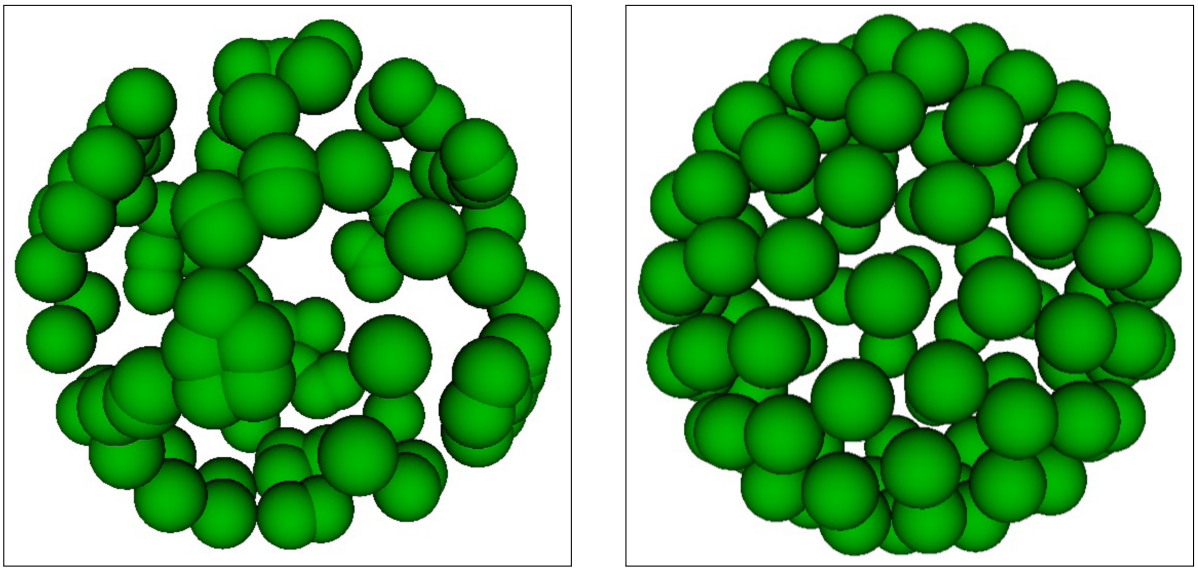

(a) Initial system (b) Minimised system

Figure 5.6: Sampled 100 PKA directions generated by solving the Thompson problem, by minimising initially randomly distributed charged points.

Three PKA energies were used: 500 eV to represent low energy cascades, 1 and 2 keV for medium energy cascades. Higher energy cascades were not contained in the simulation boxes. Bigger systems might be used, but due to the increasing computational costs were not covered in this work. For the same reason, oxygen atoms were chosen as PKA's only in the 500 eV simulations, since they tend to channel through the system more than the heavier Y and Ti atoms. To capture the effect of the temperature, simulations were carried out at 0 K and at 500 K. When simulating at 500 K, systems were initially treated with the Berendsen thermostat (see sec. 2.6) for 10 ps and thermal layers of 3 Å around the simulation box were applied in order to help to dissipate away the energy from the region where the ballistic

process occurs. All simulations have periodic boundary conditions applied.

5.3 Results

5.3.1 Y_2O_3

During the low energy cascades the maximum number of defects occurs within the first 200 fs and is followed by the recombination processes on average lasting until 1-1.5 ps. After 1.5 ps, the atoms that are not situated on the lattice sites only vibrate around their positions and diffusion of them is rarely seen. Graphs of the evolution of the defect numbers are given in Figure 5.7. The graphs indicate that Y PKA atoms produce more defects than O PKA during the peak damage phase and the recovery phase at the end of the simulations. The same behaviour was observed during radiation damage studies in Er_2O_3 bixbyite [124]. From the visual interpretation of data, it seems as the O PKA tends to channel through the system, where as the Y PKA creates more localised damage. With O PKAs most of the collisions are not head-on and they tend to glance off from the atoms, thus having more energy to channel through the system and making less defects compared to the Y PKA.

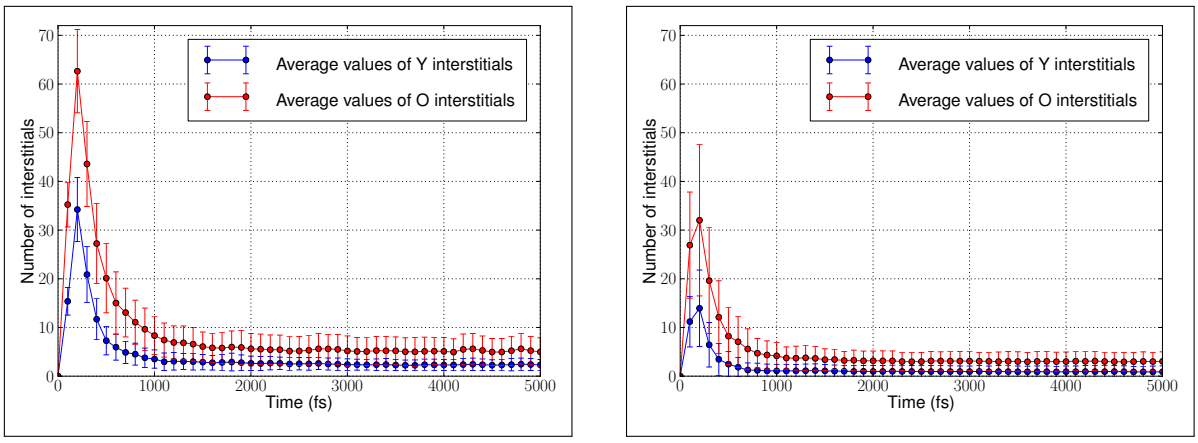

(a) Y PKA (b) O PKA

Figure 5.7: The number of interstitial defects in the Y_2O_3 system, during 500 eV collision cascade simulation at 0K when: (a) - Y PKA, (b) - O PKA.

Two distinct outcomes were observed during the simulations. The first is when the

radiation damage was contained within the vicinity of the initial PKA. A typical evolution of such simulation is shown in Figure 5.8, where the Y PKA is directed in the [-0.69, -0.67, -0.28] direction. At the end of the simulation two yttrium dumbbells, a void, formed at the initial PKA location, a few oxygen interstitials and a cluster of two oxygen and one yttrium atoms on an oxygen site are formed.

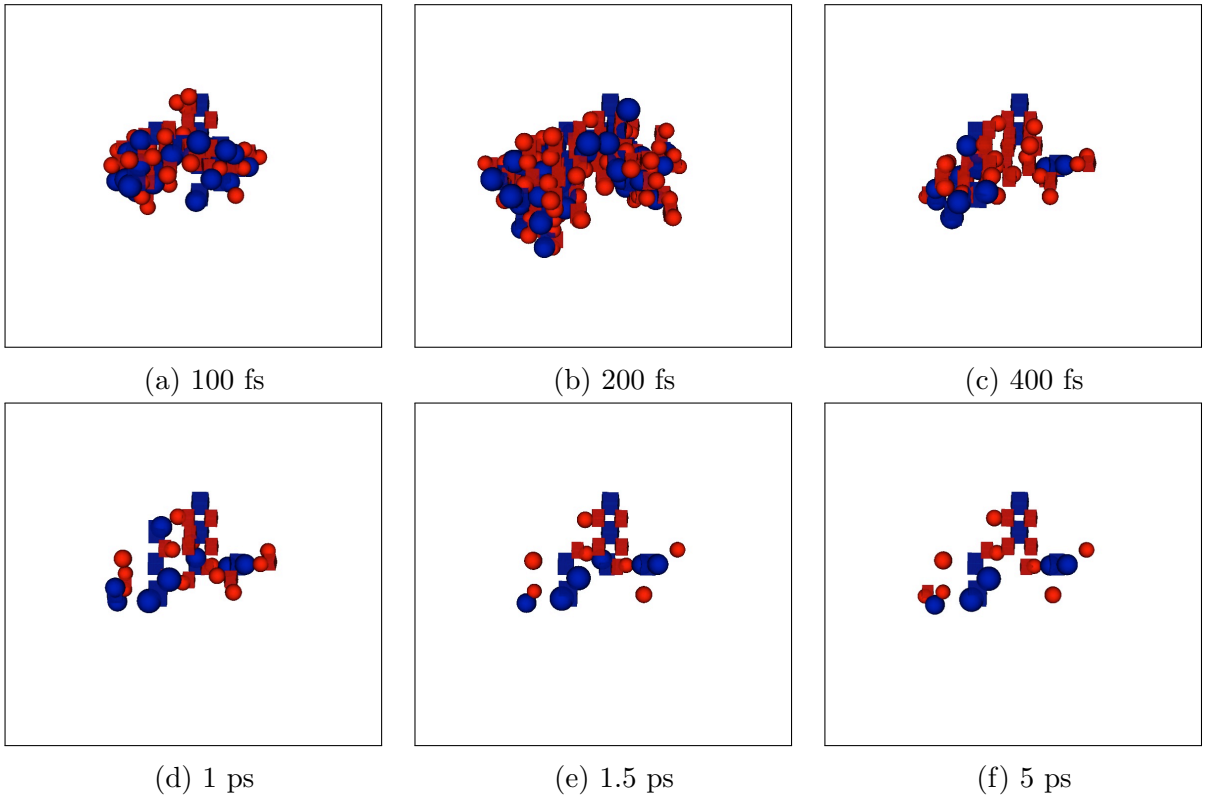

(a) 100 fs (b) 200 fs (c) 400 fs

(d) 1 ps (e) 1.5 ps (f) 5 ps

Figure 5.8: Snapshots of a 500 eV Y PKA collision cascade showing minor defect spread from the original PKA position and a void formation at the centre of the cascade. Blue spheres represent yttrium atoms and red spheres - oxygen. Lattice atoms are not shown.

The second outcome is when PKA is directed in a channelling direction and creates defects on its pathway. In this case the defects tend to recombine as illustrated in Figure 5.9, where the Y PKA was directed in [-0.83, -0.19, 0.53]. At the end of this simulation only a few oxygen defects besides original Y PKA atom are present.

Both behaviours are also a feature of medium energy cascades, where the difference is increasing number of defects and the damage peak is at 300 fs as shown in Figure 5.10. Average numbers of defects left in the system are summarized in Table 5.2. The data shows

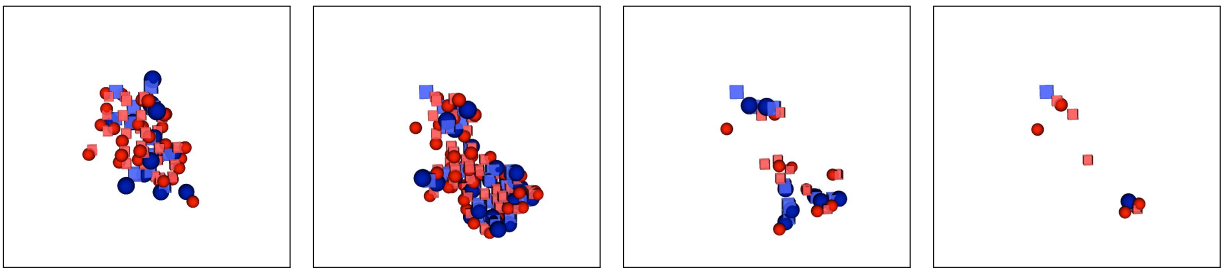

(a) 100 fs (b) 200 fs (c) 400 fs (d) 1.5 ps

Figure 5.9: Snapshots of a 500 eV Y PKA collision cascade in a channelling direction producing defects on its way which recombine during MD time scales.

minor difference of the average number of defects within the thermalized system (500 K) and the system at 0 K, and agrees with the visual analysis showing very similar behaviour in both cases. Also the effect of temperature is small and the relation between the number of defects and the PKA energy is almost linear.

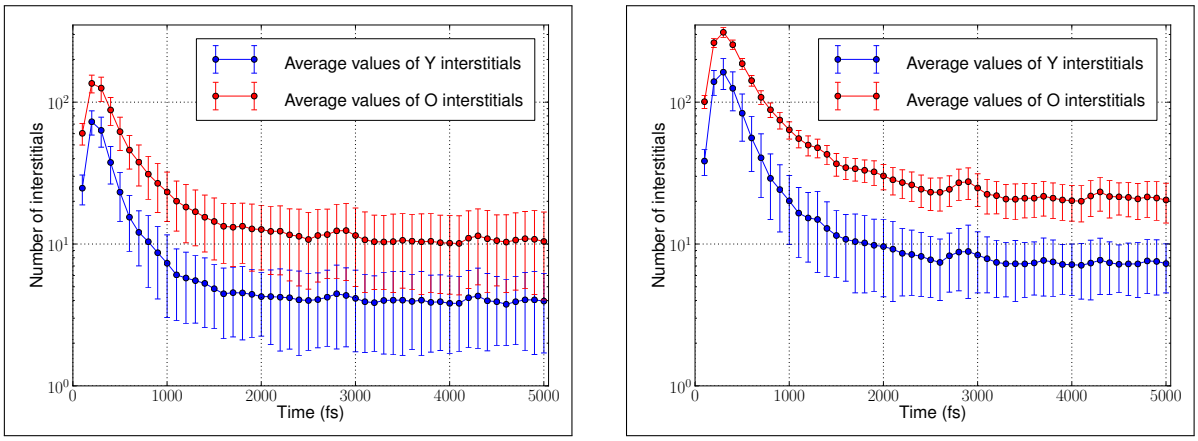

(a) 1 keV Y PKA (b) 2 keV Y PKA

Figure 5.10: The number of interstitial defects in the Y_2O_3 system, during collision cascade simulations at 0K.

By analysing these simulations typical defects after a collision cascade in a Y_2O_3 system can be described. The common defects, especially in low energy collision cascade simulations, are isolated oxygen and yttrium interstitials and their vacancies (Figure 5.11a). The isolated interstitials are often found occupying one of the structural vacancy sites (see Figure 5.1). The other common types in both, low and medium energy cascade simulations, are yttrium split interstitials, sharing an yttrium site, and di-vacancies (Y - O) (Figure 5.11b).

Average number of defects	0.5 keV Y	0.5 keV O	1.0 keV Y	2.0 keV Y
at 0 K				
Y interstitials	2.32	0.90	3.96	7.28
O interstitials	4.98	3.03	10.42	20.44
at 500 K				
Y interstitials	2.30	0.63	3.92	5.84
O interstitials	4.62	2.87	9.04	17.1

Table 5.2: The average number of defects in the Y_2O_3 system at the end of collision cascade simulations (5 ps), averaged over 60 PKA directions.

More complicated defect configurations are also observed in the simulations, as tri-vacancies (Figure 5.11c, with possible combinations of two O and one Y vacancy or vice versa, where two of the same type of vacancies surround the other type of vacancy - Figure 5.11d), and oxygen squares (Figure 5.11c), where two 2NN oxygen atoms swap their positions with two neighbouring structural vacancies.

With an increasing PKA energy more complicated defect clusters are created, especially for non-channelling directions. Typical snapshots of the systems after a 1 keV Y PKA cascade damage are shown in Figure 5.12. As was seen in the 500 eV simulations, two typical behaviours were observed, when the radiation damage is localised (Figure 5.12a) and when the PKA channels through the system (Figure 5.12b). All the simulations are a combination of these two behaviours. In both cases, the initial damage region is rich in vacancies. In the localised damage simulations, other defects tend to be chains of complicated defects configurations with only few isolated defects described previously. As for simulations where the PKA channels through the system, most of the defects are created along the path of the PKA and the displaced atoms and are mostly in the form of isolated defects.

Similarly both behaviours were seen in 2 keV Y PKA simulations, where the localised damage simulation produce even bigger and more complicated defect regions (see Figure 5.13a). Also with the increased energy another behaviour was observed - formation of sub-cascades (see Figure 5.13b). In this case at the beginning of the simulation an yttrium PKA channels through the system until almost a head-on collision with an another yttrium and transfers most of its energy to it. Then the later yttrium atom starts a sub-cascade and

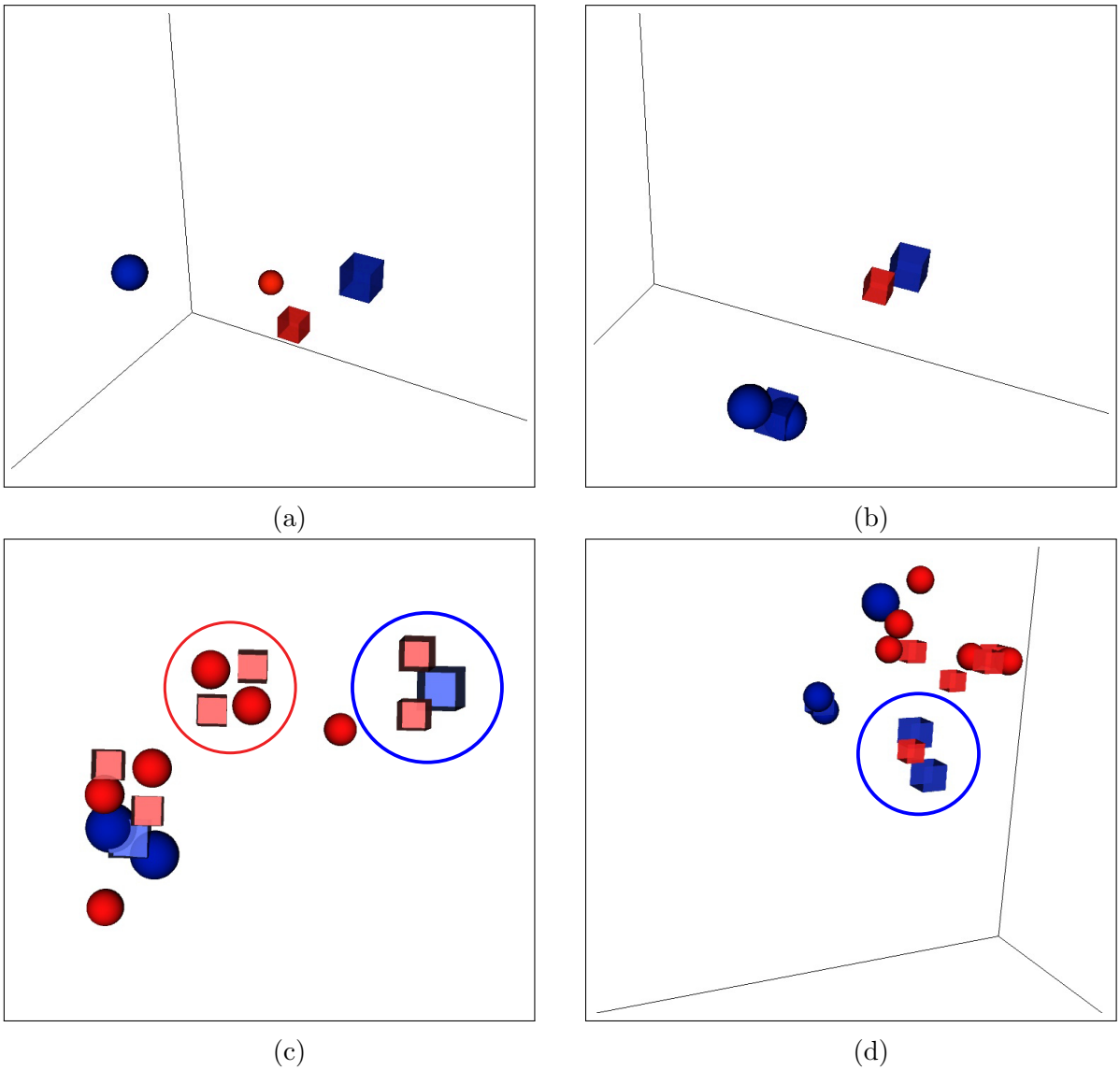

Figure 5.11: Typical defects from 0.5-2 keV collision cascades in a Y_2O_3 system: (a) - isolated oxygen and yttrium interstitials and vacancies occupying one of the tetrahedral structural vacancy sites; (b) - split yttrium interstitial and yttrium-oxygen di-vacancy; (c) - oxygen square - contains of two oxygen interstitials swapped places with two neighbouring structural vacancy sites (red circle), tri-vacancy - containing of a yttrium vacancy and two neighbouring oxygen vacancies (blue circle), (d) - tri-vacancy - containing of an oxygen vacancy and two neighbouring yttrium vacancies (blue circle).

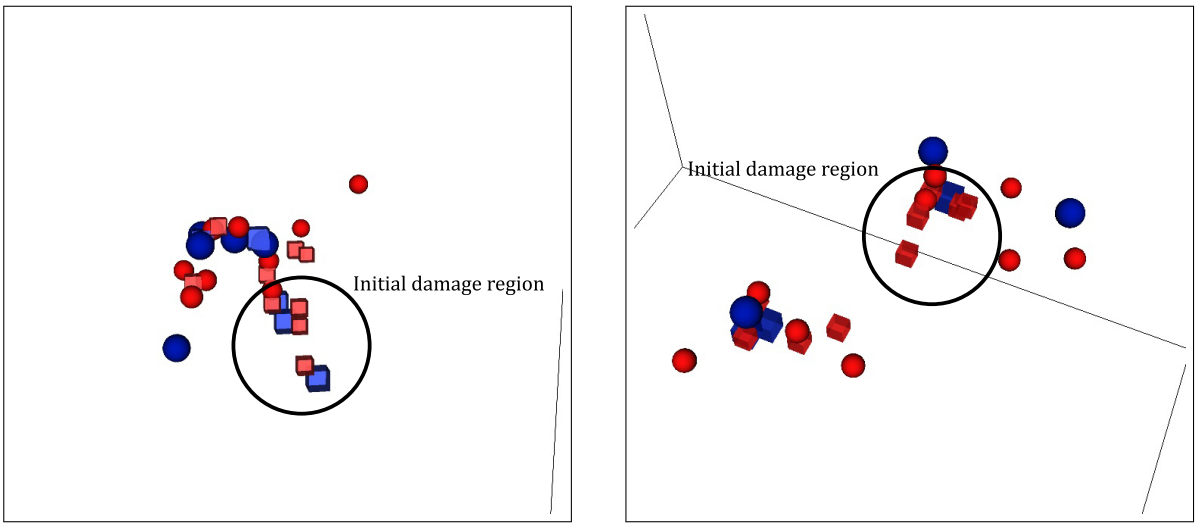

(a) (b)

Figure 5.12: Snapshots of typical cascade outcomes in a Y_2O_3 system with 1 keV Y PKA: (a) - localised defects' spread with complicated defect clusters, (b) - defects' spread in the channelling PKA direction.

creates residual damage in the vicinity of its original position. This behaviour is more likely to appear with a higher PKA energy.

5.3.2 Y_2TiO_5

Similarly, to the simulations in Y_2O_3, the peak damage in the Y_2TiO_5 systems occurs within first few hundred fs and is followed by defect recombination. The summarized data from the collision cascade simulations is given in Table 5.3. The data indicates greater dependency on the temperature than in Y_2O_3 case, especially during the low energy simulations (see Figures 5.14a and 5.14b). Also the bigger the PKA, the more residual damage it creates in terms of the number of defects present in the system at the end of simulation, as shown in Figures 5.14b, 5.14c and 5.14d.

As in the Y_2O_3 simulations, the outcome can be described in a similar manner. When PKA is directed in a channelling direction, it goes deep into the system and creates a few defects along its pathway until it loses kinetic energy and stops creating a local distortion, especially for the oxygen atoms (Figure 5.15a). The other behaviour is when the damage is localised, usually in the vicinity of the PKA. In this cases the number of defects are much

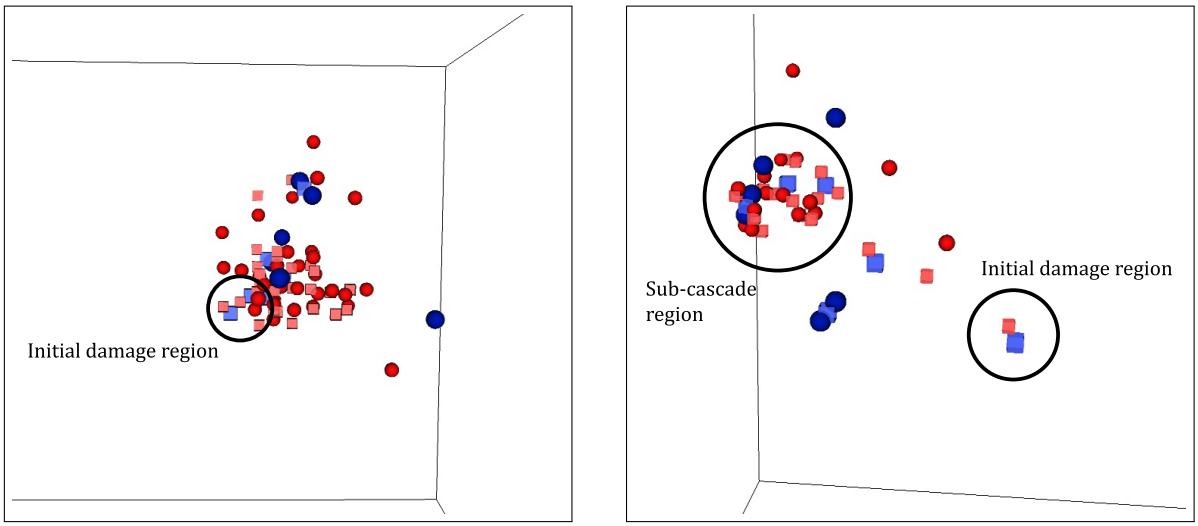

(a) (b)

Figure 5.13: Snapshots of typical cascade outcomes in a Y_2O_3 system with 2 keV Y PKA: (a) - localised defects' spread with complicated defect clusters, (b) - defects' spread in the channelling PKA direction.

Average number of defects	O PKA	Y PKA			Ti PKA		
	0.5 keV	0.5 keV	1.0 keV	2.0 keV	0.5 keV	1.0 keV	2.0 keV
at 0 K							
Y interstitials	0.37	1.86	3.22	6.76	1.12	2.60	4.18
Ti interstitials	0.50	1.68	3.04	7.10	2.16	3.00	5.36
O interstitials	4.90	10.28	18.94	43.92	12.22	19.94	35.5
at 500 K							
Y interstitials	0.32	1.72	3.03	5.18	0.93	2.05	3.27
Ti interstitials	0.25	1.17	3.22	5.5	1.93	2.78	4.33
O interstitials	3.95	7.67	19.65	38.42	11.37	19.17	30.08

Table 5.3: The average number of defects in the Y_2TiO_5 system at the end of collision cascade simulations (5 ps), averaged over 60 PKA directions.

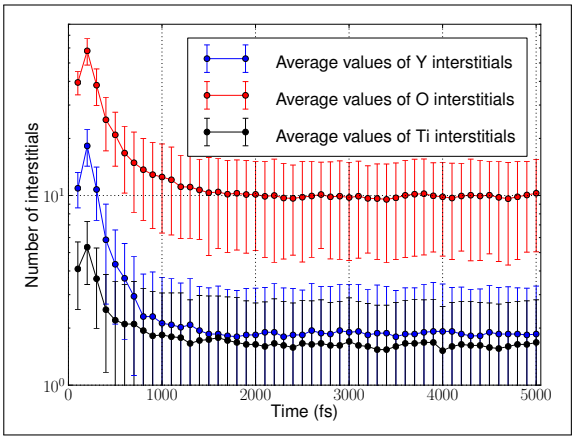

(a) Y PKA at 0K

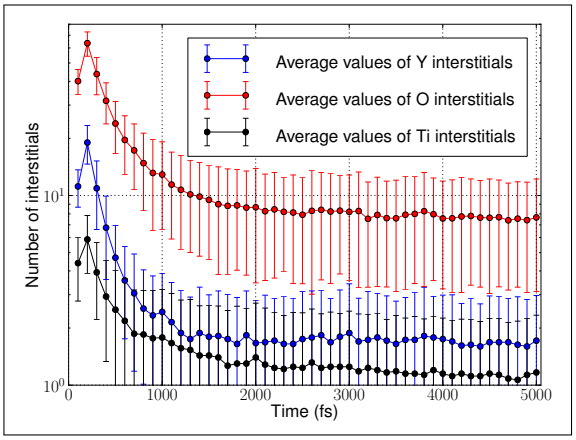

(b) Y PKA at 500K

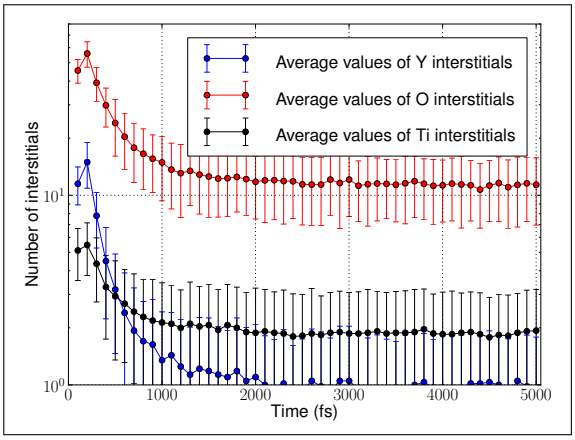

(c) Ti PKA at 500K

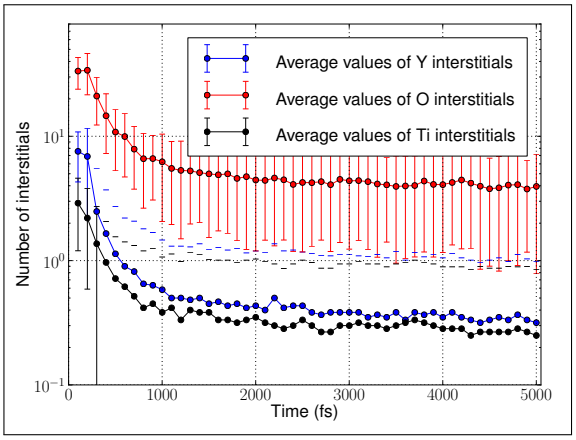

(d) O PKA at 500K

Figure 5.14: The average number of interstitial defects in the Y_2TiO_5 system, during 500 eV collision cascade simulations.

higher due to the bigger distortion in a smaller area (Figure 5.15b).

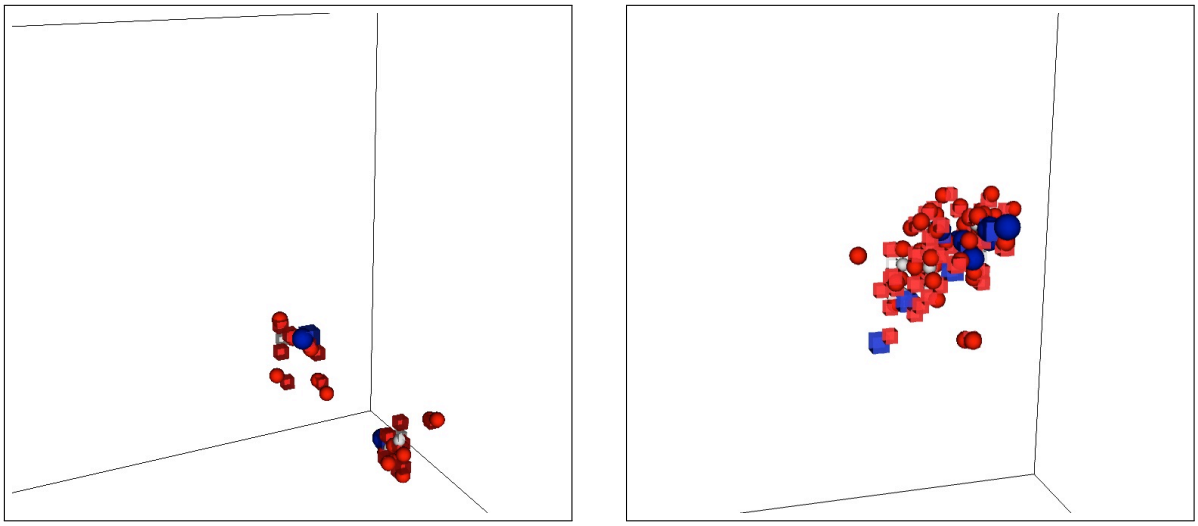

(a) (b)

Figure 5.15: Snapshots of typical cascade outcomes in a Y_2TiO_5 systems during collision cascade simulations at 500K: (a) - channelling 1keV Ti PKA direction creating defects along the path, (b) - localised damage done by 1keV Y PKA.

The most common defects are oxygen interstitials and vacancies; oxygen, yttrium and titanium split interstitials. Other types of defects are usually clusters - distortions with a complicated pattern. In most of the cases, these distortions are seen around interstitial or antisite type defects of yttrium and titanium. An additional atom or an antisite in its vicinity disturbs the local bonds between the metal and oxygen atoms and forces structural changes. In comparison with Y_2O_3 systems, at the end of collision cascade simulation, a Y_2TiO_5 system has a higher total number of defects with lots of lattice distortion around interstitials and vacancies. In contrast, the Y_2O_3 system has structural vacancies where defects prefer to be situated, thus creating less distortion.

5.3.3 $Y_2Ti_2O_7$

The typical outcome of collision cascade simulations in $Y_2Ti_2O_7$, is a heavily distorted region, its size and the level of the distortion depend on the PKA and its energy, as shown in Figure 5.16a. Also a few channelling directions were also seen in the simulations (Figure 5.16b),

but not as common than in the previous two systems.

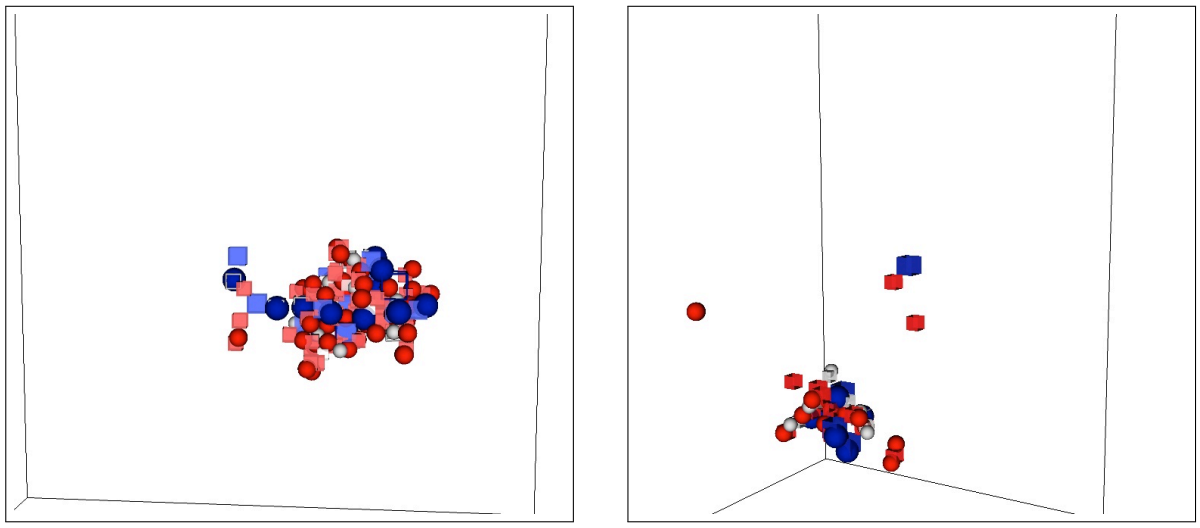

(a) (b)

Figure 5.16: Snapshots of typical cascade outcomes in the $Y_2Ti_2O_7$ systems during collision cascade simulations at 500K: (a) - residual damage created by 1keV Ti PKA, (b) - 1keV Y PKA directed in a channelling direction creating defects along the path.

The results form the collision cascade simulations are summarized in Table 5.4. An even bigger dependency on the temperature can be seen, between simulations done at 0K and at 500K, especially for the medium energy cascades. Compared to the previously analysed systems, Y_2O_3 (Table 5.2) and Y_2TiO_5 (Table 5.3), the average defects number are much greater.

Average number of defects	O PKA	Y PKA			Ti PKA		
	0.5 keV	0.5 keV	1.0 keV	2.0 keV	0.5 keV	1.0 keV	2.0 keV
at 0 K							
Y interstitials	0.77	6.42	31.16	104.88	5.04	22.12	79.24
Ti interstitials	1.98	11.84	43.76	127.58	10.24	32.88	101.04
O interstitials	9.03	40.00	140.08	421.3	34.34	112.04	331.78
at 500 K							
Y interstitials	0.2	1.90	8.75	33.48	1.15	5.5	19.35
Ti interstitials	1.07	4.75	14.58	45.4	4.30	11.47	31.88
O interstitials	4.83	14.45	47.15	150.68	13.65	36.75	100.82

Table 5.4: The average number of defects in the $Y_2Ti_2O_7$ system at the end of collision cascade simulations (5 ps), averaged over 60 PKA directions.

The evolution of the defects numbers may provide hints of the processes that are responsible for the higher defects numbers in the $Y_2Ti_2O_7$ systems. Figure 5.17 represents the

defect evolution, where the damage was create by 2keV Y and Ti PKAs. As in the previous examples, the peak damage occurs within first hundreds of fs, and then starts to gradually decrease due to the recombination processes. In contrast to the other systems, the decrease stops after 1 ps and another smaller peaks appear in the graphs, thus indicating, that the recombination and the structural damage cause rearrangements in the system structure. This reappears a few more times until system stabilizes at the end of the simulation at about 5 ps. This odd behaviour may be an indication that even though the potential was able to recreate the structure of the system, it is not suitable for radiation damage studies in $Y_2Ti_2O_7$ and further development of it is required. Also it is possible that a amorphisation processes is being observed in the pyrochlore structure as it was reported in [125].

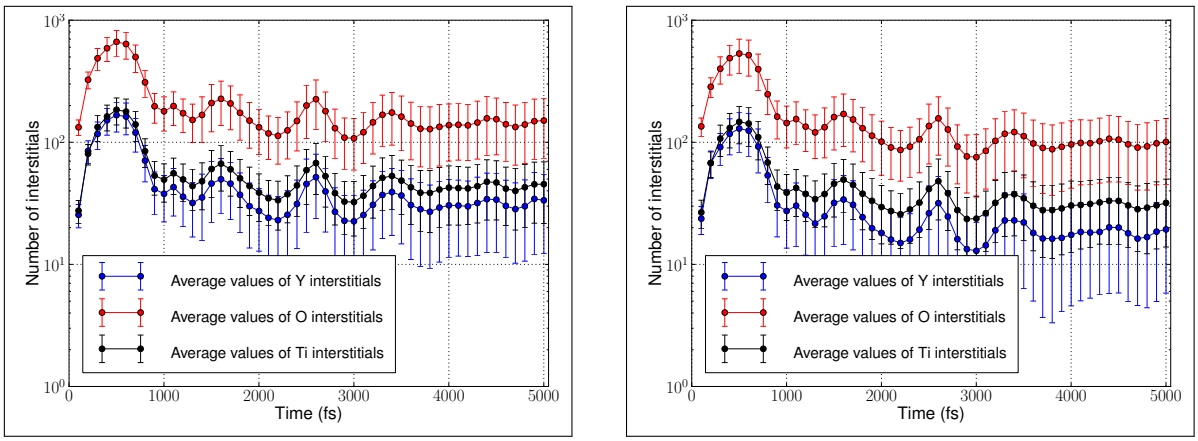

Figure 5.17: The evolution of the number of interstitial defects in $Y_2Ti_2O_7$ systems, during collision cascade simulation at 500K with : (a) - 2 keV Y PKA, (b) - 2 keV Ti PKA.

5.4 Discussion and Conclusions

The radiation damage study in the Y-Ti-O materials showed almost linear dependency between the number of defects and the PKA energies. The peak damage occurs within the first few hundred fs and is followed by the recombination processes. Also a dependency on the atom size was also observed, with the heavier atoms producing more defects and an O PKA's tendency to channel through the system. In all the simulations two types of residual damage

behaviours have been seen: the first, is when the damage is localized in a region, usually close to the initial PKA position; the second - when the PKA is directed in a channelling direction and it goes deeper into the system producing defects on the way. In general at the end of the simulation the number of defects in the second case is lower than in the first one. Y_2TiO_5 and $Y_2Ti_2O_7$ systems showed increased recombination of defects with increased temperature. The remaining defects in the Y_2O_3 systems can be categorized in terms of their point defect configurations, but Y_2TiO_5 and especially $Y_2Ti_2O_7$ tend to have more clustered defects. The highly distorted regions in $Y_2Ti_2O_7$ might be an artifact of the potential or an amorphisation processes in the pyrochlore structure as was reported by [125]. The system models, especially during collision cascade simulations, could be improved by implementing a variable charge model, which allows charge transfer among atoms, and help to understand the observed processes, if they are real or artefacts.

Chapter 6

Long-Time Scale Simulations Applied to Defect Motion in Fe

This chapter presents the results of the otf-KMC technique applied to defect motion in bcc Fe. In the chapter the Vineyard method is used to calculate the prefactor in the Arrhenius equation, rather than assuming a fixed value. The first part of the chapter discusses the influence of the calculated prefactor in detail and is the basis of a recently submitted paper [126].

Then the second part of the chapter describes long time evolution of low energy radiation damage cascades using the otf-KMC technique taking into account the variable prefactor calculations.

6.1 Influence of the Calculated Prefactor

The Arrhenius equation (Equation 3.2.1) is widely used in KMC simulations, but whereas techniques such as the NEB or the Dimer method have been used accurately to determine ΔE, the calculation of the prefactor τ has come under less scrutiny. Therefore, for this thesis, a study was carried out to examine the influence of the calculated prefactor on the long term evolution of radiation damage in α-Fe.

It has become widespread practise to use fixed τ values, usually ranging from 10^{12} to 10^{13}s^{-1}, in such KMC simulations [127, 98, 128, 44], with the assumption that the attempt frequency does not vary greatly. This is because an accurate determination is computationally expensive and 'small' variations in the energy barrier ΔE affect the transition rates much more than "small" variations in τ. However recent work has found that an accurate calculation of the prefactor is necessary in order to include important defect diffusion mechanisms that would not be accessible if a constant value would be used. An example is the formation of a stacking fault tetrahedron in Cu [129].

It is well known that a collision cascade introduces point defects and small interstitial and vacancy clusters into a perfect lattice but in this section typical defects are isolated and their transitions are examined separately. Thus defects, such as DB interstitials, di-interstitials, vacancies and di-vacancies were artificially introduced into the system to investigate their transition rate dependency on the prefactor value independently of their local environment. The defects' configurations and migration pathways are compared those determined in previous works [32, 111, 39].

6.1.1 System

For the simulations an α-Fe system described by the well known Ackland 2004 potential [36] is used containing up to 54,000 atoms with a system size of $30a_0 \times 30a_0 \times 30a_0$, where a_0 is the lattice parameter ($a_0 = 2.855$ Å). The diffusion rates between local minimum states are calculated at 450 K. In some cases, the Mendelev 2003 [35], potential is also used for comparison, but if not stated otherwise the Ackland 2004 potential is used by default.

6.1.2 Performance

In order to understand the relationship between the scaling of the computational time and the convergence of the prefactor value, a series of tests has been performed. To show the tendencies observed, a single vacancy defect system is given as an example. By changing the

radius of the volume of atoms around the defect that are included into the calculation, the convergence of the prefactor value can be tracked by determining the time taken to calculate the eigenvalues of the Hessian. The data is summarised in Table 6.1.

Radius (Å)	Atoms	Prefactor s^{-1}	Eigenvalues calc. time (s)
5.0	14	1.42×10^{13}	6.48
6.0	64	6.14×10^{13}	9.34
8.0	160	8.10×10^{13}	37.85
9.0	174	9.09×10^{13}	45.52
10.0	306	1.00×10^{14}	112.05
11.0	362	1.01×10^{14}	151.63
13.0	640	1.04×10^{14}	404.86
15.0	1042	1.06×10^{14}	1,004.60
17.0	1530	1.06×10^{14}	2,011.03
19.0	2204	1.07×10^{14}	4,063.14
21.0	3034	1.07×10^{14}	7,555.33
23.0	4020	1.07×10^{14}	13,309.30

Table 6.1: Calculated prefactor values as a function of the inclusion radius of the atoms around a vacancy defect, for the isolated vacancy diffusion process on a single core.

In Table 6.1 the first column represents the radius around the vacancy defect, which determines how many atoms will be included in to the calculation; the prefactor values are calculated using Equation 3.5.1 and the time given is only for calculating eigenvalues at the saddle state, since it takes approximately the same amount of time to calculate eigenvalues at the initial state.

As can be seen from the results in Table 6.1, to determine the prefactor to 2 figure accuracy, it requires over 2000 atoms, and in order to reach one significant figure, at least 306 atoms must be included and the calculation of one set of eigenvalues takes around 1/40 of the time. Therefore all the given data in the paper is calculated using a 10 Å radius if it is not stated otherwise. This was regarded as the best compromise between accuracy and computational speed.

6.1.3 Vibrational contributions

From the phonon density of states, vibrational contributions to the energy at finite temperature can be written as [97, 130]:

$$\Delta F_{vib} = \Delta U_{vib} - T\Delta S_{vib}, \tag{6.1.1}$$

where U_{vib} represents the vibrational internal energy and S_{vib} - the vibrational entropy.

When the prefactor is calculated using Equation 3.5.1, it incorporates only the vibrational entropy. In order to see whether the internal energy has an effect on the activation barrier, the expressions of these contributions as a sum of single-oscillation contributions is used written as follows:

$$U_{vib} = \sum_{i=1}^{3N} \left[\frac{\hbar\lambda_i}{e^{\frac{\hbar\lambda_i}{k_B T}} - 1} + \frac{1}{2}\hbar\lambda_i \right], \tag{6.1.2}$$

and

$$S_{vib} = k_B \sum_{i=1}^{3N} \left[\frac{\hbar\lambda_i}{k_B T} \left(e^{\frac{\hbar\lambda_i}{k_B T}} - 1 \right)^{-1} - \ln\left(1 - e^{\frac{-\hbar\lambda_i}{k_B T}} \right) \right], \tag{6.1.3}$$

where $\hbar$ is the Planck constant, λ_i - the eigenvalue of i-th coordinate of the system, k_B - the Boltzmann constant and T is the temperature.

These contributions were calculated for the most common defects and their main migration transitions to check whether the vibrational internal energy has an effect on the activation barrier height. The summarised data is given in Table 6.2. For these calculations a 23.0 Å inclusion radius of atoms around the defect studied is taken to achieve good accuracy when calculating the normal frequencies. The vibrational internal energy's contribution does not change much, even when a smaller inclusion radius is used, such as 9.9 Å.

As can be seen in Table 6.2, the biggest contribution to the barrier height is due to the vibrational entropy which is included when the prefactor is calculated by using the Vineyard

Defect	Migration	Initial state (eV)		Saddle state (eV)		Δ (eV)	
		U_{vib}	TS_{vib}	U_{vib} (eV)	TS_{vib}	U_{vib}	TS_{vib}
$\langle 110 \rangle$ DB	rot.-trans.	481.6656	1574.0375	481.6655	1574.1324	-0.0001	0.0949
$\langle 110 \rangle$ DB	reorient.	481.6656	1574.0375	481.6653	1574.3079	-0.0004	0.2704
VAC	1-NN	468.1563	1529.9442	486.1561	1530.0729	-0.0002	0.1287
I_2^{110}	I_2^{2a}	519.1650	1696.7286	519.1649	1696.8321	-0.0001	0.1035
I_2^{110}	I_2^{110}	519.1650	1696.7286	519.1649	1696.8321	-0.0001	0.1035

Table 6.2: Vibrational contributions to the barrier heights of the most common defects and their prime migration mechanisms. The last two entries represent di-interstitials with the transitions defined in section 6.1.4.2.

equation. The vibrational internal energy's contribution is negligible compared to the barrier heights for all the transitions investigated. Therefore, it can be concluded, that for the vibrational contributions, the Vineyard formula is accurate enough for the calculations.

6.1.4 Study on Isolated Defects

6.1.4.1 Interstitials

The case of interstitial defects and migration pathways is well studied, therefore only a summary will be given here. In the simulations the $\langle 110 \rangle$ DB is the most common configuration occurring in collision cascade simulations, but the $\langle 111 \rangle$ can appear for a short period during the collisional phase of a cascade. This is also confirmed by the experimental findings [131] and the *ab initio* studies [111] on the stability and mobility of interstitials in α-Fe, where studies predict a rapid change from the $\langle 111 \rangle$ to $\langle 110 \rangle$ DB. Therefore, this study is focused on the $\langle 110 \rangle$ DB's migration rates rather than $\langle 111 \rangle$. The data is summarised in Table 6.3. Here and in subsequent calculations the default prefactor value is taken as 1×10^{13} s^{-1}.

Mechanism	Barrier (eV)	Prefactor (s^{-1})	Rate (s^{-1}) (default)	Rate (s^{-1}) (calc.)
Translation-rotation	0.31	1.8×10^{13}	3.0×10^{9}	5.5×10^{9}
$\langle 110 \rangle$ rotation	0.43	7.5×10^{14}	1.5×10^{8}	1.1×10^{10}
$\langle 110 \rangle$ to octahedral	0.69	3.4×10^{13}	1.7×10^{5}	5.9×10^{5}

Table 6.3: The $\langle 110 \rangle$ DB migration rates.

The first and the most common migration mechanism, is the one proposed by Johnson

[32], a combination of translation and rotation. The migration barrier of 0.31 eV is in a very good agreement with the experimental value of ≈ 0.3 eV by [131]. The calculated value of the prefactor 1.8×10^{13} s^{-1} is close to the fixed default value, normally used in KMC simulations and therefore the rate calculated by using this default prefactor is approximately the same order of magnitude as when calculated by using the Vineyard method.

A quite different situation can be seen for the $\langle 110 \rangle$ DB on-site rotation between the $\langle 110 \rangle$ directions represented by the second row in Table 6.3. Here the on-site rotation has a barrier of 0.43 eV with a prefactor value almost two orders of magnitude higher than the default value.

The third case in the table represents the first nearest neighbour (NN) jump with a saddle point near the octahedral configuration with the migration barrier of 0.69 eV. It has very similar default and calculated prefactor values as for the translation and rotation mechanism.

Both migration energy values for the $\langle 110 \rangle$ DB on-site rotation and the 1st NN jump through the tetrahedral configuration are almost equal to those that were calculated by Marinica *et al.* [39] by using the ARTn method to explore the energy landscape.

The two migration pathways from the most stable $\langle 110 \rangle$ DB configuration are the main mechanisms for the mono interstitial migration. Also, the implementation of a slightly different potential energy function [35] in the KMC technique did not have any significant change in barrier heights, rate values or set of possible transitions for the $\langle 110 \rangle$ DB.

By using the default prefactor value, the migration of the $\langle 110 \rangle$ DB is dominated by the translation-rotation mechanism, where the calculated prefactor value moves the on-site rotation transition to the top in the rate table, thus is more likely to be chosen in a KMC simulation.

6.1.4.2 Di-interstitials

The lowest-energy configurations of di-interstitials reported by Marinica *et al.* [39] are studied in order to have a better understanding of migration mechanisms of these common defects

in ballistically affected systems. The Mendelev 2003 and Ackland 2004 potentials give almost the same formation energies where the configuration of two nearest neighbour parallel ⟨110⟩ DBs have the lowest energy. The same notations for the lowest di-interstitial configurations as introduced by Marinica *et al.* will be used from here on. The data for the migration mechanisms of one of the most common di-interstitial configuration $I_2^{<110>}$ is summarised in Table 6.4.

Config.	Barrier (eV)	Prefactor (s^{-1})	Rate (s^{-1}) (default)	Rate (s^{-1}) (calc.)
I_2^{2a}	0.33	1.2×10^{13}	2.0×10^{9}	2.4×10^{9}
$I_2^{<110>}$	0.36	1.4×10^{13}	9.3×10^{8}	1.3×10^{9}
$I_2^{<110>}$	0.49	9.4×10^{12}	3.3×10^{7}	3.1×10^{7}
I_2^{5}	0.48	5.8×10^{13}	4.2×10^{7}	2.4×10^{8}
I_2^{6a}	0.50	3.0×10^{13}	2.5×10^{7}	7.2×10^{7}

Table 6.4: Migration rates of the $I_2^{<110>}$ di-interstitial.

In Table 6.4 only those migration mechanisms from the $I_2^{<110>}$ configuration are presented that have highest rate (default and calculated) values, since for di-interstitials there is usually more than one migration pathway between configurations. In all the cases it can be seen that calculated prefactor value is close to the default value and has a minor effect on the rate table. Only migration to the I_2^5 configuration was found to have a prefactor that differed appreciably, at 5.8×10^{13} s^{-1}, which is five times greater than the default one and brings this migration closer to the migrations to I_2^{2a} and $I_2^{<110>}$ with barrier heights of 0.33 eV and 0.36 eV in terms of the rate values.

Also the most stable di-interstitial configurations were examined that were found by the KMC technique from the other configurations, such as $I_2^{<110>}$, I_2^5, I_2^{6a}. As in the previous example the calculated prefactor does not vary greatly and in most of the cases fluctuates between $0.5 - 5.0 \times 10^{13}$ s^{-1}. One of the more interesting cases was seen for I_2^{2a} diffusion to $I_2^{<110>}$ by two possible pathways with barriers of 0.09 eV and 0.25 eV. Both pathways have very similar rate values (1.1×10^{12} s^{-1}, 1.3×10^{12} s^{-1}) due to the estimated prefactors of 1.1×10^{13} s^{-1} and 8.0×10^{14} s^{-1}, thus making the diffusion even more favourable.

To sum up the behaviour of the di-interstitial migration, it is clear that the $I_2^{<110>}$ configuration dominates with an occasional jump to other configurations, but it is not likely for the atoms to stay in these configurations for a long time and by couple of intermediate configurations will return to $I_2^{<110>}$.

6.1.4.3 Vacancies

The second most common defect after a radiation event is a vacancy. Its migration energy is 0.64 eV and has a minor dip at the midpoint, therefore the migration mechanism has two saddle points as was shown by Johnson [32]. The configuration at the midstate is metastable due to very low energy difference of 0.04 eV. Vacancy migration gives a prefactor of 1.0×10^{14} s^{-1}, an order of magnitude greater than the default value, as is shown in Table 6.5. The higher rate value with the calculated prefactor makes the vacancy - interstitial diffusion ratio change by an order of magnitude compared to the assumption of a fixed prefactor, thus making the vacancy migration more attainable by the KMC algorithm when there are other type of defects with lower barriers and/or higher rate migrations in the simulation box.

Mig. type	Barrier (eV)	Prefactor (s^{-1})	Rate (s^{-1}) (Default)	Rate (s^{-1}) (calc.)
1-NN jump	0.64	1.0×10^{14}	6.42×10^{5}	6.43×10^{6}
2-NN jump	2.61	1.8×10^{14}	5.8×10^{-17}	1.0×10^{-15}

Table 6.5: The migration rates of a vacancy defect.

The di-vacancy migration process is a step-wise process whereby one of the two vacancies moves, by jumping to one of its 1st NN neighbours and the other one follows. The migration has a slight depression at the midpoint as in the previous example. All the observed processes for the di-vacancy defect greatly depend on the initial configuration of two vacancies.

In this work four different di-vacancy configurations were studied where two vacancies are situated by separating them from the first to the fourth NN positions.

As can be seen in Table 6.6, the calculated prefactor does not change the ordering of the rate table and the migration transitions with the lowest barriers, whether the prefactor is

Initial config.	Final config.	Barrier (eV)	Prefactor (s^{-1})	Rate (s^{-1}) (default)	Rate (s^{-1}) (calc.)
1NN	2NN	0.62	1.5×10^{14}	1.1×10^{6}	1.7×10^{7}
1NN	3NN	0.71	3.9×10^{13}	1.1×10^{5}	4.4×10^{5}
1NN	5NN	0.66	1.0×10^{14}	4.1×10^{5}	4.1×10^{6}
2NN	1NN	0.57	3.1×10^{13}	1.1×10^{6}	1.3×10^{7}
2NN	4NN	0.63	1.2×10^{14}	8.8×10^{5}	1.1×10^{7}
3NN	1NN	0.67	6.1×10^{13}	3.1×10^{5}	1.9×10^{6}
3NN	4NN	0.63	1.3×10^{14}	8.8×10^{5}	1.1×10^{7}
3NN	7NN	0.66	1.0×10^{14}	4.1×10^{5}	4.1×10^{6}
4NN	2NN	0.43	1.0×10^{14}	1.5×10^{8}	1.5×10^{9}
4NN	3NN	0.64	8.7×10^{13}	6.8×10^{5}	5.9×10^{6}
4NN	5NN	0.59	1.2×10^{14}	2.5×10^{6}	3.0×10^{7}
4NN	6NN	0.67	7.3×10^{13}	3.1×10^{5}	2.3×10^{6}
4NN	8NN	0.61	1.2×10^{14}	1.5×10^{6}	1.8×10^{7}
4NN	9NN	0.64	1.0×10^{14}	6.8×10^{5}	6.8×10^{6}

Table 6.6: The calculated rates of the most common migration mechanisms of di-vacancy defects.

calculated or the default value is used, have the highest rate. However, in all the cases the calculated prefactor is higher than the default value and in most of the cases by at least one order of magnitude. Table 6.6 also shows that di-vacancy migration is mainly carried out through 1, 2, 4 NN configurations due to the highest rate values.

6.1.5 Verification of the Rate Values

In order to check the estimated rates with the calculated prefactor, a series of tests have been carried out. The same migration mechanisms were reproduced that were seen in the KMC simulations by evolving the systems with MD as follows:

Initially a system that has only one defect at its centre is established, whose migration rates are being studied. Then the system is thermalised up 450 K (the same temperature as used in the KMC) by applying the Berendsen thermostat [79] for 10 ps of simulation time. After that, the system is evolved with regular MD until it crosses a saddle point separating two local energy minima. This moment is captured by checking the dot product of the force vector of the system and the atom separation vector between the current and the initial

(just after thermalisation) states. If the dot product is positive it means that both vectors are pointing to the same direction and the system has crossed the saddle. The time taken for the system to migrate is measured and the new minimum state is found by relaxing the system with the Conjugate Gradient method. Sets of 1,000 such transitions have been carried out for the DB interstitial and the single vacancy cases and 10,000 - for the di-interstitial defects. The results were analysed according to the migration mechanisms seen in the KMC simulations.

For the vacancy defect simulations the temperature was increased to 750 K in order to find transitions using the MD technique, due to the time scales of the migration mechanisms. Then the simulation times were recalculated at 450 K by using Equation 6.1.4 as in the Temperature-Accelerated Dynamics (TAD) [83] method:

$$t_{low} = t_{high} \exp\left(\Delta E \left(\beta_{low} - \beta_{high}\right)\right), \tag{6.1.4}$$

where t_{high} is the actual simulation time at the higher (750 K) temperature and t_{low} is the estimated simulation time at the lower (450 K) temperature, ΔE is the migration energy barrier, and β is equal to $1/(k_B T)$.

The results are compared with the ones from the KMC simulations in terms of the prefactor value. The prefactor value is calculated as follows: the rate R is calculated for a specific migration mechanism by inverting the estimated average simulation time t_{avg} for it to happen multiplied by a number possible pathways N_{paths} and converting the results into seconds:

$$r = \frac{1}{t_{avg} \times N_{paths}} \times 10^{15}. \tag{6.1.5}$$

Then, using this rate value in Equation 3.2.1 with an appropriate ΔE value (calculated using the climbing image NEB technique [93]), the prefactor value τ is being estimated. The results for the interstitial, di-interstitial and vacancy defects are given in Table 6.7.

Migration	Barrier (eV)	MD				KMC	
		%	τ (s^{-1})	r (s^{-1})	%rsd	τ (s^{-1})	r (s^{-1})
$\langle 110 \rangle$ DB							
rot.-trans.	0.31	56%	3.0×10^{13}	1.1×10^{10}	4.1	1.8×10^{13}	6.5×10^{9}
reorient.	0.42	12%	1.0×10^{15}	1.8×10^{10}	8.2	7.5×10^{14}	1.3×10^{10}
$I_2^{\langle 110 \rangle}$							
I_2^{2a}	0.32	47%	2.6×10^{13}	7.2×10^{9}	1.3	1.2×10^{13}	3.2×10^{9}
$I_2^{<110>}$	0.32	16%	3.5×10^{13}	9.8×10^{9}	2.9	1.4×10^{13}	3.9×10^{9}
VAC							
1-NN	0.62	66%	2.9×10^{13}	3.4×10^{6}	6.3	1.0×10^{14}	1.2×10^{7}

Table 6.7: Comparison of the rate and prefactor values for the common defects and their main migration pathways between MD and KMC simulations, where the migration barriers were estimated using the NEB method. In column %, the percentage occurrence of the particular mechanism is shown with respect to the total number of simulations and in column %rsd, the percentage of the relative standard error of the estimated value is measured.

In Table 6.7 the data is given only for the most common defect migration mechanisms. For example for the $\langle 110 \rangle$ DB MD results, the left 32% account for the migration mechanisms to octahedral and tetrahedral sites (3.5%) and for migration pathways which have higher migration barriers ending up in a metastable slightly tilted $\langle 111 \rangle$ configuration (28.5%). Neither MD nor KMC simulations were able to find all the migration pathways to symmetrically equivalent octahedral and tetrahedral configurations from the given initial $\langle 110 \rangle$ DB state, thus these results were excluded from the table. Nonetheless, the unaccounted migration configurations have a minor influence of the results since their barrier heights are usually high. For the similar reasons the $I_2^{\langle 110 \rangle}$ and VAC comparisons were also carried out only for the most common migration mechanisms.

Results show that there is a reasonable agreement between the MD and KMC techniques and the estimated prefactor by the Vineyard method is a good approximation for the one that was determined from the MD simulations. For the $< 110 >$ DB and $I_2^{<110>}$ defects, a difference can be seen in the prefactor values for all the migration mechanisms. This may occur, because it is possible for the system to return to the same local energy minimum, even if the saddle state was crossed, where in these simulations it is not allowed. In this way the average simulation time maybe slightly shorter, thus giving a higher prefactor value for the migration mechanisms. The same conclusion can be applied for the 1-NN jump

migration by a vacancy only partially, since the difference between the prefactor values is also caused by the higher (750 K) temperature at which simulations were carried out and where the harmonic approximation breaks down. To estimate the level of the error additional simulations for the $< 110 >$ DB at 550 and 650 K temperatures (see Table 6.8) were carried out to check the prefactor values for both most common migrations recalculated at 450 K. It can be clearly seen, that for the higher temperature, the prefactor values, recalculated at the lower temperature, are underestimated, thus the MD results for the vacancy defect are also likely to be underestimated.

T_{high} (K)	Prefactor value (s^{-1}) at T_{low} for	
	rotation-translation	reorientation
450	3.0×10^{13}	1.0×10^{15}
550	2.5×10^{13}	5.1×10^{14}
650	1.8×10^{13}	2.3×10^{14}

Table 6.8: [110] The DB migration prefactor values calculated at $T_{low} = 450$ K.

6.1.6 Influence of the Prefactor During Long-Time Scale Simulations of Collision Cascade Evolution

In order to investigate, how an accurate determination of the prefactor may influence otf-KMC simulations, simulations on defect configurations that were initially produced by a radiation event were completed. 66, 1 keV cascades were carried out in the same way as described in 4.2.1. Of these, 10 representative cases were chosen and further evolved by otf-KMC using the default and calculated prefactors. The cases were chosen in such a manner, that they would represent different defect configurations and distributions in the system in order to provide a good insight of the processes.

Usually, the outcome of a collision cascade simulation consists of a vacancy rich region close to the initial PKA site surrounded by outlying interstitials. The comparison of the behaviour of the defects has been done with further studies on the effects on the whole system in terms of energetics and defect numbers.

Due to the low barrier of the migration processes of the ⟨110⟩ DB, it dominates the initial phase of the simulations, but the migration mechanism is different between the default and calculated prefactor cases. Simulations with the default prefactor are driven by the rotation-translation of ⟨110⟩ DBs, where the calculated case switches between reorientation, which has a higher rate value, and the rotation-translation mechanisms. Therefore, in the simulations with the default prefactor, ⟨110⟩ DBs tend to explore the system more, whereas in the other case the ⟨110⟩ is not as mobile. In the first case, it is more likely that ⟨110⟩ DB will find another defect to recombine or to cluster faster by exploring the system, whereas in the second case, if there are other defects in the vicinity of the ⟨110⟩ DB, through reorientation, the DB is more likely to position itself in a direction towards the defects before migration towards them.

A clear effect of the accurately determined prefactor can also be seen for the vacancy type defects. With the default prefactor used in the simulations, vacancy defect migrations are observed quite rarely, only several in couple of thousand KMC steps, if mobile interstitials are present in the system as well. With the calculated prefactor, vacancy defect jumps appear more often, due to the higher rate values. Thus, vacancies tend to cluster and rearrange in to highly symmetrical configurations (Figure 6.1) compared to using the default value. On average, the simulation time for a vacancy type defect to migrate with calculated prefactor is $\approx 3 \times 10^{-9}$s, where the time with default value is almost an order of magnitude, longer $\approx 4 \times 10^{-8}$s. These values were calculated from the evolution of 8 systems, evolved for more than 1,000 KMC steps with calculated and default prefactors.

By counting the number of chosen transitions with a prefactor value that is $\leq 10^{12}\text{s}^{-1}$ or $\geq 10^{14}\text{s}^{-1}$ against the total number of KMC steps within a simulation, it can be checked, if the processes that drive the KMC simulation depend on the calculation of the prefactor. In 9 simulations that were carried out for at least 1,000 KMC steps, on average, over 50% of the migration jumps had a prefactor value which is $\leq 10^{12}\text{s}^{-1}$ or $\geq 10^{14}\text{s}^{-1}$. In the cases where systems contain widely separated ⟨110⟩ DBs and vacancies, the percentage of chosen

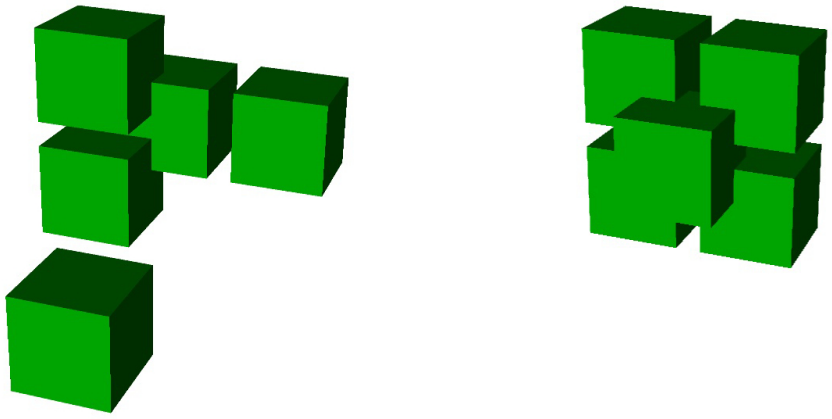

(a) Initial (b) Cluster

Figure 6.1: Clustering of 5 vacancies. a) Initial distribution of vacancies, post-cascade configuration, b) High symmetry 5 vacancy cluster after 75 KMC steps.

migrations affected by the calculation of prefactors is quite high $\approx 70\%$, where in the cases with di-, tri-interstitials, it is the opposite with the percentage $\approx 30\%$.

It was observed that accurate prefactor calculations also slightly influence the recombination of defects. If an interstitial type defect lies a few NN away from a vacancy type defect, these two are more likely to recombine with the exact prefactor. To investigate this situation further, a vacancy and $\langle 110 \rangle$ DB were initially created in defect-free system by changing the separation between them and evolving these system using otf-KMC. The cases of 1NN and 2NN separation are quite straightforward, where the recombination transitions have the lowest barriers and highest rates. The 3NN separation case is where the calculated prefactor does have an effect on the rate table. The lowest barrier (0.29 eV) transitions are jumps to 4NN separation configurations with a 1.9×10^{10} s^{-1} rate value, whereas a recombination transition with a slightly higher barrier of 0.36 eV has an order of magnitude higher rate value 2.7×10^{11} s^{-1} with a prefactor of 3.1×10^{15} s^{-1}, thus making this recombination more favourable. When a vacancy and a $\langle 110 \rangle$ DB defect are initially separated by the 4NN distance, recombination occurs as quickly as in the 1NN and 2NN cases, due to a low barrier (0.215 eV) transition. The 5NN case is very similar to the 3 NN case; the lowest transitions with a barrier of 0.25 eV and a rate value of 2.2×10^{10} s^{-1}, are jumps to the

4NN configuration and a slightly higher barrier (0.33 eV) recombination transition has an order of magnitude higher rate value of 1.5×10^{11} s^{-1} and is thus preferred. In the bigger separation cases, 6NN and more, the prefactor influence was not sufficient to influence the recombination processes.

Calculation of the prefactor has an influence on the bigger defect clusters too. One of the cases observed is the four DB cluster (Figure 6.2 (a)). In this case a few different transitions were found for this cluster to re-configure with barriers ranging between 0.1-0.2 eV. The calculated prefactors are at least one order of magnitude lower than a default value, e.g. to reconfigure from Figure 6.2 (a) to Figure 6.2 (b), a barrier of 0.1 eV must be crossed with 1.8×10^{11} s^{-1} prefactor which leads to a rate value of 1.2×10^{10} s^{-1}. The calculated prefactor puts this transition on the same time scale with smaller interstitial defects, and will not dominate the rate table, as it would, if the default value were to be used.

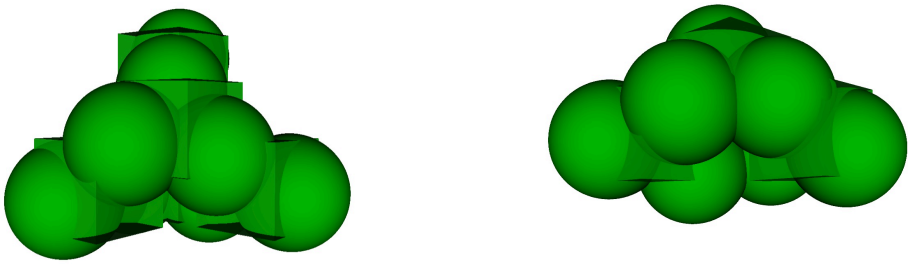

(a) Initial (b) Reconfigured

Figure 6.2: The interstitial cluster formed of 4 DBs. a) Initial, post-cascade configuration, b) The reconfigured structure after crossing a 0.1 eV barrier.

Another configuration of the four DB cluster demonstrates an example of the prefactor influencing defect recombination. In this case four DBs are located in 1st NN positions and aligned in a slightly tilted ⟨111⟩ configuration (Figure 6.3 (a)). In this case, the defect cluster's centre of mass (com) is approximately 15 Å away from the four vancancy cluster's com (Figure 6.3 (b)). The migration transitions for this interstitial cluster along the ⟨111⟩ direction have barrier heights ranging from 0.20 to 0.30 eV with the prefactor values varying from 1.0×10^{14} s^{-1} to 5.0×10^{18} s^{-1}. The higher prefactor values are estimated when migration

is happening towards the vacancy cluster, making this migration process more accessible by the KMC technique and after a couple hundreds of KMC steps these two clusters recombine.

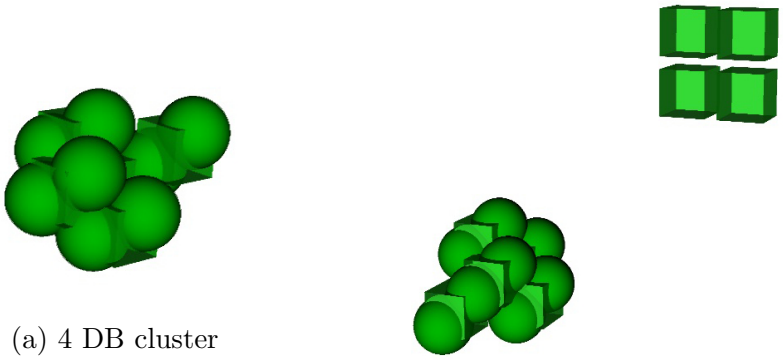

(a) 4 DB cluster

(b) DBs and Vacs clusters

Figure 6.3: A highly mobile split interstitial cluster, (a) containing four slightly tilted ⟨111⟩ DBs in 1st NN positions, (b) the DBs cluster in the vicinity of four vacancies cluster.

6.2 Long-Time Scale Simulations in bcc Fe

6.2.1 Systems and Modelling Technique

Bcc structured iron systems containing 54,000 atoms have been studied using a hybrid MD - otf-KMC technique in this way: first, all the initially created systems are thermalized up to 500 K. Then radiation damage was introduced by using the same technique described in section 4.2.1, where an irreducible symmetry region is sampled over 66 directions with 1 keV PKA. By analysing the systems after the ballistic phase, a set of them were picked to have a good representation that combines different defect formations and spreads. Finally, the systems were evolved using the previously described otf-KMC technique. Two interatomic potentials were incorporated to describe the interactions between iron atoms: the Mendelev 2003 [35] and Ackland 2004 [36], and produced very similar results.

6.2.2 Radiation Damage Simulations

Simulations were carried out with the default and the calculated prefactors using both, the Mendelev 2003 and Ackland 2004 potentials - 4 sets in total. Different criteria were used to determine when the simulations should be stopped; such as the number of defects, the achieved simulation time, the number of KMC steps and visual interpretation of the results. The summarised data of the times achieved and the number of KMC steps are given in Tables 6.9 and 6.10.

Direction	Default prefactor		Calculated prefactor	
	No of steps	Sim. time (s)	No of steps	Sim. time (s)
1.0 0.1 0.0	657	6.42E-09	-	-
1.0 0.3 0.0	534	5.89E-09	-	-
1.0 0.3 0.1	6777	1.44E-06	1166	1.27E-08
1.0 0.3 0.2	2088	1.86E-08	2547	1.89E-08
1.0 0.4 0.1	-	-	1103	5.93E-09
1.0 0.4 0.4	1671	1.15E-08	-	-
1.0 0.5 0.5	9373	1.64E-07	1000	3.59E-09
1.0 0.6 0.0	2045	2.32E-08	1641	5.82E-09
1.0 0.6 0.1	627	7.55E-09	-	-
1.0 0.7 0.5	742	3.92E-08	-	-
1.0 0.7 0.7	7069	6.52E-07	1712	5.37E-08
1.0 0.8 0.2	3793	1.01E-05	1324	5.06E-08
1.0 0.8 0.6	4145	7.35E-08	1747	5.37E-09
1.0 0.9 0.6	2058	2.68E-08	1416	1.39E-09

Table 6.9: Summary of the simulations carried out using the Mendelev 2003 potential. The direction column describes the initial direction of the PKA used in the ballistic phase of the radiation event, where the initial velocities of the PKA are resolved until components in the (x,y,z) directions in the same ratio as given in the direction column.

The objective of these simulations was not to achieve the longest simulation time, but to try to investigate the behaviour of the common defects on the longer time scales than MD. In most of the cases simulations were carried out until the final outcome can be predicted. For example, by evolving system with the Mendelev 2003 potential with the default prefactor, which was initially effected by 1 keV PKA directed in [1.0 0.5 0.5] (Figure 6.4a) for almost 10,000 KMC steps, only a 3 DBs cluster, a di-vacancy and a vacancy remained and the processes that occur while having just few defects with a wide spread were observed.

Direction	Default prefactor		Calculated prefactor	
	No of steps	Sim. time (s)	No of steps	Sim. time (s)
1.0 0.2 0.0	213	5.52E-10	489	9.52E-10
1.0 0.3 0.0	583	2.00E-08	141	5.33E-10
1.0 0.4 0.2	3302	1.18E-07	2854	1.27E-08
1.0 0.5 0.1	682	1.63E-08	825	3.25E-09
1.0 0.9 0.4	1681	1.96E-07	1522	8.65E-08
1.0 0.9 0.7	993	4.73E-08	1683	9.28E-09
1.0 1.0 0.2	636	1.14E-09	722	4.50E-09
1.0 1.0 0.6	486	4.49E-10	1862	1.07E-07

Table 6.10: Summary of the simulations carried out using the Ackland 2004 potential. The direction column describes the initial direction of the PKA atom used in the ballistic phase of the radiation event.

In such cases, during the first few hundred KMC steps, defects that are close tend to recombine. In the mentioned simulation, within the first three hundred steps (0.27 ns) a mobile three split interstitial cluster recombined with a vacancy cluster (Figure 6.4b). Then follows the stage when isolated defects explore the area around them and further recombination and/or clustering can be seen. In the given example during the next 1,500 steps ($\approx$ 17 ns), three split interstitials, that were in close proximity clustered into a very mobile tri-DB cluster (Figure 6.4c). After that, a system's exploration and defect reconfiguration stage takes place. When small defects are widely spread, evolution occurs only by defect exploring the system. In practice, this means that those defects in the bulk materials would segregate on the grain boundaries or precipitates, recombine, or be affected by the next collision event, thus the evolving of such systems is not continued. As for the examined simulation, the next 7,500 steps ($\approx$ 0.16 μs) are spent by the tri-DB exploring the system (Figure 6.4d) and reconfiguring.

Another interesting behaviour was observed in a couple of cases. When most of the defects recombine and the system is left only with few defects, e.g. a vacancy cluster and a cluster containing several split interstitials, the more mobile defect, the interstitial cluster would usually migrate through the system and rearrange its configuration. By going through a lot of rearranging it may jump into such a configuration that requires it to cross a fairly high barrier, thus advancing the simulation clock by a greater amount than usual. An

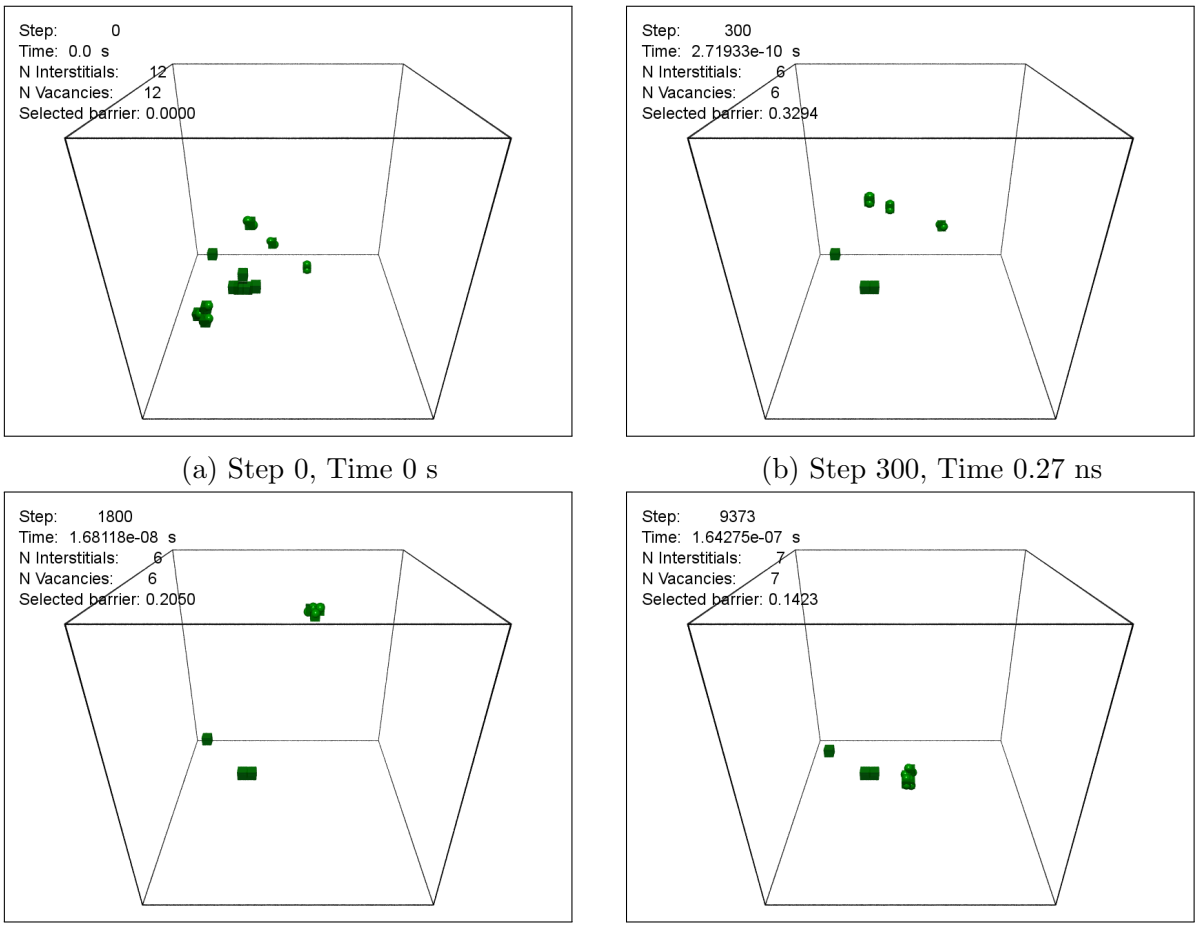

(a) Step 0, Time 0 s

(b) Step 300, Time 0.27 ns

(c) Step 1800, Time 17 ns

(d) Step 9373, Time 0.16 μs

Figure 6.4: Snapshots of defects evolution (lattice atoms not shown) after 1 keV collision cascade directed in [1.0 0.5 0.5] where the system is described by the Mendelev 2003 potential.

example of such process is given in Figure 6.5, where a very mobile cluster containing five split interstitials reconfigures by jumping over a barrier of almost 0.7 eV, thus allowing further evolution through a more energetically favourable cluster configuration. The cluster, before undergoing this reconfiguration, migrates and reconfigures for a couple thousand of steps with fairly low barriers.

By studying all the simulations, not only the final outcome, but also the intermediate processes are important to be understood. Therefore in the following two sections defect recombination and migration processes will be discussed in more detail.

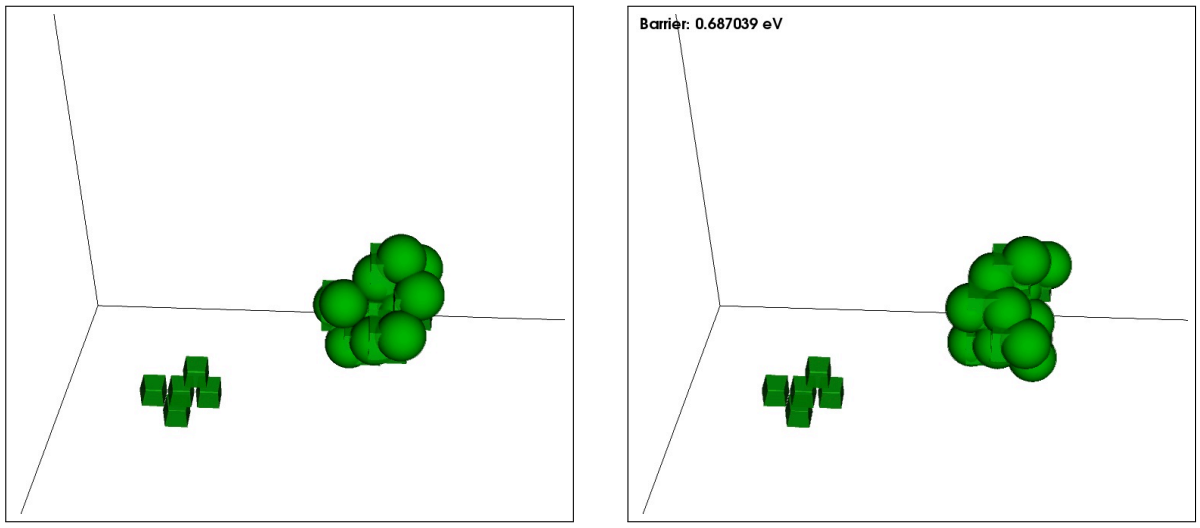

(a) (b)

Figure 6.5: Snapshots of a five interstitial cluster evolution described by the Mendelev 2003 potential. The cluster reconfigures to a more energetically favourable configuration by jumping over a 0.68 eV barrier.

6.2.2.1 Recombination Between Interstitial and Vacancy Type Defects

Recombination processes play a great role during the evolution of the system after a ballistic event and a large number of them were observed in the studied systems. Usually recombination occurred, when an interstitial type defect positioned itself in a specific configuration with respect to a vacancy type defect. Therefore, additional tests were carried out with an isolated split interstitial and a vacancy defects in order to determine how the distance between these two defects and the orientation of the split-interstitial effect the recombination process.

The tests were carried by changing the distance between the defects up to 10NN (≈ 7.5Å) and positioning the split interstitial in the $\langle 110 \rangle$ symmetries. The results given here were achieved with the Mendelev 2003 potential.

The results show that some configurations may recombine during the equilibration of the system. Such example is given in Figure 6.6, where initially the $\langle 110 \rangle$ DB is positioned in the 3NN location. They instantly recombine when the system is equilibrated through the translation-rotation mechanism to the 1NN. Similar recombinations where seen up to 5NN, except 4NN, and the detailed information is given in Table 6.11.

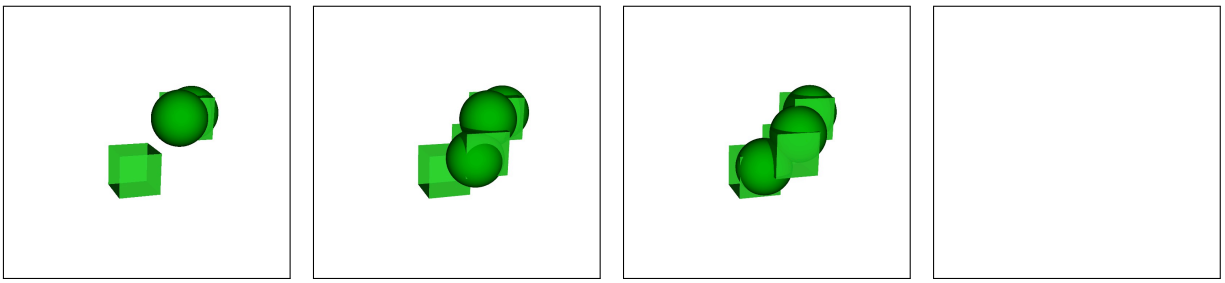

(a) (b) (c) (d)

Figure 6.6: Recombination stages of a DB positioned 3NN (≈ 4.1Å) away from a vacancy during the system relaxation (equilibration).

NN	Geometry	Approx. distance (Å)	Recomb. DB symmetries
1	[0.5,0.5,0.5]	2.5	$\langle 1,1,0\rangle, \langle 0,1,1\rangle, \langle 1,0,1\rangle$
2	[1,0,0]	2.8	$\langle 1,1,0\rangle, \langle 1,\overline{1},0\rangle, \langle 1,0,1\rangle, \langle 1,0,\overline{1}\rangle$
3	[1,1,0]	4.1	$\langle 0,1,1\rangle, \langle 0,1,\overline{1}\rangle, \langle 1,0,1\rangle, \langle 1,0,\overline{1}\rangle$
5	[1,1,1]	5.0	$\langle 1,1,0\rangle, \langle 0,1,1\rangle, \langle 1,0,1\rangle$

Table 6.11: DB symmetries with respect to the separation between the DB and the vacancy which recombine during the system relaxation. The column geometry represents the separation vector between the defects in lattice units.

In the cases (1-5 NN) when the immediate recombination did not occur, usually there were transitions with low migration barriers for the recombination processes. For example such mechanisms were seen with barriers as low as 0.050 eV, 0.125 eV, 0.209 eV for 1NN, 2NN, 3NN and 4NN cases accordingly. In Figure 6.7 an example is given of the recombination process for the 1NN case, with the recombination process visualised in terms of the defect movement and the MEP.

The other common process is when one of the defects migrates, by the translation-rotation mechanism, if it is a DB, or jumping to its 1NN, if it is a vacancy, to a special configuration from where the recombination is almost instantaneous. Usually these migrations have a slightly lower barrier height or a higher prefactor then usual, thus making them more preferable by the KMC technique. An example of such process is given in Figure 6.8 where initially defects are separated by 7NN. Then the DB by a consecutive migration through a 5 NN position recombines with the vacancy. The migration barrier is very similar to the regular translation-rotation mechanism (≈ 0.3 eV), but the prefactor is greater by an order

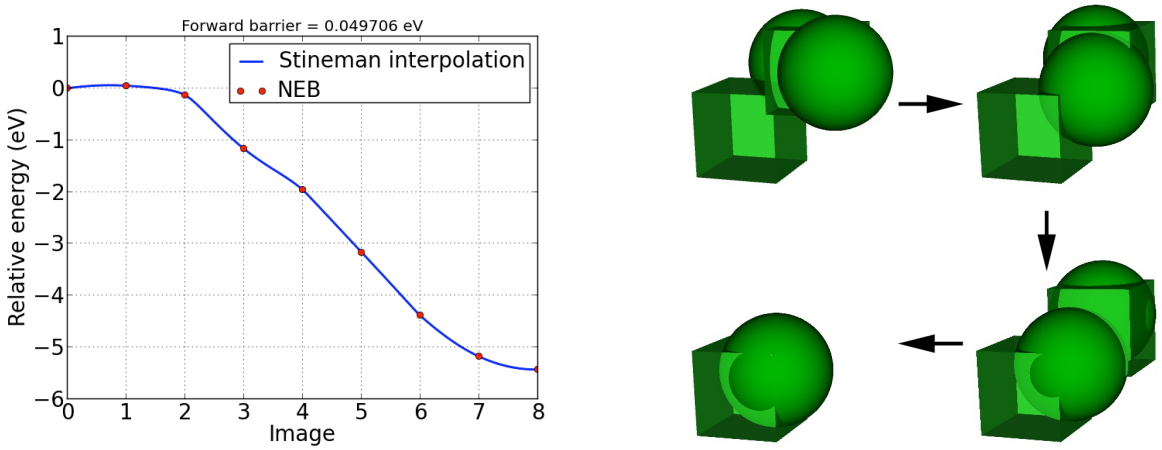

(a) (b)

Figure 6.7: Recombination of a DB and a vacancy separated by 1NN with a very low migration barrier (0.050 eV). (a) - the MEP of the transition calculated using the CI-NEB, (b) - the recombination process.

of magnitude and is equal to $\approx 2.9 \times 10^{14} \mathrm{s}^{-1}$.

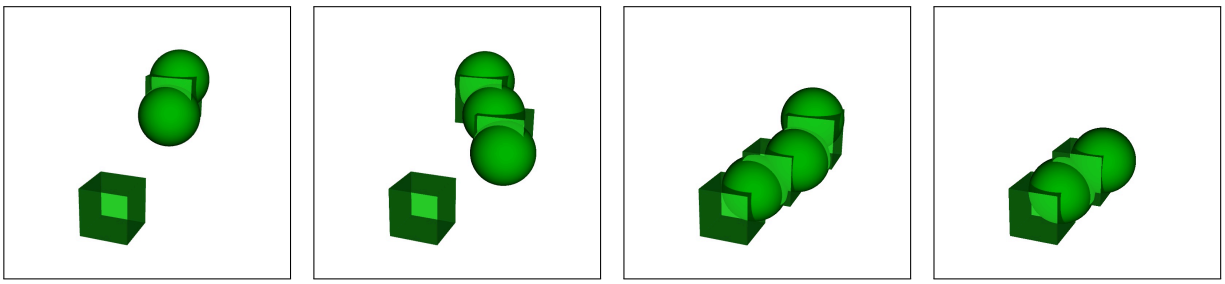

(a) (b) (c) (d)

Figure 6.8: Recombination of a DB and a vacancy separated by 7NN by going through a 5NN position.

Similarly, recombinations were observed with bigger split-interstitial clusters, containing 2-4 DBs. In general, defects tend to recombine if they are in the vicinity of each other, thus the initial debris after the ballistic damage plays a great role on how the system will evolve. If the damage spread is quite low, rapid recombination will occur, otherwise it is likely that bigger and stable defect clusters will form. Another important factor during the defect recombination is the mobility of defects. Mobile defects can find other defects to recombine or find a similar type defects to form even bigger cluster by exploring the system, as discussed in the next section.

6.2.2.2 Mobility of Defects and Defect Clusters

Split interstitials and clusters of 2 split interstitials are the most common defects in the systems after a ballistic event that are very mobile. Split interstitials explore the system through the rotation and rotation-translation mechanisms, where 2 split interstitial clusters by the Johnson mechanism [32], where one of the split interstitials jumps (rotation-translation) to its nearest neighbour position and the second one follows it or both of them jump together. Sessile 2 split interstitial clusters were also seen in the simulations as reported by Gao [132], but they were able to escape such configurations, by jumping over slightly higher barriers as usual.

3 split interstitial clusters were seen as fairly stable, but they tend to rearrange with low barriers as 0.1 eV, as has been reported by Marinica *et al.* [39]. It was shown in section 6.1 that calculated prefactors have a great influence on the rate values of such transitions.

4 split interstitial clusters depending on their configuration maybe very mobile and also quite stable as it was given in examples in section 6.1. The mobile clusters consists of 4 $\langle 111 \rangle$ DBs and glide in the $\langle 111 \rangle$ direction with low barriers ranging from 0.20 to 0.30 eV.

In the 1 keV simulations the biggest interstitial cluster observed was formed of 5 split interstitials and it has been seen only in one simulation. In other cases, defects were fairly quick to recombine or the smaller clusters dissipated in to the systems away from the centre of the initial damage volume.

Vacancy type defects are many times less mobile than interstitial type defects. This is due to the much higher migration barriers of their transitions. Previously in section 6.1 it was shown that by calculating prefactors for the transitions, vacancy migration mechanisms have a higher rate, but still the difference is very significant. Therefore, vacancy migration is not common during the simulations. It was seen by analyzing the data from simulations in Tables 6.5 and 6.6, that a 2 vacancies cluster is more mobile than a single vacancy. The preferable configuration of the 2 vacancy cluster is when the vacancies are separated by 1NN or 2NN and migration is carried out by one of the vacancies jumping to its 1NN and the

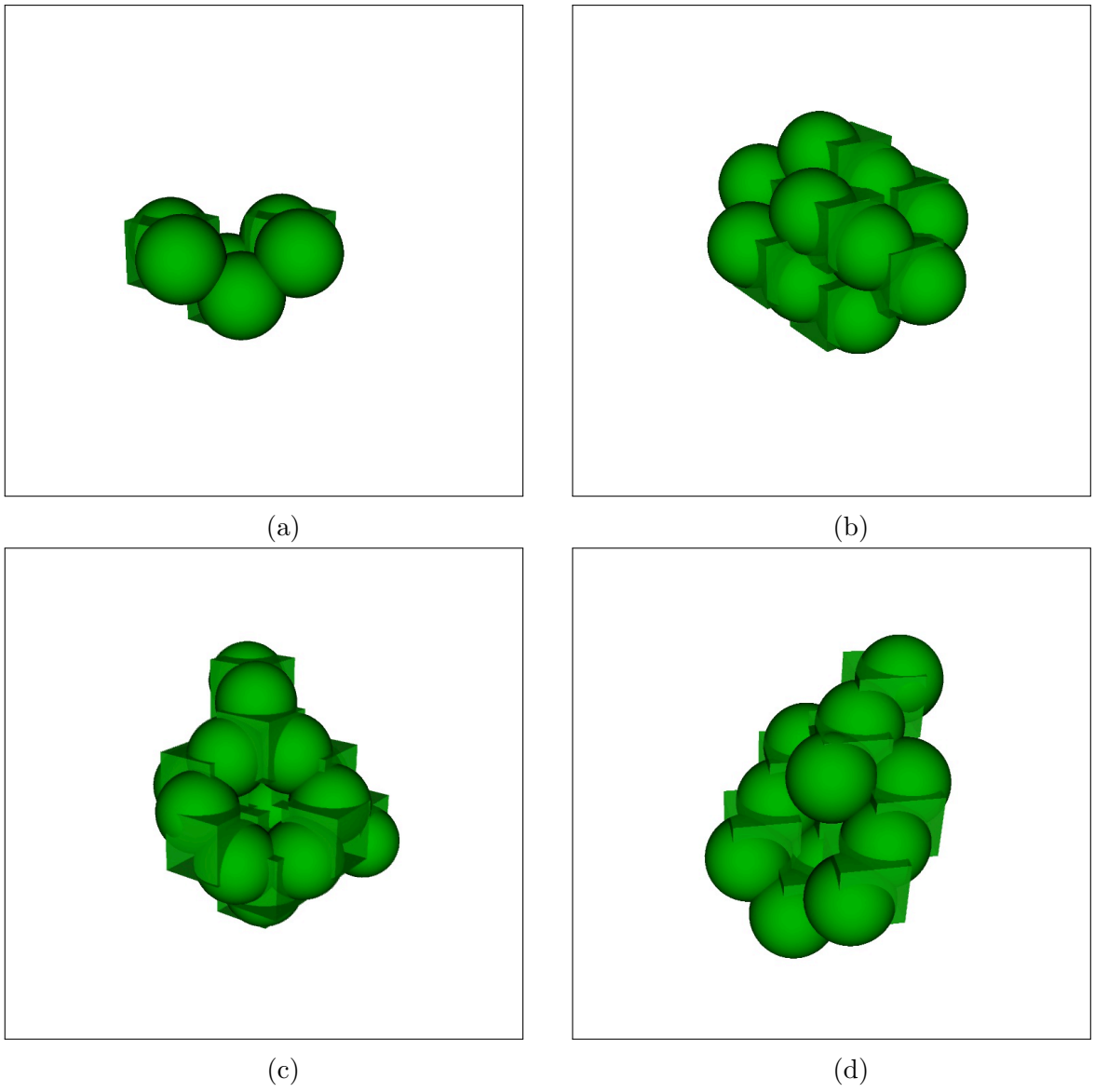

Figure 6.9: Split interstitial clusters: (a) - stable 3 split interstitial cluster, (b) - mobile 3 split interstitial cluster, (c) - stable 4 split interstitial cluster, (d) - mobile 4 split interstitial cluster. For (a), (b) - Ackland 04 and for (c), (d) - Mendelev 03 potentials used.

second one following it.

The three vacancies cluster migrates through two configurations. The first one is when one vacancy has the other two vacancies in its 2NN positions and both of them are situated at 3NN with respect to each other (Figure 6.10a). The second one consists of two vacancies sitting at 2NN positions and the third one being at 1NN with respect to both of them (Figure 6.10b). An example of the 3 vacancies cluster migrating through these two configuration is given in Figure 6.10.

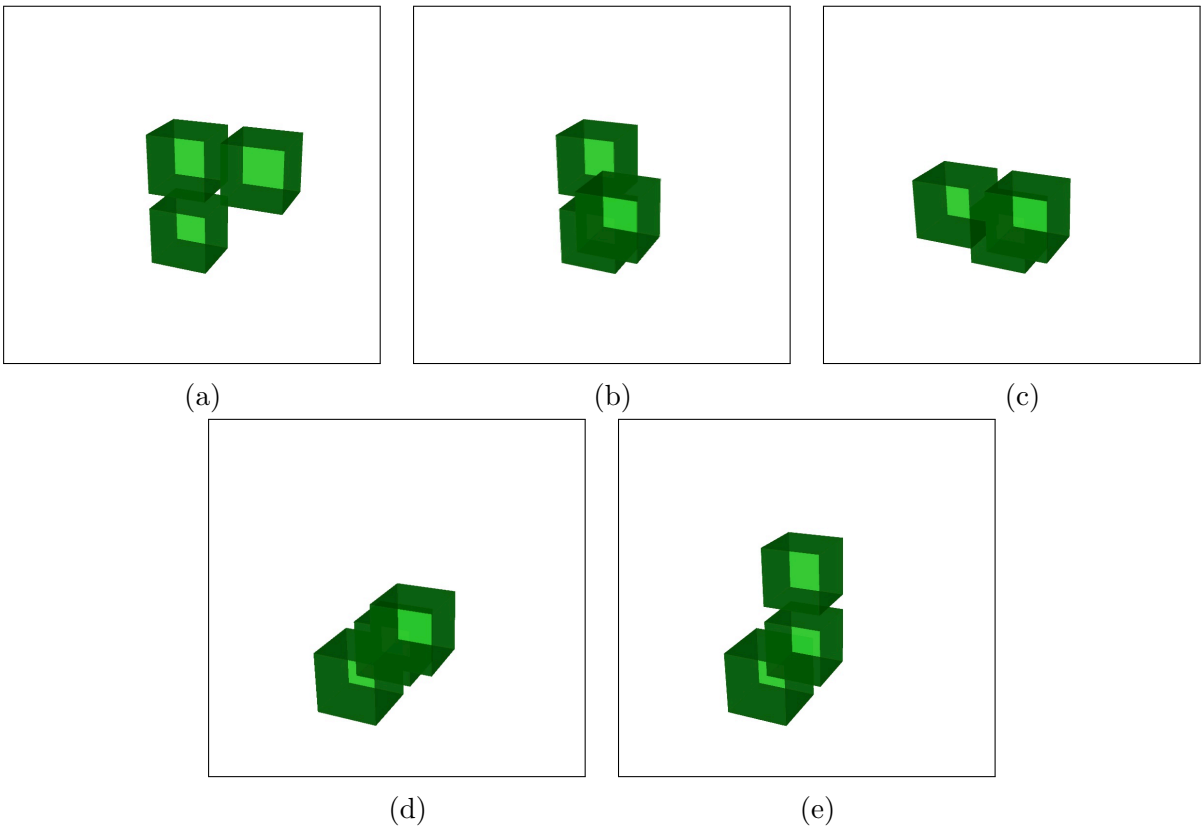

Figure 6.10: Migration process of a cluster containing 3 vacancies. The migration undergoes through two configurations and is carried out by one of the vacancies jumping to its 1 NN.

Bigger vacancy clusters tend to be immobile and form high symmetry configurations with high migration barriers. Examples of such clusters containing 4, 5 and 6 vacancies are given in Figure 6.11.

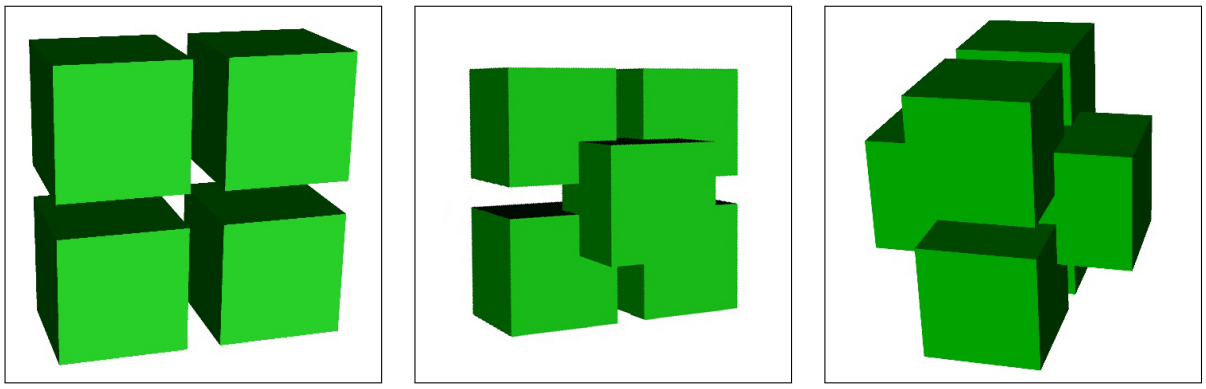

(a) (b) (c)

Figure 6.11: High symmetry configurations of vacancy clusters: (a) - 4 vacancies, (b) - 5 vacancies, (c) - 6 vacancies.

6.2.3 50 Vacancies Simulations

In order to compare the otf-KMC technique developed during this work and also to look into the evolution and clustering of vacancies, a study was carried out on long-time evolution of 50 randomly distributed vacancies in a $10a_0 \times 10a_0 \times 10a_0$ α-Fe supercell, where a_0 is the lattice parameter ($a_0 = 2.855$ Å). The initial average potential energy of the systems with periodic boundary conditions applied is -7740.66 eV. This problem has been recently studied by various groups using different techniques. The initial work was done by Fan *et al.* [133] using the autonomous basin climbing method (ABC) combined with KMC. Later comments on the work have been made by Brommer and Mousseau [134], where they have applied the kinetic activation relaxation technique (k-ART) for the same problem. And lastly Xu *et al.* [44] by employing self-evolving atomistic kinetic Monte Carlo (SEAKMC) method.

By comparing the findings of the same problem with the previous studies, the reliability and the performance of the newly developed technique can be determined. There are two main differences between the technique described in this work and the other ones. The first one is how the saddle points are being found.

The ABC + KMC approach is to climb up from the potential energy minima by filling it with Gaussian penalty functions [135]. When the saddle is crossed, MEP is reconstructed using the NEB method, by connecting the minima and determining the barrier height. The

k-ART method for finding transitions is explained previously in this work in section 3.3.1.3 and is based on the Lanczos method and the SEAKMC technique uses the Dimer method, described in section 3.3.1.1. As for this work, a combination of the Dimer method and the minimum mode following method is used. Even though the transitions search methods are different, all of them can be adjusted to the specific systems through a careful consideration of parameters, e.g. the step size in the Dimer method, or the scaling constant in the ART method, and can perform quite well by giving a good catalogue of possible transitions from the current system state. Also, since all the methods are finding reactions on the fly, there is some randomness in the outcome that must be accounted for.

The second major difference that is most likely to have a great effect on the outcome of the simulations, is the value of the prefactor in the Arrhenius equation (Equation 3.2.1). The other three methods use a fixed value, where in this work it is calculated on the fly. The ABC + KMC technique uses $5 \times 10^{12} \mathrm{s}^{-1}$, the k-ART method - $1 \times 10^{13} \mathrm{s}^{-1}$ and the SEAKMC - $1 \times 10^{12} \mathrm{s}^{-1}$ and $5 \times 10^{12} \mathrm{s}^{-1}$. The latter method showed to have a better agreement with the MD results with the value of $5 \times 10^{12} \mathrm{s}^{-1}$.

Results from 12 simulations were studied in terms of the evolution of system's energy, monovacancy fraction and average cluster size (Figure 6.12). The simulation temperature is 50 °C which lies between those of stages III and IV of the radiation damage-recovery process [133], where migration of vacancies and and their clusters occur. There are some experimental results from positron annihilation spectroscopy experiments [136] showing void nucleation even at this stage, thus providing some experimental evidence.

Similarly to the results of Brommer and Mousseau, the average cluster size of 6.5 is reached at ≈ 0.3 ms of simulation time, where Xu *et al.* reported results at least an order of magnitude faster. Likewise the potential energy on average drops under -7761 eV at ≈ 0.3 ms, as for Xu *et al.*, it is by an order of magnitude faster. Also monovacancies are reported by all three techniques when the system energy is higher than -7757 eV. This may be due to similarities shared between k-ART and otf-KMC technique developed in this work, by

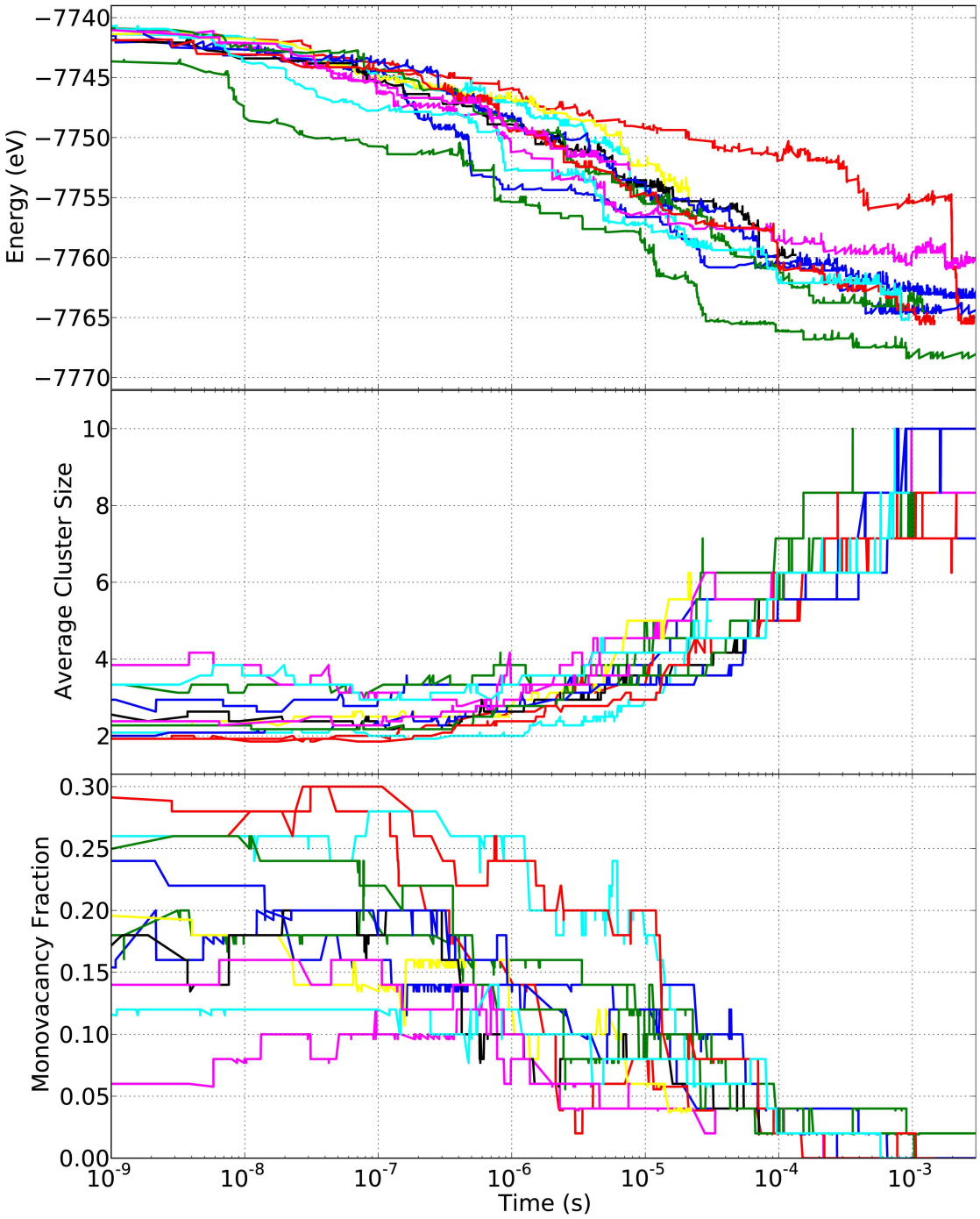

Figure 6.12: Twelve otf-KMC simulations of 50 randomly distributed vacancies in $10a_0 \times 10a_0 \times 10a_0$ α-Fe supercell. Top: Potential energy dependence. Centre: Average vacancy cluster size. Bottom: Fraction of monovacancies among all defects.

employing the Lanczos method to approach the saddles. As mentioned in the methodology section 3.3.1, this approach gives a better approximation than the Dimer method which is used by Xu *et al.*. The small changes in barrier heights and missing out of cooperative movements by SEAKMC is caused by rather small number of atoms used for the calculations might be the reason of disagreement in simulation times.

Another important aspect of simulations is the number of KMC steps required to achieve the merit values. Brommer and Mousseau reported from 3,000 to 30,000 transitions at each KMC step with the total number of KMC steps over 4733 to 5997 for their 4 simulations. In this work (Figure 6.12), the number of KMC steps varies from 600 to 1759 while performing up to 20,000 searches which leads to over 400 unique transitions at the beginning of a simulation.

By using the reuse of transitions, the consecutive steps require fewer searches to be done on the fly with also fewer defect volumes due to the defect clustering. This results in performing only a few thousand searches and a couple of hundred transitions at each KMC step. Clearly the smaller the number of KMC steps to obtain similar results between k-ART and the developed technique makes the latter more efficient without losing robustness.

An example of one of the systems is given in Figure 6.13. In this case the system was evolved for 1,759 KMC steps which resulted in 4 ms of simulation time. At the end of the simulation the system contains 7 vacancy clusters with an average size of 7.14 vacancies. The smallest cluster contains 6 vacancies and the biggest 11. All the clusters have high symmetry.

6.3 Discussion and Conclusions

The results from the tests on the influence of the calculated prefactor show that an accurate determination of the prefactor, in addition to the transition energy barriers, is necessary for accurate prediction of defect motion in KMC simulations. The contribution of the vibrational

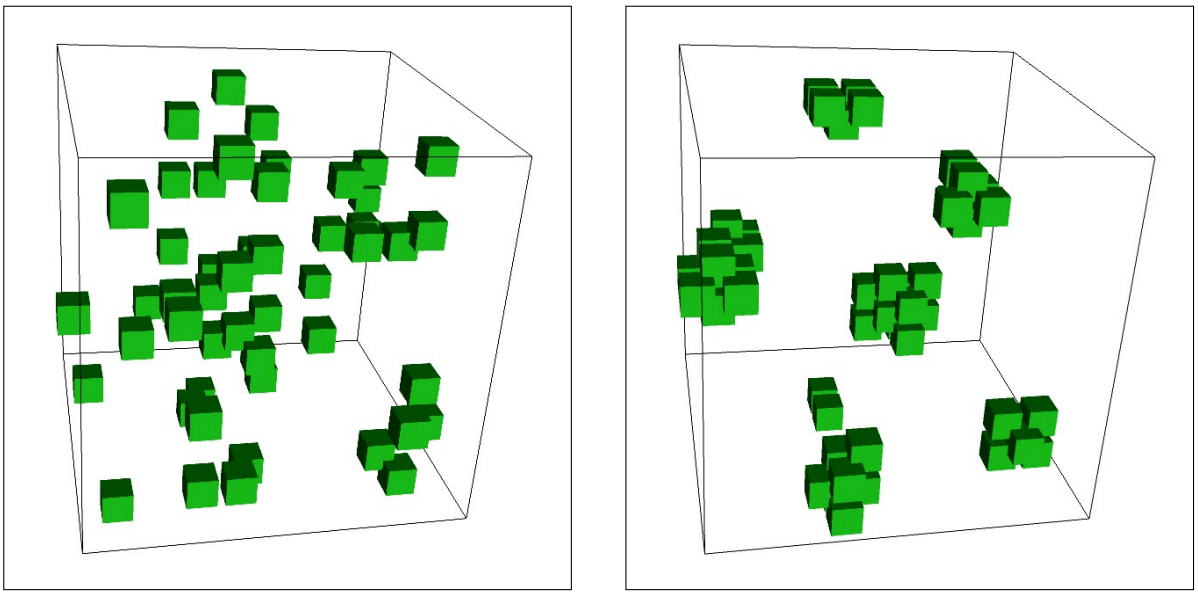

(a) (b)

Figure 6.13: An example of a system containing 50 vacancies evolved for 1,759 KMC steps (4 ms of simulation time): (a) - initial system with the randomly distributed vacancies, (b) - system at the end of simulation containing 7 vacancy clusters, varying in size from 6 to 11 vacancies.

internal energy, which is not incorporated within the Vineyard equation, showed only a minute contribution to the barrier height for the main defects types and their key migration mechanisms. In order to achieve one significant figure accuracy for the prefactor, it is necessary to include atoms at least within 10 Å radius around the defect, which results in computations that are not excessive in terms of computing time. Results for the $\langle 110 \rangle$ DB showed an almost two orders of magnitude greater prefactor value for the $\langle 111 \rangle$ DB on-site rotation, compared to a default value, making it the fastest transition and more likely to be chosen than the translation-rotation mechanism that has a lower barrier height. For most of the transitions of the vacancy type defects: single and di-vacancy, the prefactor value is at least an order magnitude greater than the default value, thus reducing the difference between the diffusion rates of interstitial and vacancy type defects.

By employing the hybrid MD - otf-KMC technique, a study was carried out on α-Fe systems. The simulations were carried out not to achieve the longest simulation time, but until the outcome of them could be predicted. In total 36 simulations were carried out with

the maximum KMC steps varying from 141 to 9373. The results showed minute difference between two potential energy functions used to describe Fe-Fe interactions: the Mendelev 2003 and Ackland 2004 potentials. As it is common for these kind of simulations, during the first few hundred KMC steps, defects that are close tend to recombine rapidly and an investigation of the immediate recombination between interstitial and vacancy type defects showed special configuration of defects, which do not have a migration barrier. Low migration barrier recombination transitions were also studied to identify the processes that the defects undergo. Most of the simulations after the initial recombination evolve by interstitial type defects (clusters containing up to 4 DBs) were they can rearrange to a stable configuration with a high energy escape barrier. Mobile clusters of 4 $\langle 111 \rangle$ DBs were also observed which tend to glide in the $\langle 111 \rangle$ direction with low barriers. Vacancy type defects containing 4 or more vacancies were found to be immobile after clustering into high symmetry configurations, were smaller ones are more mobile, especially with the calculated prefactor.

The tests with 50 vacancies introduced in the systems showed a good agreement with the results achieved by Brommer and Mousseau in terms of the system's potential energy and defect evolution against time, but the developed methodology requires less KMC steps to achieve the same results.

Chapter 7

Conclusions and Future Work

7.1 Conclusions

The need for understanding radiation effects in materials used in the nuclear applications grows as does the use of nuclear power with ever-increasing energy demand. The joint project between IGCAR, Oxford and Loughborough Universities uses both experiments and modelling to gain the knowledge on the effects of irradiation in the ODS steels for future generations of nuclear reactors. These alloys are studied due to their novelty and the lack of understanding of their key properties such as the effect of the oxide particles interface on absorbing the products of irradiation, their structural defects, the He and the radiation resistance of the nanoparticles. The main role of this work was to employ and develop modern modelling techniques to look into such effects at the atomistic level.

In order to simulate radiation damage evolution over long time scales an efficient technique was required. The initial work by Vernon [47] needed to be rewritten in more modular format for easier optimisation and extension, therefore new software was written from scratch. One of the biggest challenges was the implementation of an efficient saddle search algorithm. The most common algorithms were implemented, but in most of the cases the ART, RAT or the Dimer method had to be coupled with the NEB method in order to achieve

good accuracy of barrier heights. In this way saddle searches were computationally expensive procedures and an evolution of big or complicated systems was very slow. A combination of the Dimer method and the minimum mode following algorithm has proven to have the best mixture of accuracy and speed and a double ended search method proved to be no longer necessary for accurately determined barrier heights. The Dimer method was chosen because it has been shown to be an efficient way to escape a local minimum, but a drawback was that it required many function evaluations to converge to a saddle point. While the minimum mode following algorithm is a very efficient technique to converge to a saddle, it struggles with the initial escape from a minimum. By coupling these two methods and using them where they are most efficient, a robust algorithm was developed showing similar accuracy as the NEB method, but did not require as many function evaluations.

Another important contribution to the otf-KMC technique was made by analysing the topologies of defect volumes. "Nauty" [99] was incorporated for interpreting defect volumes as graphs and finding isomorphisms between them. This allowed an easy comparison between defect volumes and the reuse of transitions on isomorphic defect volumes, thus saving computational time that would be normally spent on failed and duplicate transition searches.

As for modelling radiation damage in ODS, the studies were carried out in α-Fe, a simplified model of ODS and Y-Ti-O systems. The work is focussed around the ODS model as an α-Fe system with 0.3 at% of Y_2O_3. The model is based on the potentials which were able to reconstruct the structure of yttria, but the interface between the nanoparticle and Fe was incoherent due to the type of interatomic potential used. Nonetheless, the radiation damage simulations were able to capture different behaviours and processes that may provide hints explaining the role of the nanoparticles in ODS under radiation.

When collisions occurred in an yttria-free region, the irradiation progressed in a similar way that was observed in pure bcc iron systems. However, when they were initiated close to a nanoparticle, the particle can act as a block to the propagation of a collision cascade by "transferring" the energy to the yttria nanoparticle. In this way instead of creating residual

defects in the Fe lattice structure, energy is absorbed by the yttria nanoparticle and gradually released through atomic vibrations over longer time-scales then the MD simulation. Fe defect attraction to the nanoparticle interface was also observed, with an active region of $3.5 - 10.0$ Å around the nanoparticle, reducing the number of defects in the matrix. Higher energy collision cascades (5 keV) indicated the radiation stability of the nanoparticles and only in the event of a near head-on collision with an incoming energetic Fe atom, atoms from the nanoparticle were ejected into the matrix.

The results from the He MD simulations have shown yttria nanoparticles interact with helium atoms by entrapping them on their surface. The trapped He decorates the interface, but does not form bubbles as in the bulk Fe.

An interesting behaviour of He clusters was observed in pure Fe systems, where clusters containing up to 4 He atoms are mobile and clusters containing 5 or more become stable by creating an Fe interstitial. MD simulations over 5 ns showed that He tends to cluster and at the end of simulations, systems contained mostly stable He bubbles. Ability of helium bubbles to act as a sink was also observed by trapping split-interstitial type defects.

Radiation damage simulations in ODS models have not been carried out using the otf-KMC. The problem originates from the "free region" which surrounds the nanoparticle. It allows the nanoparticle to make small rearrangements to itself according to the surrounding atoms structure. The evolution of the KMC technique is based on the events happening in small contained regions, but when a defect migrates towards the nanoparticle, the nanoparticle starts to interact with them and the region including the nanoparticle must be accounted in the saddle search algorithms. This makes them computationally very expensive and in most of the times the found transitions do not belong to the migrating defect but rather to the reconfiguration of the nanoparticle. This problem could be addressed by implementing a variable charge model for the Fe-Y-O interactions or a basin method, but was beyond the scope of this thesis.

The radiation damage study in the Y-Ti-O materials showed almost linear dependency

between the number of defects and the PKA energies, with heavier atoms (Ti, Y) producing more defects and O PKAs tending to channel through the system. Two types of residual damage behaviour have been seen: the first is when the damage is localized in a region, usually close to the initial PKA position; the second is when PKA is directed in the channelling direction and creating less defects compared to localised damage case, but with a wider spread. The Y_2TiO_5 and $Y_2Ti_2O_7$ systems showed increased recombination of defects with increased temperature, thus suggesting that Y_2O_3, has better performance at low temperature and Y-Ti-O systems have a potential to have a higher radiation resistance at high temperatures. The remaining defects in the Y_2O_3 systems were categorized in terms of their point defect configurations similarly as it was done in the Er-O systems, where Y_2TiO_5 and especially $Y_2Ti_2O_7$ lacked structural stability possibly indicating that used potentials need to be improved for the structures.

Results from the tests on the influence of the calculated prefactor in the Arrhenius equations showed the necessity to estimate it accurately in order to model defect motion in α-Fe. Results for the $\langle 110 \rangle$ DB showed almost two orders of magnitude greater prefactors value for the $\langle 111 \rangle$ DB on-site rotation, compared to the default value, making it the fastest transition and more likely to be chosen than the translation-rotation mechanism that has a lower barrier height. For most of the single and di-vacancy defect migrations the prefactor value is at least an order magnitude greater than the default value, thus reducing the difference between the diffusion rates of interstitial and vacancy type defects. The validity of these results were checked by the comparison of the KMC results with MD and TAD, which showed good agreement.

Also the contribution of the vibrational internal energy, which is not incorporated within the Vineyard equation, showed minimal change to the barrier heights for the main defect types and their key migration mechanisms. Therefore, accurate determination of the prefactor and transition barriers are the most important for defect motion prediction.

By employing the hybrid MD - otf-KMC technique, a study was carried out on α-Fe

systems at 450K. The implemented potentials (Mendelev 2003 and Ackland 2004) very similar behaviour in terms of defect production and their migration. Rapid recombination of defects appeared during the first few hundred KMC steps and an investigation of immediate recombination between interstitial and vacancy type defects showed special configurations of defects, which do not have a migration barrier by recombining during the equilibration of the system. Most of the simulations after the initial recombination evolve by interstitial type defects (clusters containing up to 4 DBs) where they can rearrange to a stable configuration with a high energy escape barrier. Mobile clusters of 4 $\langle 111 \rangle$ DBs were also observed which tend to glide in the $\langle 111 \rangle$ direction with low barriers. Vacancy type defects containing 4 or more vacancies were found to be immobile after clustering into a high symmetry configurations, where as smaller ones are more mobile especially using an accurately calculated prefactor.

The tests with 50 vacancies introduced in to α-Fe were in very good agreement with the results achieved by Brommer and Mousseau, and the developed otf-KMC technique on average required less KMC steps to achieve the same results.

To summarize, even though the otf-KMC was not employed to study defect evolution in ODS models, the results from the MD simulations provided interesting hints of the processes that might be responsible for the better ODS steels performance under radiation damage. The radiation damage studies in Y-Ti-O system showed necessity to develop new potentials in order to study such systems, where the defect evolution in α-Fe indicated the importance of the calculated prefactor for the defect migration and recombination processes. The developed otf-KMC technique is highly parallelised, has most common methods for saddle searching and optimization, able to reuse transitions, estimate prefactors on the fly and is efficient and reliable. The technique was not only used for this work, but is also extensively used by colleagues in the materials modelling group at Loughborough University to address various other materials problems.

7.2 Future Work

One of the modifications that is necessary for the further improvement of the developed otf-KMC technique is the ability to deal with the low barrier transitions which delay the evolution of the systems, e.g. rearrangement of 3 DB clusters. One of the methods, the basin method [137], is being implemented by a colleague Miao Yu as a possible solution for these kind of problems.

A possible extension to the developed otf-KMC technique is an implementation of one of the parallel KMC algorithms to achieve better scaling by using more processors. The idea behind parallel KMC algorithms is the system's division into smaller non-interacting regions, thus allowing them to evolve separately and reduce the linearity of the KMC. One of the promising techniques is the Synchronous Sublattice Algorithm developed by Y. Shim and J. G. Amar [138, 139]. This algorithm operates on the idea of assigning different parts of the system to different processors via the spatial decomposition. The processors simultaneously and independently carry out KMC events until the time of the next event exceeds the set time interval. Then processors communicate the changes with their neighbouring processors to compensate for boundary events and the process is restarted. Similarly, a possible modification could be done to the otf-KMC technique only instead of using the spatial decomposition to distribute processors, groups of processors could be distributed to non-interacting defect volumes and allowing to evolve them separately with occasional communication between them to ensure the same system configuration between them.

Another possible extension to the otf-KMC technique could be by having a selective evolution region. Usually a system evolves by defect rearrangement in their defect volumes or combined volumes and most likely the defects with the highest rates are selected to evolve the system.

One idea is to perform the first KMC step as it is done in the current technique, by performing transition searches on all the defect volumes. Then the sums of the transition rates for each defect volume is calculated and one of them is chosen randomly, according to

the sums of rates. Then a transition from the chosen defect volume is picked for the evolution and followed by the transition searches or the reuse of transitions performed on it. After that the sum of rates is updated for the defect volume. Assuming that the configuration of the non-interacting defect volumes do not effect each other or the effect is minute, the sums of rates of other defect volumes are left as they were. During the following steps, similarly a defect volume is chosen according to the previously calculated sum of rates. Then the transitions searches or reuse is carried out on it, the sum of rate is updated and a transitions is chosen for the system's evolution. This modification would save computational time when the system contains at least two defect volumes, since only one defect volume would be "active", during a KMC step.

As for modelling radiation damage in ODS systems, the description depends heavily on the interatomic potentials. In this work potentials used to study α-Fe-Y-O and Y-Ti-O systems were able to reconstruct oxide structures but not other properties, such as bulk modulus and elastic constants. Therefore the further development of interatomic potentials is necessary to gain better understanding of material characteristics. Also, for further studies the variable charge model, which allows charge transfer among atoms, might be used to improve the model, especially the metal-oxide interfaces due to their complexity. These improvements may help to stabilize the oxide particle in the system and the long time scale simulations might be performed on the ODS model too.

It would be also interesting to perform radiation effect studies on more complicated models of ODS systems as α-Fe-Cr-Y-Ti-O. These simulations might explain the processes that were reported during the irradiation experiments, such as the loss of Ti from the Y-Ti-O oxide particles, particles' refinement and even their dissolving. High energy cascade simulations (>5 keV) in α-Fe-Y-O and α-Fe-Cr-Y-Ti-O systems would help to further investigate the stability of the oxides.

MD or even otf-KMC simulations can also be performed to study He bubble formation in ODS systems. The more complicated study can be performed by gradually introducing

He into the system by evolving it for a certain amount of time, which represents the actual time from experiments, between following He atoms placements in the system. In this way, simulations would be able to recreate more realistic processes of the segregation on the oxide particle surfaces and bubble formations and be more comparable with the experimental findings or even provide quantitative statistics.

References

[1] K. L. Murty and I. Charit. Structural materials for Gen-IV nuclear reactors: Challenges and opportunities. *Journal of Nuclear Materials*, 383(1-2):189–195, December 2008.

[2] R. S. Barnes. Embrittlement of stainless steels and nickel-based alloys at high temperature induced by neutron radiation. *Nature*, 206:1307 – 1310, 1965.

[3] T. M. Angeliu, J. T. Ward, and J. K. Witter. Assessing the effects of radiation damage on Ni-base alloys for the prometheus space reactor system. *Journal of Nuclear Materials*, 366(1-2):223–237, June 2007.

[4] C. Capdevila and H. K. D. H. Bhadeshia. Manufacturing and Microstructural Evolution of Mechanuically Alloyed Oxide Dispersion Strengthened Superalloys. *Advanced Engineering Materials*, 3(9):647–656, September 2001.

[5] G. R. Odette, M. J. Alinger, and B. D. Wirth. Recent Developments in Irradiation-Resistant Steels. *Annual Review of Materials Research*, 38(1):471–503, August 2008.

[6] A. J. London, T. Lazauskas, S. Santra, S. Amirthapandian, B. K. Panigrahi, R. M. Sarguna, G. Nagra, M. Dholakia, M. C. Valsakumar, C. Grovenor, R. Smith, C. S. Sundar, S. Kenny, and S. Lozano-Perez. Poster on Collaborative Research Between the UK and India on Oxide Dispersion Strengthened Steels, 2013.

[7] I.-S. Kim, B.-Y. Choi, C.-Y. Kang, T. Okuda, P. J. Maziasz, and K. Miyahara. Effect of Ti and W on the Mechanical Properties and Microstructure of 12% Cr Base Mechanical-alloyed Nano-sized ODS Ferritic Alloys. *ISIJ International*, 43(10):1640–1646, 2003.

[8] V. V. Sagaradze, V. I. Shalaev, V. L. Arbuzov, B. N. Goshchitskii, Y. Tian, W. Qun, and S. Jiguang. Radiation resistance and thermal creep of ODS ferritic steels. *Journal of Nuclear Materials*, 295(2-3):265–272, June 2001.

[9] R. L. Klueh, P. J. Maziasz, I. S. Kim, L. Heatherly, D. T. Hoelzer, N. Hashimoto, E. A. Kenik, and K. Miyahara. Tensile and creep properties of an oxide dispersion-strengthened ferritic steel. *Journal of Nuclear Materials*, 307-311:773–777, 2002.

[10] S. Ukai and M. Fujiwara. Perspective of ODS alloys application in nuclear environments. *Journal of Nuclear Materials*, 307-311:749–757, December 2002.

[11] R. Schäublin, A. Ramar, N. Baluc, V. de Castro, M. A. Monge, T. Leguey, N. Schmid, and C. Bonjour. Microstructural development under irradiation in European ODS ferritic/martensitic steels. *Journal of Nuclear Materials*, 351(1-3):247–260, June 2006.

[12] P. Pareige, M. K. Miller, R. E. Stoller, D. T. Hoelzer, E. Cadel, and B. Radiguet. Stability of nanometer-sized oxide clusters in mechanically-alloyed steel under ion-induced displacement cascade damage conditions. *Journal of Nuclear Materials*, 360(2):136–142, February 2007.

[13] S. Yamashita, N. Akasaka, and S. Ohnuki. Nano-oxide particle stability of 912Cr grain morphology modified ODS steels under neutron irradiation. *Journal of Nuclear Materials*, 329-333:377–381, August 2004.

[14] J. Gan, T. R. Allen, R. C. Birtcher, S. Shutthanandan, and S. Thevuthasan. Radiation Effects on the Microstructure of a 9Cr-ODS Alloy. *Journal of Metals*, 60(1):24–28, 2008.

[15] J. Brodrick, D. J. Hepburn, and G. J. Ackland. Mechanism for radiation damage resistance in yttrium oxide dispersion strengthened steels. *Journal of Nuclear Materials*, 445(1-3):291–297, February 2014.

[16] E. E. Bloom. The challenge of developing structural materials for fusion power systems. *Journal of Nuclear Materials*, 258-263:7–17, 1998.

[17] Y. Dai, G. R. Odette, and T. Yamamoto. The Effects of Helium in Irradiated Structural Alloys. In *Comprehensive Nuclear Materials*, chapter 1.06, pages 141–193. Elsevier Inc., 2012.

[18] G. R. Odette and D.T. Hoelzer. Irradiation-tolerant Nanostructured Ferritic Alloys: Transforming Helium from a Liability to an Asset. *JOM*, 62(9):84–92, 2010.

[19] D. Stewart, Y. Osetskiy, and R. Stoller. Atomistic studies of formation and diffusion of helium clusters and bubbles in BCC iron. *Journal of Nuclear Materials*, 417(1-3):1110–1114, October 2011.

[20] Z. Di, X.-M. Bai, Q. Wei, J. Won, R. G. Hoagland, Y. Wang, A. Misra, B. P. Uberuaga, and M. Nastasi. Tunable helium bubble superlattice ordered by screw dislocation network. *Physical Review B*, 84(5):052101, August 2011.

[21] L. Yang, H. Q. Deng, F. Gao, H. L. Heinisch, R. J. Kurtz, S. Y. Hu, Y. L. Li, and X. T. Zu. Atomistic studies of nucleation of He clusters and bubbles in bcc iron. *Nuclear Instruments and Methods in Physics Research B*, 303:68–71, May 2013.

[22] P. D. Edmondson, C. M. Parish, Y. Zhang, A. Hallén, and M. K. Miller. Helium bubble distributions in a nanostructured ferritic alloy. *Journal of Nuclear Materials*, 434(1-3):210–216, March 2013.

[23] A. I. Ryazanov, O. K. Chugunov, S. M. Ivanov, S. T. Latushkin, R. Lindau, A. Möslang, A. A. Nikitina, K. E. Prikhodko, E. V. Semenov, V. N. Unezhev, and P. V. Vladimirov. Tensile properties and microstructure of helium implanted EUROFER ODS. *Journal of Nuclear Materials*, 442(1-3):S153–S157, November 2013.

[24] P. D. Edmondson, C. M. Parish, Q. Li, and M. K. Miller. Thermal stability of nanoscale helium bubbles in a 14YWT nanostructured ferritic alloy. *Journal of Nuclear Materials*, 445(1-3):84–90, February 2014.

[25] B. D. Wirth, G. R. Odette, J. Marian, L. Ventelon, J. A. Young-Vandersall, and L. A. Zepeda-Ruiz. Multiscale modeling of radiation damage in Fe-based alloys in the fusion environment. *Journal of Nuclear Materials*, 329-333:103–111, August 2004.

[26] R. A. Aziz, A. R. Janzen, and M. R. Moldover. Ab initio calculations for helium: a standard for transport property measurements. *Physical Review Letters*, 74(9):1586–1589, 1995.

[27] F. Gao, H. Deng, H. L. Heinisch, and R. J. Kurtz. A new Fe-He interatomic potential based on ab initio calculations in α-Fe. *Journal of Nuclear Materials*, 418(1-3):115–120, November 2011.

[28] M. A. Tschopp, F. Gao, L. Yang, and K. N. Solanki. Binding energetics of substitutional and interstitial helium and di-helium defects with grain boundary structure in α-Fe. *Journal of Applied Physics*, 115(3):033503, January 2014.

[29] L. Barnard, G. R. Odette, I. Szlufarska, and D. Morgan. An ab initio study of Ti-Y-O nanocluster energetics in nanostructured ferritic alloys. *Acta Materialia*, 60(3):935–947, February 2012.

[30] J. Zhang, F. Zhang, M. Lang, F. Lu, J. Lian, and R. C. Ewing. Ion-irradiation-induced structural transitions in orthorhombic Ln2TiO5. *Acta Materialia*, 61(11):4191–4199, June 2013.

[31] K. R. Whittle, M. G. Blackford, Ro. D. Aughterson, G. R. Lumpkin, and N. J. Zaluzec. Ion irradiation of novel yttrium/ytterbium-based pyrochlores: The effect of disorder. *Acta Materialia*, 59(20):7530–7537, December 2011.

[32] R. A. Johnson. Interstitials and Vacancies in α Iron. *Physical Review*, 134(5A):A1329–A1336, 1964.

[33] J. R. Beeler Jr and R. A. Johnson. Vacancy Clusters in α-Iron. *Physical Review*, 156(3):677–684, 1967.

[34] G. J. Ackland, D. J. Bacon, A. F. Calder, and T. Harry. Computer simulation of point defect properties in dilute Fe-Cu alloy using a many-body interatomic potential. *Philosophical Magazine A*, 75(3):713–732, March 1997.

[35] M. I. Mendelev, S. Han, D. J. Srolovitz, G. J. Ackland, D. Y. Sun, and M. Asta. Development of new interatomic potentials appropriate for crystalline and liquid iron. *Philosophical Magazine*, 83(35):3977–3994, December 2003.

[36] G. J. Ackland, M. I. Mendelev, D. J. Srolovitz, S. Han, and A. V. Barashev. Development of an interatomic potential for phosphorus impurities in -iron. *Journal of Physics: Condensed Matter*, 16(27):S2629–S2642, July 2004.

[37] R. E. Stoller, G. R. Odette, and B. D. Wirth. Primary damage formation in bcc iron. *Journal of Nuclear Materials*, 251:49–60, 1997.

[38] R. E. Stoller. The role of cascade energy and temperature in primary defect formation in iron. *Journal of Nuclear Materials*, 276:22–32, 2000.

[39] M.-C. Marinica, F. Willaime, and N. Mousseau. Energy landscape of small clusters of self-interstitial dumbbells in iron. *Physical Review B*, 83(9):094119, March 2011.

[40] M. J. Caturla, N. Soneda, T. Diaz de la Rubia, and M. Fluss. Kinetic Monte Carlo simulations applied to irradiated materials: The effect of cascade damage in defect nucleation and growth. *Journal of Nuclear Materials*, 351(1-3):78–87, June 2006.

[41] T. Suzudo, S. I. Golubov, R. E. Stoller, M. Yamaguchi, T. Tsuru, and H. Kaburaki. Annealing simulation of cascade damage in α-Fe Damage energy and temperature dependence analyses. *Journal of Nuclear Materials*, 423(1-3):40–46, April 2012.

[42] H. Xu, Y. Osetsky, and R. E. Stoller. Simulating complex atomistic processes: On-the-fly kinetic Monte Carlo scheme with selective active volumes. *Physical Review B*, 84(13):1–4, October 2011.

[43] H. Xu, Y. N. Osetsky, and R. E. Stoller. Cascade annealing simulations of bcc iron using object kinetic Monte Carlo. *Journal of Nuclear Materials*, 423(1-3):102–109, April 2012.

[44] H. Xu, R. E. Stoller, and Y. N. Osetsky. Cascade defect evolution processes: Comparison of atomistic methods. *Journal of Nuclear Materials*, 443(1-3):66–70, November 2013.

[45] J. B. Gibson, A. N. Goland, M. Milgram, and G. H. Vineyard. Dynamics of Radiation Damage. *Physical Review*, 120(4):1229–1253, 1960.

[46] G. Henkelman and H. Jónsson. Long time scale kinetic Monte Carlo simulations without lattice approximation and predefined event table. *The Journal of Chemical Physics*, 115(21):9657, 2001.

[47] L. J. Vernon. *Modelling Growth of Rutile TiO2*. PhD thesis, Loughborough University, 2010.

[48] J. M. Haile. *Molecular Dynamics Simulation: Elementary Methods*. John Wiley & Sons, Inc., New York, 1st edition, 1992.

[49] B. J. Alder and T. E. Wainwright. Phase Transition for a Hard Sphere System. *The Journal of Chemical Physics*, 27(5):1208, 1957.

[50] J. A. McCammon, B. R. Gelin, and M. Karplus. Dynamics of folded proteins. *Nature*, 267:585–590, 1977.

[51] W. C. Swope, H. C. Andersen, P. H. Berens, and K. R. Wilson. A computer simulation method for the calculation of equilibrium constants for the formation of physical clusters of molecules: Application to small water clusters. *The Journal of Chemical Physics*, 76(1):637–649, 1982.

[52] M. W. Finnis and J. E. Sinclair. A simple empirical N-body potential for transition metals. *Philosophical Magazine A*, 50(1):45–55, 1984.

[53] J. F. Ziegler, J. P. Biersack, and U. Littmark. *The Stopping and Ion Range of Ions in Matter*. Pergamon Press, New York, 1985.

[54] R. A. Buckingham. The classical equation of state of gaseous helium, neon and argon. *Proceedings of the Royal Society of London. Series A, Mathematical and PhysicalSciences*, 168(933):264–283, 1938.

[55] G. V. Lewis and C. R. A. Catlow. Potential models for ionic oxides. *Journal of Physics C: Solid State Physic*, 18:1149–1161, 1985.

[56] C. R. A. Catlow. Point Defect and Electronic Properties of Uranium Dioxide. *Proceedings of the Royal Society A: Mathematical, Physical and Engineering Sciences*, 353(1675):533–561, April 1977.

[57] T. S. Bush, J. D. Gale, C. R. A. Catlow, and P. D. Battle. Self-consistent interatomic potentials for the simulation of binary and ternary oxides. *Journal of Materials Chemistry*, 4(6):831, 1994.

[58] PM Morse. Diatomic molecules according to the wave mechanics. II. vibrational levels. *Physical Review*, 34:57–64, 1929.

[59] R. C. Lincoln, K. M. Koliwad, and P. B. Ghate. Morse-Potential Evaluation of Second- and Third-Order Elastic Constants of Some Cubic MEtals. *Physical Review*, 157(3):463–466, 1967.

[60] R. A. Aziz and M. J. Slaman. An Analysis of the ITS-90 Relations for the Non-Ideality of 3He and 4He: Recommended Relations Based on a New Interatomic Potential for Helium. *Metrologia*, 27(4):211–219, 1990.

[61] M. S. Daw and M. I. Baskes. Semiempirical, Quantum Mechanical Calculation of Hydrogen Embrittlement in Metals. *Physical Review Letters*, 50(17):1285–1288, 1983.

[62] M. S. Daw and M. I. Baskes. Embedded-atom method: Derivation and application to impurities, surfaces, and other defects in metals. *Physical Review B*, 29(12):6443–6453, 1984.

[63] R. Smith, M. Jakas, D. Ashworth, B. Oven, M. Bowyer, I. Chakarov, and R. Webb. *Atomic and Ion Collisions in Solids and at Surfaces.* Cambridge University Press, 1997.

[64] J. P. Biersack and J. F. Ziegler. Refined universal potentials in atomic collisions. *Nuclear Instruments and Methods in Physics Research*, 194(1-3):93–100, 1982.

[65] P. P. Ewald. Die Berechnung optischer und elektrostatischer Gitterpotentiale. *Annalen der Physik*, 64:253–287, 1921.

[66] C. J. Fennell and J. D. Gezelter. Is the Ewald summation still necessary? Pairwise alternatives to the accepted standard for long-range electrostatics. *The Journal of Chemical Physics*, 124(23):234104, June 2006.

[67] L. Kittiratanawasin, R. Smith, B. P. Uberuaga, and K. Sickafus. Displacement threshold and Frenkel pair formation energy in ionic systems. *Nuclear Instruments and Methods in Physics Research Section B: Beam Interactions with Materials and Atoms*, 268(19):2901–2906, October 2010.

[68] D. Wolf, P. Keblinski, S. R. Phillpot, and J. Eggebrecht. Exact method for the simulation of Coulombic systems by spherically truncated, pairwise r1 summation. *Journal of Chemical Physics*, 110(17):8254–8282, 1999.

[69] U. Essmann, L. Perera, M. L. Berkowitz, T. Darden, H. Lee, and L. G. Pedersen. A smooth particle mesh Ewald method. *The Journal of Chemical Physics*, 103(19):8577, 1995.

[70] R. Fletcher and C. M. Reeves. Function minimization by conjugate gradients. *The Computer Journal*, 7:149–154, 1964.

[71] W. H. Press, S. A. Teukolsky, W. T. Vetterling, and B. P. Flannery. *Numerical recipes: the art of scientific computing.* Cambridge University Press, 2nd edition, 1992.

[72] E. Polak and G. Ribiere. Note sur la convergence de méthodes de directions conjuguées. *ESAIM: Mathematical Modelling and Numerical Analysis - Modélisation Mathématique et Analyse Numérique*, 3(R1):35–43, 1969.

[73] J. Lindhard, M. Scharff, and H. E. Schioett. Range concepts and heavy ion ranges. *Kgl. Danske Videnskab. Selskab. Mat. Fys. Medd.*, 33(14):3543, 1963.

[74] M. M. Jakas and D. E. Harrison Jr. Influence of electronic energy losses on atom ejection processes. *Physical Review B*, 30(6):3573–3574, 1984.

[75] R. H. Byrd, P. Lu, J. Nocedal, and C. Zhu. A limited memory algorithm for bound constrained optimization. *SIAM Journal on Scientific Computing*, 16(5):1190–1208, 1995.

[76] J. L. Morales and J. Nocedal. Remark on algorithm 778: L-BFGS-B: Fortran subroutines for large-scale bound constrained optimization. *ACM Transactions on Mathematical Software*, 38(1):1–4, November 2011.

[77] W. G. Hoover. Canonical dynamics: Equilibrium phase-space distributions. *Physical Review A*, 31(3):1695–1697, 1985.

[78] T. Schneider and E. Stoll. Molecular-dynamics study of a three-dimensional one-component model for distortive phase transitions. *Physical Review B*, 17(3):1302–1322, 1978.

[79] H. J. C. Berendsen, J. P. M. Postma, W. F. van Gunsteren, A. DiNola, and J. R. Haak. Molecular dynamics with coupling to an external bath. *The Journal of Chemical Physics*, 81(8):3684, 1984.

[80] A. F. Voter, F. Montalenti, and T. C. Germann. Extending the Time Scale in Atomistic Simulation of Materials. *Annual Review of Materials Research*, 32(1):321–346, August 2002.

[81] A. F. Voter. Parallel replica method for dynamics of infrequent events. *Physical Review B*, 57(22):R13985–R13988, June 1998.

[82] A. F. Voter. Hyperdynamics: Accelerated Molecular Dynamics of Infrequent Events. *Physical Review Letters*, 78(20):3908–3911, May 1997.

[83] M. R. So/rensen and A. F. Voter. Temperature-accelerated dynamics for simulation of infrequent events. *The Journal of Chemical Physics*, 112(21):9599–9606, 2000.

[84] G. Henkelman and H. Jónsson. A dimer method for finding saddle points on high dimensional potential surfaces using only first derivatives. *The Journal of Chemical Physics*, 111(15):7010–7022, 1999.

[85] G. T. Barkema and N. Mousseau. Event-Based Relaxation of Continuous Disordered Systems. *Physical Review Letters*, 77(21):4358–4361, November 1996.

[86] N. Mousseau and G. Barkema. Traveling through potential energy landscapes of disordered materials: The activation-relaxation technique. *Physical Review E*, 57(2):2419–2424, February 1998.

[87] C. J. Cerjan and H. M. William. On finding transition states. *The Journal of Chemical Physics*, 75(6):2800, 1981.

[88] A. Pedersen, S. F. Hafstein, and H. Jónsson. Efficient Sampling of Saddle Points with the Minimum-Mode Following Method. *SIAM Journal on Scientific Computing*, 33(2):633–652, 2011.

[89] C. C. Paige. Computational Variants of the Lanczos Method for the Eigenproblem. *IMA Journal of Applied Mathematics*, 10(3):373–381, 1972.

[90] B. N. Parlett and D. S. Scott. The Lanczos algorithm with selective orthogonalization. *Mathematics of computation*, 33(145):217–238, 1979.

[91] J. M. Ortega and H. F. Kaiser. The LLT and QR methods for symmetric tridiagonal matrices. *The Computer Journal*, 6(1):99–101, 1963.

[92] G. Henkelman and H. Jónsson. Improved tangent estimate in the nudged elastic band method for finding minimum energy paths and saddle points. *The Journal of Chemical Physics*, 113(22):9978–9985, 2000.

[93] G. Henkelman, B. P. Uberuaga, and H. Jónsson. A climbing image nudged elastic band method for finding saddle points and minimum energy paths. *The Journal of Chemical Physics*, 113(22):9901–9904, 2000.

[94] E. Weinan, R. Weiqing, and E. Vanden-Eijnden. String method for the study of rare events. *Physical Review B*, 66(5):052301, August 2002.

[95] B. Peters, A. Heyden, A. T. Bell, and A. Chakraborty. A growing string method for determining transition states: comparison to the nudged elastic band and string methods. *The Journal of chemical physics*, 120(17):7877–86, May 2004.

[96] E. Weinan, R. Weiqing, and E. Vanden-Eijnden. Simplified and improved string method for computing the minimum energy paths in barrier-crossing events. *The Journal of Chemical Physics*, 126(16):164103, April 2007.

[97] G. H. Vineyard. Frequency factors and isotope effects in solid state rate processes. *Journal of Physics and Chemistry of Solids*, 3(1-2):121–127, 1957.

[98] F. El-Mellouhi, N. Mousseau, and L. J. Lewis. Kinetic activation-relaxation technique: An off-lattice self-learning kinetic Monte Carlo algorithm. *Physical Review B*, 78(153202):1–4, October 2008.

[99] B. D. McKay. Practical Graph Isomorphism. *Congressus Numerantium*, 30:45–87, 1981.

[100] B. D. McKay. Nauty user's guide (version 2.4). *Computer Science Dept., Australian National University*, page 70, 2007.

[101] Z. Al Tooq. *Simulating Radiation Damage in Austenitic Stainless Steel and Ni-based alloys*. PhD thesis, Loughborough University, 2013.

[102] X. Gai, T. Lazauskas, S. D. Kenny, and R. Smith. Helium bubbles in iron. *To be published in Journal of Nuclear Materials*.

[103] T. Lazauskas, S. D. Kenny, R. Smith, G. Nagra, M. Dholakia, and M. C. Valsakumar. Simulating radiation damage in a bcc Fe system with embedded yttria nanoparticles. *Journal of Nuclear Materials*, 437(1-3):317–325, June 2013.

[104] C. S. Sundar. Private Communication at Indo-UK Civil Nuclear Collaboration Review Meeting, Mamallapuram, India: Characterization of the Small-scale Structure of the Yttria-based Particles in ODS, March 6-9, 2011.

[105] W. Schroeder, K. Martin, and B. Lorensen. *The Visualization Toolkit: An Object-oriented Approach to 3D Graphics.* Kitware, Inc., New York, 4 edition, 2006.

[106] A. F. Calder and D. J. Bacon. A molecular dynamics study of displacement cascades in α-iron. *Journal of Nuclear Materials*, 207:25–45, 1993.

[107] D. J. Bacon, Y. N. Osetsky, R. Stoller, and R. E. Voskoboinikov. MD description of damage production in displacement cascades in copper and α-iron. *Journal of Nuclear Materials*, 323(2-3):152–162, December 2003.

[108] C. S. Becquart, C. Domain, J. C. van Duysen, and J. M. Raulot. The role of Cu in displacement cascades examined by molecular dynamics. *Journal of Nuclear Materials*, 294(3):274–287, April 2001.

[109] RE Stoller. The role of cascade energy and temperature in primary defect formation in iron. *Journal of Nuclear Materials*, 276:22–32, 2000.

[110] C. S. Becquart, C. Domain, A. Legris, and J. C. van Duysen. Influence of the interatomic potentials on molecular dynamics simulations of displacement cascades. *Journal of Nuclear Materials*, 280:73–85, 2000.

[111] C.-C. Fu, F. Willaime, and P. Ordejón. Stability and Mobility of Mono- and Di-Interstitials in α-Fe. *Physical Review Letters*, 92(17):175503, April 2004.

[112] L. Malerba. Molecular dynamics simulation of displacement cascades in α-Fe: A critical review. *Journal of Nuclear Materials*, 351(1-3):28–38, June 2006.

[113] D. E. Harrison Jr, R. J. Rodriguez, and R. Smith. A simulation of liquid Cu and a comparison of sputtering of solid and liquid Cu under 1 keV Ar+ bombardment. *Journal of Physics: Condensed Matter*, 1:7113–7122, 1989.

[114] S. Ikeda and K. Ogawa. Structure Images of Y2O3 Corresponding to the Shift of Y-atoms. *Journal of Electron Microscopy*, 41:330–336, 1992.

[115] K. D. Hammond, H.-J. L. Voigt, L. A. Marus, N. Juslin, and B. D. Wirth. Simple pair-wise interactions for hybrid Monte Carlo-molecular dynamics simulations of titania/yttria-doped iron. *Journal of Physics: Condensed Matter*, 25(5):055402, March 2013.

[116] J. A. Nelder and R. Mead. A simplex method for function minimization. *Computer Journal*, 7(4):308–313, 1965.

[117] R. W. G. Wyckoff. *Crystal Structures*. Interscience, New York, 2nd edition, 1960.

[118] L. Kittiratanawasin. *Some Aspects of Radiation Effects in Ionic Systems*. PhD thesis, Loughborough University, 2011.

[119] Y. Jiang, J. R. Smith, and G. R. Odette. Prediction of structural, electronic and elastic properties of Y2Ti2O7 and Y2TiO5. *Acta Materialia*, 58(5):1536–1543, 2010.

[120] W. G. Mumme and A. D. Wadsley. The Structure of Orthorhombic Y2TiO5, an Example of Mixed Seven- and Fivefold Coordination. *Acta Crystallographica Section B Structural Crystallography and Crystal Chemistry*, 24(10):1327–1333, October 1968.

[121] B. P. Uberuaga, D. A. Andersson, and C. R. Stanek. Defect behavior in oxides: Insights from modern atomistic simulation methods. *Current Opinion in Solid State and Materials Science*, 17(6):249–256, December 2013.

[122] J. J. Thomson. XXIV. On the structure of the atom: an investigation of the stability and periods of oscillation of a number of corpuscles arranged at equal intervals around the circumference of a circle; with application of the results to the theory of atomic structure. *Philosophical Magazine Series 6*, 7(39):237–265, March 1904.

[123] M. Robinson, N. A. Marks, K. R. Whittle, and G. R. Lumpkin. Systematic calculation of threshold displacement energies: Case study in rutile. *Physical Review B*, 85(10):104105, March 2012.

[124] L. Kittiratanawasin, R. Smith, B. P. Uberuaga, and K. E. Sickafus. Radiation damage and evolution of radiation-induced defects in Er(2)O(3) bixbyite. *Journal of Physics: Condensed Matter*, 21(11):115403, March 2009.

[125] J. Lian, J. Chen, L. M. Wang, R. C. Ewing, J. M. Farmer, L. A. Boatner, and K. B. Helean. Radiation-induced amorphization of rare-earth titanate pyrochlores. *Physical Review B*, 68(13):134107, October 2003.

[126] T. Lazauskas, S. D. Kenny, and R. Smith. Influence of the prefactor to defect motion in α-Iron during long time scale simulations. *Submitted to Journal of Physics: Condensed Matter*.

[127] A. F. Voter. Introduction to the kinetic Monte Carlo method. In *Radiation Effects in Solids*, volume 235, chapter 1, pages 1–23. Springer Netherlands, 2007.

[128] C. Scott, S. Blackwell, L. Vernon, S. Kenny, M. Walls, and R. Smith. Atomistic surface erosion and thin film growth modelled over realistic time scales. *The Journal of Chemical Physics*, 135(17):174706, November 2011.

[129] B. P. Uberuaga, R. G. Hoagland, A. F. Voter, and S. M. Valone. Direct transformation of vacancy voids to stacking fault tetrahedra. *Physical Review Letters*, 99(13):135501, September 2007.

[130] G. Lucas and R. Schäublin. Vibrational contributions to the stability of point defects in bcc iron: A first-principles study. *Nuclear Instruments and Methods in Physics Research Section B: Beam Interactions with Materials and Atoms*, 267(18):3009–3012, September 2009.

[131] H. Schultz. Defect parameters of bcc metals: group-specific trends. *Materials Science and Engineering: A*, 141(2):149–167, 1991.

[132] F. Gao, D. J. Bacon, Y. N. Osetsky, P. E. J. Flewitt, and T. A. Lewis. Properties and evolution of sessile interstitial clusters produced by displacement cascades in α-iron. *Journal of Nuclear Materials*, 276:213–220, 2000.

[133] Y. Fan, A. Kushima, S. Yip, and B. Yildiz. Mechanism of Void Nucleation and Growth in bcc Fe: Atomistic Simulations at Experimental Time Scales. *Physical Review Letters*, 106(12):125501, March 2011.

[134] P. Brommer and N. Mousseau. Comment on Mechanism of Void Nucleation and Growth in bcc Fe: Atomistic Simulations at Experimental Time Scales. *Physical Review Letters*, 108(21):219601, May 2012.

[135] A. Kushima, X. Lin, J. Li, J. Eapen, J. C. Mauro, X. Qian, P. Diep, and S. Yip. Computing the viscosity of supercooled liquids. *The Journal of Chemical Physics*, 130(22):224504, June 2009.

[136] M. Eldrup and B. N. Singh. Accumulation of point defects and their complexes in irradiated metals as studied by the use of positron annihilation spectroscopy a brief review. *Journal of Nuclear Materials*, 323(2-3):346–353, December 2003.

[137] B. Puchala, M. L. Falk, and K. Garikipati. An energy basin finding algorithm for kinetic Monte Carlo acceleration. *The Journal of Chemical Physics*, 132(13):134104, April 2010.

[138] Y. Shim and J. Amar. Semirigorous synchronous sublattice algorithm for parallel kinetic Monte Carlo simulations of thin film growth. *Physical Review B*, 71(12):125432, March 2005.

[139] Y. Shim and J. G. Amar. Recent advances in parallel kinetic Monte Carlo: synchronous sublattice algorithm.